This electronic thesis or dissertation has been downloaded from the King's Research Portal at https://kclpure.kcl.ac.uk/portal/

Integrating c-Met Molecular Imaging into the Optimisation of Cancer Therapy.

Arulappu, Appitha

Awarding institution:
King's College London

The copyright of this thesis rests with the author and no quotation from it or information derived from it may be published without proper acknowledgement.

END USER LICENCE AGREEMENT

Unless another licence is stated on the immediately following page this work is licensed

under a Creative Commons Attribution-NonCommercial-NoDerivatives 4.0 International

licence. https://creativecommons.org/licenses/by-nc-nd/4.0/

You are free to copy, distribute and transmit the work

Under the following conditions:

- Attribution: You must attribute the work in the manner specified by the author (but not in any way that suggests that they endorse you or your use of the work).
- Non Commercial: You may not use this work for commercial purposes.
- No Derivative Works - You may not alter, transform, or build upon this work.

Any of these conditions can be waived if you receive permission from the author. Your fair dealings and other rights are in no way affected by the above.

Take down policy

If you believe that this document breaches copyright please contact librarypure@kcl.ac.uk providing details, and we will remove access to the work immediately and investigate your claim.

Download date: 04. May. 2023

Integrating c-Met Molecular Imaging into the Optimisation of Cancer Therapy.

A thesis submitted to the King's College London for the degree of Doctor of Philosophy

By

Appitha Arulappu

The Richard Dimbleby Laboratory

Division of Cancer Studies and

Randall Division of Cell and Molecular Biophysics,

School of Medicine

King's College London, London SE1 1UL

July 2016

Dedicated to My Excellent Dad

One who inspired, encouraged and never gave up

ACKNOWLEDGEMENTS:

First and above all, I would like to thank God for this opportunity. The projects I have been working on were very interesting but I felt very much out of my comfort zone. I truly believe that God has been my help and guidance in those challenging times.

I would like to thank Prof Tony Ng, for selecting me on this PhD programme, for his endless support and patience and encouraging me to work on a project I did not initially think I could achieve. I am truly grateful to have had a good supervisor with a great wealth of knowledge and wisdom.

I would like to thank every member of the Dimbleby department and Randall Division for their help and support throughout the past few years and this includes Dr James Monypenny and Dr Gregory Weitsman who have both taught me many useful things which include great laboratory skills and for teaching me to build up my work ethics, Dr Fabian Flores, for his great scientific support and friendship, Dr Rachel Evans, for her kindness, professionalism and proofreading my entire thesis, Dr Oana Coban, for her lively personality and authenticity, Dr Ruhe Chowdhury, for her baking skills, clinical knowledge and help, Dr Myria Galazi, for her kindness and friendship. I would also like to thank Dr Peter Gordon and Dr Jonathan Caron, for their cheerful attitudes and Tamara de Koning who has been a great friend and individual. I would also like to acknowledge Felix Wong and Ines Garcia, who have been great lab bench buddies. I would also like to thank past members of this team, Dr Hanna Milewicz, Dr Anthony Cheung, Dr Sheeba Khan, Dr

Paulina Szyszka and Dr Michel Eisenblaetter as it has been a pleasure to work with them. I would like to thank Dr Michaela Perani for her kind help and expertise, the physicists, especially Dr Viviane Devauges and Camille Perrin for being great individuals. Big thanks to Dr Rebecca Marlow, Erika Franscesch, Dr Patrycja Gazinska, Dr Enrique Miranda-Rota and Natalie Woodman for their teaching skills and valuable scientific support.

As part of my PhD involved collaborating with GE Healthcare, I had the privilege to meet some amazing individuals, with great expertise in the imaging field, and experience the world of industry. I would like to give special thanks to Dr Sven Macholl who initially supervised me at the GE, and always made me feel very welcomed as well as providing a huge amount of support on the scientific side, both intellectually and technically. I would also like to thank Mark Battle, who took over Sven's role on the technical side, and helped me hugely in the completion of my project at the GE. I would also like to give my warmest thanks to Dr Susan Hoppmann, who has been very supportive during my time at the GE, imparting her invaluable knowledge and experience in medical imaging and proofreading part of my thesis. I would also like to thank the radiochemists Dr Graeme McRobbie and Dr Imtiaz Khan for the provision of the tracer and their cheerful nature. I would also like to acknowledge Joanne Nesbitt, Rochelle Lear and David Gendle who have provided great support for the in-vivo side of my project. I would like to thank Grethe Dalsgaard, the project leader in early clinical development at the GE who ensured that my project was going smoothly, despite the changes that were made during my time there. I am very grateful for all those people, who showed great professionalism, scientific support and kindness.

I would also like to thank the radiochemists and imaging scientists based at St Thomas' hospital: Dr Michelle Ma for providing support in the radiolabelling of the fragment variable antibody and Dr Julia Blower for her help and useful suggestions. I would like to thank Dr Gilbert Fruhwirth who has been beyond helpful and his team, especially Alessia Volpe and Bruce Fanshawe for their undivided support in the SPECT imaging experiment.

Thanks to my amazing 'King's crew': Rebecca Alade, Saleha Hassan, Natasha Khalife and Tabetha Bhatti for being there through thick and thin. Huge thanks to my lovely friends Dami, Natalia and Lydia for their love and care.

Last but not least, I would like to thank my mum and my sisters for moral support and for their supply of homemade food and laughter. Huge thanks to my amazing husband John who encouraged me to work hard, took me on holidays when I needed a break, and proofreading my entire thesis.

Thank you all!

ABSTRACT:

Basal-like subtypes of breast cancer (BLBC) account for about 15-20% of all breast cancer, affecting younger women (<50 years old) of predominantly African and Hispanic descent [1] with rapid relapse ([2]. c-Met is overexpressed in various solid tumors, lung, breast, ovary, kidney, colon, thyroid, liver, and gastric carcinomas [3]; [4]; [5]; [6]; [7]; [8]; [9]; [10]; [11]; [12]; [13]; [14]. In breast cancer, a higher c-Met expression level is displayed in BLBC in comparison to other intrinsic breast cancer subtypes [15] . In the first part of this thesis, the basal-like breast tumour xenograft mouse model was used to investigate early signs of locoregional recurrence of primary tumour using a ^{18}F radiolabelled c-Met binding peptide, [^{18}F]AH113804. [^{18}F]AH113804 exhibited significantly higher uptake in the tumours (in comparison to mammary fatty tissue) with a target to background (muscle) ratio of approximately 3:1 ($p<0.01$). In addition to this, [^{18}F]AH113804 was able to detect local tumor recurrence as early as six days after tumour resection [16]. Following publication of this work, I designed an in-house radiolabelled single chain Fv-Fc fusion against human c-Met, which was selected from a phage display library, and labelled with Cy5 dye initially. It was then labelled with the radioisotope ^{111}In that was conjugated with the chelator CHX-A''DTPA for an increase in radiolabelling efficiency. Both the optical and the radiolabelled version of the scFv-Fc were injected into dual tumour-bearing female mice. The tracer's uptakes at the c-Met positive tumour (basal-like breast tumour) and in the c-Met negative but ER positive breast adenocarcinoma), were visualised using an optical detector (for the

Cy5 labelled tracer) and a gamma camera (using the SPECT tracer). We detect a higher uptake in the c-Met positive basal-like breast tumour in comparison to the c-Met negative control tumours using both versions of the tracer.

EGFR expression has been reported in at least 50% of basal-like breast cancers (BLBCs) [17]. Due to the essential role of EGFR in both proliferation and cell survival pathways in breast epithelium and other epithelia, EGFR inhibitors have been used in clinical trials to treat patients with BLBC [18]. Unfortunately, this was shown to be of limited success [19]. There is a need to gain a deeper understanding of EGFR signalling in order to identify potential therapeutic targets. In the third part of this thesis, assays were carried out to investigate further the effect of PTPN11 knockdown on EGFR and c-Met phosphorylation, cell proliferation and E-cadherin level of expression in basal like breast cancer cells. PTPN11 was identified as an EGFR modulator based on the outcome from a high content screen based on FRET sensing of EGFR activity in situ, monitored by fluorescence lifetime imaging (FLIM). Validation of this novel regulator of EGFR activity in BLBC confirmed a significant slowing of the kinetics of EGFR dephosphorylation upon ligand stimulation, as well as c-Met hyperphosphorylation in cells that were depleted of PTPN11 in PTPN11-silenced cells following EGF stimulation.

Table of Contents

LIST OF FIGURES:

LIST OF TABLES:

LIST OF ABBREVIATIONS:

Abbreviation	Meaning
% ID/g	Percentage Injected Dose per gram
% ID/mL	Percentage Injected Dose per millilitre
18F-FDG	18F-Fluoro-Deoxyglucose
	A
Anti-CEA	Anti–Carcinoembryonic Antigen
AP2	Adaptor Protein 2
ATP	Adenosine Tri Phosphate
	B
BC	Breast Cancer
BCL2	B-Cell CLL/Lymphoma 2
BCL-XL	B-Cell Leukemia XL
BCS	Breast Conserving Surgery
BCT	Breast-Conserving Treatment
BLBC	Basal like Breast Cancer
BSA	Bovine Serum Albumin
	C
CAD	Computer-Aided Detection
Cbl	Casitas B-lineage Lymphoma
CCVs	Clathrin-Coated Vesicles
CDR	Complementary Determining Region
CT	Computed Tomography
	D
DABCO	1,4-diazabicyclo[2.2.2]octane
DARPs	Designed Ankyrin Repeat Proteins
DBT	Digital Breast Tomosynthesis
DEP-1	Density-Enhanced Phosphatase-1
DMEM	Dulbecco's Modified Eagle Media

DMSO	Dimethyl sulfoxide
DNA	Deoxyribonucleic acid

E

ECL	Enhanced Chemiluminescence
EDTA	Ethylenediaminetetraacetic Acid
EGF	Epidermal Growth Factor
eGFP	Enhanced Green Fluorescent Protein
EGFR	Epidermal Growth Factor Receptor
ELISA	Enzyme-Linked Immunosorbent Assay
EMT	Epithelial to Mesenchymal Transition
ER	Estrogen Receptor
ER	Endoplasmic Reticulum
Erk	Extracellular signal-Regulated Kinase
ESCRT-1	Endosomal Sorting Complexes Required for Transport-1
EtOH	Ethanol

F

FA	Focal Adhesion
FBS	Fetal Bovine Serum
FFPE	Formalin Fixed Paraffin Embedded
FLIM	Fluorescence Lifetime Imaging Microscopy
FLT	Fluorothymidine
FRET	Förster (or fluorescence) Resonance Energy Transfer

G

GAB1	Growth factor receptor-bound protein 2-Associated Binder 1
GBq	Gigabequerel
Grb2	Growth factor Receptor-Bound protein 2

H

H&E	Haematoxylin and Eosin
HEPES	4-(2-hydroxyethyl)-1-piperazineethanesulfonic acid
HER2	Human Epidermal Growth Factor Receptor 2
HER2	Human Epidermal Growth Factor receptor 2
HER3	Human Epidermal Growth Factor receptor 3
HER4	Human Epidermal Growth Factor receptor 4
HGF	Hepatocyte Growth Factor

HGF	Hepatocyte Growth Factor
HPRD	Human Protein Reference Database

I

IgG	Immunoglobulin G
IHC	Immunohistochemistry
IKK	Inhibitor-α Kinase
IVIS	*In-vivo* Imaging System
IκB	nuclear factor-κB inhibitor-α

J

JMML	Juvenile Myelomonocytic Leukemia

K

K_d	dissociation constant
kDa	Kiloaaltons
KeV	Kilo Electron Volt
kVp	Peak Kilovoltage

L

LB	Luria-Bertani
LRR	Locoregional Recurrence

M

mAb	monoclonal Antibody
MAPK	Mitogen-Activated Protein Kinase
MBC	Metastatic Breast Cancer
MBD	c-Met Binding domains
MPD	Myeloproliferative Disorder
mRFP1	Monomeric Red Fluorescent Protein 1
MRI	Magnetic Resonance Imaging
MVB	Multivesicular Bodies

N

NF-kB	Nuclear Factor-κB
NIR	Near Infra-Red
NIS	Nikon Instrument Software
NSCLCs	Non Small Cell Lung Cancer
NSG mice	NOD Scid Gamma mice

O

OCT	Optimal Cutting Temperature
ORR	Objective Response Rate
OS	Overall Survival

P

p.i	Post Injection
PARPi	Poly(ADP-ribose) Polymerases Inhibitors
PBS	Phosphate Buffer Saline
pCR	pathologic Complete Response
PEI	Polyethylenimine
PET	Positron Emission Tomography
PFA	Paraformaldehyde
PFS	Progress Free Survival
PI3-K	Phosphoinositide 3-Kinase
Picchu	Phosphorylation Indicator of Crk Chimeric Unit
PKC	Protein Kinase C
PLC	Phospholipase C
PMSA	Prostate-Specific Membrane Antigen
PR	Progesterone Receptor
PTB	Phosphotyrosine Binding
PTP1B	Protein-Tyrosine Phosphatase 1B
PTPN11	Non-receptor type 11 protein tyrosine phosphatase
PTPN12	Non-receptor type 12 Protein Tyrosine Phosphatase
PTPs	Protein Tyrosine Phosphatases

R

RFU	Relative Fluorescent Units
RHS	Right hand side
ROI	Region Of Interest
Rpm	Revolutions Per Minute
RPMI	Roswell Park Memorial Institute

RTK	Receptor Tyrosine Kinase

S

SABCS	San Antonio Breast Cancer Symposium
ScFv	Single Chain Fv fragment
ScFv-Fc	Single-Chain Fv-Fc
SD	Standard Deviation
SDS-PAGE	SDS-Polyacrylamide Gel Electrophoresis
SE-HPLC	Size Exclusion-High-Performance Liquid Chromatography
SEM	Standard Error of the Mean
SF	Scatter Factor
SH2	Src homology-2 domains
SHC	Src homologous and collagen
SHP2	Src Homology 2 domain-containing Phosphatase
shRNA	Short Hairpin Ribonucleic Acid
SILAC	Stable Isotope Labelling with Amino Acids in Cell Culture
siRNA	Short Interfering Ribonucleic Acid
SOS	Son of Sevenless
SPE	Solid Phase Extraction
SPECT	Single Photon Emission Computed Tomography
Src	Sarcoma
STAT3	Signal Transducer and Activator of Transcription 3

T

TBS	Tris Buffered Saline
TK	Tyrosine Kinase
TKI	Tyrosine Kinase Inhibitors
TMRR	Target-to-Muscle Retention Ratio
TNBC	Triple Negative Breast Cancers

U

US	Ultrasound
UV	Ultraviolet

V

VEGF	Vascular endothelial growth factor
VH	Variable Heavy
VL	Variable Light

W

WST-1	Water Soluble Tetrazolium-1

LIST OF PUBLICATIONS:

- **Arulappu A**, Battle M, Eisenblaetter M, McRobbie G, Khan I, Monypenny J, Weitsman G, Galazi M, Hoppmann S, Gazinska P, Wulaningsih W, Dalsgaard G, Macholl S, Ng T. c-Met PET Imaging Detects Early Stage Loco-Regional Recurrence of Basal-Like Breast Cancer, J Nucl Med. **2015** Dec 3

- Beatson R, Maurstad G, Picco G, **Arulappu A**, Coleman J, Wandell HH, Clausen H, Mandel U, Taylor-Papadimitriou J, Sletmoen M, Burchell JM. The Breast Cancer-Associated Glycoforms of MUC1, MUC1-Tn and sialyl-Tn, Are Expressed in COSMC Wild-Type Cells and Bind the C-Type Lectin MGL. PLoS One. **2015** May 7;10(5):e0125994

International Conference Poster presentation:

- **Arulappu A**, Battle M, Eisenblaetter M, McRobbie G, Khan I, Monypenny J, Weitsman G, Galazi M, Hoppmann S, Gazinska P, Wulaningsih W, Dalsgaard G, Macholl S, Ng T. c-Met PET Imaging Detects Early Stage Loco-Regional Recurrence of Basal-Like Breast Cancer, Abstract of the European Society for Molecular Imaging, no 195, March **2016**

Chapter 1: INTRODUCTION

1.1 Basal like breast cancer

Breast cancer (BC) is not a single entity, but rather a class of distinct biological subtypes [20]. It is a worldwide disease and has been associated with urbanisation, an increased in the life expectancy and personal behaviours such as smoking, obesity, alcohol consumption, hormone replacement therapy and inactivity [21]. BC is the most commonly diagnosed cancer in women in the UK, affecting one in nine women [22].The Stanford group has pioneered the gene expression microarray-based class discovery studies which have led to the identification of at least five molecular breast cancer subtypes: luminal A, luminal B, normal breast-like, HER2, and basal-like [23]. It has been observed that the difference in histopathological and biological features between subtypes of breast cancer exhibit distinct behaviours causing different treatment responses and the devise of different therapeutic strategies [24] For example, the luminal tumours begin in cells that line the ducts and glands and tend to display a slow tumour growth while the basal-type sprout from the deep layers of the ducts and glands and grow much quicker than the luminal types [24]. Table 1-1 provides a clear description of the characteristics and prognosis for the various breast cancer subtypes. BLBCs are characterized by high histological grade and mitotic indexes, pushing borders and large areas of necrosis [25]. Epidemiologically, BLBCs and triple negative breast cancer (TNBC) are more common in younger women (<50 years old) of African and

Hispanic descent [1]. Basal like breast cancer (BLBC) is a particularly aggressive subtype of breast cancer, and accounts for less than 15% of all invasive breast cancers affecting younger women with rapid relapse [2]. Clinically, those patients have higher grade tumors, and present with higher tumor stage at diagnosis. Histologically, they display invasive ductal carcinomas, metaplastic and medullary cancers, and are often poorly differentiated [26]. Previous studies have shown that the basal-like is an independent marker of poor prognosis in breast cancer [27]. Gene expression profiling defines the basal like subtype in three different categories: **1)** negative for estrogen receptor (ER), progesterone receptor (PR), and human epidermal growth factor receptor 2 (HER-2) (also called triple negative) **2)** positive for one of more cytokeratins (CK5/6, CK14 and CK17) **3)** lack ER and HER2 along with the expression of epithelial growth factor receptor (EGFR) and CK5/6 and **4)** lack ER, PR, HER2 along with the expression of CK5/6 and/or EGFR [28].Up to 15%–45% of BLBCs have been shown to express ER and 14% of BLBCs express HER-2, which suggest that not all BLBCs are Triple Negative Breast Cancers (TNBCs) [29]. TNBC is characterised by a lack of expression of estrogen, progesterone receptor and human epidermal growth factor receptor. BLBC and TNCBCs are subtypes that overlap due to the similarity in their lack of hormone receptors, and have therefore limited targeted therapeutic options [30].

Table 1-1. Summary of the breast tumor molecular subtypes

Breast Cancer subtypes	These tumours tend to be	Grade	Outcome
Luminal A	ER positive and/or PR positive HER2 negative Low Ki67	1 or 2	Good
Luminal B	ER positive and/or PR positive HER2 positive (or HER2 negative with high Ki67)	2 or 3	Intermediate Poor
HER2 over-expression	ER negative and/or progesterone negative HER2 positive	2 or 3	Poor
Basal	ER negative and progesterone negative HER1 negative basal marker positive	3	Poor
Normal-like	ER positive and/or PR positive HER2 negative Low Ki67	1 or 2 or 3	Intermediate

1.1.1 Recurrence patterns in BLBCs:

Both TNBC and BLBCs are considered to be more aggressive than other breast cancer subtypes, with early recurrence patterns [31]. A study has shown that the rate of recurrence for triple-negative breast cancer was 33.9% in comparison to 20.4% for other subtypes. Recurrence occurs most often in the first 5 years. After relapse, the overall survival is much shorter than in patients with other types of breast cancer [31].

It has been shown that basal-like breast cancers are more likely than other types of breast cancer to metastasize to the viscera (particularly to the lungs, brain and soft tissue), to be node negative and do not often metastasize to bone [28]. Locoregional recurrence (LRR) is defined as the reappearance of breast cancer in the breast where the primary tumour has been removed

surgically. LRR is a well-established predictor of distant outcomes [20] so it is important to detect the regrowth as early as possible. Local recurrence as a whole was shown to be a strong independent predictor of a higher likelihood of developing metastases as well as a reduction for overall survival rate [32]. From the early 1900s onwards, surgical excision of the breast tumours mass was the core method in treating breast cancer. This excision comprises radical mastectomy, which is the removal of the whole breast, including the underlying chest muscle and lymph nodes of the axilla, and breast-conserving treatment (BCT), in which only part of the breast tissue, affected by the tumour, is being removed. Recently, some patients are treated with radiotherapy instead of surgery as a first line treatment. While the long term survival rate of patients that underwent BCT or mastectomy is the same, numerous studies have shown that there is a higher risk of local recurrence in young patients after BCT than those that has had mastectomy [33]. Additionally, other studies have shown a significant increase in LRR rate after BCT for patients lacking ER and PR expression in comparison to other subtypes [34, 35]. A recent study that identified 11,073 patients who had breast cancer surgery performed between November 1995 and December 2011 showed that 787 of those patients ended up with locoregional recurrence [36]. The involvement of chest wall in the tumour regrowth would make another surgical intervention very risky. Additionally, Montagna et al. showed in their study that in patients with TNBC, locoregional recurrence was predictive of a higher risk of subsequent events and death.[36]

1.1.2 Current treatments and potential future treatments for TNBCs and BLBCs:

Following surgical removal of the breast tumour tissue via mastectomy or BCT, treatments for triple negative breast cancer and basal-like breast cancer include either radiotherapy and/or systemic chemotherapy with third generation (taxane containing) adjuvant [37]. Taxane based neoadjuvant therapy increase the pathological complete response (pCR) by 45% in BLBC in comparison to 6% in the luminal subtype [38]. A number of studies have shown the sensitivity of tumours with aberration in the *BRCA1* gene, such as TNBCs, to platinum-based therapies [39]. It is thought that BRCA1 mutant cancer cells have a defect in the homologous recombination-based repair of double stranded DNA breaks, and would therefore be sensitive to platinum salts, that are inter-strand cross-linking agents. The addition of cisplatin to metronomic methotrexate and cyclophosphamide, in a randomised phase II trial (N = 126), led to an improvement in median time-to-progression (TTP) of 6 months (from 7 to 13 months) and OS of 4 months (from 12 to 16 months) in second-line metastatic TNBC patients. [40]

Another type of treatment currently being assessed, in clinical trials, is the use of PARP inhibitors (PARPi). Poly(ADP-ribose) polymerases (PARPs) are nuclear enzymes which synthesise the ADP-ribose polymer driving the assembly of DNA-repair complex at sites of DNA damage, and supporting BER and single strand break repair (SSBR) pathways [41]. PARPi have the

ability to interfere with the DNA damage repair systems of cancer cells [42]. The data generated so far shows more promise in BRCA-related TNBCS than for sporadic TNBCs. Indeed, a recent study shows 63% of the BRCA1/2 carriers have a reduced tumour size and a stable disease for more than 8 weeks in comparison to only 13% of sporadic tumours [43].

Antiangiogenic agents are also being assessed in clinical trials as mean of therapeutic agents in TNBC patients. In particular bevacizumab, a monoclonal antibody (mAb) targeted against VEGF, was given in addition to the physician's choice of chemotherapy to Metastatic Breast Cancer (MBC) patients. This phase III clinical trial demonstrates that there is a median Progress Free Survival (PFS) of 6 months for TNBC treated with bevacizumab, in comparison to 2.7 months for first line of chemotherapy regimens [44]. More recently, the addition of bevacizumab to standard neoadjuvant chemotherapy significantly improved pathologic complete response (pCR) rates in women with basal-like breast cancer compared with non-basal-like subtypes, according to an analysis of the CALGB 40603 trial (2014 San Antonio Breast Cancer Symposium (SABCS)). Further data presented at the 2015 San Antonio Breast Cancer Symposium showed that, after 3 years of follow-up, the researchers have now found that women who had a pathologic complete response were 70% less likely to have the cancer come back (recurrence) and 80% more likely to be alive than women who didn't have a pathologic complete response.

Approximately half of BLBC express EGFR based on immunohistochemistry, are dependent on the EGFR pathway for proliferation and are sensitive to EGFR inhibitors [17]. The latter (e.g. cetuximab) have shown to have low efficacy as single agents in BLBCs and TNBC. However, in conjunction with cisplatin, as demonstrated in the phase II BALI-1 trial, there is an increase in PFS by 2.2 months in comparison to cisplatin alone [18].

Another popular targeted agent for treatment of BLBC and TNBCs is c-Met. c-Met and its ligand HGF are upregulated in at least 20-30% of BC [45]. Numerous studies have demonstrated a preferential overexpression of c-Met in basal-like subgroup [46]. Currently MetMAb is being assessed in a randomised phase II study for metastatic TNBC in combination with paclitaxel and bevacizumab [47]. Likewise ARG 197, an oral c-Met inhibitor is under clinical trial [48].

1.2 The implications of c-Met in BLBC:

1.2.1 The structure of c-Met and its ligand HGF

The hepatocyte growth factor (HGF), which is the ligand for the c-Met tyrosine kinase receptor is a potent inducer of invasive growth [49]. Initially secreted as a single-chain inert precursor, it is then converted into a functional heterodimer. HGF is highly distributed in the extracellular matrix of most tissues, mainly in its inactive form, and is sequestered by heparin-like proteoglycans. HGF/SF is believed to be a mesenchymal cell-derived cytokine [50]. HGF-MET signalling has many biological functions and

includes playing a protective role in liver cirrhosis, lung fibrosis and wound healing [51].

Due to the importance of c-Met in basal like breast cancer, it is worth discussing its structure, functionality and biological effects in detail. c-Met is classified as a member of a RTK subfamily [52]. It is expressed by a variety of normal and malignant cells [53] and is predominantly distributed in epithelial cells of many organs which include the liver, pancreas, prostate, kidney, muscle and bone marrow [50, 54]. Initially, c-Met is produced as a 170 kDa precursor which is broken down into a 50 kDa extracellular α-subunit and a 145 kDa transmembrane β-subunit [55];[56]. Both subunits are joined via a disulphide bond [56]. The extracellular portion of c-Met is made of three domain types: a Sema domain (which comprises the whole α-subunit and part of the β-subunit), a PSI domain (present in plexins, semaphorins and integrins) and four IPT domains (immunoglobulin-like fold shared by plexins and transcription factors) which connects the PSI domain to the transmembrane helix. The SEMA–PSI domain was shown to provide a binding site for the α-chain of the ligand HGF [57]. The intracellular domains include three further domains which are the following: the juxtamembrane region, the catalytic domain and the multifunctional carboxy-terminal docking site [49, 51]. (Fig 1-1)

Those domains are functional and the juxtamembrane region has a key tyrosine residue (Y1003) which is implicated in downregulating c-Met; the catalytic domain holds the Y1234 and Y1235 residues and contains the

catalytic kinase domain; and finally, the multifunctional carboxy-terminal docking site which serve as a docking site to other signalling proteins [58].

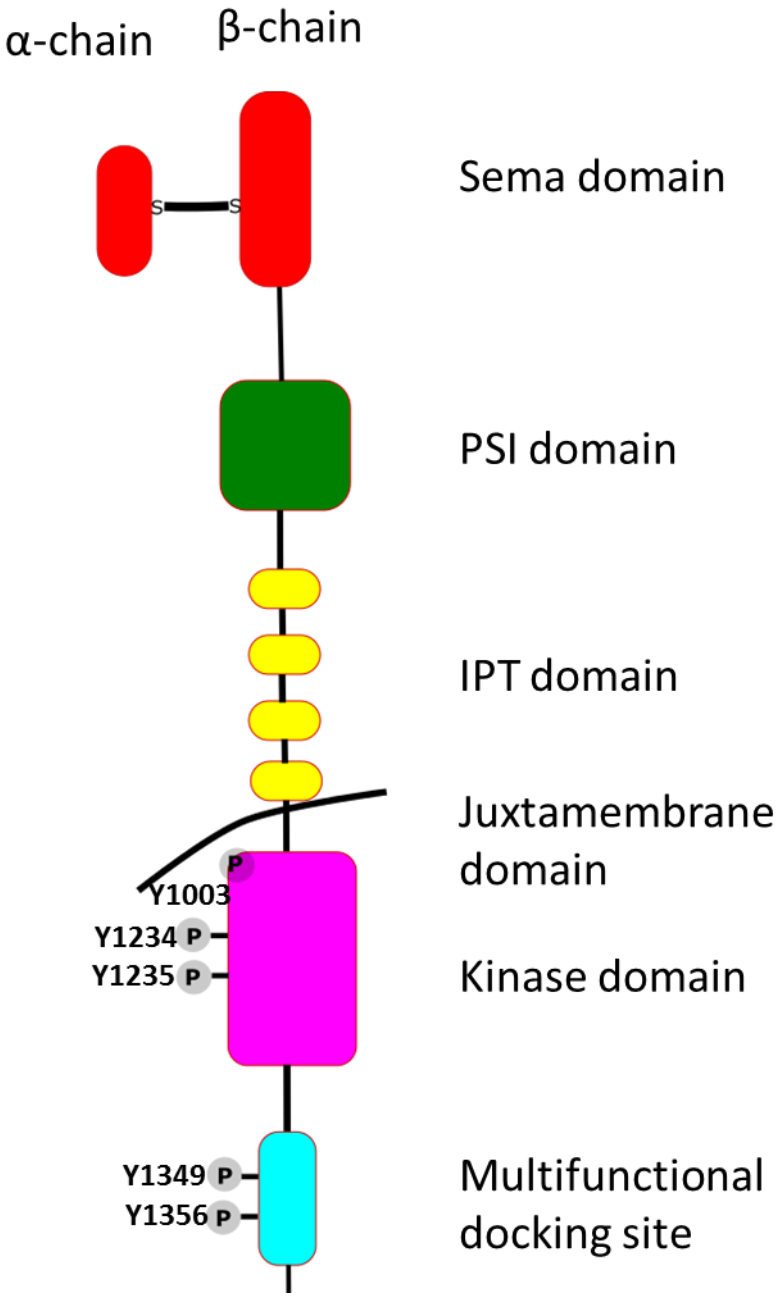

Figure 1-1. Domain structure of c-Met and hepatocyte growth factor (HGF).

The c-Met receptor is formed into a disulphide-linked α/β heterodimer. The extracellular portion of c-Met is composed of three domain types: the N-terminal with a large semaphorin (Sema) domain, with the whole a-subunit and part of the b-

subunit, a plexin semaphorin integrin (PSI) domain, and a transmembrane helix via four immunoglobulin plexin transcription (IPT) domains. Intracellularly, the c-Met receptor contains a tyrosine kinase catalytic domain with a juxtamembrane and carboxy terminal sequences. This portion of c-Met contains the catalytic tyrosines Y1234 and Y1235, which positively modulate enzyme activity. The juxtamembrane tyrosine 1003 negatively regulates c-Met by recruiting the ubiquitin ligase casitas B-lineage lymphoma (c-CBL). The C-terminal tail that serves as a multifunctional docking site contains tyrosines Y1349 and Y1356, which recruit several transducers and adaptors following c-Met activation.

1.2.2 c-Met signalling

Following HGF binding, c-Met gets activated by receptor dimerisation which is followed by a trans-phosphorylation of Y1234 and Y1235 within the kinase activation loop. This activates the intrinsic kinase activity of c-Met. Two 'docking' tyrosines in the carboxyl-terminal tail (Y1349 and Y1356) get phosphorylated (figure 1-2), activating the multisubstrate signal transducer docking site (Y1349VHVX3Y1356VNV) , which consists of the docking sites that bind Src homology-2 (SH2) domains, phosphotyrosine binding (PTB) domains, and c-Met Binding domains (MBD) of signal transducers and adapter proteins [51, 52]. Analysis using a mutated version of this multisubstrate docking site suggests that Y1349 and Y1356 mediate the interactions with SHC, Src, and growth factor receptor-bound protein 2-associated binder 1 (Gab1) while recruitment of growth factor receptor-bound protein 2 (Grb2), PI3-K, PLC-g, and SHP2 is mediated by Y1356 alone [59]. In addition, Y1365 regulates cell morphogenesis. The Y1003 residue, as observed in Figure 1-1, binds to c-Cbl, and therefore plays an important role in regulating c-Met internalisation. The activation of c-Met has been implicated to the best-known intracellular pathways which include the

Erk/mitogen-activated protein kinase cascade, the phosphoinositide 3-kinase/Akt pathway, STAT3 and the Rac1/Cdc42 pathway [49, 60] (Fig 1-2). These signalling pathways modulate migration, cellular proliferation, invasion and tubulogenesis [56, 60]. It has been discovered that KRAS and the downstream MAPK pathway are activated through the binding of SHC and GRB2 to the activated c-Met [61]. In addition, the p85 subunit of PI3K binds to the activated c-Met directly or indirectly through GAB1 and consequently promotes cell survival [62]. Thereby the transcription of the anti-apoptotic proteins BCL2 and BCL-XL, which sustain the pro-survival signal, are prompted through the activation of the PI3K-AKT pathway [63] (fig 1-3). In addition to this, STAT3 gets phosphorylated by binding to c-Met thereby inducing tubulogenesis and invasion by migrating to the nucleus.[64] (Fig 1-3).The c-Met-SRC-FAK interaction causes the induction of anchorage-independent growth and cell migration [65]. c-Met generated signals can cause modifications of phosphorylation of important cytoskeletal regulatory and structural proteins. An example is the phosphorylation of focal adhesion kinase (p125FAK) at pY397 (autophosphorylation site, with binding to Src family SH2 and the p85 subunit of PI3-K) and pY861 (the major Src phosphorylation site) following c-Met activation by HGF and promotes cell proliferation, cell survival and migration [66]. Further to this, the activation of NF-kB has been shown to be essential for HGF-mediated proliferation and tubulogenesis in studies characterizing the liver derived MLP29 cell line [67].

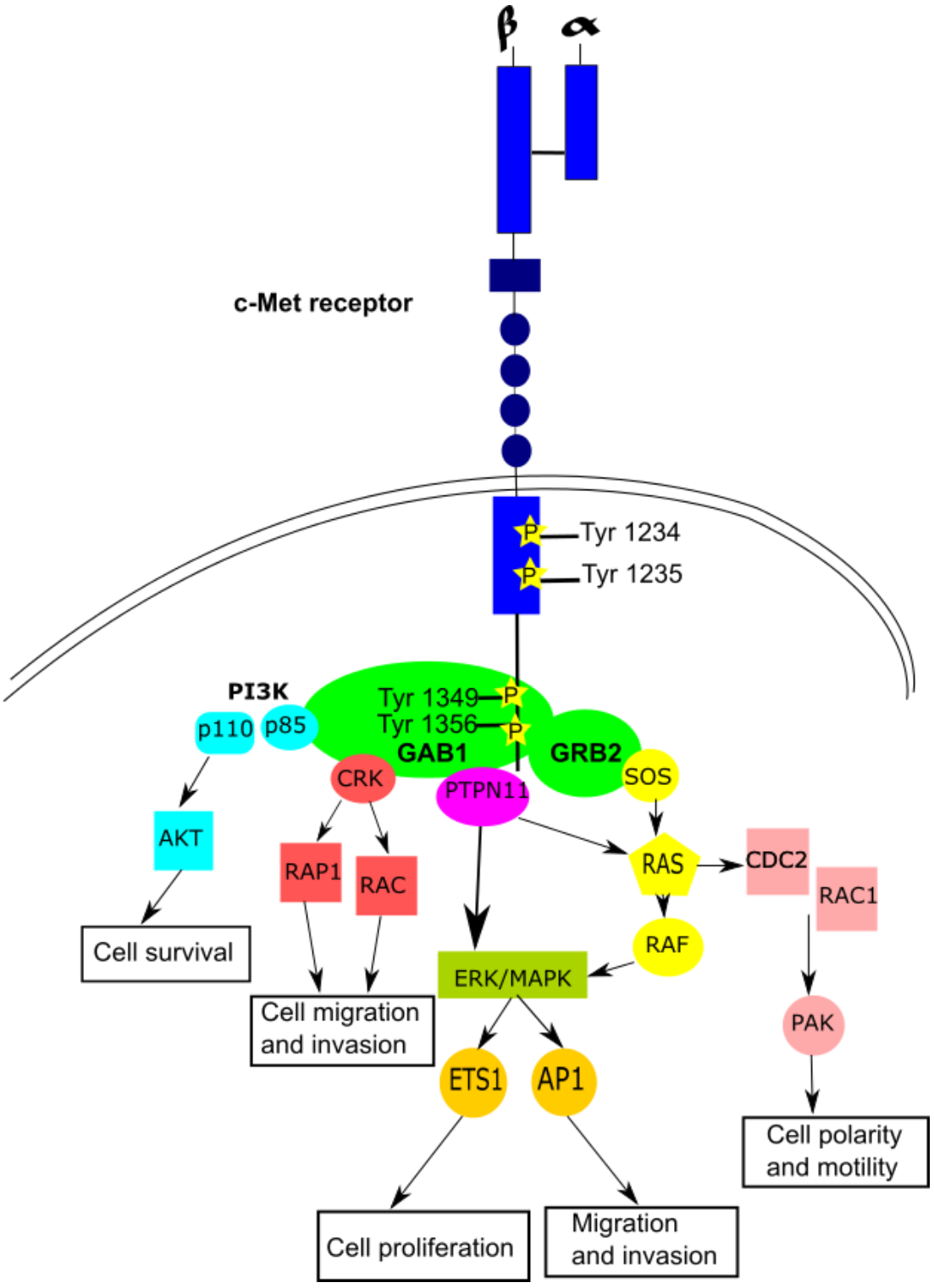

Figure 1-2. Structure and signaling machinery of the Met receptor.

c-Met is an α/β heterodimer formed by a completely extracellular α subunit and a transmembrane β subunit that contains the tyrosine kinase activity. The extracellular region of Met encompasses a large Sema domain, a cysteine-rich domain and four repeats of an unusual type of immunoglobulin-like domain. The intracellular portion of Met includes the kinase domain – with two catalytic tyrosines (Tyr1234 and

Tyr1235) that enhance the receptor enzymatic activity following transphosphorylation – and key tyrosine residues in the carboxy-terminal tail (Tyr1349 and Tyr1356). Phosphorylation of these distal tyrosines creates docking sites for several interactors, many of which are schematized here. Shp2 is a protein tyrosine phosphatase (PTP) and is also known as PTPN11 (please also refer to section 1.4.2 and Chapter 6 of this thesis).

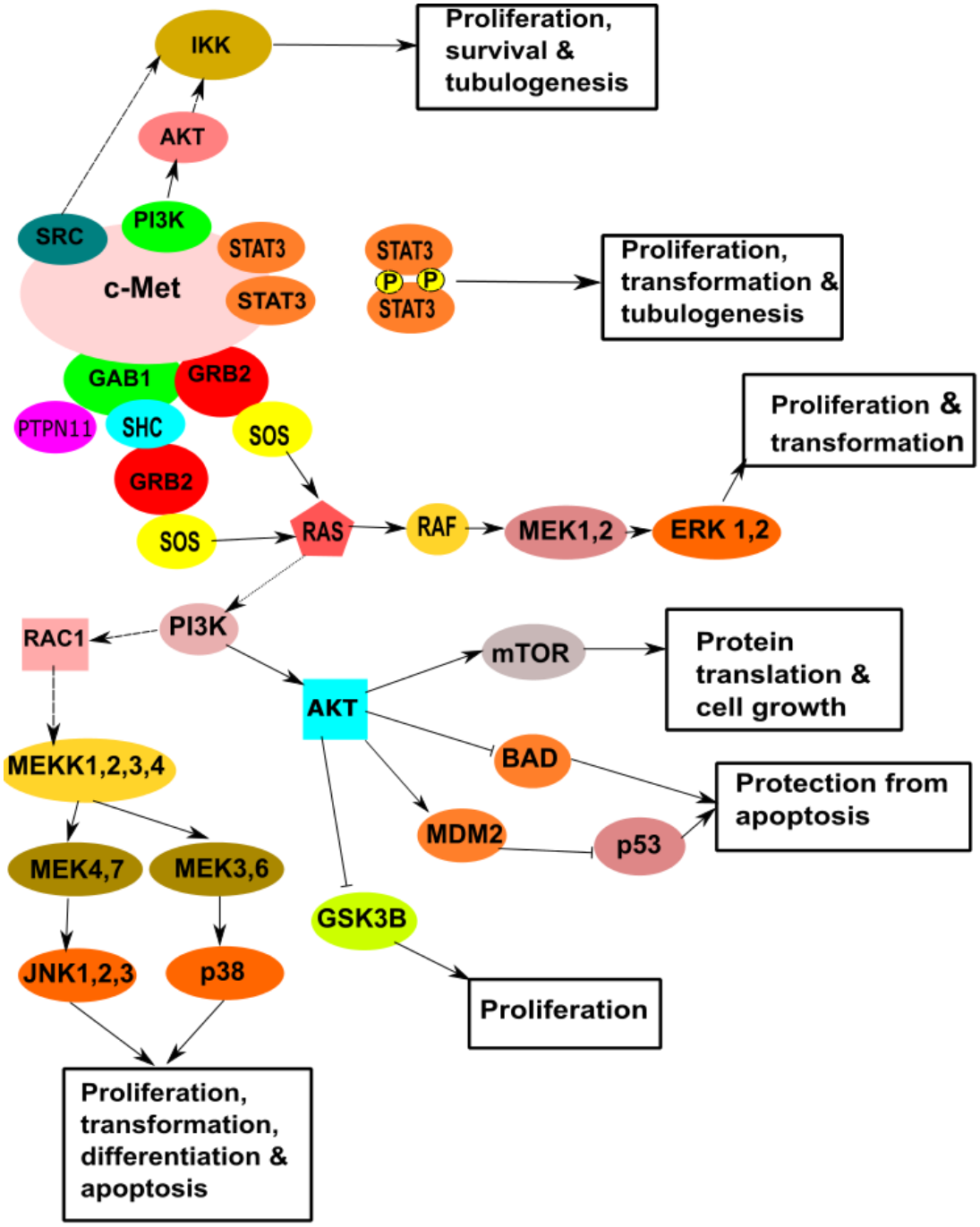

Figure 1-3. c-Met (also known as HGF receptor) triggers several downstream pathways.

The mitogen-activated protein kinase (MAPK) cascades consist of three subfamilies, each of which comprises three protein kinases that activate one another sequentially. Phosphoinositide 3-kinase (PI3K) is a lipid kinase and associates with the multifunctional docking site of c-Met catalysing the formation of phosphatidylinositol (3,4,5)-triphosphate (PtdIns(3,4,5)P3). Production of PtdIns(3,4,5)P3 creates a docking site for Akt. Signal transducer and activator of

transcription 3 (STAT3) monomers bind to c-Met through their Src-homology-2 domain (SH2 domain) and become trans-phosphorylated. In response to c-Met stimulation and the activation of PI3K- and Src-dependent pathways, nuclear factor-κB inhibitor-α kinase (IKK) is activated, and phosphorylates the nuclear factor-κB inhibitor-α (IκB) proteins (which are bound to nuclear factor-κB (NF-κB)).

1.2.3 c-Met endocytosis

After signalling, c-Met associates with E3 ubiquitin protein ligase Cbl, which leads to the phosphorylation of Tyr1003, causing the targeting of c-Met into an early endosome and then a multivesicular body which is subjected to lysosomal degradation. (Figure 1-4b) [49]. PKC, when activated, also causes the internalisation of c-Met, but promotes c-Met's signalling [49]. It induces the internalisation of c-Met into an early endosome, leading onto ERK activation, hence favouring the delivery of Erk to focal adhesion (FA) which then induces cell migration and promotes c-Met signalling (Figure 1-4a).

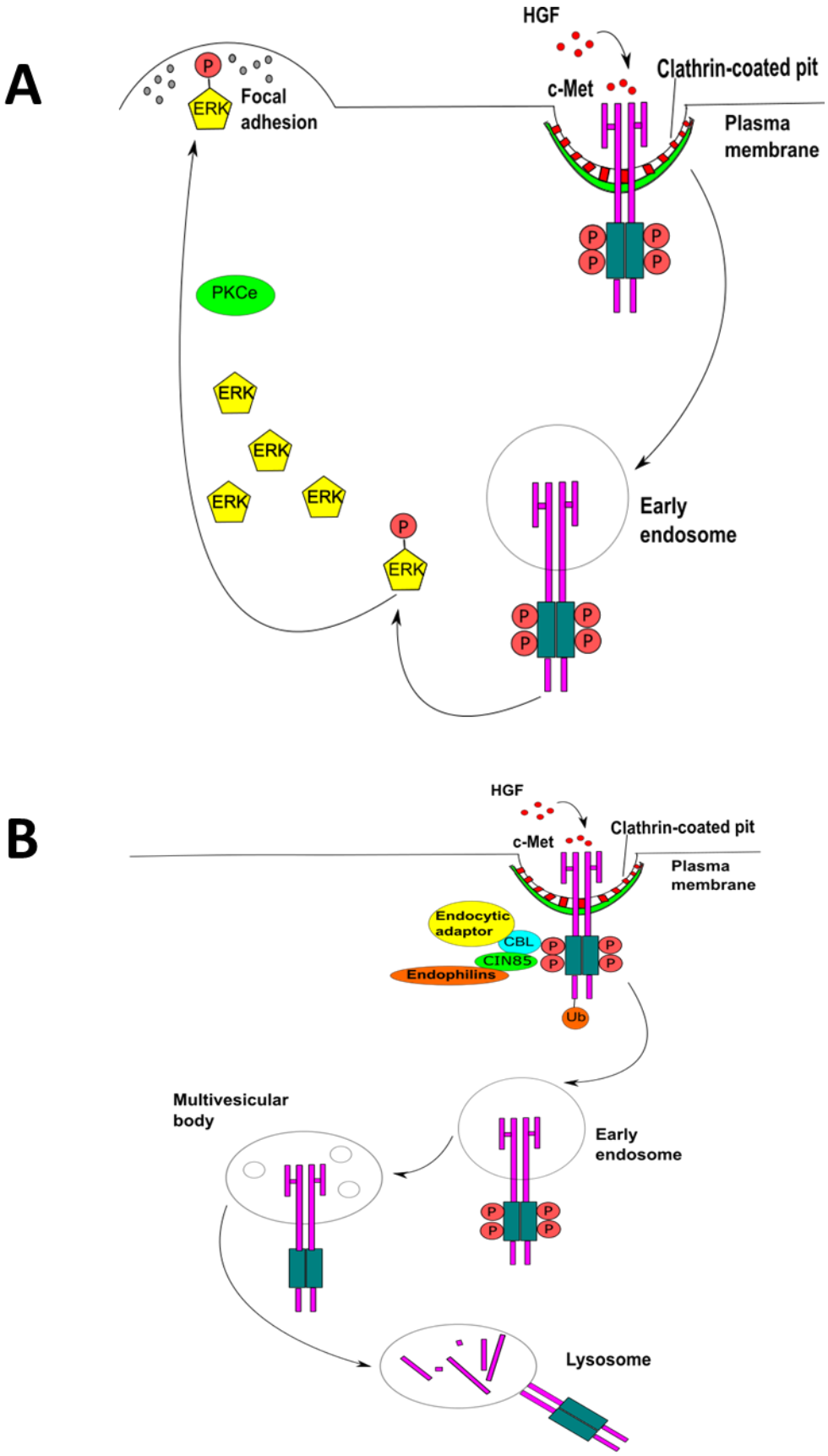
A
HGF
Clathrin-coated pit
c-Met
Plasma membrane
P
ERK
Focal adhesion
PKCe
ERK
ERK
ERK
ERK
P
ERK
Early endosome
B
HGF
c-Met
Clathrin-coated pit
Plasma membrane
Endocytic adaptor
CBL
CIN85
Endophilins
Ub
Multivesicular body
Early endosome
Lysosome

Figure 1-4. c-Met endocytosis.

A) c-Met recruited into early and favours the delivery of active extracellular signal-regulated kinase (ERK) to focal adhesions (mediated by PKC), where it can mediate hepatocyte growth factor (HGF)-induced cell migration. **B)** Downregulation of active c-Met is initiated by c-Met association with casitas B-lineage lymphoma (CBL), an E3 ubiquitin (Ub)-protein ligase that bridges c-Met and endocytic adaptors.

1.2.4 Overexpression of c-Met in cancer

c-Met is overexpressed in a variety of carcinomas including lung, breast, ovary, kidney, colon, thyroid, liver, and gastric carcinomas [3-14, 68].

Numerous studies demonstrate the overexpression and upregulation of c-Met in the basal like breast cancer cell lines [69-73]. A recent study performed by CoIan et al investigated the expression level for c-Met in a large cohort of invasive breast cancer (1896 tumour samples) using tissue microarray technology, with the aim to find a correlation with a specific subtype of BC. In this study, they discovered that c-Met scoring was significantly higher in patients with tubular carcinoma (P = .003), and BL breast cancer (P = .037) [46]. In addition, a great number of clinical studies have demonstrated c-Met-receptor overexpression and pathway hyperactivation in tissues extracted from breast cancer patients [74] as well as a strong relationship between high HGF/c-Met signaling and tumor progression [56].

In many cases HGF and c-Met are co-expressed in mammary tumors, and those tumours display a high histological grade and high proliferative index [45]. In axillary lymph node-negative patients, c-Met overexpression is

significantly associated with reduced survival, a 5-year survival rate of 62% compared with 97% of Met low-expressing patients. A recent comprehensive meta-analysis, composed of 6,010 cases, gives evidence to a link between c-Met overexpression and poor survival in BC patients, and more particularly TNBCs [75].

1.2.5 c-Met deregulation leads to the resistance to TKI

Several studies suggest that c-Met deregulation plays a prominent role in the development of acquired resistance to targeted agents. This can occur through MET mutations, MET amplification, c-Met protein overexpression, increased HGF-dependent c-Met signalling [56] and the interaction with other TK receptors [76]. Studies have shown that c-Met amplification was responsible for acquired resistance to first-generation EGFR TK inhibitors in up to 20% of EGFR-mutant NSCLCs [77]. Likewise, a different study by Bardelli et al. showed that MET amplification caused acquired resistance to anti-EGFR monoclonal antibodies cetuximab and panitumumab in metastatic colorectal cancers [25]. These were observed in both *in-vitro* and *in-vivo* models.

Additionally, the cross talk of c-Met with other tyrosine kinase (TK) receptors can explain the failure of target agents (e.g EGFR TKIs).

1.2.6 Anti-c-Met therapies

c-Met inhibitors are being developed in preclinical and early clinical studies, and are being investigated as a monotherapy as well as in combination with other targeted agents or chemotherapy in numerous cancers, including breast cancer, colorectal cancer, Non-Small Cell Lung Cancer (NSCLC) and brain tumours [78].

c-Met targeted therapies in clinical trials for the treatment of advanced TNBC have taken place. Phase II clinical trials were recently completed for MetMab (onartuzumab) [79] , foretinib (XL880) [80], cabozantinib (alternatively known as XL184) [81] and tivantinib (also known as ARQ197) [82] in TNBCs.

In greater detail, Cabozantinib, a multitargeted tyrosine kinase inhibitor (TKI) against MET, VEGFR2 and RET was under investigation in a phase II randomised trial in 45 Metastatic Breast Cancer (MBC) patients [81]. In this cohort, 64% of the patients displayed tumour regression with an objective response rate (ORR) of 14% along with a disease control rate of 48%.

Onartuzumab, a c-Met monoclonal antibody was under investigation in breast cancer and other cancers (e.g. NSCLC). In NSCLC, the combination of onartuzumab with erlotinib demonstrated a benefit over erlotinib and placebo only as the progress free survival (PFS, HR=0.53) and overall survival (OS, HR=0.4) were improved in those patients [47]. Erlotinib is a quinazoline derivative that selectively and reversibly inhibits the tyrosine kinase activity of the EGFR [83].

Finally, phase II and III clinical studies, evaluating c-Met inhibition in gastroesophageal cancer, lung cancer and hepatocellular carcinoma have shown encouraging results with clear benefit for the individual patient [84-86].

1.3 Epidermal Growth Factor Receptor (EGFR)

1.3.1 EGFR link with c-Met:

Initial studies have identified two different EGFR-TKI resistance mechanisms, a secondary mutation in EGFR, EGFR T790M, and amplification of the MET oncogene, which have been reported in ~50% and 20%, respectively, of patients acquiring resistance to EGFR-Tyrosine Kinase Inhibitors (TKIs) [87]. Lately, a third mechanism of gefitinib resistance induced by hepatocyte growth factor has been identified. Gefitinib is an EGFR TKI used in patients with NSCLC [88]. It has been reported that HGF activated c-Met and restored the phosphoinositide 3-kinase (PI3K)/Akt signaling pathway, inducing gefitinib resistance of lung cancer cells with EGFR-activating mutations. In breast cancer, studies have shown that 'constitutive phosphorylation of Met contributes to EGFR TKI resistance and that decreasing Met kinase activity decreases EGFR tyrosine phosphorylation and proliferation in the presence of EGFR TKI' (e.g. gefitinib) [76]

A recent study has shown that HGF-induced proliferation of basal-like breast cancer cells (HCC1954) was suppressed when treated with the SGX523 (c-

Met inhibitor)/erlotinib (EGFR TK inhibitor) combination while the proliferation of these cells in the absence of HGF (serum free or induced by EGF alone) was completely suppressed by erlotinib alone. This suggests the existence of a cross-talk between c-Met and EGFR pathways, which is HGF-induced [89]. Physical interactions between c-Met, the EGFR family (EGFR and HER3, for instance) and other cell surface protein families, contribute to the mechanisms of how these receptor signal crosstalks underpin the process of oncogenesis and drug resistance [90].

1.3.2 Brief description of EGFR and its family members' involvement in cancer

EGFR is part of the ErbB receptor family, along with HER2, HER3 and HER4 (Fig 1-5). Reports have shown that the overexpression of EGFR, HER2 or HER3 in tumours of breast cancer patients correlate with a reduced survival rate [91]. On the other hand, breast cancer patients with upregulation of HER4 appear to have a good prognosis. This group also investigated the proliferative potential of the EGFR family members and identified that EGFR, HER2 and HER3 drive proliferation. On the other hand, the HER4 receptor did not seem to be linked with proliferation and appears to have a protective role [92].

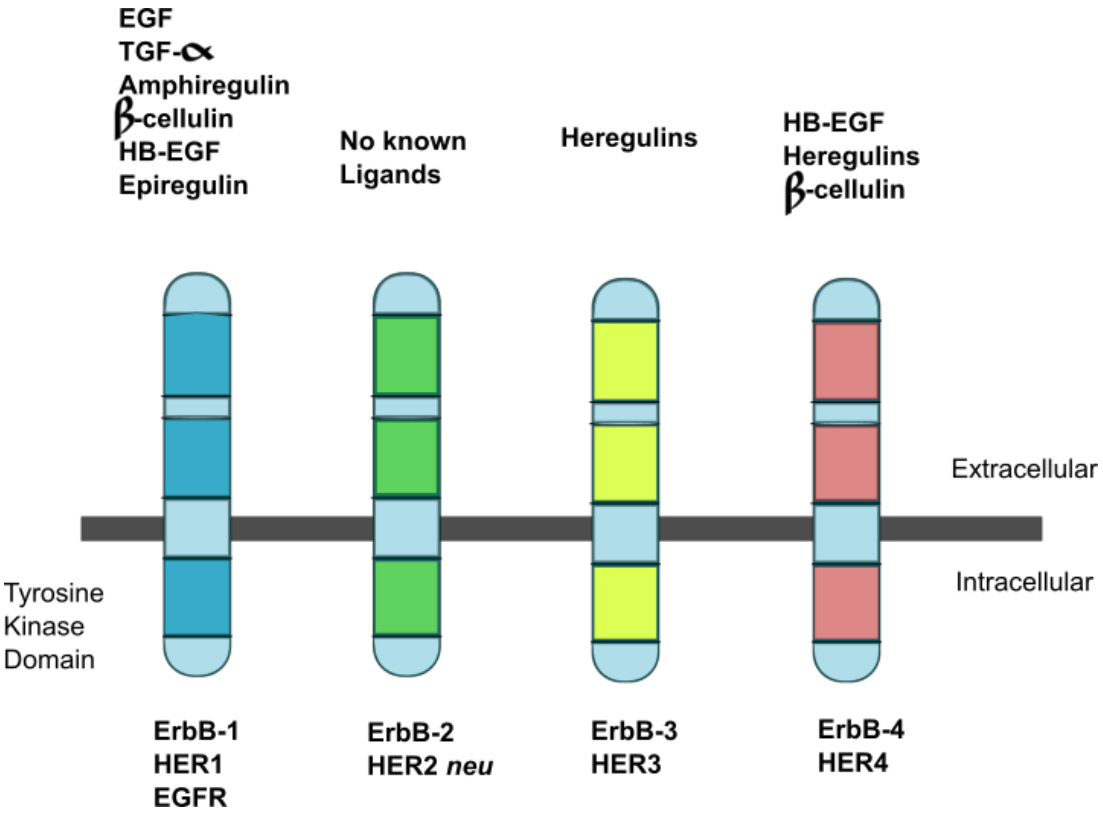

Figure 1-5. EGFR family members - Epidermal Growth Factor Receptor Family.

Conserved domains of the four different EGFR family members are indicated by similar shading. L = ligand binding domain, CR = cysteine-rich domains. TM = transmembrane domain. CT = C-terminal domain which contains the phosphorylation sites. JM = juxta membrane domain. Her2 does not bind a ligand. The kinase domain in Erb3 is defective. Alternative names for each receptor are written underneath each receptor. Ligands which bind the receptors are indicated above the receptors. EGF and HB-EGF stand for epidermal growth factor and heparin binding-EGF respectively.

Mutations in the kinase domain of EGFR and amplification of EGFR have been detected in breast cancer [93, 94]. The EGFRvIII protein is detected in various human cancers, but not in normal tissues [95].

1.3.3 Structure of EGFR and its signalling:

EGFR is overexpressed in epithelial tumours. The EGFR family exhibit the same receptor tyrosine kinase (RTK) molecular architecture, with a ligand-binding extracellular domain (which has a regulatory portion binding to an allosteric regulator – ligand growth factor- for receptor dimerisation), a transmembrane helix, a cytoplasmic tyrosine kinase domain (that undergoes activation and transfers phosphate groups to Tyr residues) as well as an additional c-terminal tail and juxtamembrane regulatory regions (Fig 1-5).

The amount of EGFR receptors in a normal cell vary from 40,000 to 100,000 receptors [96]. However, there is an overexpression of EGFR in the majority of solid tumors, including breast cancer, head-and-neck cancer, Non-small cell lung cancer (NSCLC), renal cancer, ovarian cancer, and colon cancer [97].

EGFR binding to its respective ligand results in homo- or hetero-dimerization, followed by activation of the highly conserved intracellular kinase domain and then autophosphorylation of tyrosine residues by γ-phosphate from ATP [98]. EGFR has five autophosphorylation sites that have been identified, all of which are clustered near the carboxyl-terminal 194 amino acids. Those sites include tyrosine (Tyr) 1068, Tyr1148, and Tyr1173 (which are major sites), whereas Tyr992 and Tyr1086 are minor sites [99]. Depending on EGFR phosphorylation pattern, distinct downstream signaling cascades can be initiated. The phosphorylated Tyr binds to of a range of proteins, whose recruitment activate downstream signaling pathways such as

Ras/Raf/mitogen-activated protein kinase (MAPK) pathway (activated by Phosphorylation of Tyr1173), extracellular signal-regulated kinase (ERK), phosphatidylinositol 3-kinase (PI3K)/Akt pathway, signal transduction and activator of transcription (STAT), and other pathways. The role of ERK1 and ERK2 is to regulate cell growth and proliferation, whereas Akt and STAT direct cell survival and apoptosis. PI3K regulates cell migration along with cell proliferation and survival [100]. When EGFR is overexpressed and /or constitutively activated, those signalling cascades are amplified, contributing to cancer progression. Studies have shown that numerous cancer cell lines display an increase in the level of phosphorylated EGFR [101].

1.3.4 EGFR Trafficking:

EGFR trafficking is an important topic: EGFR localisation in a given cell determines the cell fate and the distribution of EGFR is determined by the ratio of its internalisation and recycling rates. The ErbBs (otherwise called EGFRs) family starts off by being co-translationally translocated through the endoplasmic reticulum (ER) membrane, then are transported to the Golgi apparatus (in which the extracellular domain undergoes N-linked glycosylation), to finally being sent to the plasma membrane. At steady state of cell growth conditions, the bulk of cellular ErbBs proteins are located in the plasma membrane. In most cells, EGFR is constitutively internalised at the rate comparable to the rate of basal membrane recycling. (internalisation rate constant Ke 0.02-0.05 min-1) [102].

A disrupted EGFR trafficking could potentially provide a molecular etiology for EGFR overexpression in cancers that overexpress EGFR. Mutations and deletions of proteins involved in trafficking have been reported to be associated with hepatocellular carcinomas, breast and prostate cancer [103].

1.3.4.1 Ligand-mediated endocytic pathway:

A number of mechanisms within EGFR endocytic pathways regulate EGFR signalling. Indeed, one of the most important mechanisms is ligand-mediated endocytosis. Progression through the endocytic pathway is characterized by the shedding of clathrin, a decrease in the internal pH and the accumulation of hydrolytic enzymes. EGFR trafficking from early to late endosomes/multivesicular bodies (MVB) is dependent on its continued association with Cbl and its sustained ubiquitylation [104].

The formation of clathrin-coated vesicles (CCVs) is mediated by the AP2 adaptor, which binds to the cytoplasmic domain of EGFR [102] while the GTPase dynamin triggers the detachment of the vesicle from the plasma membrane, or fission. The early endosome is then formed as the CCV sheds clathrin and fuse with an internal vesicle. This enables the endocytic pathway to proceed into the formation of the late endosome, facilitated by the involvement of both phosphoinositides [105] and regulatory proteins. Early and late endosomes differ by their internal pH (the late endosome having a very acidic environment) and by their kinetics and morphology. Indeed, the early endosomes are regulated by Rabex/Vps, STAM/Hse1, as illustrated in

figure 1-6, while the late endosomes are regulated by ESCRT-1 and ubiquitin-related proteins [106] among other proteins. In addition to this, early endosomes are often localised at the cell periphery and are more tubular while the late endosomes are more spherical and closer to the nucleus. Multivesicular bodies (MVBs) are a type of late endosomes and contain internal vesicles that are formed through the invagination of the limiting membrane and its budding into the lumen. It is important to mention that EFGRs can still associate with signalling proteins to activate intracellular effectors while at the limiting membrane of MVBs, but this feature is lost when EGFRs get sorted into the internal vesicle of MVBs, segregating the EGFRs' cytoplasm domain away from the signalling proteins and hence terminating its signalling. EGFR is finally degraded when the MVB fuses with the lysosome.

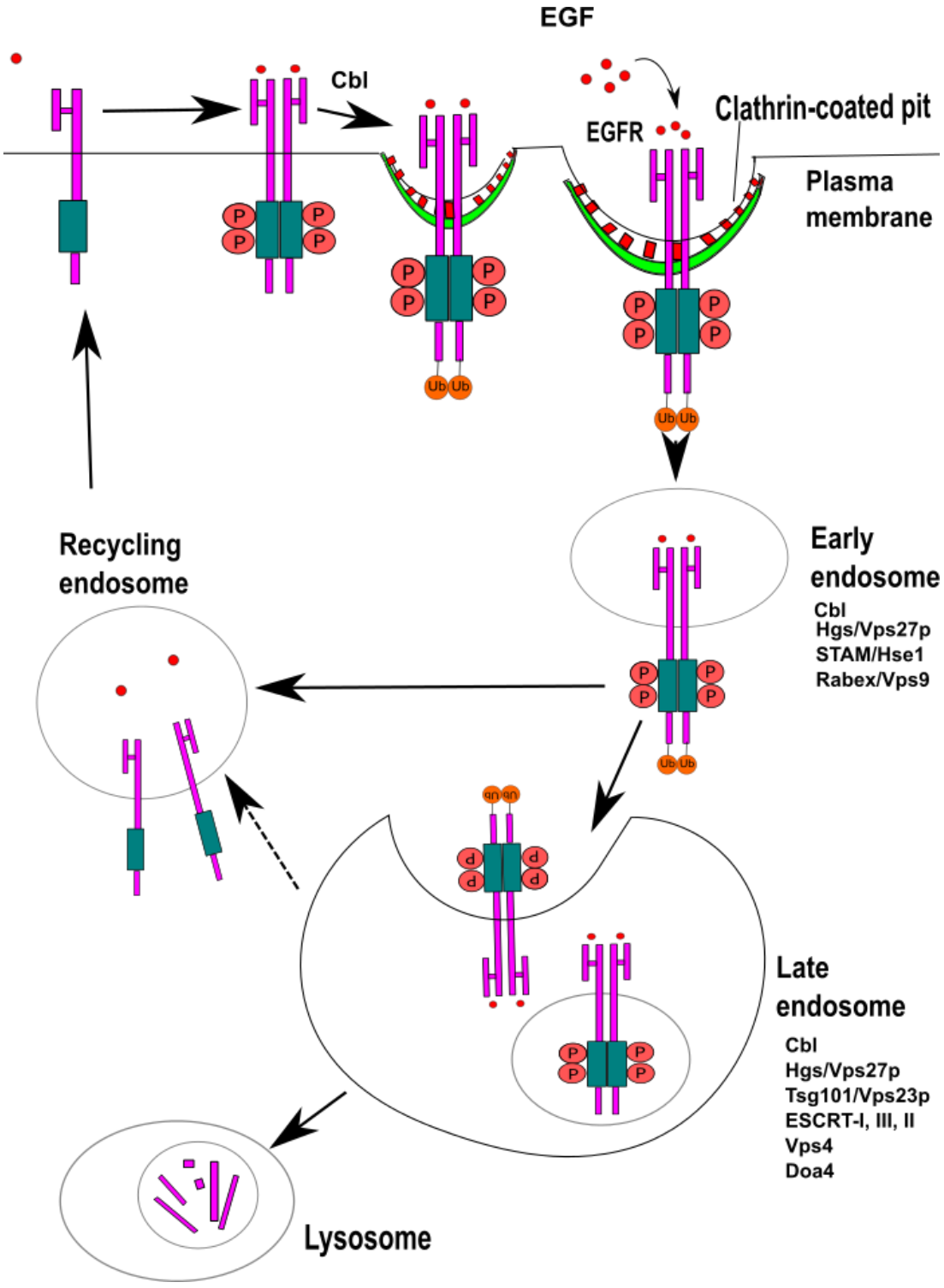

Figure 1-6. RTK: journey to the lysosome.

Stimulation with ligand induces activation of RTKs like EGFR, autophosphorylation and recruitment of Cbl. Cbl is then phosphorylated and ubiquitylates the EGFR. Ubiquitylated receptors are sorted into clathrin-coated pits by a multiprotein complex that includes coat adaptors. Progression through the endocytic pathway is characterized by the shedding of clathrin. EGFR trafficking from early to late

endosomes/MVB is dependent on its continued association with Cbl and its sustained ubiquitylation. The guanine nucleotide exchange factor Rabex/Vps9 regulates endosomal membrane fusion through activation of another GTPase, Rab5. MVB sorting is regulated through recognition of ubiquitylated cargo by Hgs/Vps27p, Tsg101/Vps23p and other components of ESCRT complexes. Fusion of the MVB with the lysosome results in degradation of the contents of the internal vesicles. Recycling of receptors back to the plasma membrane can occur throughout the endocytic pathway, with decreasing efficiency. (Modified from [106]).

1.3.4.2 Regulation of receptor endocytosis mediated by phosphorylation and ubiquitylation:

Phosphorylation and ubiquitylation are dynamic post-translational modifications, which may be reversed by phosphatases and de-ubiquitylating enzymes respectively [107]. Ubiquitin is a 76-amino-acid polypeptide that is conjugated post-translationally to a wide variety of substrates. Substrate ubiquitylation is mediated by a series of enzymatic reactions [108]. Treatment with EGF results in the recruitment of Cbl, a ubiquitin ligase, to phosphotyrosine 1045 of EGFR [109]. c-Cbl can also bind to EGFR indirectly through the adaptor protein Grb2 [110]. Subsequently, Cbl is itself subject to tyrosine phosphorylation by EGFR at residue 371, which stimulates the ubiquitin ligase activity [109]. Receptor ubiquitylation then regulates its endocytic degradation. Recognition of ubiquitylated cargo by Hgs/Vps27p, Tsg101/Vps23p and other components of ESCRT complexes [111] enables MVB sorting and subsequent degradation of EGFR when Cbl binds to CIN85 adaptor, coupling Cbl to endophilins [112]. It has been suggested that ubiquitinated cargo is handed from ESCRT-0 to consequently ESCRT-1,2 and 3 complexes to form concentric rings around HRS complexes, and result

in inward membrane invigination and finally degradation in the lysosome [113]

1.3.4.3 Receptor recycling:

As illustrated in Figure 1-6, most of the receptor recycling occurs after entry to the early endosomes. Nonetheless, it can also occur after entry to the MVB, considering that EGFR remains in the outer MVB membrane and are not sorted to internal vesicles [114, 115]. Receptor recycling does not require tyrosine kinase activity [115]. Binding of EGFR with PKC also enhances recycling.

1.3.5 Use of FLIM/FRET to identify EGFR regulators

1.3.5.1 Principles of FLIM/FRET

Förster (or fluorescence) resonance energy transfer (FRET) is a non-radiative, dipole-dipole coupling process in which the energy from a donor fluorophore molecule is transferred to an acceptor fluorophore that is positioned in close proximity (< 10 nm). The initial step of a FRET process consists of the absorption of the photon energy from the donor molecule, which goes through excitation from the ground state to a higher electronic state. Once it reaches thermal equilibrium, the energy is transferred from the excited donor to the acceptor, generating an excited acceptor. The latter releases the energy by emitting a photon before returning to ground state.

The average length of time spent in the higher electronic state is termed as fluorescence lifetime (tau or τ) [116-119].

FRET efficiency is inversely proportional to the sixth power of the molecular distance between donor and acceptor and the fluorescence life-time of the interacting fraction by:

$$\eta_{fret} = \left(\frac{R_0^{\,6}}{R_0^{\,6} + r^6} \right) = 1 - \frac{\tau_{fret}}{\tau_d}$$

Where R_0 is the Förster radius (at which 50% of the excitation energy is transferred to the acceptor); r is the separation between the fluorophores; τ_{fret} is the lifetime of the interacting fraction and τ_d is the lifetime of the donor in the absence of acceptor. FRET can only be observed when the two fluorophores are within nanometre range, indicating interaction between the molecules [120].

A few methods have been established to detect FRET, for example acceptor photobleaching, fluorescence polarization imaging and fluorescence lifetime imaging microscopy (FLIM).

FLIM is an imaging technique that provides a high resolution and sensitive readout of the donor fluorescence signals and produces an image based on the differences in the exponential decay rate of the fluorescence from a fluorescent sample. The fluorescence lifetime can be measured by frequency

domain or by time domain-based methods. A more thorough explanation is provided by Peter and Ameer-Beg 2004 [120].

1.3.5.2 Identifying EGFR regulators using SP-FLIM screen and the Picchu-X sensor

A genome-scale library of siRNA reagents was used to identify EGFR regulators. A high-content SP-FLIM screen using the Picchu-X sensor (Cheung et al, publication under submission) was used to detect changes in EGFR activity between the control siRNA and the protein siRNA, by comparing the lifetime difference and homogeneity of linear regression slopes before and after the EGF treatment, enabling the detection of candidates for the involvement in EGFR signalling.

This assay led to the identification of 22 potential targets, including EGFR (Cheung et al, publication under submission). For this particular project, PTPN11 was selected for further validation, as described in chapter 6, to establish its biological importance in basal-like breast cancer in relation to EGFR and c-Met.

1.4 Protein Tyrosine Phosphatases

1.4.1 Description of protein tyrosine phosphatases (PTPs)

PTPs regulate equilibrium of tyrosine phosphorylation [121]. They are important antagonists of tyrosine kinase-dependent signaling, regulating cell proliferation, migration and transformation [122]. The PTP family comprises around 100 genes in humans [123] which are subdivided into pTyr-specific enzymes, dual specificity phosphatases (DUSPs), the low molecular weight PTPs [124] and the rhodanese-derived PTP cdc25 [125].

The first crystal structure of a protein phosphatase that was isolated is the 37kDa PTP1B [126]. PTP1B is a cytoplasmic PTP, whose C-terminal segment is involved in subcellular targeting and in the direct regulation of PTP1B activity [126]. In addition to the PTPs' role in RTK dephosphorylation, PTPs also regulate cell adhesion. For example DEP-1, another PTP, can associate with and have the ability to dephosphorylate the cadherin-catenin complex at epithelial junctions, and therefore promotes the cadherin-mediated adhesion [127].

Evidence has shown that PTPs can either behave as an oncogene or as a tumour-suppressor gene [128]. In the case of DEP-1, numerous studies show its involvement as a tumour suppressor. Balavenkatraman et al mentions in his review that DEP-1 re-expression in cultured breast cancer cells leads to up to 10 fold reduction in cell growth. Those findings were also identified in pancreatic, thyroid and colon cancer cells [128].

PTPN12 is another example of PTP with a role of a tumour suppressor. A review mentioned its role in TNBC in which the restoration of PTPN12 leads to an inhibition in cell proliferation and tumorigenicity *in-vivo*. It was also found that the ectopic expression of PTPN12 led to a decrease in the colony formation by TNBC cells [121]. Additionally, another study indicated that the low expression level for PTPN12 was strongly associated with worse prognosis, increased tumour size and other malignant features [129].

1.4.2 PTPN11, a versatile phosphatase

Src homology 2 domain-containing phosphatase (SHP-2, encoded by the protein tyrosine phosphatase, nonreceptor type 11 [*PTPN11*], or *SHP2*, gene) is composed of two SH2 domains (N-SH2, C-SH2), a PTP domain, a C-terminal tail with tyrosyl phosphorylation sites (Y542 and Y580) and a proline-rich motif. PTPN11 is a widely found cytoplasmic tyrosine phosphatase (PTP) which regulates tyrosine phosphorylation and is expressed ubiquitously [130]. Many studies have exposed the importance of SHP2 in the full activation of the Ras/Erk pathway when initiated by receptor tyrosine kinases (RTKs) and cytokine receptors [131].

1.4.3 Mechanism by which PTPN11 gets activated

In unstimulated cells, Shp2 is kept inactive through an interaction of the N-terminal SH2 domain with the phosphatase domain, blocking access to the

catalytic site [130]. Upon stimulation of cells, interaction of the SH2 domains with specific phosphotyrosine binding sites on activating proteins induces a conformational change in the N-SH2 domain that releases this autoinhibitory interaction and allows substrate access to the catalytic site (Figure 1-7) [132]. Overexpression of PTPN11 binding proteins and PTPN11 mutations disrupt this normal auto-inhibitory mechanism causing several human diseases, including cancer [133].

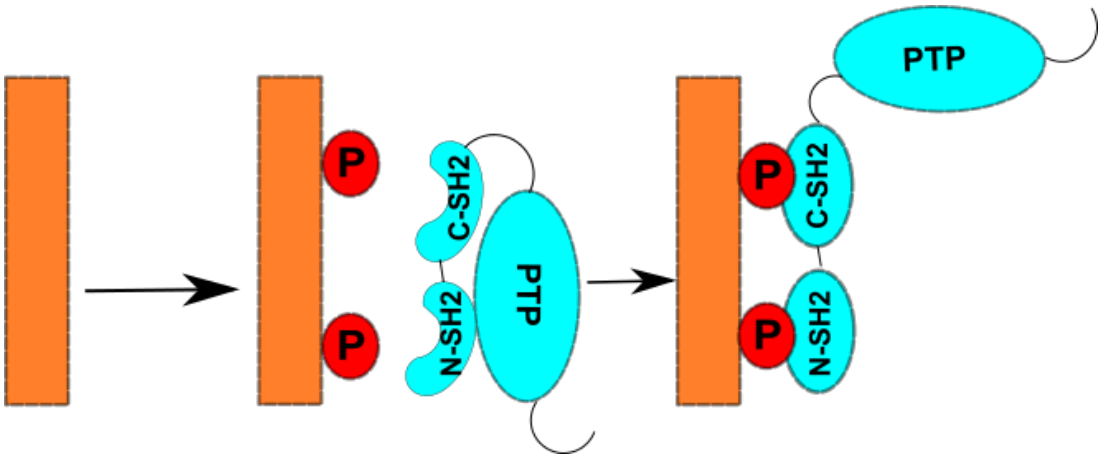

Figure 1-7. Regulation of SHP2 activity by its SH2 domains.

In its basal state, WT SHP2 is auto-inhibited by the binding of its N-SH2 domain to the PTP domain. Addition of an appropriate SH2 domain ligand leads to exposure of the PTP domain and SHP2 activation

1.4.4 PTPN11 role in cancer

Some of PTPN11 regulated signalling pathways have been uncovered. Figure 1-8 illustrates 4 important mechanisms that PTPN11 regulates in a cell. The major signalling pathway that PTPN11 regulates is the Ras/Erk MAP kinase cascade, in which PTPN11 dephosphorylates RasGAP binding sites on specific receptors and adaptor proteins or alternatively, dephosphorylates Sprouty, which is a negative regulator for Ras/ERK. In

addition to this, PTPN11 has the ability to directly dephosphorylate Src, or via the regulation of Csk, hence enhancing Erk activation.

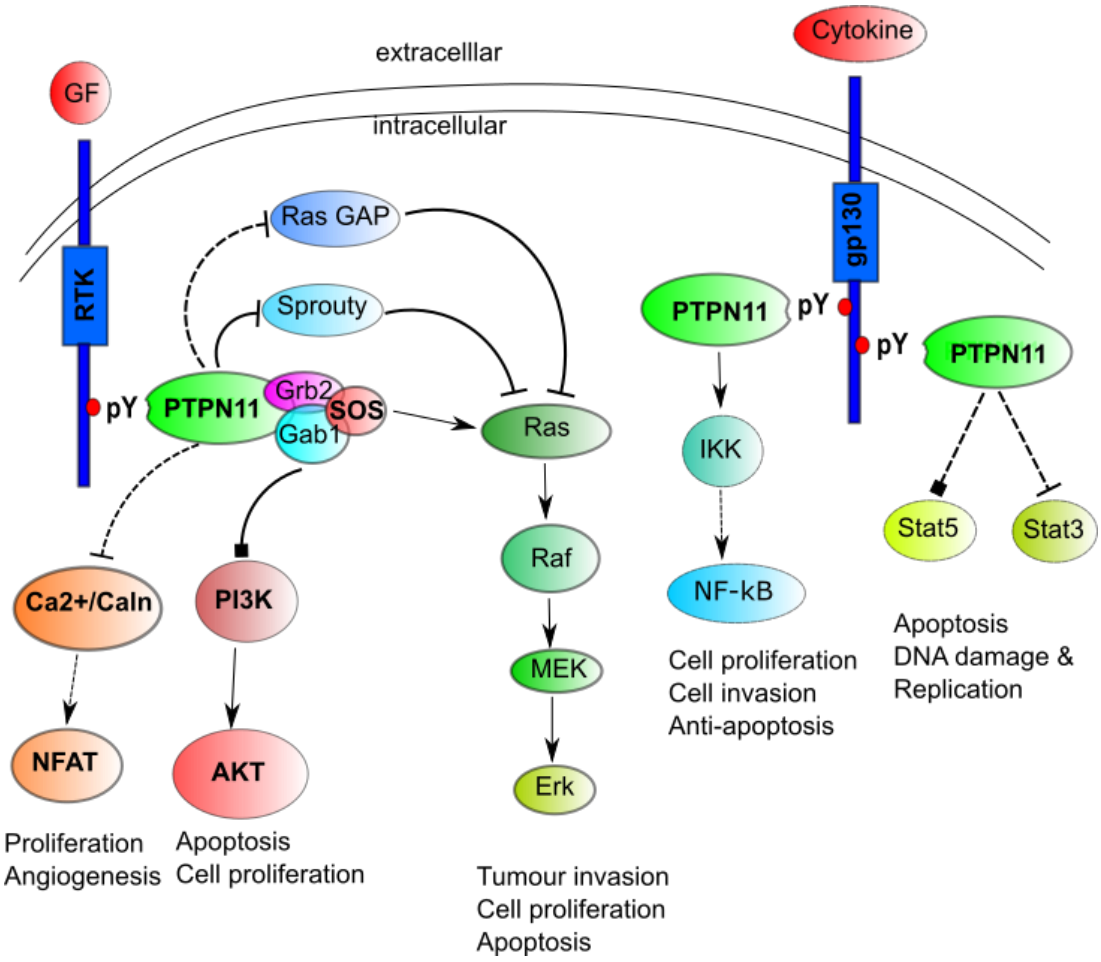

Figure 1-8. Shp2-regulated signalling pathways.

The major signaling pathway activated by Shp2 downstream of receptor tyrosine kinases (RTKs) and growth factors (GF) is the Ras/ERK MAP kinase cascade. Shp2 has also been described to regulate PI3K, in the regulation of Jak/Stat signaling pathways and in the activation of NF-κB. Activation is indicated by arrows, inhibition by black lines, activating and inhibitory relationships by black squares, direct interactions by solid lines, and indirect interactions by dashed lines.

PTPN11 mutants can cause cancer. Indeed, somatic PTPN11 mutations are found in ~35% of patients with sporadic JMML *[134],* 'a clonal pediatric myeloproliferative disorder (MPD) characterized by massive expansion and

tissue infiltration of myeloid cells, and a macrocytic anaemia with persistent fetal hemoglobinemia' [135]. These PTPN11 mutants are gain-of-function mutants and the concept to which those Shp2 mutants cause MPD is beginning to emerge. It has been found that the SH2 domain requirement may reflect the need for leukemogenic Shp2 to bind to Gab2, a major Shp2 binding protein (Gab1 (referred to in Figure 1-2), and Gab2 are two members of Gab family docking proteins in human), as the potent leukemogenic allele $Shp2^{E76K}$ cannot induce tumour formation in $Gab2^{-/-}$ BM cells [136]. Despite the rarity of PTPN11 mutations in most human malignancies, the latter is an important observation as Gab2 was found to be frequently amplified in human breast cancer. In a PTPN11-dependent manner, GAB2 over-expression increases the proliferative potential of human MCF10A cells [137]. Another observation is that GAB2 cooperation with HER2/Neu over-expression was needed to evoke an invasive-like phenotype in these cells. Consistent with these findings, GAB2 over-expression specifically enhances ERK activation while PTPN11 shRNA blocks the biological and biochemical effects of GAB2 over-expression ex vivo, clearly demonstrating the importance of the interaction between PTPN11 and Gab2 [138].

Despite some clear evidence of increase in tumour progression due to PTPN11's overexpression in human cancers such as leukemogenesis [134, 136] , gastric cancers [139] and breast cancer[140], another study has highlighted PTPN11 potential role as a tumour suppressor in hepatocarcinogenesis [141]. This study showed the development of spontaneous macroscopic adenomas in $PTPN11^{hep-/-}$ mutants in one year old

(and over) mice. However, early in life (less than a year old), this mutant would generate regenerative foci and nodular regenerative hyperplasia [142]. The mechanism behind this tumour suppressor role that PTPN11 seems to display has not yet been elucidated.

1.4.5 PTPN11 interaction with EGFR

PTPN11 is involved in the EGFR signalling pathway promoting Ras activation by blocking the Ras GTPase-activating protein (RasGAP)-induced downregulation of Ras, via dephosphorylation of a docking site Tyr992 on the EGFR [143]. Another study has shown that high concentration of EGF downregulates PTPN11 protein expression level [144]. An interesting study has shown an increase in phosphorylated EGFR when PTPN11 is knockdown in colon cancer cells [101], denoting some type of interaction between EGFR and PTPN11. This same increase is not seen when another member from the phosphatase family is being knockdown (SHP-1), which emphasises on the importance of PTPN11's interaction with EGFR. Finally, a study, undertaken by Mann et al, uses the SILAC method to provide evidence of EGFR interaction with PTPN11. This study uses the SH2 domain of the adapter protein Grb2 (GST-SH2 fusion protein), that specifically binds phosphorylated EGFR and Src homologous and collagen (Shc) protein to detect proteins that are bound to Grb2 (and are therefore indirect EGFR interactors) after EGF stimulation. The binding of Grb2 to Shc occurs only after the latter has already been recruited to and phosphorylated by the

activated EGFR which makes this strategy specifically enrich proteins involved in EGF signalling [145].

1.5 Failure of drug trials and the need for *in-vivo* imaging

The BALI-I trial involved the administration of cetuximab (an EGFR monoclonal antibody) with cisplatin in patients with metastatic TNBC. Despite the overall response rate being better (a two-fold increase) than the one observed when patients were given cisplatin only, this trial failed to reach its primary endpoint, which consisted of a significant increase in overall response [18, 146].

A recent phase III trial, undertaken by Roche, investigated the effect of onartuzumab's addition to Tarceva (erlotinib) as a second- or third-line therapy for patients with non-small cell lung cancer (NSCLC) [147]. Unfortunately, despite promising results from Phase II, no clinical benefit was demonstrated in Phase III. The onartuzumab/erlotinib combination could not show an overall survival benefit [148]. However, following the publication of these results, it was found that the design of this trial was somehow faulty, as the researchers enrolled many patients without elevated c-Met level in this trial. It was actually observed that the c-Met-positive patients who received both drugs had an increased overall survival time of 12.6 months in comparison to 3.8 months for c-Met-positive patients who received erlotinib only [149].

This particular scenario demonstrates the importance of stratification prior to the choice of therapy in patients. Many clinical trials face failures due to a

poor recruitment and due to the inability to monitor the expression level of a particular target during treatments in those patients. Repeat biopsy would be useful to determine the molecular signature at progression of the patient but is not feasible as this procedure is invasive. However, the use of *in-vivo* non-invasive molecular targeted imaging, in clinical trials would provide a feasible way to monitor the efficacy of a drug.

1.6 Imaging modalities used into clinical practice in Breast Cancer:

1.6.1 Mammography

Mammogram is the first line imaging investigation, in the UK, for almost all abnormalities in patients aged 40 or above when investigating possible breast cancer lesions. However, the breast tissue tends to be denser below the age of 35 and reduces the sensitivity of mammography. Hence, an ultrasound is used as a primary imaging method for women of this age group. The radiologist assesses the mammogram and gives a grade to indicate the likelihood of the malignancy, which ranges from M1 (normal) to M5 (malignant) [150]. Mammography is also used for surveillance, after surgical treatment of primary breast cancer. Recurrence can occur up to 20 years after surgery. The computer-aided detection (CAD) has been designed and uses computer algorithms to analyse digital mammograms in order to bring any suspected abnormalities to the radiologist. The UK-bases CADET II trial shows that double-reading screening mammograms give a similar cancer detection rate than a single reading from CAD.

Digital breast tomosynthesis (DBT) has been developed to allow radiologists to further assess the mammographic morphology of different pathologies, as a 2D mammography masks pathology due to the overlaying with the normal glandular tissue [151]. The principle behind DBT is to acquire multiple images at different angles to the compressed breast and stack them so this set of images can be scrolled through at a workstation [150].

1.6.2 Ultrasound

As mentioned previously, an ultrasound is used to detect abnormalities in women with dense breast. However, it is not recommended for every patient as a thorough screening ultrasound examination of both breasts is very time consuming. Additionally, an ultrasound is more likely to yield false positive than a mammography. Nevertheless, the ultrasound is the optimal modality to assess abnormalities in patients with implants in augmented or reconstructed breasts, as the ultrasound can distinguish breast lesions from implant complications [150, 152, 153].

1.6.3 Magnetic Resonance Imaging (MRI)

Breast MRI has the highest sensitivity for cancer but is expensive and has a low availability. It also has a high false positive rate but its high sensitivity for invasive cancer detection and its ability to provide detailed high resolution soft tissue in multiple planes makes the MRI a very useful tool in clinical imaging. Currently, women with lobular breast cancer might get a MRI scan

to help doctors decide whether breast conserving surgery (BCS) is an option. Women with breast tissue that is too dense to get accurate information from a mammogram might be eligible for a MRI scan.

For a breast surgical intervention, radiologists may aid surgeons to localize impalpable lesions by performing an ultrasound with a guide-wire inserted through an introducer needle under local anaesthetic [150, 154-157].

1.6.4 Computed Tomography (CT)

Computed tomography (CT) is a diagnostic and anatomical imaging modality that is essentially a 3D version of an X-ray. In a CT, the X-ray tube and detectors rotate around the patient. The CT scanner would then record the x-ray absorption by the patient's body per each direction of the x-ray beam. The image is then reconstructed from a large number of measurements of attenuation coefficient. The main role of CT in breast cancer would be a whole body staging investigation. Lately, breast CT scanners have been developed to yield images of the breast for a similar dose to standard mammography [150, 158, 159].

1.6.5 Positron emission tomography (PET)

Recent years have shown the power Positron emission tomography (PET) has as a metabolic imaging technique and retains the fastest growing diagnostic speciality. PET is highly sensitive and only requires 10^{-11} – 10^{-12} mol/L levels of probe for detection [160]. PET is a gamma imaging technique

that gives *in-vivo* measurements in absolute unit of the radiotracer [158, 159]. PET uses radiolabelled biological agent that emit positrons (and are produced mainly by cyclotrons), the anti-matter counterpart for electrons. After emission, the positron loses its kinetic energy through numerous collisions with electrons present in the neighbouring tissues. After almost losing all its kinetic energy, the positron interact with an electron, producing a positronium which is then annihilated, causing the emission of two photons of 511 keV each in opposite direction (this is to conserve momentum). Those annihilated photons are detected by the detectors surrounding the subject, and precisely locate the source of the annihilation event (Figure 1.9). The detectors electrics are linked and the 'coincidence events' will be stored in arrays that correspond to projections that will be reconstructed using standard tomographic techniques [161]. PET has evolved considerably in the clinics. From its initial applications in neurology and cardiology, it has now evolved into having a primordial role in assessing oncology patient. 90% of clinical studies performed in clinical PET centres represent oncology PET studies [159, 162]. The unique versatility of PET is that it has the ability to assess a number of physiologic and biochemical processes *in-vivo*. Indeed, it is possible to measure tissue blood flow, oxygen metabolism, glucose metabolism, amino acid and protein synthesis and nucleic acid metabolism [159, 162].

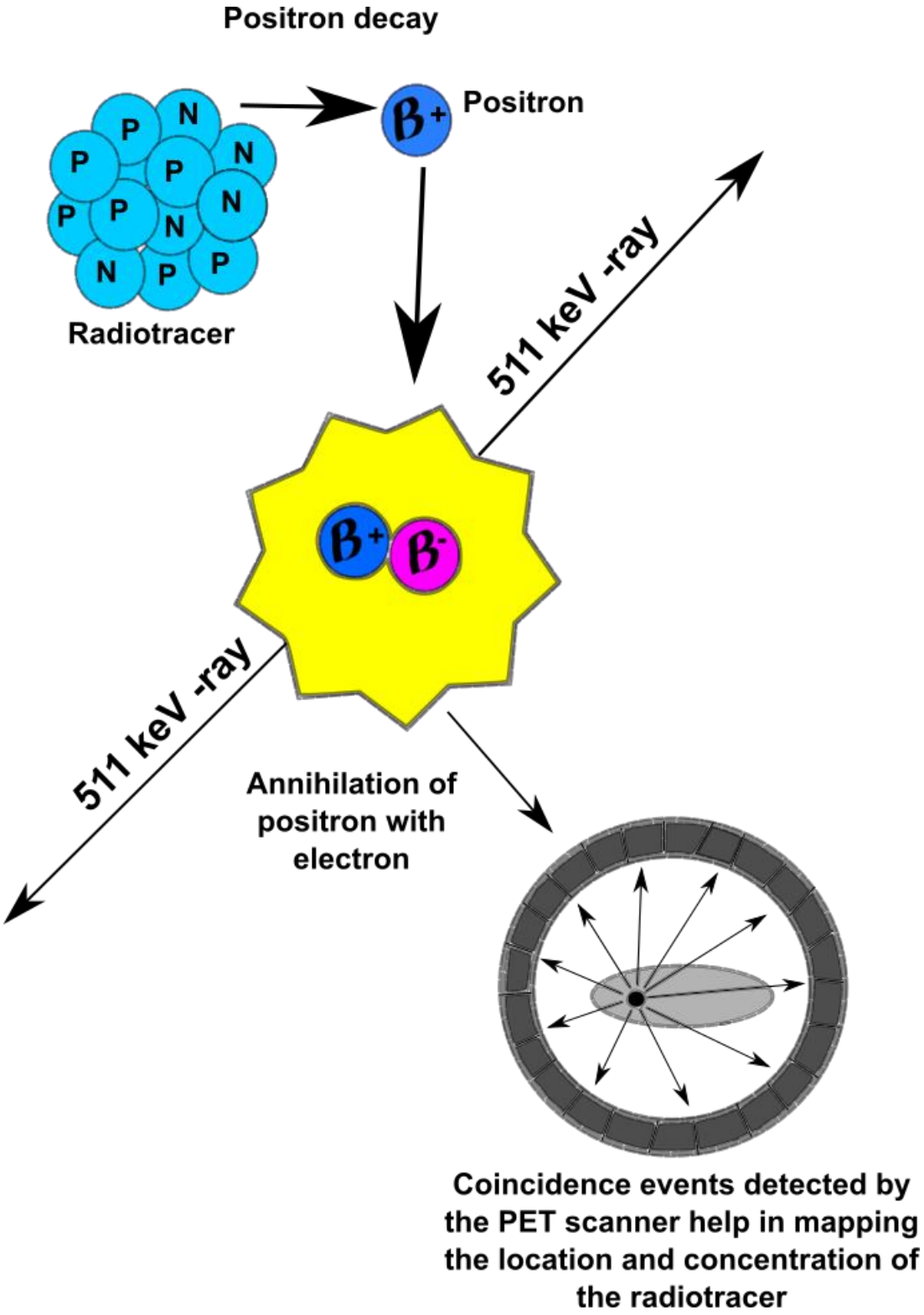

Figure 1-9. The physical principles underlying PET imaging.

A biologically active molecule labelled with a positron emitting radionuclide is administered into the subject. Once injected, the radioisotope emits a positron, which upon traveling a certain distance in the neighbouring tissue, annihilates with a

nearby electron, emitting two antiparallel 511 keV gamma-ray photons. Pairs of annihilation photons are detected in co-incidence by a multi-ring PET camera, and reconstructed into a whole-body image to map the distribution and concentration of the radiotracer.

As PET has high sensitivity, it revolutionises the way patient's treatment is managed. Studies show that PET guide decisions on surgical resection for metastatic colorectal cancer, the staging and treatment of lymphoma, the surgical treatment for non-small cell lung cancer etc. In addition, PET scanners are becoming a greater deal more sensitive than they used to be, enabling faster patient throughput. In addition to this, due to the progress made in instrumentation, it is now possible to combine anatomy and molecular events into a single image through fused imaging modalities through the use of PET/CT, PET/MRI and SPECT/CT.

1.7 Imaging probes used in the clinic

1.7.1 FDG-PET

In clinical practise, it is standard to use 18F-fluoro-deoxyglucose ([18F]-FDG). Once injected into the patient, this radiolabelled glucose analogue would be taken up avidly by tissues with increased metabolic activity, such as cancer cells, as they consume more glucose than the surrounding , less 'active' tissues [163]. However, 18F-FDG PET on its own lacks the superior anatomic clarity that is provided by the CT, therefore both are used. Currently, 18F-FDG PET is not used in breast cancer screening [164]. It has been introduced for diagnostic purposes as a complementary aid to

mammography and breast ultrasound [165]. 18F-FDG PET can be used in patients with inoperable breast cancer, as it is most useful when the results of conventional imaging methods are unclear. It also has a role in progressive disease and in early breast cancer, when standard imaging results are inconclusive. Unfortunately, there is limited evidence for the use of 18F-FDG PET in assessing recurrent or metastatic disease [163]. Studies have shown that the identification of recurrent BC from inflammatory or infectious processes, and the identification of small lesions (tumor size <10 mm) still impose challenges for FDG-PET [166-168]. Another limitation of FDG-PET is its lack of uptake in metabolically inactive malignant tissues [169].

In order to overcome the limitations presented by FDG-PET, imaging scientists have lately been focusing on the design of target molecules which can specifically localise to cell-surface markers, and include growth factor receptors, differentiation and activation markers and adhesion molecules [169].

1.8 Other imaging probes currently investigated in pre-clinical studies in Breast cancer:

1.8.1 FLT

Others, such as FLT hold a great potential role in molecular imaging. While FDG accumulates in chemotherapy-induced inflammatory tissues, hence causing misinterpreted results, 18F-FLT has been used to demonstrate

proliferative activity in numerous tumours and is not susceptible to uptake due to inflammatory changes [170]. 18F-FLT's specificity for cell proliferation is in its relationship to thymidine kinase 1, which sequesters FLT for phosphorylation [171]. A recent meta-analysis show 18F-FLT PET/CT sensitivity to assess chemotherapy ranging from 56.3% to 92.2% [171]. Its pooled sensitivity (77.3%) is lower than the 18F-FDG PET (84%), while its specificity (68.5%) is slightly higher than the 18F-FDG's (66%). The relative lack of specificity is due to the increased FDG uptake in inflammatory cells [172].

Even though PET-CT scans are widely used in the imaging of many types of cancer, its role as imaging modality in breast cancer is still progressing. Up to now, PET-CT is not used for the assessment of stage I breast cancer due to its low sensitivity in detecting small (<1cm) and low grade breast lesions. PET-CT also has a role in the staging, and in patients with known breast cancer recurrence [173]. Despite the fact that MRI avoids the use of ionising radiation, and offers excellent soft tissue discrimination, it lacks the functional information that PET can yield, making PET particularly useful in the assessment of the response to therapy *in-vivo*.

1.9 Other imaging modalities currently investigated in pre-clinical studies for Breast Cancer:

1.9.1 SPECT

The single Photon Emission Computed tomography (SPECT) imaging uses nuclides such as ^{99}mTc, ^{123}I, ^{111}In which decay while emitting single y-ray photons of different energies. Those standard radionuclides emit gamma-ray photons with energies that are much lower than 511 keV (found in PET). ^{99}mTC, for example, only emits 140 keV photons. Those photons that exit the subject's body will pass through a collimator and will be detected by a position-sensitive detector (typically a scintillation camera). A typical SPECT system will consist of one or more scintillation cameras with the acquisition of multiple two-dimensional planar projection images around the patient. Those projection data are then reconstructed into 3D images [174]. A SPECT imaging system can have from one to four scintillation cameras. The higher the number of cameras, the higher the detection efficiency or improved spatial resolution of the SPECT system would be. Despite the fact that PET is more sensitive than SPECT, SPECT radionuclide has the advantage of emitting photons with different energies, enabling the use of several biomarkers at once when performing the imaging. In addition, SPECT display a much lower cost of radioisotopes and gamma-scanning instruments than PET [169].

1.9.2 Optical Imaging

1.9.2.1 Optical molecular imaging

Optical imaging is also one of the non-invasive methods used in the pre-clinical studies, due to being cost-effective in comparison to nuclear medicine

approaches. An antibody or antibody fragment can be detected using bioluminescence (luciferase - with a sensitivity of 10^{-15} to 10^{-17} mol/L), quantum dots or fluorescence (near infrared dyes, with a sensitivity of 10^{-9} to 10^{-12} mol/L) for optical imaging [175]. Despite the high sensitivity of those probes, its major disadvantage is the poor tissue penetration (which is usually less than 1 cm), as the visible light scatters and gets absorbed [169]. The reaction that takes place in bioluminescence consists of enzymes, luciferases, catalysing a light-producing reaction. This light is produced after injection of luciferin, which is a substrate for the enzyme [169, 176]. Table 2 displays the advantages and disadvantages between PET, SPECT and optical imaging modalities.

1.9.2.2 Intraoperative imaging-guided cancer surgery

Much effort is devoted to improve the use of optical imaging in intraoperative cancer surgery [177]. Currently, the pathology report is the standard for the direct result of a surgical resection [178], which takes about 4-7 days to obtain. This is not ideal as a surgical intervention could be greatly improved if only the surgeon could get direct feedback at the time of surgery. Indeed, a complete surgical resection of breast cancer is a powerful determinant of patient outcome.

The use of NIR (Near-Infra-Red) fluorescence is currently being assessed in intraoperative image-guided surgery [178]. NIR light cannot be seen directly with the naked eye and therefore many imaging systems for intraoperative NIR FMI are being developed [179] [180]. Several preclinical studies have demonstrated the beneficial use of therapeutic antibodies conjugated with a

NIR fluorescent dye, such as the intravenous injection of the antibody-IRDye800 bioconjugates in nude mice bearing human breast cancer to act as optical contrast agents for the detection of the borders of malignant tissue intraoperatively [181]. This preclinical study has shown that the bioconjugates were specific for the tumor cells and that it was possible to accurately differentiate malignant areas from normal tissue in vivo. This led to a clinical study in which its feasibility in patients with breast cancer is being assessed (NCT01508572).

Additionally, photoacoustic imaging is currently of interest in the diagnosis, treatment, assessment and follow up of breast cancer [182]. In photoacoustic imaging, non-ionizing laser pulses (such as a short near-infrared (NIR) light pulse) are absorbed by a small molecular target from the tissues. This is then converted to heat leading to transient thermoelastic expansion, decaying broadband acoustic pressure waves. The latter are detected by ultrasonic transducers which are analysed to produce images [182]. Initial findings show that photoacoustic tomography provides molecular imaging at high image resolution and that it can detect breast cancer [183].

Table 1-2. Summary of common pre-clinical imaging modalities

Imaging modalities	CT	PET	SPECT	MRI	US	Optical
Means of detection	Ionising radiation (X-rays)	Ionising radiation (ϒ-rays)	Ionising radiation (ϒ-rays)	Electromagnetism	Acoustic waves	Light
Resolution	50 µm	1 - 2 mm	0.3 - 1 mm	10 - 100 µm	50 µm	1 - 5 mm
Depth	No limit	No limit	No limit	No limit	Centimetres	<3 cm
Quantitative	Yes	Yes	Yes	Yes	Yes	Yes
Agents	Iodinated molecules	^{18}F, ^{64}Cu, ^{68}Ga and others	^{99}mTc, ^{111}In, ^{67}Ga and others	Paramagnetic and magnetic compounds	Microbubbles	Luciferin, fluorochromes
Target	Anatomical, physiological	Physiological, molecular	Physiological, molecular	Anatomical, physiological	Anatomical	Physiological, molecular
Relative cost	Moderate	Moderate	Moderate	High	Low	Low

1.10 **Key gaps in imaging modalities**

To improve patient's survival, understanding the molecules and pathways that drive cell proliferation in breast cancer and those that allow the tumour cells to become resistant to treatment is necessary. Hence, developing better ways of using imaging for breast cancer diagnosis and for response to treatment would have a major beneficial impact on the survival rate and quality of life of the patient. In order to detect changes in tissue that correlate with the onset of the disease or its progression, it is necessary to characterise a suitable molecular imaging agent-target interaction. An imaging probe can interact with target biomarkers to define, temporally, the quantitative expression level and spatial localisation of specific targets for a therapeutic drug [184]. Hence selection of a specific and most sensitive imaging probe facilitates personalised patient's treatment. Numerous studies are now devoted to identify a molecular agent that targets specific proteins that are for example, overexpressed in a particular cancer [185] . PET radiopharmaceutical will be selected depending on the application of the study. The diagnosis, grading of malignancy, the staging or residual disease

and the detection of recurrence are criteria that will be considered for the choice of the PET radioisotope to be used. Other criteria such as the assessment of the response to therapy, the identification of the site of the disease or the detection of the primary tumour when the metastases are present will also need to be taken into account [186].

1.11 Antibody and antibody-fragments in nuclear imaging:

Various targeting molecules of varying size and composition, such as antibodies, small-molecule ligands, peptides, affibodies, aptamers, single chain Fv, F(ab')2, F(ab'), diabodies and minibodies (Fig 1-10) can be used for whole-body imaging [169, 187]. The progression of recombinant DNA techniques led to the design of antibody fragments, which show faster pharmacokinetics than full length monoclonal antibody [187, 188].

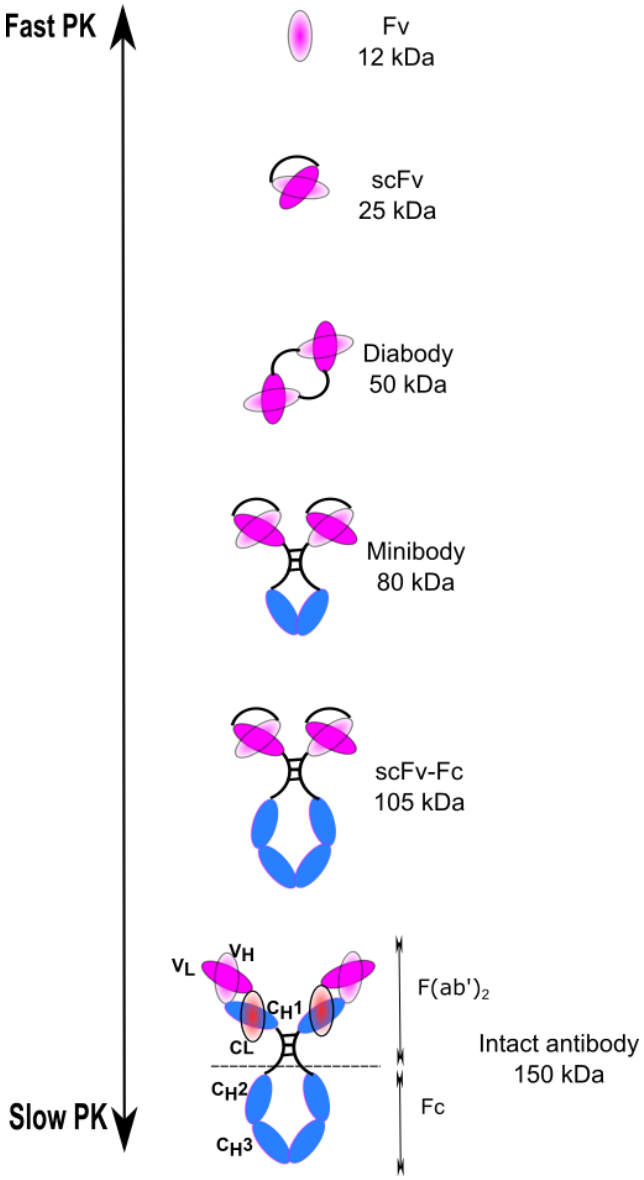

Figure 1-10. Schematic presentation of an intact antibody and engineered antibody.

This consists of scFv (25 kDa), diabody (50 kDa), minibody (80 kDa), scFv-Fc (105 kDa) and intact antibodies (150 kDa). Larger fragment antibodies correlate with slow pharmacokinetics and blood clearance.

1.11.1 Full length antibody

Intact antibodies have a high specific targeting ability. The antibody that is mostly found in our serum is IgG, has a Y-shape linker and has two antigen-binding sites present on the two Fab tips (Fig 1-10). The IgG's Fc domain

mediates the recruitment of effector functions. IgG is mainly used in therapeutics [187]. IgG antibodies demonstrate a strong affinity to its target due to their bivalency. Indeed, IgG has the ability to bind to two antigens as well as having a high avidity to numerous cell surface receptors, for example [189]. The affinity differs from the avidity as the affinity measures the strength of interaction between an epitope and an antibody's antigen binding site. On the other hand, the avidity of an antibody gives a measure of the overall strength of an antibody-antigen complex.

Despite monoclonal antibodies' highly specific targeting ability, they tend to circulate in blood for a very long time, sometimes for days. The interaction between the Fc domain of the IgG and the yF receptors, leads to an interaction with the neonatal Fc receptor (FcRn). FcRn will then transport the IgG in intact form across cells preventing them from degradation [190]. This can make them unsuitable imaging probes in patients. A study has shown the inverse correlation of the size of the protein, which was used as an antibody-based imaging agent, and its blood rate clearance in the subject. It shows that the clearance rate of Fab' is greater than F(ab')2 which itself is greater than IgG [191].

For an optimal tumour targeting, biodistribution and rapid clearance, it is possible to design antibody fragments of intermediate size that will prove to be useful in clinical imaging [192].

1.11.2 Antibody Fragments

1.11.2.1 ScFvs:

The single chain Fv fragment (Fig 4 & 5) is the smallest functional antigen-binding domain of an antibody (~30 kDa), in which the variable heavy (VH) and variable light (VL) domains are joined together by a flexible peptide linker which is 12 to 25 residues long. The orientation of the V-domain can affect the expression, the stability and the antigen binding activity [193]. The scFv displays the same binding specificity of the parent antibody and offers several improved pharmacokinetic properties, such as better tissue penetration and rapid blood clearance [194]. However, due to their monovalency, it has a modest retention time in the target tissue causing the image to be of an inferior quality. In addition, its short size also leads to a short *in-vivo* half-life decreasing the exposure of the target molecule to the scFv. Hence, scFvs have been engineered to produce multivalent and multifunctional multimers (diabodies, triabodies and tetrabodies) which possess higher avidity and demonstrate a lower blood clearance, without affecting tissue penetration abilities [195]. Despite the faster clearance of scFvs making them difficult to be used for therapeutic applications, it is a much wanted property when it comes to *in-vivo* diagnostic applications [194]. The future of scFv also lies in providing binding specificities to targets that are otherwise inaccessible by standard antigen-binding sites [189].

1.11.2.2 Diabody:

On the other hand, bivalent fragments such as scFv-fusion proteins and scFv dimers make great candidates as imaging probes, as their larger size make them circulate longer in the blood, without ill effects to the patients, and therefore enable a higher tumour accumulation, and signal-to-noise background [169]. The diabodies (Fig 1-10), also called scFv dimers, form stable non-covalent dimers as the linker has been shortened to less than 10 residues between the variable domains enabling the scFv to open up and to cross-pair with another scFv molecule [196]. They show slightly longer blood clearance than scFv molecules and demonstrate a higher tumor uptake than the scFv monomer, due to their larger size (55 kDa). Studies show that scFv dimers display a better target uptake than monomers. ScFv dimers are bigger in size and therefore have a longer biological half-life and due to their bivalency, display a higher avidity [192].

Numerous studies have shown the successful use of radiolabelled diabodies. Cai et al have coupled 18F to a diabody fragment, that targets HER-2, called [^{18}F]FB-anti-HER2 Cys-Db, and injected it into HER2-expressing tumor xenografts in mice [197]. Using this radiolabelled diabody, Cai et al were able to show high contrast images at 2, 4 and 6 hours post injection as well as fast tumour localisation. The biodistribution data also shows that the probe preferentially binds to the tumours that overexpress HER2, rather than the HER-2 negative C6 control tumours, with a difference in the ratio uptake of 2.9 [197].

Another example is a diabody derived from the full length antibody J591, which is targeted against an extracellular epitope of Prostate-specific membrane antigen (PMSA) [198]. PMSA is an established marker for

prostate cancer. Fung et al shows that when mAb J591 is radiolabelled either with 89-Zr or 124-I, the average tumour to blood ratio reaches a peak of 7.7 and 8.5 respectively [199] at 96 hours after injection. On the other hand, Kampmeier et al shows in their study that their diabody J591Cdia, chelated to 99-Tech, otherwise called [99mTc(CO)3]+-labelled J591Cdia, shows specific accumulation in PSMA positive tumours from 4h post injection onwards. The highest uptake of the radiolabelled diabody was observed at 8h post injection, with an uptake of 12.1%±1.7%ID/g, a tumour to blood ratio of 8.0 and a tumour to muscle ratio of 16.8 [198]. The pharmacokinetics of this diabody seems more favourable than its parental antibody for imaging purposes, without compromising the sensitivity and specificity of detection of the target.

The reduction of scFv linker length (between zero to five residues) has been a successful design as it causes self-assembly into either bivalent dimers (diabodies, 55kDa), trivalent trimmers (triabodies, 80 kDa) or tetravalent tetrabodies (110 kDa). It has been shown that diabodies of a zero-residue form are more stable in human serum at 37°C than ones with linkers five residues in length.

A major disadvantage of radiolabelling smaller antibody fragment is the risk of reactive residues to be found in critical regions of the antibody. To circumvent such issue, it is possible to modify specific sites of the diabody for its binding with the radioisotope [200].

1.11.2.3 Minibodies:

A minibody (Figure 1-10) is slightly larger than a diabody, with a molecular mass of 60 kDa, which exceeds the renal clearance threshold (<60 kDa). A minibody is a scFv that is joined with a IgG C_H3 domain [169]. Minibodies with different specificities would display a tumour uptake that is dependent on the antigen-antibody system while their pharmacokinetics will be similar [201]. Iodinated anti-CEA (anti–carcinoembryonic antigen) minibody was produced to target colon cancer cells [192]. The anti-CEA scFv was fused to the human IgG1 Ch3 domain, using two peptide linkers, and enables stabilization of the dimerization. This anti-CEA minibody assembled into a chimeric protein with a molecular mass of 80 kDa. Two forms of the anti-CEA minibody were designed by Wu et al, a non-covalent LD (in which a simple two-amino acid residue linker was used) and a covalent Flex minibody (in which a human IgGl hinge region was used). In the Flex minibody, a human IgG1 hinge region was incorporated into the molecule forming disulphides bridges between the subunits and stabilised the dimer. The tumour targeting and biodistribution of these minibodies were assessed in athymic mice/LS174T xenografts. The results show they both display different rates for blood clearance. The LD minibody cleared a lot quicker from the blood circulation than the FLEX minibody but not to its advantage. The tumour to blood ratio for the FLEX minibody was 65 by 48h after injection, in comparison to 47 for the LD minibody, at a comparable timepoint [192]. It is thought that the difference in blood clearance between these two minibodies could be due to the difference in the separation of the scFv within each minibody, the scFv units in the LD minibody were joined to the two CH3

domains at 40 A apart while it was of 23 A in the FLEX minibody. In addition to this, the access of key residues in the CH3 domains might have been masked in the LD minibody explaining its quick blood clearance and consequentially its lower tumour targeting ability in comparison to the FLEX minibody [192].

1.11.2.4 Single chain Fv-Fc:

In order to minimize slow blood clearance of the antibody, deletions of domains to reduce its size are performed. Kenanova et al have mutated the Fc-FcRn binding site of chimeric anti–carcinoembryonic antigen (CEA) antibodies, producing five mutants in a single-chain Fv-Fc format. A wild type was also designed in the single chain Fv-Fc format (Fig 5), where the anti-CEA scFv (VL-linker-VH) fragment was joined to the intact Fc region (CH2 and CH3 domains) of human IgG1 via a hinge region [202]. The presence of an intact Fc domain enables interactions with the neonatal Fc receptor (FCRn), which prevent IgGs from degrading as much as other serum proteins, by diverting them from the lysosomal degradation pathway [203].

This study shows that the mutants CEA scFv-Fc, for which the Fc-FcRn binding site were mutated, display a faster serum clearance than that of wild type. The double mutant had a 50-fold less remaining blood activity at 72 hours after injection in comparison to the wild-type ($P < 0.0001$) [202]. It is also interesting to see that at 48 hours after injection, the tumour-to-background ratio is 0.6:1 for the wild-type scFv-Fc, while the ratio for the double mutant scFv-Fc is of 11.7:1 at its last timepoint (52h post injection).

Hence, the double mutant scFv-Fc produced clear and high-contrast images at earlier timepoints than the wild type scFv-Fc. This study clearly demonstrates that a scFv-Fc is an excellent substitute for intact antibodies as the tumour targeting ability of the scFv-Fc is comparable to the parental intact antibody, with the advantage of a much faster blood clearance rate, with the introduction of specific mutations [202].

In order to optimize for the efficiency of mAbs and their fragments in cancer therapy, it is crucial that those agents are able to identify tumour-associated antigens at low levels. It has been a bigger challenge so far to use antibody therapy in solid tumour than in circulating cancer cells due to the low accessibility of the imaging agent to the solid tumours [189].

1.12 Non-Antibody derivatives: a brief outlook

Other molecular agents that could be used for diagnosis and possibly therapeutic purposes in nuclear medicine are the non-antibody based engineered proteins [204]. They consist of affibodies, knottin, fibronectin domain, Designed Ankyrin Repeat Proteins (DARPs) and natural ligands (such as VEGF, EGF…).

1.12.1 Affibodies:

An affibody molecule is a small non-immunoglobulin single domain protein (6.5 kDa), and has three alpha-helical Z-domain scaffold (Fig 6) [205]. They

present major advantages over antibodies in the field of molecular imaging. Antibodies, especially the IgG, are large, multidomain protein and can display a complex glycosylation. Only a small part of the bulky antibody is used for antigen recognition. Due to the large size of antibodies, manufacturing is more expensive, difficult and they display poor heat stability [206]. Affibodies, otherwise called alternative scaffold proteins, are small, highly stable, lack cysteine residues and can be produced easily, which makes them a potential candidate for non-invasive imaging, provided they demonstrate high specificity and affinity to the target of interest.

Recent studies show that affibodies are good candidates for HER-2 specific molecular imaging in comparison to antibodies, antibody fragments and DARPins (see section 1.12.2). Sorensen et al recently demonstrated that a Ga-68 labelled affibody against HER2, [68Ga]ABY-025, specifically discriminates HER2 positive metastases from HER2 negative lesions with a mean SUVmax uptake of 15.0±3.4 and 2.7±2.1 respectively at 4 hours post injection [207]. There was a significant correlation between the uptake of [68Ga]ABY-025 and the HER-2 scoring from the staining of the biopsies. Hence, PET [68Ga]ABY-025 led to a change in the HER2-targeted treatment in 3 out of 16 patients and allowed a PET acquisition to be made on the same day of the injection.

In addition to this, another study proves the fast clearance rate and the consequential higher tumour to organ ratio when using radio-iodinated affibody of HER2. This HER2 affibody is only 6.5 kDa. The latter shows slow blood hepatobilliary clearance. However, it has also been shown that such

fast clearing fragments tend to have a low accumulation in tumours as they are not exposed to the target site for a very long time [169].

1.12.2 DARPins:

The designed ankyrin repeat proteins (DARPins) are recombinant binding proteins with ankyrin repeats (Fig 6). Those repeats stack together and form a contiguous binding surface. DARPins are made of 4-6 repeat units of 33 amino acids, which form one β turn followed by 2 anti-parallel α-helices [204].

A recent study, conducted by Goldstein et al, shows a higher tumour-to-blood ratio than any other reported HER2 radioligands [208-210] when HER2-positive tumour xenografts were injected intravenously with ^{111}In-(HE)3-G3 DARPin, a radiolabelled DARPin that targets HER2, within 24h of administration [211]. This small radioiodinated high affinity protein demonstrates its ability to image both trastuzumab-treated patients and non-treated patients as the DARPin G3 and trastuzumab bind to different epitopes of the HER2 domain IV [211]. In addition, ^{111}In-(HE)3-G3 display favourable kinetics for HER2 imaging with its short half-life in serum, high tumour-to-blood ratio , a low non-targeted tissue uptake and a lower normal liver uptake, advantageous here due to the liver being a common site in breast cancer metastases.

1.13 c-Met, a pre-clinical molecular imaging target of interest:

Several studies have focused on the use of c-Met molecular targeted imaging for diagnostic or therapeutic purposes in cancer. c-Met molecular imaging offers the potential for quantification of c-Met expression in living tissue. Liu et al used a Cy5-labelled (λmax ex = 648 nm) peptide against c-Met, GE137, to detect submillimeter deposits of ovarian cancer *in-vivo*. GE137 is a 26 amino acid cyclic peptide (AH111972) and is water soluble. It has a high affinity (Kd = 2 nM) to human c-Met (a low nanomolar dissociation constant) and is selected from a phage display library. It does not activate downstream signalling pathway. This probe also gives a signal-to-noise ratio greater than 1.5 at a submillimetre resolution level. However, it is not possible to assume that this probe could not miss microscopic tumour deposits in this study [212]. The *in-vitro* assay also shows cytoplasmic accumulation of GE137 which enables a prolonged GE137 retention and consequently a high signal-to-noise uptake that lasted for 8 hours after injection. Another recent study, performed by Burggraaf et al, uses the same probe in colorectal cancer [213]. In their study, they present results following fluorescence-guided colonoscopy using the imaging agent GE-137 in 15 patients with high risk of colorectal neoplasia. After the first pass inspection with white light, 101 lesions were detected, however, after a second round inspection using the GE137 with fluorescence, a further 22 lesions were detected, and 17 of them are only detectable with the fluorescence imaging. Staining of the biopsies of those lesions shows a clear correlation between histological classification of lesions and the level of fluorescence observed in them *in-vivo* (P = 0.00003). This study concludes that GE-137 is safe in

humans, and has the potential to increase the sensitivity of polyp detection during colonoscopy [213]. Part of my study will explore the use of this same peptide, GE-137, radiolabelled with fluorine-18 [16]. This agent was used to investigate the detection of early stage locoregional recurrence in basal-like breast cancer.

In a different study, an anticalin that is specific to c-Met (a binding affinity of 0.6 nmol/L), PRS-110, was labelled with Zr-89 [214] and injected into high MET-expressing H441 non–small cell lung cancer xenografts. PRS-110 acts both as an antagonist of HGF dependent Met signalling and acts as a ligand dependent inhibitor in c-Met tumour progression. *In-vitro* assays show that ^{89}Zr-PRS-110 is taken up by the c-Met positive cells, H441, despite the fact that this tracer is a non-MET-receptor-activating binder as it is monomeric. In this study, we find that ^{89}Zr-PRS-110 uptake is significantly higher in the MET-expressing tumour models H441 and U87-MG in comparison to the MET-negative A2780 tumours [214].

Another interesting study is the use of recombinant human HGF (rh-HGF), labelled with ^{64}Cu as a PET tracer, which detects c-Met expression *in-vivo*. PET imaging acquired 9h after the injection of this tracer shows a significantly higher uptake in the higher-Met-expressing tumours (U87MG) in comparison to the low-Met-expressing tumours (MDA-MB-231). ^{64}Cu-NOTA-rh-HGF uptake in the U87MG tumour was much faster than that shown with the use of ^{89}Zr-PRS-110 [214], and displayed a significantly higher tumour-to-muscle ratio (13.5 ±6.1 at 9 h after injection (n= 4) [215].

1.14 **Summary:**

BLBC accounts for 15% of all invasive breast cancers, and affects younger women with rapid relapse [2] and early recurrence patterns [31]. Studies have shown that locoregional recurrence was predictive of a higher risk of subsequent events and death in patients with TNBC [36]. Due to a lack of hormone receptors, .BLBC and TNBCs have limited therapeutic options [30].

c-Met is overexpressed in a variety of carcinomas including breast cancer [4]. Numerous studies have demonstrated a preferential overexpression of c-Met in the basal-like subgroup [46, 56]. Several studies suggest that c-Met deregulation plays a prominent role in the development of acquired resistance to targeted agents. Indeed, in breast cancer, studies have shown that 'constitutive phosphorylation of Met contributes to EGFR TKI resistance and that decreasing c-Met kinase activity decreases EGFR tyrosine phosphorylation and proliferation in the presence of EGFR TKI' (e.g. gefitinib) [76]. Due to c-Met overexpression in many cancers, a number of c-Met inhibitors are being developed in preclinical and early clinical studies, and investigated as a monotherapy as well as in combination with other targeted agents or chemotherapy in breast cancer, colorectal cancer, Non-Small Cell Lung Cancer (NSCLC) and brain tumours [78].

Current imaging modalities used in clinical practise in breast cancer include Mammography [150] , Ultrasound [152], Magnetic Resonance Imaging (MRI) [154], Computed Tomography (CT) [158] and Positron emission tomography

(PET) [162]. FDG-PET is currently being used in the clinic for the detection and staging of many cancers [216]. However, due to its inability to detect small lesions (<10mm) [166-168] and its incapacity to provide a direct readout for the expression level of a specific protein, it seems necessary to develop molecular targeted imaging probe with high specificity to the protein target of interest.

Molecular imaging with anti-c-Met probe allows for the non-invasive and whole-body assessment of c-Met tumour burden. It will also allow for better stratification for patient selection for anti-c-Met therapy, as well as optimising dose and schedule for anti-c-Met treatment. It will supply a complementary option to obtain real-time information to assess the immediate response to therapeutic interventions. The collection of biopsies is not always feasible due to the lack of detection of recurrent or metastatic lesions and is an invasive procedure. An imaging probe against c-Met would circumvent this important issue.

Chapter 2: Aims

In this thesis, we will be:

1. Investigating the use of a radiolabelled c-Met binding peptide tracer, [^{18}F]AH113804, in the *in-vivo* detection of locoregional recurrence in BLBC at its early stages (see Chapter 4).

2. Validating the use of a fragment variable antibody, with an engineered Fc, otherwise named as scFv-Fc, against human c-Met in BLBC. Two versions of this tracer were designed, the optical version, Cy5-labelled scFv-Fc, and the radiolabelled version, ^{111}In-CHX-A''-DPTA-scFv-Fc (see Chapter 5).

3. Investigating the effect of PTPN11 knockdown in EGFR and c-Met phosphorylations in BLBC (see Chapter 6).

Chapter 3: Material and Methods

3.1 : Reagents

Reagents for Cell Culture

Dulbecco's Modified Eagle Media - DMEM (Life Technologies Ltd)

RPMI Media 1640 (Life Technologies Ltd)

Full medias contain 10% Penicillin/ Streptomycin (10,000IU Penicillin and 10,000µg/ml Streptomycin) (Life Technologies Ltd) 2mM L-Glutamine (Life Technologies Ltd), and 10% heat inactivated Foetal Bovine Serum (Sera Laboratories International Ltd)

Trypsin/EDTA (0.25% trypsin, 0.02% EDTA) (PAA)

Puromycin (ThermoFisher Scientific)

Reagents for cellular transfection

Opti-MEM-1 (Gibco)

FuGene 6 (Roche Diagnostics)

Lipofectamine RNAiMAX (Life Technologies Ltd)

Pei reagent (Polysciences)

Reagents for Molecular Biology

DH5α bacterial cells (Invitrogen)

LB agar and LB broth (Sigma)

Ampicillin (Sigma) used at 100µg/ml

PureYield Plasmid Miniprep System Kit (Promega)

PureLink HiPure Plasmid FilterMaxiprep Kit (Life Technologies Ltd)

Ligands for receptors

EGF: recombinant human epidermal growth factor (PeproTech, USA) used at 100ng/ml

HGF: recombinant human hepatocyte growth factor (R & D Systems) used at 50ng/ml

Cell signalling inhibitors

SGX523 (Millipore): anti-CMET, used at final concentration of 5μM in DMSO

Reagents for Western Blotting

Five-fold sample buffer: 100mM Tris (pH 6.8), 10% w/v SDS, 50% Glycerol; after protein determination in the sample, 100mM Dithiothreotol (DTT) and 0.002% w/v bromophenol blue were added

Gels: 30% Acrylamide/Bis solution 37.5:1 (BioRad) ammonium persulphate (Sigma)

Precision Plus protein dual colour standard (BioRad)

Running buffer: 25mM Tris Base, 0.19M glycine, 0.1% SDS

Transfer buffer: 25mM Tris Base, 0.19M glycine, 20% w/v methanol

Wash buffer: Tris-buffered saline (TBS): 0.02mM Tris, 0.05M NaCl, 0.01M KCl, pH 7.4

TBS-Tween (TBST): TBS containing 0.1% Tween-20

Blocking solution: 4% Bovine Serum Albumin (BSA) (BioSera) made up in TBS-Tween

Amersham Hybond ECL nitrocellulose membrane (GE Healthcare)

Re-blot Plus (Millipore)

Pierce ECL Western Blotting substrate (ThermoScientific)

Coomassie stain: 0.25% w/v Coomassie brilliant blue R-250, 7% acetic acid, 40%methanol, made up to 1L in distilled water)

Destain solution (7% acetic acid, 10% methanol, made up to 1L in distilled water)

Reagents for Dot Blot:

TBS:20 mM Tris-HCl and150 mM NaCl at pH 7.5

TBS-T: 0.05% Tween20 in TBS

BSA/TBS-T: 4% BSA in TBS-T

Nitrocellulose membrane (BIO-RAD)

Reagents for cell proliferation:

WST-1 (Roche)

Table 3-1. List of Primary Antibodies

Antibody	Target	Species	Size (kDa)	Company
p c-Met	Tyr1234/1235	Rabbit	145	Cell signalling
c-Met		Rabbit	140, 170	Cell signalling
pEGFR	Tyr1173	Rabbit	175	Cell signalling
EGFR		Rabbit	175	Cell signalling
e-cadherin		Mouse	135	Abcam
PTPN11		Rabbit	71	Cell signalling
pAKT	S473	Mouse	60	Cell signalling
AKT		Rabbit	60	Cell signalling
Tubulin		Mouse	57	In-house
pErk	T202/Y204	Rabbit	44/42	Cell signalling
Erk		Mouse	44/42	Cell signalling
GAPDH		Mouse	37	Sigma

Dilutions used for Western Blotting:

Phospho c-Met (1:500), total c-Met (1:1000), phospho EGFR (1:1000), total EGFR (1:1000), E-cadherin (1:1000), PTPN11 (1:500), AKT (1:1000), phospho AKT (1:1000), Tubulin (1:10,000), GAPDH (1:1000), Erk (1:1000), phospho Erk (1:1000).

Secondary antibodies for Western Blotting:

Goat anti-rabbit antibody, used in 1: 2000

Goat anti-mouse antibody, used in 1:3000

Reagents for immunofluorescence staining

Primary antibody: mouse anti-flag (1:400), total Met (1:100), phospho c-Met (1:50), total EGFR (1:100), e-cadherin (1:50)

Secondary antibodies: Cy3 anti-rabbit, goat Cy5 anti-mouse,

Mowiol: 10% (w/v) Mowiol 4-88, 25% glycerol, 100mM Tris-HCl pH 8.5 (Calbiochem)

DABCO: 2.5% (w/v) 1,4-diazabicyclo[2.2.2]octane (Sigma-Aldrich)

TBS: Tris-buffered saline (25mM Tris, 100mM NaCl, pH 7.5)

4% (w/v) paraformaldehyde (PFA) (Sigma-Aldrich)

Sodium Borohydride (Sigma-Aldrich)

Immersol 510 Immersion oil (Zeiss)

3.2 Cell culture

MCF-7 and HEK293 were cultured in DMEM medium, HCC1954, HCC1954 with luciferase, shPTPN11-HCC1954 (GFP-tagged), shNT-HCC1954 (GFP-tagged) and shC-Met-HCC1954 (GFP-tagged) were cultured in RPMI medium.

BT20 was cultured in MEME. All media were supplemented with 10% foetal bovine serum (FBS), 2mM L-glutamine and penicillin/streptomycin antibiotics. Cell lines with knockdown (including control non-targeted HCC1954) were supplemented with 1µg/ml Puromycin. The HCC1954-

luciferase tagged cell line was supplemented with 7.5µg/ml Blastocydin. The cell cultures were kept at 37°C in humidified air containing 5% CO2.

Media were changed frequently to remove dead cells and to refresh nutrients. The cells were split once they became 80-90% confluent.

3.2.1 Transient transfection and cell treatments

To achieve 50–80% confluence required for transfection, cells were plated at $4x10^3$ MCF-7 cells per well in 96 well plates or $5x10^4$ cells per well in 24 well plates. FuGENE 6 (Promega) reagent was used for plasma c-Met DNA transfection. The number of cells for plating and the amount of DNA/reagent used were adjusted according to the table below.

Table 3-2. Guidelines on cell transfection according to surface area of the cells that have been seeded.

Type of dish or plate	Surface area per well or plate (cm^2)	Total media volume per well or plate (ml)	Starting volume of FuGENE 6 Reagent (µl/well or plate)	Starting mass of DNA (µg/ well or plate)
60 mm	21	4	6.0	2.0
35 mm	8	2	3.0	1.0
6-well	9.4	2	3.0	1.0
12-well	3.8	1	1.5	0.5
24-well	1.9	0.5	0.6	0.2
96-well	0.3	0.1	0.15	0.05

Pei reagent (Polysciences) was used for transfecting DNA for scFv-Fc against human c-Met. $10x10^6$ HEK293 cells were seeded onto a corning flask with DMEM media (with 10%FBS serum, 2mM L-glutamine and 1% penicillin/streptomycin). The following day, the media was replaced with fresh

DMEM media onto the corning flask. 300µg of the scFv-fc DNA plasmid was resuspended and incubated in 10ml of DMEM serum free media for 5 minutes in a 50 ml falcon tube, while 900µl of the PEI buffer was resuspended and incubated in another 10ml of DMEM serum free media for 5 minutes too. After those 5 minutes, the PEI buffer that was incubated in the DMEM free serum media was added onto the DNA (which was diluted in the DMEM media). The mixture DNA:Pei reagent was thoroughly resuspended and left incubated for another 20 minutes before adding it into the corning flask.

3.2.2 RNA Interference (RNAi)

siRNA Knockdown was achieved by treating cells with three different predesigned sequences targeting the sequence of interest. In the control group, cells were treated with scrambled non-targeting siRNA. Cells were transfected following the manufacturer's instructions. Briefly, basal like breast cancer cells were seeded in 6-well plates 1 day before transfection in RPMI media that was supplemented with 10% fetal calf serum without antibiotics. 2µg of targeting (siPTPN11) or non-targeting siRNA was mixed with 6µl of Lipofectamine RNAiMAX (Invitrogen) in 100µl Opti-MEM medium (Invitrogen) for 20 min at room temperature and then added to the cell culture medium at a final concentration of 20 nmol/liter. The cells were incubated at 37°C for 24-72 hours in 5% CO_2 prior to any further experiments or fixation. At the end of this incubation, protein expression was determined by immunoblotting analysis to assess knockdown efficiency.

3.2.3 Stable infection

Cells with stable knockdown of PTPN11 and non-targeting cells were provided by Dr Ruhe Chowdhury and Dr James Monypenny. In brief, viral particles (transfer vector, packaging vector, enveloping vector and Rev expressing vector) with specific shRNA or non-targeting were generated by transfection into 293T cell cultures. The supernatants, which contained viral particles, were collected and added to target cells (seeded in a t-25 flask) for infection. 48hr post infection, media were refreshed daily with puromycin selection (1µg/ml) for five days for the selection of antibiotic resistant cells due to the expression of a resistance gene associated with shRNA. Cells were cultured in 1µg/ml puromycin from here onwards to maintain the protein knockdown. I generated a stable knockdown of c-Met-HCC1954 cell line using the viral particles provided by the Breakthrough laboratory (Breast cancer NOW, Guy's hospital) and cells of interest (HCC1954) were infected as described previously.

3.3 Cell Lysates

Cells were seeded into 6 well plates and when at 90% confluency were lysed using cell lysis buffer. Cell debris was removed by centrifugation at 3,000rpm for 10 mins at 4°C. The supernatant was placed in 1.5ml eppendorf tubes and gel sample buffer was added. Samples were boiled for 3 mins and stored at -20°C until use.

3.3.1 Protein expression- immunoblotting

The expression of proteins was tested by western blotting. 1.7 x 10^5 cells were seeded in 6-well-plates if they were to be transiently transfected. If not, 3 x 10^5 were seeded in 6-well plates. At 80% confluence, the monolayer of cells was then exposed to biochemical treatment of inhibitors or ligands. The cells were washed twice with ice-cold PBS and protein extracts were prepared in 1 X SDS lysis buffer solutions. Protein concentrations were measured by the BCA protein assay kit using known concentrations of BSA protein as standards. For immunoblot, cell lysates were heated at 95˚C for 15min, and then 100mM DTT reducing agent and 0.004% bromophenol blue was added onto the samples. The samples were then electrophoresed on self-made 7.5% or 10% Tris-glycine SDS-polyacrylamide gels. Gels were run on an Invitrogen X-Cell mini-gel system, which were initially subjected to constant voltage electrophoresis at 120V until the blue loading dye reached the resolving gel in which case the voltage was then increased to 180V and run until the samples reached the bottom of the gel.

After separation, proteins were electrophoretically transferred onto nitrocellulose transfer membrane at 300mAmp for 2hr on ice using the Invitrogen XCell II Blot Module. Membranes were blocked 60min in 4% BSA in TBS-Tween and then incubated with specific primary antibody overnight at 4°C followed by appropriate secondary antibody for 45min at room temperature. Detection of bound antibody was with horseradish peroxidase-conjugated secondary antibodies and enhanced chemiluminescence (ThermoScientifc Fisher) with G-Box, Syngene. It was possible to re-use the

transfer membrane for a second incubation with different primary antibody. The protein bound to the transfer membrane were stripped off with Re-BLOT Plus Strong solution, diluted 1:10 with TBS-Tween, for 15min at 37°C, followed by blocking and antibody incubation steps as above. Western blot results were analysed and normalised with Quantity One software (Bio-Rad Ltd).

3.4 Dot Blot Assay

Firstly, we needed to have a nitrocellulose membrane ready and drew a grid by pencil to indicate the region that will be blotted. Then, using a narrow-mouth pipette tip, 2 µl of samples were spotted onto the nitrocellulose membrane at the centre of the grid.

Following this, the membrane was let dry for 20 minutes. The membrane was then soaked in 4% BSA in TBS-T for 1hour at RT to block non-specific sites. The membrane was then incubated with primary antibody dissolved in 4%BSA/TBS-T overnight at 4°C. The membrane was then washed three times with TBS-T (3 x 5 min). After this, the membrane was incubated with a secondary antibody conjugated with HRP for 1 hour at RT. The membrane was then washed three times with TBS-T (15 min each), and once with TBS (5 min). It was then incubated with chemiluminescence (ThermoScientifc Fisher) for 1 minute before being detected with G-Box, Syngene ECL reagent for 1 min.

3.5 Cell proliferation assay

Cells were cultured in 96-well plates, in a final volume of 100µl/well, at 37ºC, with a cell density of $4x10^3$ per well. 5 plates were set up; one each to be assessed at 24, 48, 72, 96 and 120 hours. Media containing inhibitor or ligand was refreshed every 24 hours and a 96-well plate was assessed every 24 hours for the duration of the experiment. In order to assess a plate, 10µl of Cell Proliferation Reagent Alarmar Blue was added to each well and the plate was returned and incubated at 37ºC for 4 hours. The plate was then removed, shaken thoroughly and the fluorescence of the samples measured on a plate reader (POLARstar Galaxy, BMG LabTechnologies) at excitation wavelength 544 nm and emission wavelength 590 nm to obtain the relative fluorescent units (RFU). A control blank was included on all plates to normalise the values. Each experimental group consisted of triplicates and were repeated in four independent experiments. The growth rate for each cell line, with and without stimulation was calculated to compare their k values. The equation used to calculate the k value was : ln(N4/N1)/(t4-t1). N4 stands for the amount of fluorescence at day 4, N1 stands for the amount of fluorescence at day 1, t4 stands for the day the assay was completed while t1 stands for the day when the assay has started.

3.6 Immunofluorescent Staining

Cells were seeded onto the ethanol washed and autoclaved coverslips (Section 2.2.3) at a density of $5x10^4$/ml per well in a 24 well plate. The following day, cells were fixed with 4% paraformaldehyde (PFA) for 20 mins

at room temperature. Following this, cells were washed three times (3 minutes per wash) with phosphate buffer saline plus calcium and magnesium (PBS+/+). Cells were then incubated with sodium borohyrate (1mg/ml) for 5 min to reduce auto-fluorescence followed by 3 washes with PBS+/+, 5 mins each. The cells were then permeabilised for 10 mins using 0.3% triton X- 100 and followed with another 3 washes with PBS+/+, 5 mins each. Non-specific binding was blocked by incubating for 30 mins at room temperature with 1% bovine serum albumin (BSA):TBS. After blocking, coverslips were incubated for 2 hours at room temperature with the primary antibody diluted in 1% BSA:TBS. The unbound antibody was removed by washing three times with PBS+/+ (5 mins each wash) and cells were incubated for 1h at room temperature with either the appropriate fluorophore conjugated secondary antibody in 1% BSA:TBS or with the mouse anti-flag antibody (when staining for the detection of scFv-Fc). When required, nuclei were stained with Hochst33342 at concentration of 0.1µg/ml for 3 mins at room temperature prior to mounting. The coverslips
were then washed two times with PBS+/+ and once with distilled water before the mounting with mowiol mounting medium mixed with 2.5% DABCO as an antifading agent, and dried overnight at room temperature. The slides were then stored in -20°C for long term storage.

The fluorescence was visualised using an “open” microscope automated FLIM system with epifluorescence using the TRI2 software. Confocal images were taken using a Nikon Eclipse Ni-E Upright with NIS (Nikon Instrument

Software) Element 64-bit software. Image analysis was performed using ImageJ software.

3.7 Preparation of high-content phage display library screen, for the production of scFv-Fc against human c-Met, using automated liquid handling robot

For the high-content scFv-Fc against human c-Met screen, JANUS Automated Workstation (PerkinElmer) was employed for the efficient automation of sample preparation and to ensure accuracy of the pipetting across all wells. Its dual-arm system offered a 96-tip Modular Dispense Technology (MDT) Dispense Head or a 4- tip Dispense Arm for optimal precision pipetting, processing from tubes to vials and from vials to plates.

The three 96-well plates that were provided by McCafferty et al, and consist of 240 clones with varying affinity for human c-Met were defrosted at room temperature on ice for 1 hour. This stock solution per well was diluted with the addition of 20µl of distilled water in each well, and each plate was then span down. The concentration of the wells was then assessed using a NanoDrop 1000 spectrophotometer (Thermo Fisher Scientific) and absorbance was measured at 260nm. The mean average of the DNA concentration in each well across each plate was 60ng/ul.

3000 HEK293 cells were robotically pipetted to three new 96 well plates, under sterile conditions. One day later, JetPEi (10µl/well) at the ratio 3:1 were robotically pipetted to another three 96 well plates, and incubated with DNA plasmid (0.24µg/well) from the scFv-Fc phage display library for 20min. At the end of this incubation, the transfection mixtures were added and

resuspended in each of the wells from the 96 well plates that were seeded with HEK293 cells the day before. Those plates were then stored in an incubator at 37°C in humidified air containing 5% CO_2. They were left there for 3 days and then span down and 180µl per well was collected and transferred into 3 new 96 well plates. The initial 96 well plates were stored in the freezer at -20°C while the new plates were stored at -4°C.

One day after transfection, MCF-7 cells were seeded into 384-well-plate using the automated liquid handling robot. 5000 MCF-7 cells resuspended in 200µl of media were added onto each of the 240 wells and kept in an incubator at 37°C in humidified air containing 5% CO2. After 24hr, Fugene 6 transfection reagent was used to transfect c-Met plasmid DNA (pCAGGS c-Met, at a concentration of 0.05µg/well) and Raf1-GFP (the latter was used as a positive control for efficient transfection) in 3:1 ratio. Cells were incubated for an additional 24h for sufficient c-Met overexpression and were then fixed with 4%PFA to perform the immunofluorescence staining of both c-Met and anti-flag from the scFv-Fc. The protocol outlined in section 3.5 in material and methods was followed for the immunofluorescence staining. The primary antibody used was the supernatant for the clones from the phage display library. After an hour incubation, and followed by three 5 minutes washes with PBS, the cells were incubated with the mouse anti-flag antibody at a dilution of 1:400. An hour later, more washes were performed, as stated in the protocol, and cells were incubated with the fluorophore conjugated secondary antibody goat anti-mouse Cy3 at a 1:400 dilution. This last incubation lasted for an hour before more washes and finally nuclear staining.

3.8 Plasmid purification and transformation

DNA construct was transformed into DH5α competent cells and plated on Luria- Bertani (LB) agar plates containing appropriate antibiotic (Ampicillin (1mg/ml) . Bacterial colonies were incubated in LB medium (4ml for miniprep or 200ml for Maxiprep) and were allowed to grow overnight at 37°C.

Miniprep and Maxiprep Kits were used to isolate plasmid DNA from bacterial cultures, following the manufacturer's protocol (Protocol overview: cells were harvested from bacterial cultures by centrifugation and cell pellets were resuspended in buffer containing RNase A; cells were lysed and mixed with precipitation buffer then flowed through an anion-exchange column fitted with the filtration cartridge unit; cell lysates were clarified and negatively charged phosphates of the DNA backbone interacted with the positive charges on the surface of the anion exchange resin; DNA was eluted under high salt condition and was desalted and concentrated by alcohol precipitation using 70% isopropanol prior to centrifugation; DNA pellets were washed with 70% ethanol and were air-dried after centrifugation; DNA was resuspended in nuclease-free water). DNA extract was quantified and its purity was determined with the NanoDrop 1000 spectrophotometer (Thermo Fisher Scientific). For quantity, absorbance was measured at 260nm and purity was determined by the ratio of absorption at 260nm:280nm. Pure DNA has a ratio of between 1.8 and 2.0, while a ratio below 1.8 shows high protein contamination.

3.8.1 Sequencing of maxipreps

Once the plasmids were produced, they were sent for sequencing to Eurofins. Briefly, the plasmids for scFv-Fc were diluted down to 100 ng/µl (in dH_2O). 10µl of 10µM of reverse primer and 15µl of the dilute DNA were mixed into an eppendorph. The pervious step was repeated using the forward primer (10µl of 10µM of forward primer) in a different eppendorph. Once the mixtures were made, a sticky tag was positioned on those samples and sent for sequencing to Eurofins. The primers used were the following:

pBIOCAM5 1404 REVERSE (sequence: **GAA CAG GAA CAC GGA GGGTC)**

pBIOCAMS 1219 FORWARD (sequence: **TTA ACA GTA GCA GGCTTG AGG)**

3.8.2 Coomassie staining

Polyacrylamide gels were left in Coomassie blue staining for 10 minutes on a shaker. The solution was then removed and replaced with a de-stain solution, on a shaker for 5 minutes. It was then removed and replaced by fresh de-stain solution and left until the bands on the gel became visible.

3.9 Mass production of scFv-Fc and Protein purification:

Corning flasks (Sigma-Aldrich) were used to scale up the production of scFv-Fc against human c-Met. Pei reagent was used to transfect the plasmid, as described under the section 3.2.1 '**Transient transfection and cell treatments'**. Five days after transfection, the supernatants from 4 corning flasks were collected, which was a total of 1.6L. These supernatant were then span down for 10min at 4000 RPM to remove cells and debris. They were then filtered through a 0.22 µm membrane filter using a vacuum pump. Once done, this was followed by the purification step. A HiTrap Protein A column (5ml preferably – GE Healthcare) is then used with a peristaltic pump. The column is then equilibrated with 5 column volumes of binding buffer (0.02M sodium phosphate, pH 7.0) on a high speed. The filtered sample is then applied to the column and the speed of the peristaltic pump is then reduced to 5 ml/min. Once the entire sample has gone through the column, the column is then washed with 5–10 column volumes of the binding buffer to remove impurities and unbound material. The bound Ig is then eluted with 5 column volumes of elution buffer and collected in vials that contain neutralisation buffer (100 µl of 1M Tris-HCl pH 9.0). The Ig purified eluted solution will then have its concentration determined by UV absorbance at 280 nm using a spectrophotometer (Nanodrop). The HiTrap column is then re-equilibrate with 5–10 column volumes of binding buffer. The column is then washed with 20% ethanol and stored at + 4-8°C.

3.9.1 Cy5 labelling of fragment antibody (scFv-Fc)

Tumour xenografts, cells and tissues were stained with scFv-Fc against human c-Met (an antibody fragment), labelled directly fluorophores. The antibody fragment was conjugated to Cy5-dye (GE Healthcare) according to protocol (FlurolinkTM) at pH 9.5 by Dr Gregory Weitsman. Briefly, un-conjugated dye was separated from the labelled antibody on a PD-10 desalting column (GE Lifesciences). A 10µl aliquot of the labelled antibody was diluted and absorption measured at 280nm and 650 nm for Cy5. The dye:protein final ratio was estimated by the following equations: (Cy5 D/P) final = [0.68 (A650)] / [A280 – (0.05 x A650)] where Ax is the absorbance at wavelength x. The final ratio of protein:dye was aimed for 1:2 for acceptor fluorophore Cy5-labelled protein. Final dye/protein ratio was of 2.4:1, with a concentration of 1.11mg/ml.

3.9.2 *In-vivo* breast cancer xenograft model establishment for whole- body optical imaging

Animal studies were carried out in accordance with UK Research Councils' and Medical Research Charities' guidelines on Responsibility in the Use of Animals in Bioscience Research, under UK Home Office license. Animals were maintained in either the Hodgkin, New Hunt’s House or Rayne BSU, Kings College London.

Female six to eight week old NSG mice were purchased from Charles River Laboratories (UK). The animals were maintained under sterile conditions in filter topped cages on sterile bedding and fed an irradiated diet of standard mouse chow.

Mycoplasma negative HCC1954 cell line (positive control) engineered to stably express luciferase (supplied by Dr Rebecca Marlow) and MCF-7 cell line (negative control) were used to establish *in-vivo* tumour models for longitudinal imaging (bioluminescence or SPECT). To establish subcutaneous models, four million cells of HCC1954 were suspended in 50µl sterile PBS was injected into the 4^{th} mammary fat pad in the right hand side and four million cells of MCF-7 cells also suspended in 50µl sterile PBS was injected into the 4^{th} mammary fat pad on the left hand side at day 0. Mice were monitored post procedure, the day following injection and at least twice weekly thereafter. Subcutaneous tumours were measured using calliper's (mm) and volume calculated using the formula Volume= $(length*width)^{2)}/2$). Mouse monitoring comprised of the assessment of weight, behaviour and palpable tumour size up to three times per week. In accordance with the PPL evidence of weight loss greater than 10%, moderate signs of behavioural distress and/or palpable tumour diameter ≥15mm (single tumour or combined tumours) precipitated humane killing by Schedule 1 method.

3.9.3 Bioluminescence and Fluorescence imaging

Bioluminescent and fluorescence imaging were performed using (IVIS® Lumina Series III, Perkin Elmer). Imaging and quantification of signals was controlled by the acquisition and analysis software Living Image®.

3.9.4 Luciferin stock preparation

30mg/ml stock solution D-Luciferin Firefly, potassium salt (Caliper life Sciences, Hopkinton, USA) for use in *in-vitro* and *in-vivo* experiments was prepared by dissolving 1g of D-Luciferin in 33.3mls DPBS without magnesium or calcium and mixed prior to filtering through a 0.2µm syringe filter (Merck Milliporem Watford, UK). Aliquots were frozen and stored at -80˚C. Prior to use aliquots were protected from light and thawed on ice.

3.9.5 *In-vivo* bioluminescence and fluorescence imaging

Following cell injection at day 0, animals were serially imaged to monitor tumour formation using bioluminescence imaging (IVIS™ Lumina Series III, Perkin Elmer) until an experimental end point defined by severity limit (Tumour Max Diameter 10mm). Animals were imaged in cohorts of 2-4 mice. At each imaging session mice were intraperitoneal injected with D-Luciferin Firefly, potassium salt (Caliper life Sciences, Hopkinton, USA) 150mg/kg (30 mg/mL stock) at time 0. In addition, at time 0, 25ug of Cy5-labelled-scFv-Fc against human c-Met tracer (predetermined by a previous experiment) was injected into the tail vein of each animal. Animals were then anaesthetised in a clear Plexiglas anaesthesia box (2% isofluorane) and once fully anaesthetised transferred to the nose cones (2% isofluorane) attached to the manifold on the warmed stage of the light tight imaging chamber. Imaging times ranged from 1-30 seconds and was performed at 10 minutes post luciferin injection. On completion, mice were returned to their cages and monitored until recovery.

Bioluminescence and fluorescence imaging were performed at time 0h, 2h, 4h, 8h and 24h post i.v injection of Cy5 labelled scFv-Fc against human c-Met. Following their final imaging session, mice were culled using a schedule 1 method. Removal of all tissues of interest was confirmed by ex vivo fluorescence imaging of tissues and the residual cadaver using the IVIS® camera system. Excised tissues of interest were snap-frozen and prepared for immunofluorescence staining.

Light emitted from bioluminescent tumours was detected by the IVIS® camera system, integrated, digitalised and displayed. Fluorescence from the Cy5 labelled tracer was also detected by the IVIS camera system, Image analysis was performed using the Living Image® software (Xenogen). Settings used for fluorescence were the following, exposure: 3 seconds, binning factor: 4 and excitation filter: 640 using Living Image® software. Serial scans across were reviewed and the colour scale normalised across the longitudinal series to facilitate visual comparison across scans. For quantitative comparison an appropriately sized region of interest (ROI) was selected to encompass subcutaneous tumour or lung areas and the total flux (photons per second) within these ROIs was measured.

3.9.6 Preservation of fresh frozen tissue

Tissues (e.g. primary tumours) were dissected out and embedded in the optimal cutting temperature (OCT) compound. The tissue was then

immersed into isopentane which had been cooled by suspension in liquid nitrogen. Tissue was not removed from the isopentane until freezing was complete (5 seconds or less depending on size). We then transferred the snap frozen sample from the isopentane to a pre-chilled storage container for transfer to a -80°C freezer until further use. Frozen tumours were cut into 4-5µm sections with a cryostat for immunostaining.

3.9.7 Confocal microscopy

Confocal fluorescence images were acquired on a confocal fluorescence laser scanning microscope (A1 Confocal; Eclipse Ni-E Upright; Nikon) equipped with 4x, 10x, 20x dry objectives and 40x, 60x and 100x oil immersion objectives. Aperture was set to one Airy unit for the longest wavelength. The various colour filters that were used for detecting the different fluorophores were as follow (excitation wavelength): DAPI (405-450nm), FITC (488- 510nm), Cy3 (543- 573nm) and Cy5 (633- 738nm). Images at each wavelength were acquired with the use of a constant exposure time. Images were visualised using NIS Elements and analysed using ImageJ.

3.10 Radiolabelling

The scFv-Fc was reconstituted in HEPES buffer (0.1 M, pH 8.5) using disposable PD10 size exclusion columns. Fractions containing the scFv-Fc were combined and applied to a Vivaspin column (30 kDa molecular weight cut off, 2 mL). Four successive ultracentrifugation cycles were performed to

ensure that no residual buffer salts from previous scFv-Fc preparation remained. This was particularly important, as any residual amine-containing compound, such as tris buffer salts, react with SCN-pBn-CHX-DTPA, effectively prohibiting reaction between SCN-pBn-CHX-A''-DTPA and the scFv-Fc. The chelator SCN-pBn-CHX-A''-DTPA (0.3 mg), in 20 molar equivalent excess, was reacted with the scFv-Fc (2 mg) in HEPES buffer overnight at ambient temperature. Following this, the reaction solution was applied to a PD10 size exclusion column, eluted with ammonium acetate (0.2 M), and fractions (0.5 mL) collected.

The purified conjugate CHX-A''DTPA-scFv-Fc was either stored at −20°C or immediately used for radiolabelling.

3.10.1 Quality control of 111In-CHX-A''DTPA-scFv-Fc against human c-Met

Radiochemical purity was determined by size exclusion-high-performance liquid chromatography (SE-HPLC) (Fig 3-1). The HPLC system used consisted of an Agilent 1200 Series HPLC system and a Phenomenex Biosep 2000 (300 × 7.8 mm^{2-} Phenomenex, Macclesfield, UK) size-exclusion column with an isocratic mobile phase of 0.1M phosphate buffer containing 2 mM EDTA, pH 7 and a flow rate of 1 mL/min. The retention time of the immunoconjugate was typically 7-8 min and that of the unbound 111In impurities was approximately 11-12 min. This was coupled to a radiation detector with in-line UV and gamma detection (Flow-Count, LabLogic).

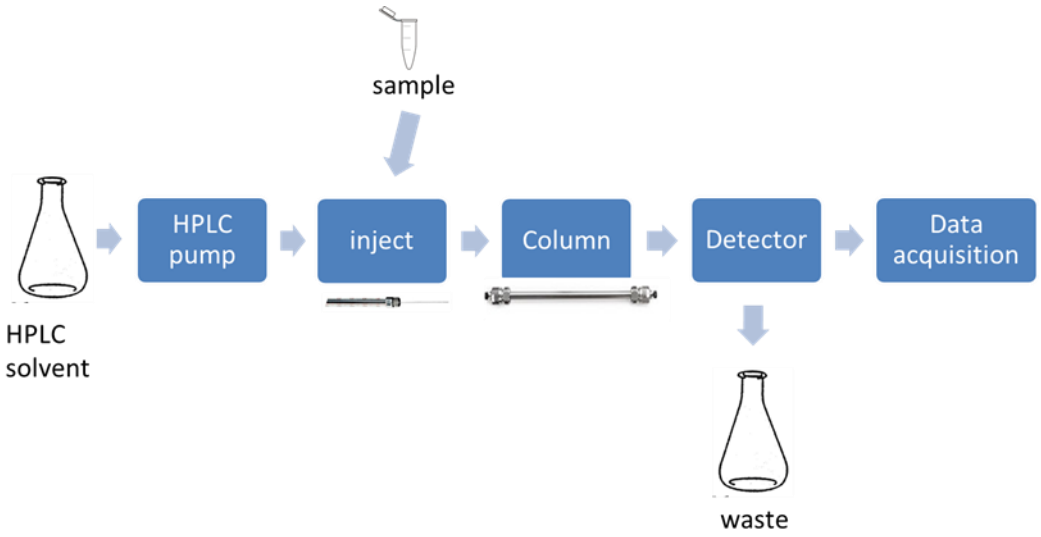

Figure 3-1. Flow chart of a HPLC system.

The HPLC instrumentation includes a pump, injector, column, detector and integrator or acquisition and display system. A high-pressure pump (solvent delivery system) is used to generate and meter a specified flow rate of mobile phase. An injector (sample manager or autosampler) is able to introduce (inject) the sample into the mobile phase stream that carries the sample into the HPLC column. The column contains the chromatographic packing material needed to effect the separation and is called the stationary phase. A detector enables the visualisation of the separated compound bands as they elute from the HPLC column. The mobile phase exits the detector and can be sent to waste, or collected, as desired.

3.10.2 Serum stability testing of the radiolabelled compound

The stability of the labelled compound was evaluated in human serum. Stability of the ^{111}In-CHX-A''DTPA-scFv-Fc was determined by incubating the ^{111}In-CHX-A''DTPA-scFv-Fc for 3h, 7h and 24 hours in human serum before performing SEC-HPLC analysis to determine radiochemical purity (as

described in section 3.10.1). HPLC-UV analysis of the conjugated product was performed to monitor for degradation products or other impurities. Concurrently, a solution of Indium-111 in ammonium acetate (0.33 M, 8 MBq, 300 µL) was added to human serum and incubated at 37 °C for 3h, 7h and 24 hours followed by analysis using size-exclusion HPLC.

3.11 *In-vivo* SPECT imaging

Animals bearing subcutaneous mammary tumours were imaged using c-Met targeted radiotracer at a time point estimated from the IVIS data and animal monitoring to be optimal for tumour establishment. On the day of imaging the tracer, ^{111}Indium-CHX-A''DTPA-scFv-Fc, was radiolabelled by Dr Michelle Ma. On day of scanning, mice were transferred from the Rayne BSU to the imaging laboratory and anaesthetised with isofluorane, O_2 flow rate of 1.0-1.5L/min and isofluorane levels of 2-2.5%. Under anaesthesia mice were injected intravenously with tracer. Syringe weights prior to and subsequent to injection were recorded for each mouse to permit calculation of the delivered injected volume. Residual activity in the syringe and on the gauze used to compress the injection site was measured using the capintec and recorded for each mouse.

For image acquisition, mice were positioned on the bed of the NanoSPECT/CT Silver Upgrade (Mediso Ltd., Budapest, Hungary) equipped with a multiplexed multipinhole (nine pinholes, aperture 1.0 mm) collimator. Imaging was performed under 2% isofluorane anaesthesia. Helical SPECT

images were acquired over 30-40 minutes (SPECT 60-70 seconds per frame, CT images 55kVp, 1000ms and 1 degree angular stepping.). On completion of their final scan, mice were culled using a schedule 1 method. The weight and activity of each culled mouse was measured using a gamma counter (1281 gamma counter, LKB Wallac, Turku,Perkin Elmer, UK Finland). Mouse organs (gut, liver, kidneys, spleen, lungs, heart, tail and palpable tumour sites) were removed and weighed. The residual carcass weight and activity were noted. Tumour tissues were snap frozen for subsequent histological verification and stored in the hot lab -80°C freezer. Radionuclide images were reconstructed and fused with CT images prior to image analysis, performed using VivoQuant™ version 1.23 software.

3.12 Statistical Analyses:

Microsoft Excel and GraphPad were used to calculate mean, standard deviation and standard error of the mean and generate graphs for visual comparison of mouse groups. Other statistical analysis such as the one-way ANOVA test was used to compare means between more than two independent groups. For parametric data, means of two independent groups were compared using the Student's t-test. Mean values with standard deviation and/or standard error means were calculated using Excel.

Chapter 4: c-Met PET Imaging Detects Early Stage Loco-Regional Recurrence of Basal-Like Breast Cancer

4.1 Introduction

Basal-like breast cancer (BLBC) and triple negative breast cancer (TNBC) remain the greatest challenge among all the molecular subtypes of breast cancer, due to their clinically aggressive nature and poorly characterized molecular pathogenesis [217]. Unlike oestrogen (ER)-positive luminal tumors and HER2-positive tumours, the basal-like subtype and TNBCs typically lack expression of the molecular targets that confer a response to highly effective hormonal targeted therapies such as trastuzumab (HER2 amplification), tamoxifen (ER) and aromatase inhibitors (ER) [218]. However, numerous studies pinpoint the overexpression of c-Met and EGFR in these subtypes and sensitivity to EGFR and c-Met tyrosine kinase inhibitor (TKI) [69, 219].

Additionally, TNBC patients display a high rate for locoregional recurrence (LRR), after mastectomy or breast conserving surgery (BCS) [31, 220, 221]. Locoregional recurrence is a major issue as it is associated with a poor survival rate [222].

71%-91% of triple negative breast cancer, defined as lacking ER-, progesterone (PR)- and HER-2 receptors, have a basal-like phenotype [223]. Dent et al identified a defined pattern for locoregional recurrence in patients

with TNBC [31]. The pattern is characterised by rapidly rising rate in the first 2 years following diagnosis, followed by a peak at 2 to 3 years, and a decline in recurrence risk over the next 5 years, along with a negligible risk of recurrence thereafter [31].

Predictions for LRR in breast cancer are currently based on clinical factors such as tumour size, axillary lymph node involvement, hormone receptor status, age at diagnosis, lymphovascular invasion. However, those predictions are not reliable, especially for patients with 1 to 3 axillary lymph nodes involved [224]. Complementary imaging, such as mammography may be considered in symptomatic patients and patients at high risk for recurrent disease [225]. Unfortunately, mammography can only detect 25-45% of recurrences as the post-operative and post-radiation changes of breast conservation therapy decrease mammography's sensitivity and specificity compared with a standard screening population [226]. Other non-invasive methods, such as the use of circulating serum tumour markers in the detection of LRR has been discouraged due to a lack of evidence for its suitability [225]. There is therefore a clear need to find a modality, which is sensitive and non-invasive for the detection of a LRR at its early stages.

In this project, we focus on the use of a c-Met binding peptide PET tracer for the detection of early locoregional recurrence in BLBC. PET has many advantages which are its non-invasiveness, its high sensitivity, requiring only 10^{-11} – 10^{-12} mol/L levels of probe for detection [160] and the ability to yield excellent quality images allowing a quantitative assessment of tracer binding.

In our study, the radionuclide ^{18}F was selected for the radiolabelling of the c-Met peptide binding tracer, [^{18}F]AH113804. Well standardised, ^{18}F labelling chemistry can be adapted for the automated preparation of a wide variety of ^{18}F tracers in high yields and high radiochemical purity. This makes ^{18}F suitable for PET imaging [227]. In addition, with a half-life of $T_{1/2}$ = 109.8 min, ^{18}F poses less constraints on synthesis time and allows the investigation of processes of slower tracer kinetics up to about 6h. The relatively long half-life of ^{18}F also enables the distribution of ^{18}F radiopharmaceuticals to clinical services within a few hours of transport [227]. Additionally, ^{18}F emits positron particles with a low kinetic energy during nuclear decay (mean energy of 250 keV, Emax 635 keV), hence making it safer than other radioisotopes for handling purposes, and it has a short path in soft tissues (less than 0.3 mm) prior to annihilation which is conveyed into a high spatial image resolution [228].

^{18}F-FDG was first manufactured in 1978 [229] and has become the most commonly used radiopharmaceutical for PET oncology studies. The use of FDG-PET/CT has recently been adopted by many clinics, although not used in primary breast cancer screening [164]. However, it has been introduced for diagnostic purposes as a complementary aid to mammography and breast ultrasound [165]. Despite ^{18}F-FDG PET's ability to detect cells with increased metabolic activity, such as cancer cells, studies have shown its struggle in the differentiation of recurrent BC from inflammatory or infectious processes and its inability to identify small lesions (<10 mm) [166-168]. This is regardless of PET resolution as the newest PET/CT systems have a spatial resolution which is as good as 4mm [230].

Lately, huge interest has been drawn onto c-Met, a tyrosine kinase receptor, and its clinical significance in BLBC and TNBC [46, 56, 219]. A study conducted by Kim et al found that c-Met is most frequently expressed in BLBC (57.5%) and that c-Met expression was mainly localised to the cell membrane, with some weak expression in the cytoplasm. In this study, they identified a correlation between c-Met expression with ER ($p<0.001$) and PR ($p<0.001$) negativity and no correlation between HER2 expression with c-Met expression. There was also a strong correlation with EGFR expression ($p<0.001$) and CK5/6 ($p<0.001$) [219]. The knockdown of c-Met in high c-Met expressing BLBC cell lines, such as HCC1954 and BT549 resulted in a significant decrease in cell proliferation and migration ($P < 0.05$), indicating a potential contribution of c-Met in the tumorigenicity of BLBCs [219]. In addition to basal-like breast cancer, c-Met is overexpressed in many other solid cancers which include lung, ovary, kidney, colon, thyroid, liver, and gastric carcinomas [3-11].

Hence, due to c-Met's involvement in a wide range of cancers, much focus has been given to the development of c-Met inhibitors in preclinical and early clinical studies. c-Met inhibitors are being investigated as a monotherapy and in combination with other targeted agents or chemotherapy in breast cancer, colorectal cancer, Non-Small Cell Lung Cancer (NSCLC) and brain tumours [78]. Most of the c-Met inhibitors showed promising results when used in drug combinations, which is likely due to the complexity of tumour biology. c-MET inhibitors have demonstrated very few side-effects in patients [231].

Tivantinib (also known as ARQ197) [86], cabozantinib (known as XL184) [81], MetMab (onartuzumab) [232] and foretinib (XL880) [80] have recently completed their phase II clinical trials for the treatment of advanced TNBC.

In a phase 2 randomised trial in 45 Metastatic Breast Cancer (MBC) patients, [233] 64% of the patients, that were administered Cabozantinib, displayed tumour regression with an objective response rate (ORR) of 14% along with a disease control rate of 48%.

Additionally, a phase II clinical trial in NSCLC showed that the combination of onartuzumab (anti-c-Met mAb) with erlotinib (anti-EGFR TKI) led to an increase in progress free survival in comparison to erlotinib and placebo only (PFS, HR=0.53). The overall survival (OS, HR=0.4) was improved in those patients [148]. However, surprisingly the phase III did not confirm the efficacy results observed in the phase II and needs further investigation [147].

Furthermore, there is increasing evidence for the involvement of c-Met as a mechanism of resistance to anticancer treatment [234]. C-Met targeted therapies show promising results and have a great future in cancer.

Additionally, a recent report demonstrates that there is a significant increased risk of recurrence (1.52-fold) in TNBC and is associated with c-Met overexpression [75]. These accumulated evidences make c-Met an ideal target for the detection of tumour locoregional recurrence in BLBC as well as for the screening of treatment monitoring method of the efficacy of anti-c-Met therapies *in-vivo*.

[^{18}F]AH113804, a c-Met molecular targeted agent used in this project has a high affinity for human c-Met (K_d≈2 nM). This highly specific c-Met binding peptide has previously been conjugated with the fluorescent cyanine dye, named GE-137, and used for the detection of polyps in humans [213]. In this optical clinical study, this low-molecular weight small peptide showed favourable pharmacokinetics and safety profile. The use of GE-137 led to the identification of another 9 adenoma polyps, which overexpress c-Met, that were not detected by light alone [213].

Based on the sum of evidence regarding the suitability of c-Met as a molecular target in basal-like breast cancer and the positive features displayed by GE-137 as an optical molecular targeted agent, we assessed [^{18}F]AH113804-driven PET for the early detection of loco-regional recurrence in BLBC, using the HCC1954 tumour xenografts. This study has now been published in the Journal Nuclear of Medicine [16], named as ‘c-Met PET Imaging Detects Early Stage Loco-Regional Recurrence of Basal-Like Breast Cancer’, in which I am the leading first author. To avoid redundancy of the material, King’s College London regulations state that I can incorporate my publication as part of my thesis chapter, found below. Extensive work, which include an additional eleven supplementary figures are found in this publication. Material & Methods related to this project are also described in this publication.

4.2 Results from my publication – original copy

c-Met PET Imaging Detects Early Stage Loco-Regional Recurrence of Basal-Like Breast Cancer

Appitha Arulappu[1*], Mark Battle[2*], Michel Eisenblaetter[1,3,4*], Graeme McRobbie[2], Imtiaz Khan[2], James Monypenny[1], Gregory Weitsman[1], Myria Galazi[1], Susan Hoppmann[2], Patrycja Gazinska[5], Wulan Wulaningsih[1], Grethe Tang Dalsgaard[2], Sven Macholl [2, 6**], Tony Ng[1,5,7**]

1. Richard Dimbleby Department of Cancer Research, Kings College London, London, UK

2. GE Healthcare, Life Sciences, Amersham, UK

3. Division of Imaging Sciences & Biomedical Engineering, King's College London, London, UK

4. Department of Clinical Radiology, University Hospital Münster, Münster, Germany

5. Breast Cancer NOW Unit, King's College London School of Medicine, London, UK

6. Barts Cancer Institute, Queen Mary University of London, London, UK

7. UCL Cancer Institute, University College London, London, UK

* Contributed equally to this work

** Co-senior authors

Corresponding author:

Professor Tony Ng

The Richard Dimbleby Department of Cancer Research

New Hunt's House

Guy's Hospital Campus

London SE1 1UL, UK

E-mail: tony.ng@kcl.ac.uk

Telephone: +44 (0)207 848 8056 Fax: +44 (0)20 7848 6220

Short running title:

cMet imaging of loco-regional recurrence

ABSTRACT

Loco-regional recurrence of breast cancer poses significant clinical problems due to frequent inoperability once the chest wall is involved. Early detection of recurrence by molecular imaging agents against therapeutically targetable receptors, such as c-Met, would be of potential benefit. The aim of this study was to assess [^{18}F]AH113804,a peptide-based molecular imaging agent with high affinity for human c-Met, for the detection of early-stage loco-regional recurrence in a human basal-like breast cancer model, HCC1954. **Methods:** HCC1954 tumor-bearing xenograft models were established, and [^{18}F]AH113804 was administered. Distribution of radioactivity was determined via positron emission tomography (PET) at 60 min post radiotracer injection. PET and CT (computerized tomography) images were acquired 10 days after tumor inoculation, to establish baseline distribution and uptake, and then on selected days after surgical tumor resection. CT images and caliper were used to determine the tumor volume. Radiotracer uptake was assessed by [^{18}F]AH113804 PET imaging. c-Met expression was assessed by immunofluorescence imaging of tumor samples and correlated with [^{18}F]AH113804 PET imaging results. **Results:** Baseline uptake of [^{18}F]AH113804, determined in tumor-bearing animals after 10 days, was approximately 2-fold higher in the tumor as compared to muscle tissue or the contralateral mammary fat pad. The tumor growth rate, determined from CT images, was comparable between the animals with recurrent tumors, with detection of tumors of low volume (<10 mm^3) only possible by Day 20 post

tumor resection. [^{18}F]AH113804 PET detected local tumor recurrence as early as six days after surgery in the recurrent tumor-bearing animals, and exhibited significantly higher [^{18}F]AH113804 uptake (in comparison to mammary fatty tissue) with a target to background (muscle) ratio of approximately 3:1 (p<0.01). The c-Met expression of individual resected tumor samples, determined by immunofluorescence, correlated with the respective [^{18}F]AH113804 imaging signals (r=0.82; p<0.05). **Conclusion:** [^{18}F]AH113804 PET provides a new diagnostic tool for the detection of c-Met-expressing primary tumor and has potential utility for the detection of loco-regional recurrence from an early stage.

Keywords

PET/CT imaging, basal-like breast cancer, HCC1954, c-Met, AH113804, cancer, loco-regional recurrence

INTRODUCTION

The proto-oncogene c-Met is a receptor tyrosine kinase activated by the ligand hepatocyte growth factor (HGF). The HGF/c-Met signaling axis has been described as a promoter of cancer cell growth, angiogenesis, invasion and metastasis [235]. Overexpression of c-Met is associated with poor prognosis and a more malignant tumor phenotype [236, 237]. Several c-Met inhibitors are currently under evaluation in clinical trials, either as stand-alone therapies or in concomitant treatment [79]. c-Met is overexpressed in various solid tumors [238], including breast cancer (BC), with higher expression in Basal-like Breast Cancer (BLBC) than in other intrinsic cancer subtypes [239] . BLBC, which accounts for up to 15% of all BCs, exhibits a high rate of loco-regional recurrence after initial therapy [31, 220, 221, 240].

Although treatment of localized disease has improved over the past decades, up to 45% of BC patients suffer a local, regional or systemic relapse within 8 years after initial therapy [220]. While systemic relapse in the form of distant metastasis is still regarded as incurable according to current treatment guidelines, loco-regional recurrence of BC should be treated with curative intention [241]. Treatment success crucially depends on the earliest possible diagnosis, before chest wall involvement or further organ invasion prevents any form of aggressive treatment [242]. Established guidelines for post-therapy monitoring in BLBC feature mammography and clinical examination which frequently fail to identify local tumor relapse at a sufficiently early stage [243].

Magnetic resonance imaging (MRI) and FDG-PET/CT offer a comparably higher sensitivity and specificity for detection and

characterization of BC relapse [225]. However, differentiation of recurrent BC from inflammatory or infectious processes, and the identification of small lesions (tumor size <20 mm) still impose challenges for FDG-PET [167, 168]. c-Met targeted imaging could provide such a tool to further improve the performance of post-treatment surveillance, and could aid patient stratification for targeted therapy.

For this study we chose the novel, peptide-based molecular imaging agent [^{18}F]AH113804 (Fig 1A) which binds to human c-Met with high affinity (*K*d≈2 nM), has a favorable kinetic profile, exhibits specific uptake in c-Met positive tumor tissue and rapid systemic clearance [244]. This enables for diagnostic PET imaging as early as one hour after administration [244]. The safety, pharmacokinetics and imaging characteristics have all been assessed using GE-137, the fluorescent-labelled analogue of AH113804, in healthy volunteers and in patients at high risk of colorectal neoplasia [244].These initial studies in humans suggested that GE-137 was safe, and that it may improve visualization of colonic polyps, which display a high level for c-Met [244].

In this study, we assessed [^{18}F]AH113804-driven PET for the early detection of loco-regional tumor recurrence in a preclinical model of BLBC.

MATERIALS AND METHODS

Cell culture

Human basal-like subtype breast cancer cells HCC1954 (CRL-2338) were obtained from the American Type Culture Collection and cultured in RPMI 1640 (Invitrogen) with 10% fetal calf serum (Bodinco BV) and 2 mM L-

glutamine (Invitrogen) at 37 °C in a fully humidified atmosphere containing 5% CO_2.

Western blotting

Immunoblotting was performed as described in ref [245]. Detection of bound antibody was with horseradish peroxidase-conjugated secondary antibodies and enhanced chemiluminescence (ThermoScientifc Fisher) with G-Box, Syngene.

Tumor xenograft model

All animal studies were performed in compliance with the UK Home Office Animals (Scientific Procedures) Act 1986. Female SCID (Severely Immunodeficient) mice (17 to 19 g at time of first procedure, Charles River UK) were subcutaneously injected with 4×10^6 cells in 0.1 mL of a 1:1 mixture of medium and Matrigel (BD Biosciences) in the second right mammary fat pad. Tumor size was measured twice per week by caliper. The volume for the tumor was estimated as length*width^2/2. Further details on the tumor xenograft model are given in the Supplementary Methods.

Radiosynthesis of [^{18}F]AH113804

Synthesis of the peptide is described in the supplementary section of ref [244]. Details of the radiosynthesis of [^{18}F]AH113804 are given in the Supplementary Methods.

CT and PET imaging

Small-animal PET/CT imaging was performed using microPET P4 (Concorde) and microCAT II (ImTek Inc.) systems as described earlier [246]. Each animal was injected intravenously (iv) with approximately 7 MBq (0.1 mL) [^{18}F]AH113804. Further details of the imaging procedure are given in the Supplementary Methods.

Tumor and contralateral mammary fat pad uptake are presented as target-to-muscle retention ratio (TMRR). Further details are given in the Supplementary Methods.

Ex vivo tissue analyses

Details of all ex vivo tissue analyses are given in the Supplementary Methods. These include histology of formalin-fixed, paraffin-embedded tumor and quadriceps muscle, and [^{18}F]AH113804 autoradiography and immunofluorescence staining of snap-frozen tumor tissue.

Statistical analysis

Unless otherwise stated, group averaged data are presented as mean ± standard error of the mean (SEM). The observed skewed distribution of TMRR measures was lessened by logarithmic transformation, see Supplementary Methods. All statistical analyses were performed in R version 3.1.2 (R Project for Statistical Computing, Vienna, Austria).

RESULTS

Synthesis of [^{18}F]AH113804

Total synthesis time on the automated platform was 49 min. For all synthesis runs, the decay corrected end-of-synthesis yield was between 38 and 41%, with a radioactive concentration (RAC) between 600 and 800 MBq/mL. The radiochemical purity was always >90%, the chemical content between 15 and 20 µg/mL, and specific activity approximately 100 GBq/µmol for each test item.

c-Met expression level in HCC1954

Human c-Met protein expression level was assessed in HCC1954, compared to HT-29 (high c-Met expressing) and U87 (moderate c-Met expressing) cell line lysates. The data shows upregulation of c-Met in the HCC1954 cell line (Suppl Fig 1). Burggraff *et al*. assessed the specificity of GE-137, performing a competition study in HT-29 tumor bearing mice which showed a reduction in tumor uptake of GE-137 when co-administrated with an excess of unlabeled peptide [244].

Tumor targeting of [^{18}F]AH113804

Baseline uptake of [^{18}F]AH113804 (Fig 1A) was assessed in 8 tumor-bearing animals using PET imaging at 10 days post tumor inoculation (Fig. 1B). Levels of radioactivity at 60 minutes pi were 4.9±0.6% ID/mL in kidney, 2.9±0.3% ID/mL in liver, and 2.0±0.2% ID/mL in blood. PET imaging (Fig 1C) revealed a significant difference between the uptake of [^{18}F]AH113804 at the tumor site (1.5±0.2% ID/mL, white arrowhead) compared to both contralateral mammary fat pad (0.8±0.1% ID/mL, blue arrowhead) and muscle (0.8±0.1% ID/mL) at 60 minutes p.i. *Ex vivo* biodistribution studies,

following PET imaging on Day 50 post tumor resection, confirmed [^{18}F]AH113804 accumulation in tumor was significantly higher compared to muscle (2.5±0.6% ID/g *vs*. 0.9±0.2%ID/g at 70 min pi, n=3. p<0.05. Suppl Fig 2).

Early-stage recurrent tumor growth is first detected with [^{18}F]AH113804, later by CT, and last by palpation

Following tumor resection 14 to 16 days after inoculation, 5 animals were found to exhibit recurrent tumor growth, confirmed by necropsy after final imaging. The remaining 3 animals did not exhibit any tumor re-growth (by caliper measurements). However, there was lack of correlation between tumor size by caliper and uptake of the tracer at the tumor site (Suppl Fig. 3). Tissue from the site of injection for one of the non-recurrent mice was stained. Negativity for tumor cells and human c-Met expression by IHC was confirmed (Suppl Fig. 4). In this case, the %ID/g in the ROI was 0.6 (c.f. the %ID/g at the contralateral site was 0.5).

Analysis of [^{18}F]AH113804 PET images provided evidence for the presence of loco-regional recurrence from Day 6 post-resection in these 5 animals (Figure 2A). There was some degree of variation in the uptake of radioactivity at the tumor site in individual animals on each study day (Suppl Table 1). However, overall uptake on each day was comparable to that observed in the tumors pre-resection. The TMRR was significantly higher at the tumor resection site in comparison to the contralateral mammary fat pad on Day 6 (2.7±0.3 *vs*. 1.0±0.3, p<0.001; n=5; Fig 2B). Uptake of [^{18}F]AH113804 at the site of resection remained clearly visible in the PET

images on subsequent days, with the TMRR significantly smaller in the contralateral mammary fat pad on Day 13 (1.6±0.2 vs 0.9±0.2, $p<0.01$), Day 20 (1.6±0.1 vs 0.9±0.2, $p<0.001$) and Day 36 (1.5±0.8 vs 0.9±0.2, $p<0.01$). At Day 50 post tumor resection, the TMRR was also higher for the tumor site (1.7±0.7) than for the contralateral mammary fat pad (1.0±0.0), although this difference was not statistically significant. No specific [^{18}F]AH113804 retention was detected in the contralateral mammary fat pad with levels of radioactivity in this region comparable to muscle tissue for all time points (Suppl Fig 5).

By Day 20 post tumor resection, the mean tumor volume determined by CT measurement was approximately 7.0±12.5 mm^3 (Fig 3A&B). Palpable tumor recurrence was detected from Day 29 post tumor resection (Fig 3A).

[^{18}F]AH113804 retention in tumor tissue versus systemic clearance

Systemic clearance of [^{18}F]AH113804 was studied in selected tumor-bearing mice over the first 60 min pi by dynamic PET imaging. Figure 4A shows the distribution of [^{18}F]AH113804 at 15 min (13-18 min) and 60 min (55-65 min) p.i. A decrease in [^{18}F]AH113804 signal is observed in the major perfused organs, and retention of [^{18}F]AH113804 at the tumor site (Fig 4B). Figure 4C displays the change in TMRR from 5 min to 60 min pi in relation to TMRR at 5 min p.i. While the tumor TMRR continuously increased, TMRRs for lungs, liver, heart and others decreased.

Autoradiography and immunohistochemical analysis confirm [^{18}F]AH113804 accumulation in c-Met positive tumor tissues

A heterogeneous pattern of [^{18}F]AH113804 distribution was observed within the tumor, with viable tissue in the tumor periphery exhibiting a positive signal while the central tumor regions exhibited only low activity (Figure 5A). H&E staining and immunohistochemistry of consecutive tumor slides revealed a large number of c-Met positive tumor cells (Figure 5B, left and right panels respectively). Both recurrent and primary tumors showed necrotic areas in H&E devoid also of c-Met (IHC) and displaying low [^{18}F]AH113804 uptake (Suppl. Fig 6&7).

Ex vivo histology correlates with the PET images

Following immunofluorescent staining (Figure 6A), c-Met expression levels were quantified across whole tumor slides (Figure 6B).A significant correlation was found between c-Met expression and *in-vivo* PET (r =0.82, p=0.023. n=7), suggesting [^{18}F]AH113804 signal in tumor at 60 min pi to be representative of c-Met expression. A similar correlation was observed between c-Met expression determined by IHC and [^{18}F]AH113804 signal *in-vivo* (r=0.83, p=0.0015) (Suppl Fig 8).

In addition, it was found that the variation in the c-Met expression levels observed across the tumor samples (displayed in Fig 6B) was due to the tumor size. Indeed, a correlation (r = 0.83; p = 0.0005) was identified between the total c-Met intensity level and the surface area of the tumor sample (Suppl. Fig 9).

DISCUSSION

Early detection and identification of tumor relapse enables improved loco-regional recurrence control resulting in an increased quality of life and better overall survival for BC patients [247]. Current surveillance guidelines have been shown to be less effective in the detection of loco-regional recurrence than the more expensive, yet more sensitive, approaches such as MRI or radionuclide imaging (Single-photon emission computed tomography, PET) [225, 243]. It is believed that either individually, or as a companion test for established diagnostic approaches, targeted molecular imaging of specific tumor markers bears the potential to positively change BC follow-up; especially in patients presenting with a high risk of relapse such as BLBC patients [247, 248].

[^{18}F]AH113804 is known to have a high affinity for human c-Met, as demonstrated in studies by Evans *et al*., where the *in-vivo* affinity of [^{18}F]AH113804 was determined via receptor blocking in HT-29 xenograft tumour mouse models [249] . [^{18}F]AH113804 clears fast from plasma and non-target tissues (such as liver, lungs and heart), allowing for high contrast imaging after injection, and improving the sensitivity for tumor detection, as confirmed by PET imaging in this study.

Our study shows that [^{18}F]AH113804-driven PET imaging allowed for early detection of loco-regional tumor recurrence in HCC1954 tumor-bearing mice after surgery. [^{18}F]AH113804 uptake and retention in the lungs and heart, reflecting the non-specific blood pool distribution of [^{18}F]AH113804 decreased constantly over the observation period. In contrast, a constant

signal was observed within the region of tumor regrowth, indicative of specific accumulation of [^{18}F]AH113804 due to target binding. [^{18}F]AH113804 allows for excellent tissue penetration, and the *in-vivo* PET imaging revealed satisfactory tumor to non-target (muscle) tissue ratio from one hour p.i.

We were able to detect statistically significant differences in tumor uptake compared to contralateral mammary fat pad at Days 6, 13, 20 and 36 after tumor resection. The lack of statistical significance at the latter timepoints is most likely due to the lower, inhomogenous distribution of radioactivity in the tumors. PET images from some of those recurrent tumor bearing animals (images not shown) showed evidence of peripheral uptake only, indicative of necrosis in the tumor core.

Currently [^{18}F]FDG is used in PET diagnostics for detection and staging in cancer. Numerous studies have revealed that other, more target-specific tracers would be beneficial for the detection of loco-regional recurrence [156]. In a study of patients with breast cancer, it was shown that tumour size was an important factor when correctly diagnosing patients [250]. A review of 111 patients showed that a tumor size of less than 10 mm was a significant predictor of a false negative [^{18}F]FDG PET result [168]. In our study, a specific signal from [^{18}F]AH113804 could be detected, even when the recurrent tumor was not yet observable via CT. A previous study by Cullinane *et al.* found [^{18}F]FLT to be superior over [^{18}F]FDG in assessing the effect of the c-Met inhibitor crizotinib in human glioblastoma and human gastric cancer pre-clinical models [251]. When tumor size decreased within 1

week of treatment, [^{18}F]FDG uptake remained unchanged while [^{18}F]FLT PET showed a marked decrease in uptake. [^{18}F]FLT is reflective of cell proliferation, and as such was indicative of tumor therapy response. Still the use of [^{18}F]FLT as a marker for proliferation has been heavily debated, with reports suggesting that results should be viewed with caution [252]. Such studies denote the importance of targeting radiotracers such as [^{18}F]AH113804 for accurate tumor detection and patient monitoring.

Our study demonstrates correlation between c-Met from the tumor samples and the maximum uptake (% ID/mL) from [^{18}F]AH113804 at those sites in the corresponding PET images. A recent study using an optical analogue of AH113804 (GE-137) also showed a good concordance between the expression of c-Met and the optical signal detected [212, 244].

Other groups have investigated the use of both monoclonal antibodies and anticalins as probes for c-Met imaging. ^{89}Zr-db-/^{76}Br-ornartuzumab and ^{89}Zr-PRS-110 were developed and assessed for visualization of c-Met positive tumors in preclinical models [214, 253]. Optimal imaging time points were identified to be between 2 and 5 days after tracer administration, thus hampering potential routine clinical use as diagnostic agents. In contrast, the biodistribution of [^{18}F]AH113804 permitted early imaging after tracer administration. Similarly, Li *et al*. explored the use of c-Met targeting scFv-cys dimers in Non-Small Cell Lung Cancer xenografts. Despite showing very high affinity for c-Met, good contrast immunoPET imaging was achieved only at 20 hours after injection [254].

The ubiquity of c-Met dysregulation in malignant disease and its known influence on tumor progression make c-Met an attractive target for diagnostic targeting and therapeutic intervention in multiple cancer types. Phase II and III clinical studies, evaluating c-Met inhibition in gastroesophageal cancer, lung cancer and hepatocellular carcinoma have shown encouraging results with clear benefit for the individual patient [79-81].

It is hypothesized for BC, as well as for those cancer types that react more favourably to c-Met inhibition, that stratification of patients according to aberration in the c-Met axis resulting in target overexpression would strongly increase the efficiency of targeted treatment.
[^{18}F]AH113804 mediated PET signals proved to reflect the c-Met expression in individual tumors in our BC model, suggesting that this tracer could also serve as such a companion diagnostic for patient selection and for therapeutic purposes. Future studies to evaluate this utility are required.

CONCLUSION

This study demonstrates that [^{18}F]AH113804 PET provides a new diagnostic tool for the detection of c-Met-expressing primary tumor and has potential utility for the detection of loco-regional recurrence from an early stage. Further preclinical work is warranted to determine whether

[^{18}F]AH113804 uptake in the regrowth provides a useful predictive tool for anti-c-Met therapeutic intervention.

ACKNOWLEDGMENTS

We thank GE Healthcare for the provision of [^{18}F]AH113804, and for providing access to their laboratory facilities and staff. In particular, we thank Joanne Nesbitt, Rochelle Lear, David Gendle and Chris Beazley (all GE Healthcare at the time of study) for excellent technical support. We also like to thank Sven Macholl and Mark Battle (both GE at the time of study) for both excellent technical and intellectual support. We thank Anthony Cheung and Fabian Flores-Borja (both KCL) for preparatory experiments.

This work was supported by a MRC UK/GE Healthcare CASE studentship to Appitha Arulappu, MR/L001640/1 to Michael Eisenblaetter, FP7-HEALTH-2010 grant 'Imagint' (number 259881) to Gregory Weitsman, CR-UK/EPSRC funding for the KCL-UCL CCIC (C1519/A10331, C1519/A16463; Myria Galazi, Michael Eisenblaetter), an endowment fund from Dimbleby Cancer Care to KCL (Tony Ng, James Monypenny), and a Breakthrough Breast Cancer fund to Patrycja Gazinska.

REFERENCES

1. Birchmeier C, Birchmeier W, Gherardi E, et al. Met, metastasis, motility and more. *Nat Rev Mol Cell Biol.* 2003;4:915-925.

2. Bean J, Brennan C, Shih JY, et al. Met amplification occurs with or without T790M mutations in EGFR mutant lung tumors with acquired resistance to gefitinib or erlotinib. *Proc Natl Acad Sci U S A.* 2007;104:20932-20937.

3. Rong S, Segal S, Anver M, et al. Invasiveness and metastasis of NIH 3T3 cells induced by Met-hepatocyte growth factor/scatter factor autocrine stimulation. *Proc Natl Acad Sci U S A.* 1994;91:4731-4735.

4. https://clinicaltrials.gov/ct2/show/NCT01186991. Study evaluating the safety and efficacy of onartuzumab (Metmab) and/or bevacizumab in combination with paclitaxel in patients with metastatic, triple negative breast cancer. Aug 2010.

5. Bandla S, Pennathur A, Luketich JD, et al. Comparative genomics of esophageal adenocarcinoma and squamous cell carcinoma. *Ann Thorac Surg.* 2012;93:1101-1106.

6. Gastaldi S, Comoglio PM, Trusolino L. The Met oncogene and basal-like breast cancer: another culprit to watch out for? *Breast Cancer Res.* 2010;12:208-217.

7. Dent R, Trudeau M, Pritchard KI, et al. Triple-negative breast cancer: clinical features and patterns of recurrence. *Clin Cancer Res.* 2007;13:4429-4434.

8. Lowery AJ, Kell MR, Glynn RW, et al. Locoregional recurrence after breast cancer surgery: a systematic review by receptor phenotype. *Breast Cancer Res Treat.* 2012;133:831-841.

9. Pogoda K, Niwinska A, Murawska M, et al. Analysis of pattern, time and risk factors influencing recurrence in triple-negative breast cancer patients. *Med Oncol.* 2013;30:388-395.

10. Eiermann W, Vallis KA. Locoregional treatments for triple-negative breast cancer. *Ann Oncol.* 2012;23:(Suppl 6):vi30-34.

11. Wapnir IL, Anderson SJ, Mamounas EP, et al. Prognosis after ipsilateral breast tumor recurrence and locoregional recurrences in five national surgical adjuvant breast and bowel project node-positive adjuvant breast cancer trials. *J Clin Oncol.* 2006;24:2028-2037.

12. Voogd AC, van Oost FJ, Rutgers EJ, et al. Long-term prognosis of patients with local recurrence after conservative surgery and radiotherapy for early breast cancer. *Eur J Cancer.* 2005;41:2637-2644.

13. Montgomery DA, Krupa K, Cooke TG. Alternative methods of follow up in breast cancer: a systematic review of the literature. *Br J Cancer.* 2007;96:1625-1632.

14. Schneble EJ, Graham LJ, Shupe MP, et al. Current approaches and challenges in early detection of breast cancer recurrence. *J Cancer.* 2014;5:281-290.

15. Schneble EJ, Graham LJ, Shupe MP, et al. Future directions for the early detection of recurrent breast cancer. *J Cancer.* 2014;5:291-300.

16. Kumar R, Chauhan A, Zhuang H, et al. Clinicopathologic factors associated with false negative FDG-PET in primary breast cancer. *Breast Cancer Res Treat.* 2006;98:267-274.

17. Burggraaf J, Kamerling IM, Gordon PB, et al. Detection of colorectal polyps in humans using an intravenously administered fluorescent peptide targeted against c-Met. *Nat Med.* 2015;21:955-61.

18. Ng T, Shima D, Squire A, et al. PKCalpha regulates beta1 integrin-dependent cell motility through association and control of integrin traffic. *EMBO J.* 1999;18:3909-3923.

19. Battle MR, Goggi JL, Allen L, et al. Monitoring tumor response to antiangiogenic sunitinib therapy with 18F-fluciclatide, an 18F-labeled alphaVbeta3-integrin and alphaV beta5-integrin imaging agent. *J Nucl Med.* 2011;52:424-430.

20. Meyers MO, Klauber-Demore N, Ollila DW, et al. Impact of breast cancer molecular subtypes on locoregional recurrence in patients treated with neoadjuvant chemotherapy for locally advanced breast cancer. *Ann Surg Oncol.* 2011;18:2851-2857.

21. Sohn YJ, Jang JS, Choi SR, et al. Early detection of recurrence after endoscopic treatment for early gastric cancer. *Scand J Gastroenterol.* 2009;44:1109-1114.

22. Evans P BM, Getvoldsen G, McRobbie G, et al. Nonclinical tumor efficacy studies of [18F]AH113804, a novel PET imaging agent with high affinity for the human c-Met receptor [Abstract]. . *Proceedings of the AACR 103rd Annual Meeting 2012 31 Mar – 4 Apr 2012, Chicago, IL.* 2012.

23. Gaeta CM, Vercher-Conejero JL, Sher AC, et al. Recurrent and metastatic breast cancer PET, PET/CT, PET/MRI: FDG and new biomarkers. *Q J Nucl Med Mol Imaging.* 2013;57:352-366.

24. Vallabhajosula S. (18)F-labeled positron emission tomographic radiopharmaceuticals in oncology: an overview of radiochemistry and mechanisms of tumor localization. *Semin Nucl Med.* 2007;37:400-419.

25. Cullinane C, Dorow DS, Jackson S, et al. Differential (18)F-FDG and 3'-deoxy-3'-(18)F-fluorothymidine PET responses to pharmacologic inhibition of the c-Met receptor in preclinical tumor models. *J Nucl Med.* 2011;52:1261-1267.

26. McKinley ET, Ayers GD, Smith RA, et al. Limits of [18F]-FLT PET as a biomarker of proliferation in oncology. *PLoS One.* 2013;8:e58938.

27. Liu S, Zheng Y, Volpi D, et al. Toward operative *in-vivo* fluorescence imaging of the c-Met proto-oncogene for personalization of therapy in ovarian cancer. *Cancer.* 2015;121:202-213.

28. Jagoda EM, Lang L, Bhadrasetty V, et al. Immuno-PET of the hepatocyte growth factor receptor Met using the 1-armed antibody onartuzumab. *J Nucl Med.* 2012;53:1592-1600.

29. Terwisscha van Scheltinga AG, Lub-de Hooge MN, Hinner MJ, et al. *In-vivo* visualization of MET tumor expression and anticalin biodistribution with the MET-specific anticalin 89Zr-PRS-110 PET tracer. *J Nucl Med.* 2014;55:665-671.

30. Li K, Tavare R, Zettlitz KA, et al. Anti-MET immunoPET for non-small cell lung cancer using novel fully human antibody fragments. *Mol Cancer Ther.* 2014;13:2607-2617.

31. https://clinicaltrials.gov/ct2/show/NCT01147484. A Study of Foretinib in Patients With Recurrent/Metastatic Breast Cancer (IND197). May 2010.

32. https://clinicaltrials.gov/show/NCT01738438. Cabozantinib for Metastatic Triple Negative BrCa. Institute D-FC. Nov 2012.

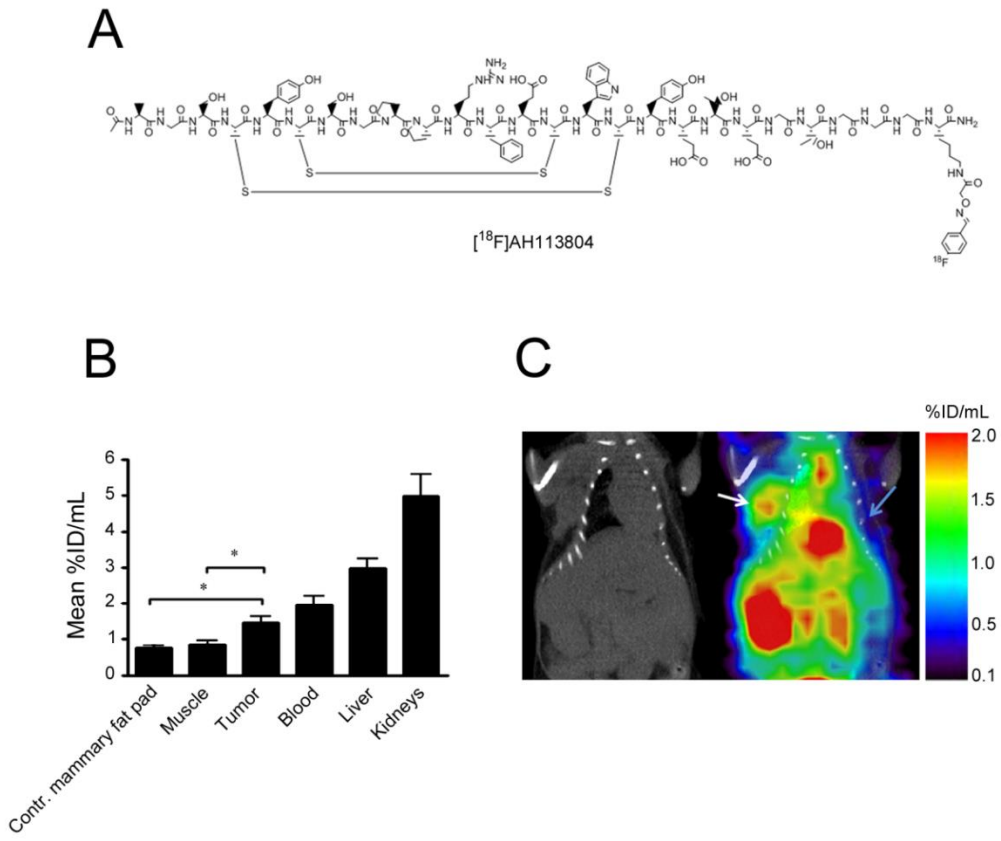

Figure 1. Biodistribution of [18F]AH113804 and HCC1954 tumor.

(A) Molecular structure of [^{18}F]AH113804. **(B)** Distribution of [^{18}F]AH113804 in selected organs and tissues in HCC1954 tumor xenografts 10 days p.i. Statistically significant differences were observed in the uptake of [^{18}F]AH113804 in tumor versus muscle and contralateral side (Students *t*-test, mean±SEM, n=8, *: $p<0.05$). **(C)** CT and PET/CT images of a representative tumor-bearing mouse 10 days p.i. demonstrates [^{18}F]AH113804 signal at the tumor site (white arrow), but not at the contralateral site (blue arrow).

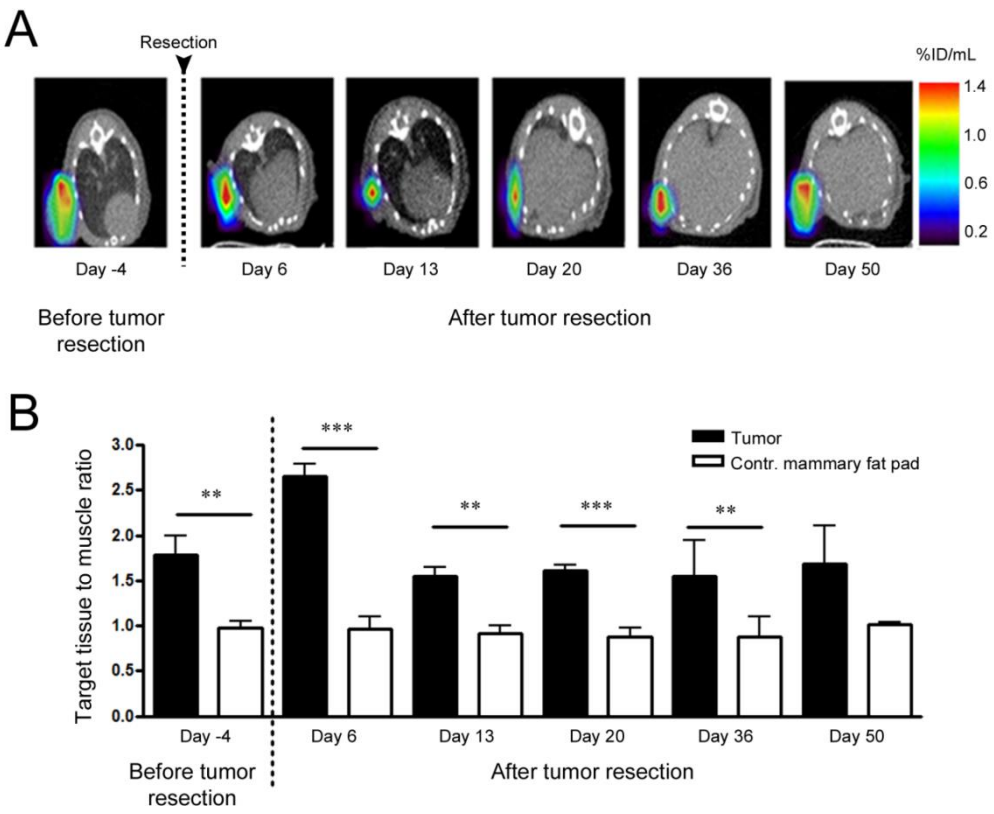

Figure 2. Early detection of tumor regrowth using [18F]AH113804 for PET imaging.

(A) PET/CT images of a transverse section of a representative tumor-bearing mouse, 4 days before tumor resection and at selected days after resection, show [^{18}F]AH113804 signal at the tumor site at 60 min p.i. For clarity, the PET signal only in the ROI is shown. **(B)** Target-to- muscle ratio in the tumor and contralateral sites. Statistically significant differences between both sites observed at Days 6, 13, 20 and 36 (Students *t*-test, mean±SEM, Day 4 pre-resection: n=8, Days 6 and 13 post resection: n=5, Days 20 and 36: n=4, Day 50: n=3. ** $p<0.01$, *** $p<0.001$).

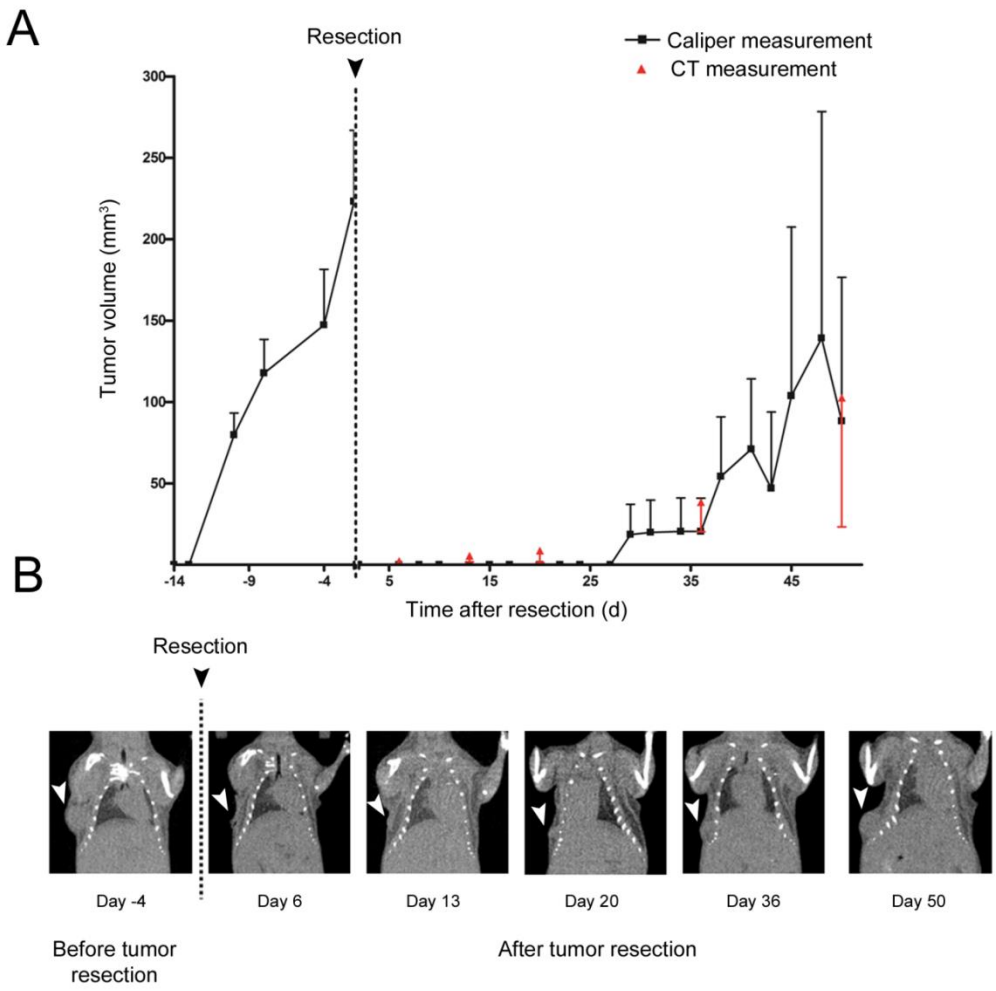

Figure 3. Detection of loco-regional tumor recurrence via CT and caliper measurements.

(A) Growth curve of mean tumor volume obtained from caliper and CT measurements of the same group of animals, before and after primary tumor resection (mean±SEM, n=5 per study day, except days 20 and 36: n=4, day 50: n=3). **(B)** Coronal CT slices of a representative tumor-bearing mouse before and after resection show the presence (white arrow) and regrowth of the tumor after resection. Tumor growth was observed by CT from day 20 onwards.

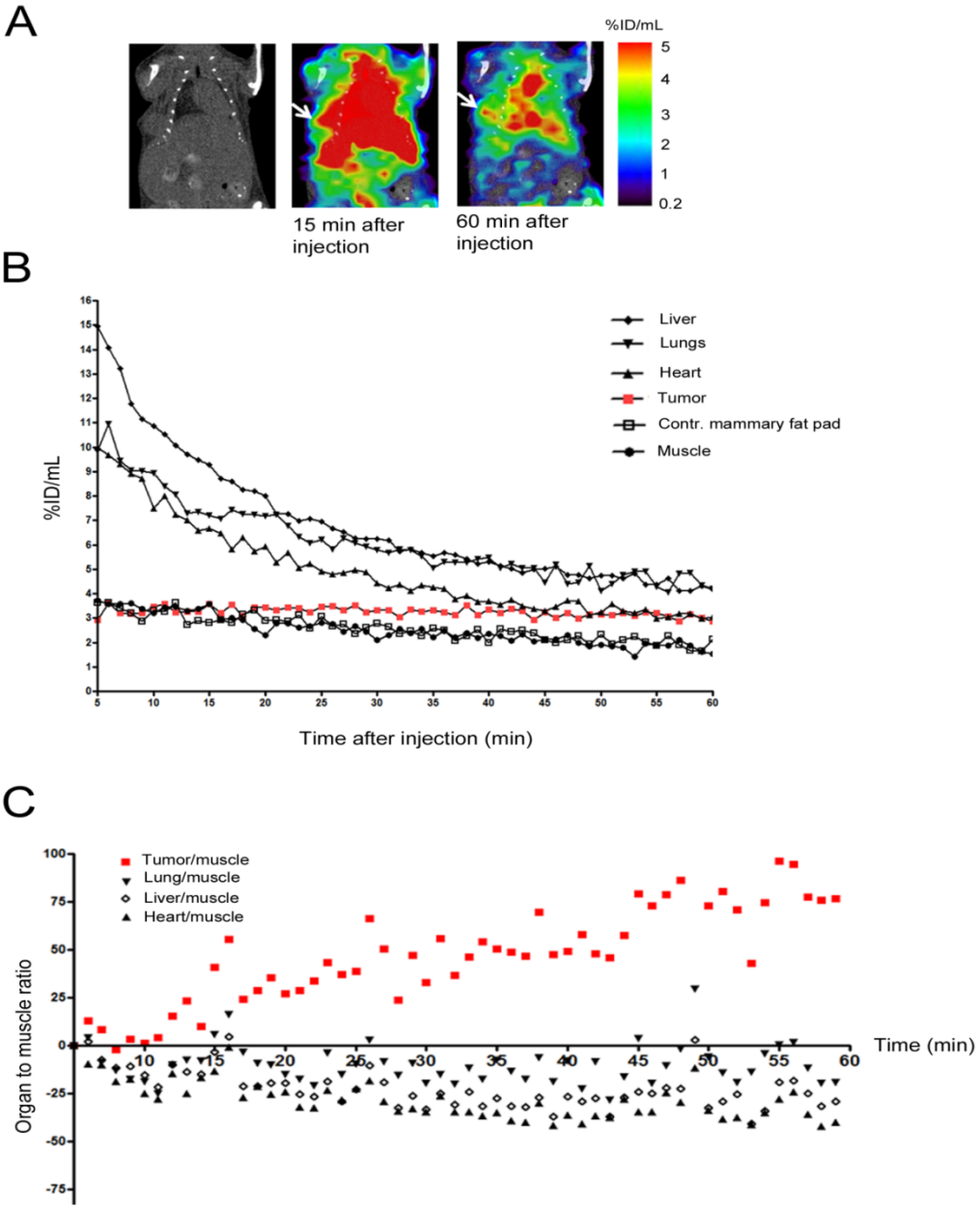

Figure 4. Biodistribution of [18F]AH113804 in a recurrent HCC1954 tumor-bearing mouse.

(A-left) Representative CT image of a HCC1954 xenograft mouse, acquired at Day 36 post resection. Recurrent tumor observed (White arrowhead). **(A-middle and right)** PET/CT at 15 min and 60 min p.i. of [^{18}F]AH113804, with retained radioactivity in the tumor visible by 60 min p.i.. **(B)** Dynamic ROI analysis of PET/CT shows a constant concentration at the tumor site but steady decline in all other organs (n=1). **(C)** Data of panel B normalized to the first time point show the relative change with a clear increase for tumor (n=1).

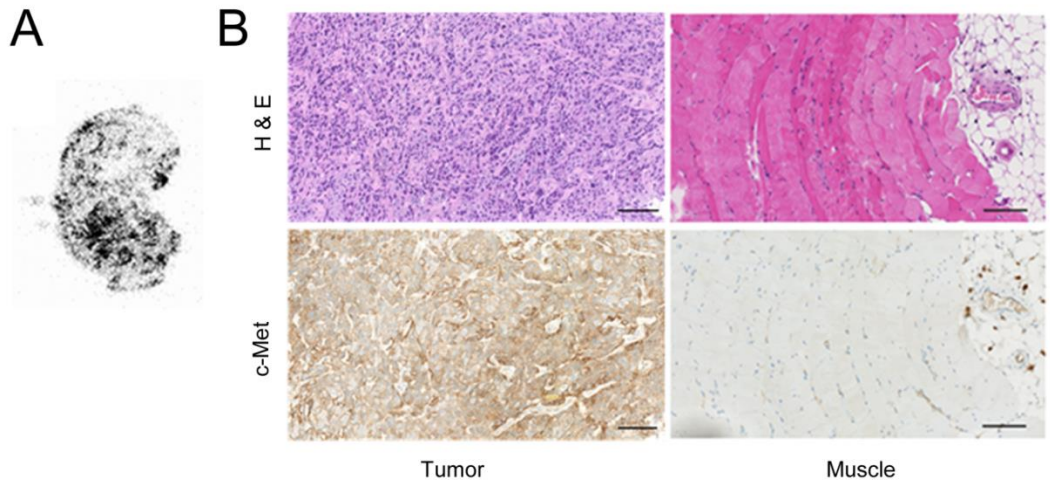

Figure 5. Autoradiography and immunohistochemistry demonstrate [18F]AH113804 retention in c-Met positive HCC1954 tumor tissue.

(A) Autoradiography performed *ex vivo* on a resected tumor confirms retention of the [^{18}F]AH113804 radiotracer in tumor tissues. A heterogeneous distribution of tracer within the tumor section could be observed, not visible at the limited spatial resolution of PET imaging. **(B)** H&E staining (upper) and c-Met immunostaining (lower) of paraffin-embedded tumor and control skeletal muscle tissue (left and right columns respectively). H&E staining reveals the large, mitotic and disorganized phenotype characteristic of tumor cells, while immunohistochemistry reveals membranous c-Met staining in these cells. Scale bars=100 µm.

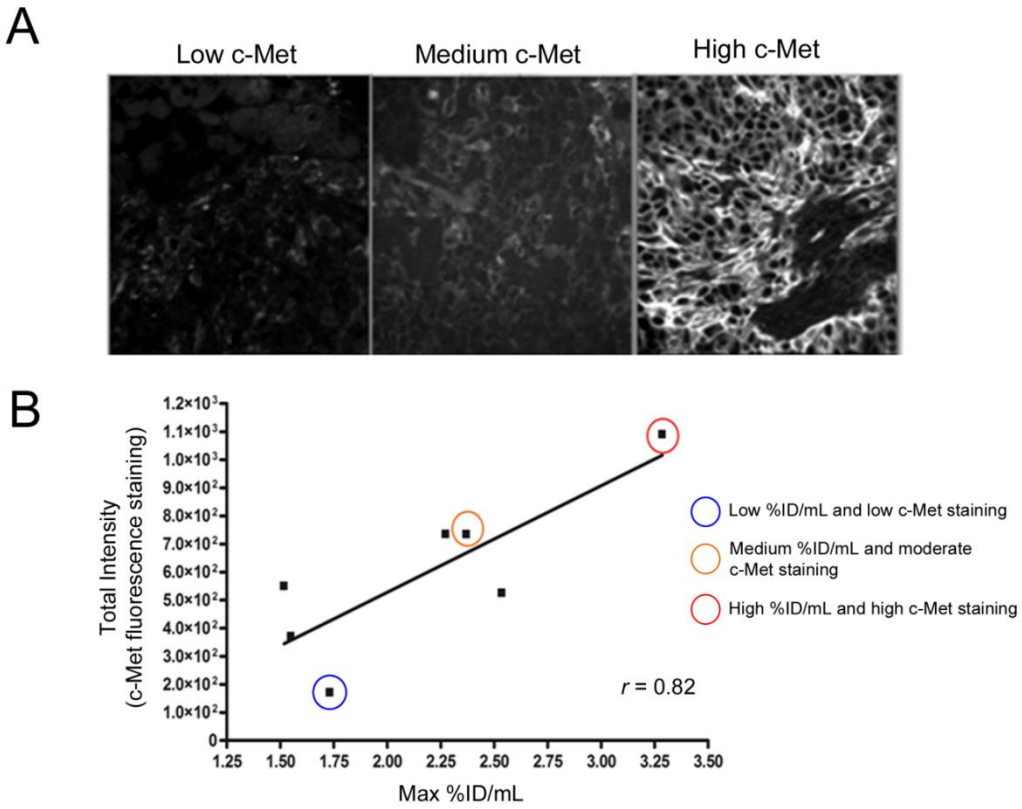

Figure 6. Uptake of [18F]AH113804 correlate with the c-Met expression level in the corresponding resected tumor samples.

(A) Immunofluorescent staining for c-Met in resected tumor samples (Day 14, n=7). Low, medium and high c-Met staining examples highlighted panel B. **(B)** A positive correlation is found between (a) the Max %ID/mL of tumor ROIs from *in-vivo* PET images, and (b) the c-Met protein expression level from immunofluorescent staining in the same tumors after resection. Pearson's correlation coefficient=0.82 (P<0.05, n=7).

SUPPLEMENTARY MATERIAL

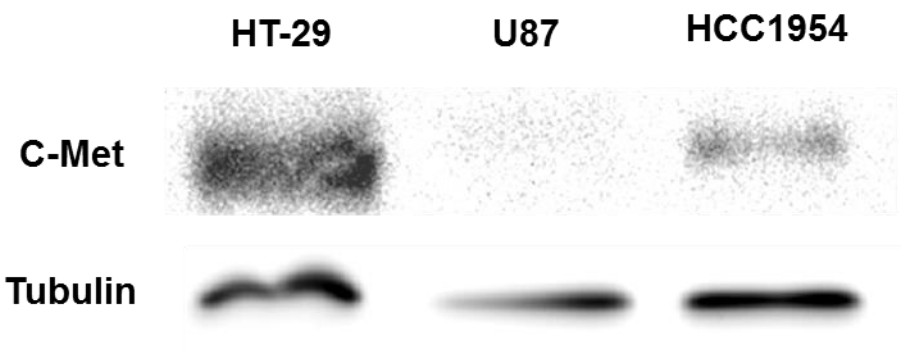

Suppl Figure 1. Western blot of c-Met expression.

Highest expression level of c-Met is found in HT-29, less in HCC1954 and very little in U87 cell lysate. Tubulin was used as a loading control.

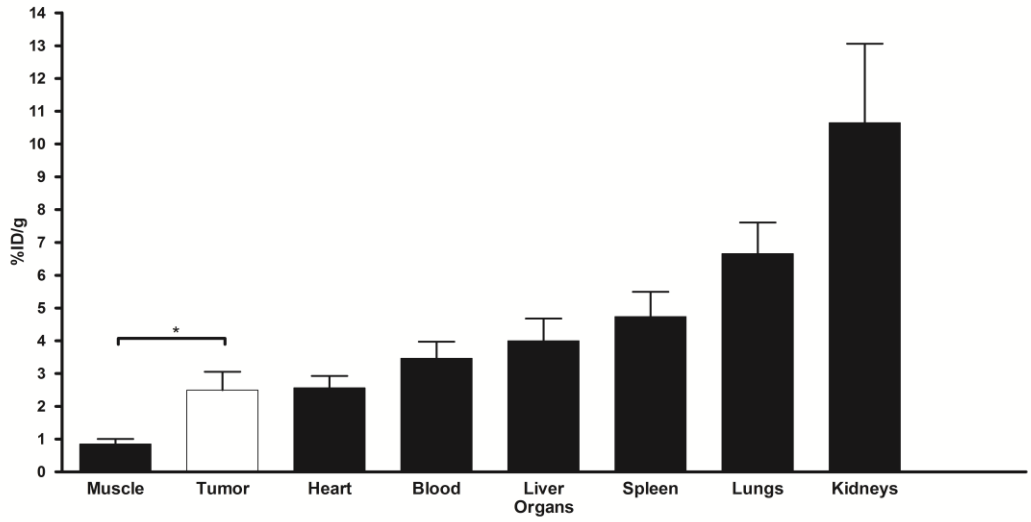

Suppl Figure 2. [18F]AH113804 activity (% ID/g) from ex vivo assay of dissected organs and tissue samples from HCC1954 tumor bearing mice.

Organs were excised at 70 min p.i. on Day 50 post tumor resection. A single *t*-test was performed to compare uptake of [^{18}F]AH113804 uptake in tumor and muscle. A statistically significant difference was observed ($p<0.05$, $n=3$). *P* value was calculated in R version 3.1.2.

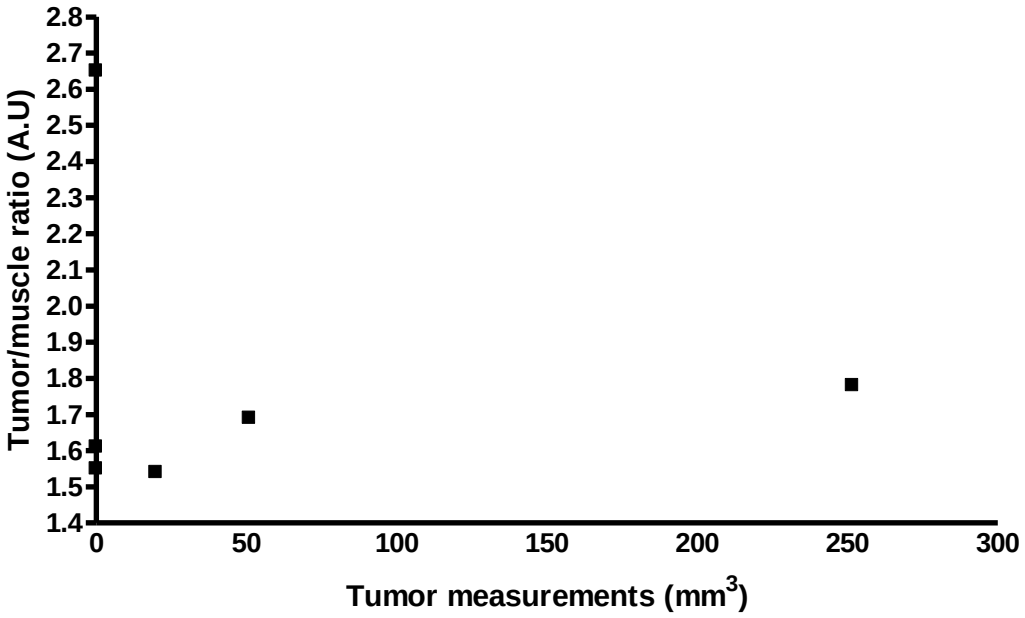

Suppl Figure 3. No correlation observed between tumor size by caliper measurement and the uptake of the tracer at the tumor site.

This graph shows the mean tumour measurement of all tumour-bearing mice at 6 timepoints, with its matching mean uptake of the tracer (measurement taken at day 4 pre tumor resection, day 0, day 6, day 13, day 20, day 36 and day 50 post tumor resection).

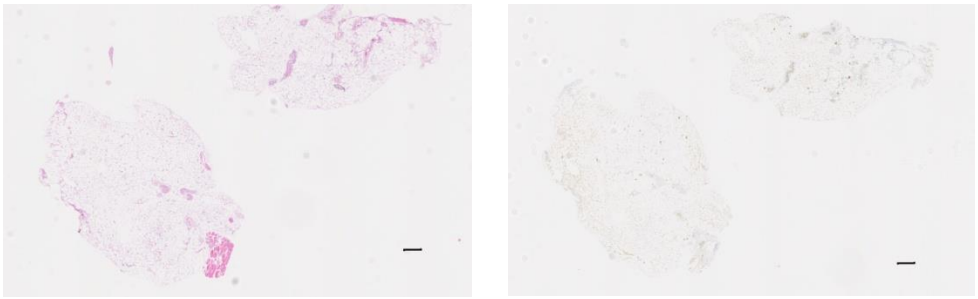

Suppl Figure 4. Immunohistochemical staining of mammary fat pad from a mouse that did not have a recurrent tumor after resection.

The left panel represents the H&E staining of the sample that shows a clear presence of adipose tissue and ducts. No tumor cells were detected. The right panel shows staining for c-Met. No significant c-Met staining was observed. Scalebar represents 200 µm.

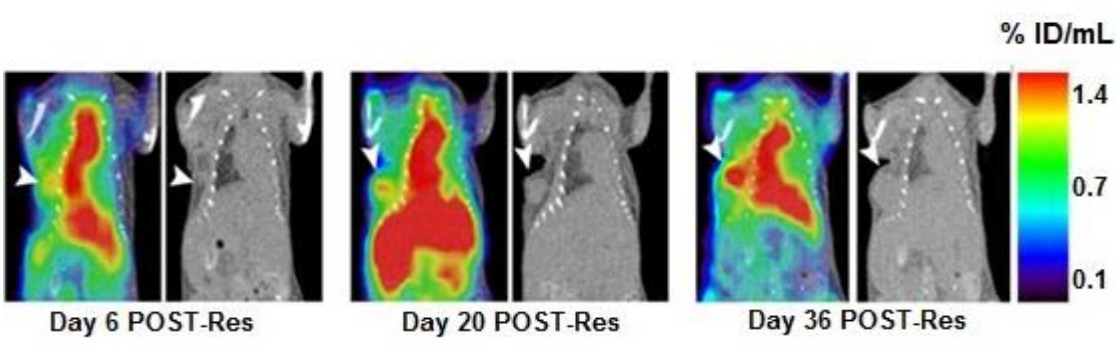

Suppl Figure 5. Progressive increase in uptake of [18F]AH113804 at the tumor site post tumor resection.

PET and CT image of a same tumor bearing mouse acquired on Day 6, Day 20 and Day 36 post resection showing uptake of [^{18}F]AH113804 at 60 min p.i. The recurrent tumour is clearly visible on the right flank of the animal (white arrowhead).

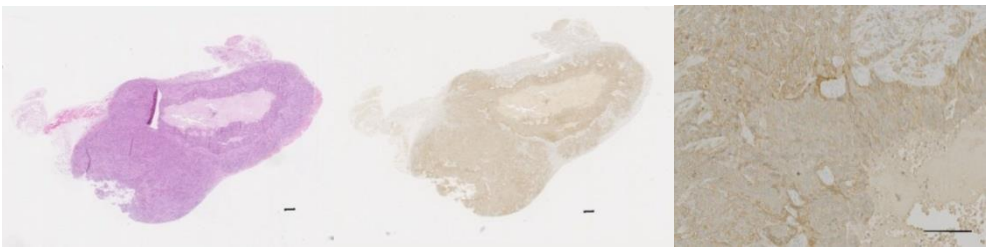

Suppl Figure 6. H&E staining E (left) and immunohistochemical staining for human c-Met (middle and right) on a representative tumour sample that was collected at day 14 post tumour inoculation.

The tumour sample displays an area at its core devoid of cells. It also displays tumour cells at the periphery with fairly strong human c-Met staining. Presence of necrosis and membranous c-Met staining on tumor cells is visible on the right panel. Scalebars represent 200 µm.

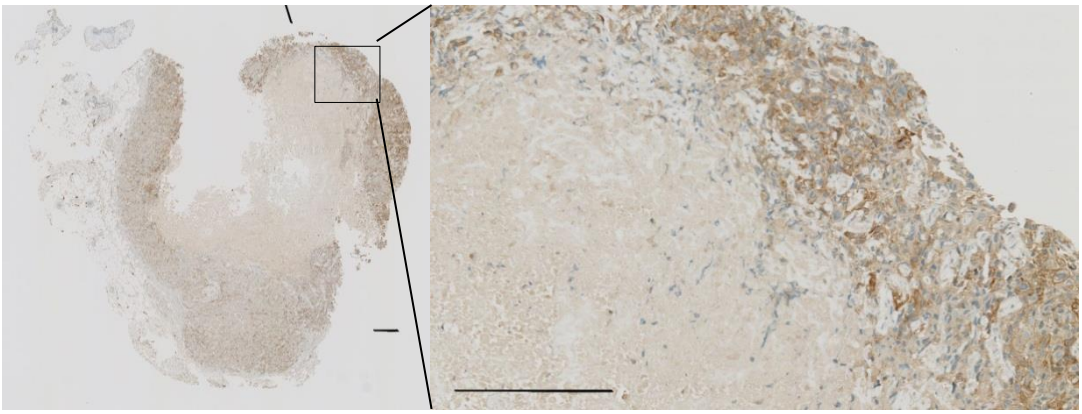

Suppl Figure 7. Immunohistochemical staining for c-Met on a representative recurrent tumor sample.

Left panel shows the whole tumor sample while the right panel shows a magnified area of this tumor sample. The tumor sample displays a core of necrosis. The right panel shows membranous staining for c-Met around the tumor cells while the necrotic area shows no staining for c-Met. Scalebars represent 200 µm.

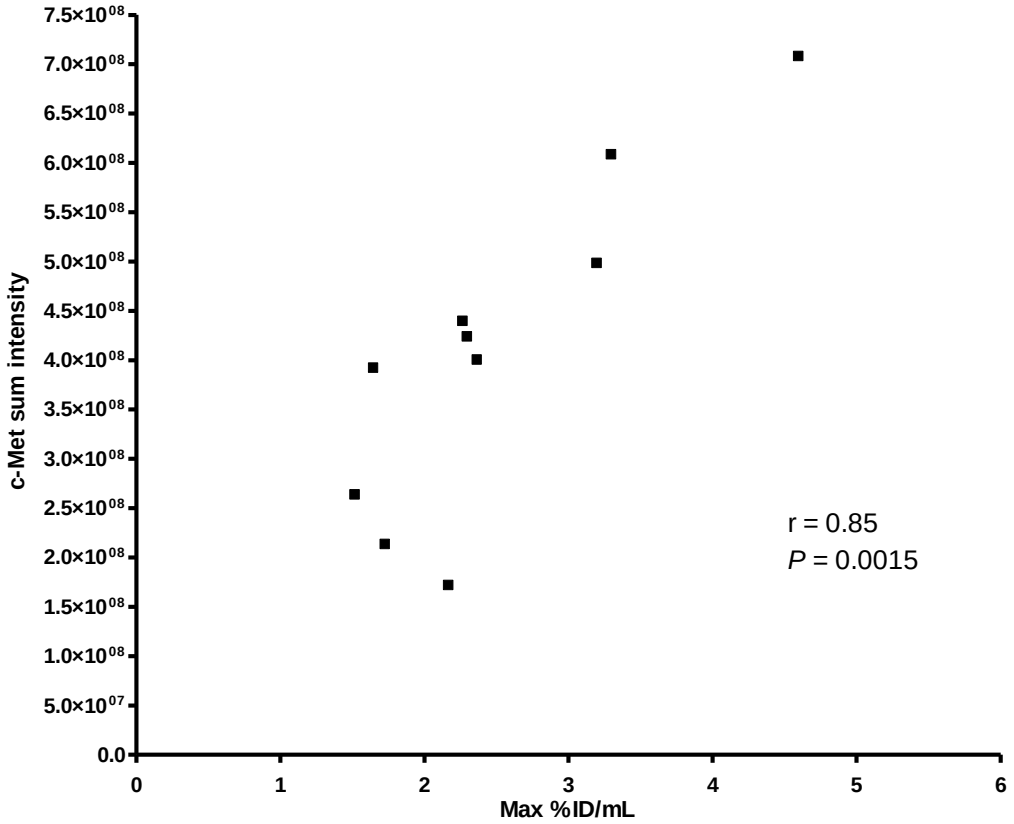

Suppl Figure 8. Uptake of [18F]AH113804 in tumors correlates with the c-Met expression level in samples of the same HCC1954 tumors.

IHC detection of c-Met expression in FFPE preparation of tumor samples. Statistical analysis gave a Pearson's correlation coefficient of 0.85 (*P*= 0.0015, n = 10). Pearson *r* and *P* values were calculated in R version 3.1.2.

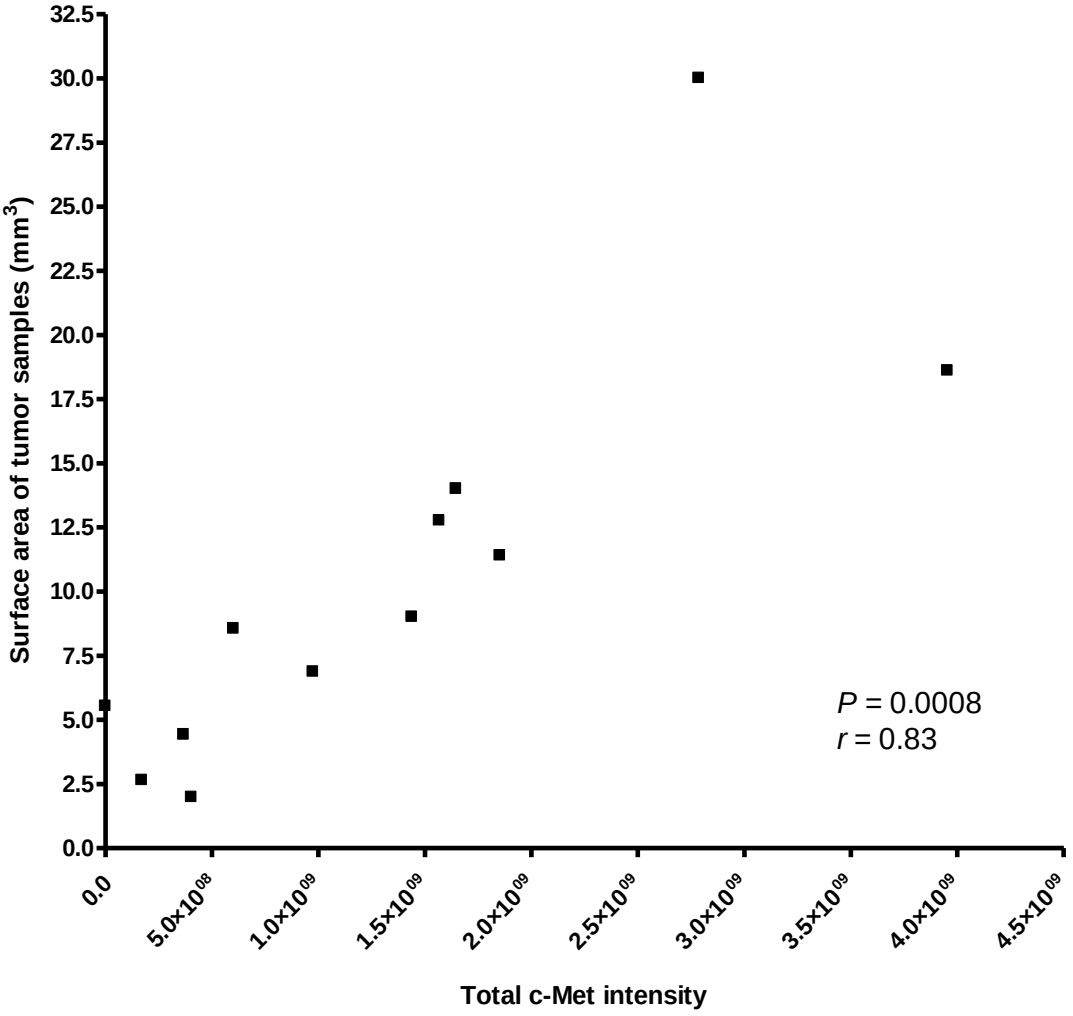

Suppl Figure 9. Correlation between the surface area of viable tumour cells and the total c-Met intensity.

The surface area measured includes areas with tumour cells only while excluding areas without cells, necrotic areas, and stroma. Statistical analysis gave a Pearson's correlation coefficient of 0.83 (P = 0.0008, n = 12). P and r values were calculated in R version 3.1.2.

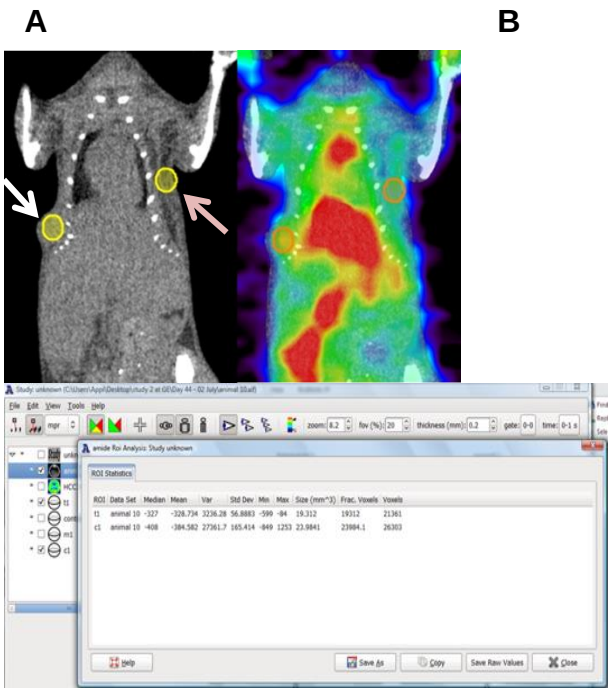

Suppl Figure 10. ROIs drawn in tumor and contralateral mammary fat pad.

A. Representative CT (left) and CT/PET image (right) of HCC1954 tumour xenograft bearing mouse at day 36 post tumour resection. The ROI drawn at the tumour site (white arrow) was then replicated at the contralateral mammary fat pad (pink arrow) using the coronal and transverse section. **B.** ROI volumes for the tumour (t1) and the contralateral site (c1) are very similar. The ROI were drawn manually separately but attention was given to draw similar sized shape ROI for both sites and then checking that the volume of the respective ROI were very similar using the analysis section of the AMIDE software.

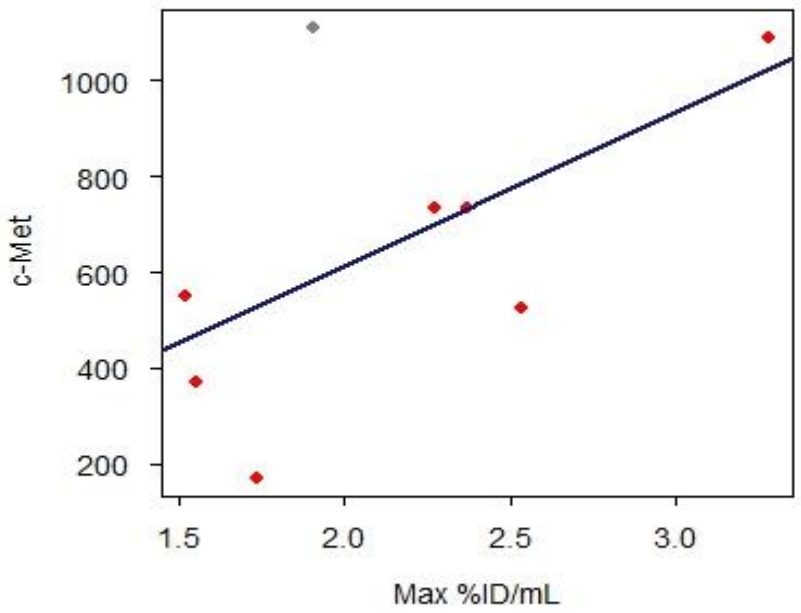

Suppl Figure 11. Identification of an outlier through the fitting of a regression line.

Red dots fall between the upper and lower 1 percentile of all residuals while the grey dot is identified as an outlier. Statistical analysis performed in R version 3.1.2.

Supplementary Table 1. Uptake of radioactivity (%ID/mL) in HCC1954 tumors following [18F]AH113804 administration, as determined by PET imaging.

Day	MEAN (± SEM)	Lowest Individual Uptake Observed	Highest Individual Uptake Observed	n
-4	1.4 (0.2)	1.0	2.5	8
6	2.1 (0.1)	1.6	2.4	5
13	1.5 (0.2)	0.9	2.2	5
20	1.5 (0.3)	1.1	2.5	4
36	1.9 (0.7)	1.0	4.1	4
50	1.2 (0.3)	0.9	1.7	3

Supplementary Table 2. Number of mice used in this study and imaged at different PET imaging timepoints. Inclusion of the number of mice with visible recurrent tumors after tumor surgery.

PET Imaging timepoint	Number of mice imaged	Number of mice with recurrent tumors
10 days post implantation	8	N/A
6 days post resection	8	5
13 days post resection	8	5
20 days post resection	6	4
36 days post resection	6	4
50 days post resection	6	3

Supplementary Methods:

Tumor xenograft model (continuation):

Initial PET scans with [^{18}F]AH113804 were acquired 10 days after tumor inoculation. Fourteen to sixteen days after tumor cell implantation, animals underwent surgery for tumor excision, and were subsequently allowed to recover under sufficient analgesia.

The animals were anaesthetized using 2.5% isofluorane in medical oxygen during the surgery. Area of the tumor site was cleaned using povidone-iodine. A 1 cm incision was then made around the tumor. A cotton swab was used to expose the tumor from the mammary fat pad. The tumor was then removed gently and completely from the mammary fat pad using scissors. In some cases, when the tumor was stuck to the skin, the skin was also removed to ensure that there would be no visible remnant of the tumor. Sham surgery was not performed on the contralateral mammary fat pad as the project license would not allow 2 surgeries to take place in one animal.

The animals were monitored for up to 50 days post tumor resection for local tumor recurrence, with PET imaging carried out on selected days post resection (Suppl. Table 2).

For autoradiography studies, female nude mice were inoculated with HC1954 cells in the second right mammary fat pad, according to the methods described above. Tumors were allowed to develop for 25 days before use.

Radiosynthesis of [^{18}F]AH113804 (continuation):

[^{18}F]AH113804 (chemical structure presented in Fig. 1A) was synthesized on a FASTlab automated synthesizer (GE Healthcare, Chalfont St Giles, UK) in a 2-step process. First, [^{18}F]fluorobenzaldehyde was synthesized from [^{18}F]fluoride and purified on a MCX+ (Mixed Cation Exchange, Waters) cartridge. Then, [^{18}F]fluorobenzaldehyde was conjugated to the peptide precursor and [^{18}F]AH113804 was purified and formulated.

[^{18}F]Fluoride was recovered from irradiated target water on a QMA cartridge (Waters) and then eluted using Kryptofix and $KHCO_3$ into a cyclic olefin copolymer reaction vessel and dried under a flow of nitrogen at 120 °C. Subsequent reaction with trimethylammonium benzaldehyde triflate in DMSO resulted in [^{18}F]fluorobenzaldehyde.

In the second step, the peptide precursor was dissolved in an aqueous solution of aniline hydrochloride and added to the purified [^{18}F]fluorobenzaldehyde to give crude [^{18}F]AH113804. Purification was done on a tC18 SPE (Solid Phase Extraction) cartridge with acetonitrile in PBS (21.4% v/v) followed by PBS to remove residual acetonitrile. [^{18}F]AH113804 was eluted into PBS (34 mL) from the tC18 cartridge with ethanol (2.4 mL) followed by PBS (2.6 mL) to give the formulated product (total volume 39 mL, ca. 6% EtOH).

CT and PET imaging:

Anesthesia (approximately 2% isoflurane in oxygen) was induced shortly before and maintained throughout imaging. PET imaging at 55-65 min post injection (pi) of [^{18}F]AH113804. A whole body CT scan followed

(projection exposure time 400 ms, tube voltage 45 kVp). Animals were allowed to recover from anesthesia. Occasionally static PET imaging was replaced by a dynamic series at 5-65 min pi [^{18}F]AH113804.

PET data were attenuation and scatter corrected, then reconstructed by filtered back projection. Images were manually coregistered and analyzed by Regions of Interest (ROI) employing AMIDE (http://amide.sourceforge.net).

Imaging was performed at baseline (10 days post tumor inoculation, i.e. 4 days pre-resection) and on Days 6, 13, 20, 36 and 50 post tumor resection.

3D ellipsoid ROIs were placed on the tumor in CT images to estimate tumor volume (Suppl Fig 10). Additional ROIs were placed in skeletal muscle (left forelimb), liver, left and right kidney, and heart (blood pool). All ROI PET data were expressed as decay corrected radioactivity concentration normalized to the injected dose (% ID/mL).

Biodistribution of [^{18}F]AH113804 was obtained for the mice on the final imaging day (Day 50 post resection). Following PET/CT imaging, animals were sacrificed (approx. 70 min p.i.). Organs and tissues of interest were excised, weighed and radioactivity measured using a custom-built twin-crystal gamma counter. Ex vivo [^{18}F]AH113804 uptake is expressed as percentage radioactive dose per gram of tissue (% ID/g).

Autoradiography:

Autoradiography was performed on tumors harvested from nude mice 25 days after tumor inoculation. Mice were sacrificed 40 min after injection of

approximately 7 MBq [^{18}F]AH113804 and corresponding PET imaging. Tumors were excised, snap frozen and cut into 8 µm thick sections. Sections were then imaged in a Micro Imager (Biospace Lab, Paris) which provides a spatial resolution of 25 µm for ^{18}F. Image acquisition duration was 90 min.

Histology:

Hematoxylin and eosin staining and c-Met immunohistochemistry were performed on consecutive 3µm thick tissue sections, employing the monoclonal rabbit antibody D1C1 (Ventana; diluted 1:30) against total c-Met. Antigen retrieval was employed (Standard Cell Conditioning 1/ Ventana). DAB (3,3'-diaminobenzidine) served as chromogen. Slides were processed with an automated system Ventana (BenchMark ULTRA, Roche, Switzerland), scanned with a Hamamatsu Nanozoomer 2.0 HT (Hamamatsu Photonics, Hamamatsu, Japan) and initially analyzed with Hamamatsu NDP.view2 viewing software. Quantitative analysis of the c-Met expression level was made using HistoQuest 4.2 (Tissugnostic, Vienna, Austria) software. IHC detection and quantification of c-Met expression in FFPE preparation of tumor samples are described in the section below.

Immunohistochemistry Data Analysis:

All the histological slides were digitalized at magnification x20 (0.46 µm/pixel) using Hamamatsu Nanozoomer 2.0 HT. Digital images in ndp format were submitted for quantitative image analysis using HistoQuest software. HistoQuest uses patented algorithms to detect the individual cells of interest and assesses intensity of antigens in the cell nucleus, membrane

and cytoplasm. The program automatically detects tissue which is subjected to color separation module to differentiate between the blue and the brown shade. Nucleus detection algorithm on the hematoxylin shade was used to detect all cell nuclei and was defined as master channel. A ring mask around each nucleus was used to analyze the staining intensity of non-master chromogen (DAB) in given cellular location. The staining intensity is measured as mean intensity of all pixels of a cell and the range of values is from 0 to 255.

c-Met staining intensity was analyzed within 1.7 mm^2 regions of interest (ROI) that were visually identified over the tumor enriched region. Staining intensity was analyzed in ring masks around each nucleus using an algorithm that identifies stained cytoplasmic and membranous areas. Raw data included minimum and maximum pixel value for every individual cell within the ROI. The average minimum and maximum pixel values were calculated for the whole region. The obtained data correlated with values acquired from PET scans.

Immunofluorescence:

Tissues were permeabilized and stained similar to the procedure outlined previously [245]. A monoclonal rabbit c-Met antibody (1:100, D1C2, Cell signaling), followed by an incubation with a goat anti-rabbit Cy3 secondary antibody (1:500, Sigma), were used. Total fluorescence in each sample was measured and total c-Met-related intensity was corrected for differences between each animal using the same threshold. It was quantified

using the software package TRI2 (Paul Barber, Oxford Institute for Radiation Oncology).

Statistical Analysis:

SEM was calculated to estimate the precision of the sample mean. Paired *t*-test of log-transformed TMRR was conducted to evaluate the difference between tumor and contralateral mammary fat pad uptake (Fig 2B). The correlation between total c-Met intensity from frozen tumor samples and the corresponding max %ID/mL for the uptake of [^{18}F]AH113804 at the tumor site (Fig 6B) is visualized with a scatter plot and Pearson correlation coefficients were calculated. The analysis was restricted to observations which fell between the upper and lower 5 percentile of all residuals, assigning any observation beyond this range as an outlier. This resulted in exclusion of one observation and the remaining seven observations were used in the final analysis (Suppl. Fig. 11). A two-sided P-value <0.05 was used to determine significance.

4.3 Concluding Remarks

This study has identified for the first time a unique radiolabelled c-Met binding peptide (K_d≈2 nM), [^{18}F]AH113804, which has the ability to detect locoregional recurrence in BLBC tumour xenografts as early as six days after surgical removal of the primary tumour. Early detection of the locoregional recurrence in patients with BLBC and TNBC is a clinical problem that needs to be addressed. Locoregional recurrence was found to be associated with a poor survival rate [222] and studies have shown a higher rate for locoregional recurrence in TNBCs patients [31, 220, 221] in comparison to other intrinsic breast cancer subtypes.

We observed a decrease in the retention of [^{18}F]AH113804 in the blood pool over time accompanied by an accumulation at the tumour site. This suggested the specificity of the tracer at the tumour site, which was later confirmed by *ex-vivo* immunostaining. The *in-vivo* PET images revealed a satisfactory tumour to non-target tissue ratio uptake, with a 2-fold difference. The difference was significant between the uptake of the tracer at the tumour site and at the control site. It was necessary to validate for the specificity of the tracer in the c-Met positive tumours by conducting *ex-vivo* staining of c-MET in the resected and pre-resected tumours. We were able to identify a strong correlation between c-Met expression level from the tumours with the quantitative values of the uptake of the tracer in those tumours (r =0.82).

The importance of this study lies in a current lack of c-Met specific radiolabelled tracers in the clinic. Several radiolabelled antibodies against c-Met have already been tested preclinically for *in-vivo* tumour targeting. An anticalin, PRS-110 (Pieris Pharmaceuticals, Inc.) with monovalent specificity for c-Met, and a binding affinity of 0.6 nmol/L, was labelled with ^{89}Zr (half-life, 78.4 h) for the imaging of H441 NSCLC (which expresses high c-Met level) and U87MG glioblastoma (which expresses lower c-Met level) tumour xenografts [214]. In this study, they used a 'control tracer', ^{89}Zr-Tlc-PEG that was used as a negative control due to its inability to bind to c-Met and it was used alongside the c-Met binding tracer, ^{89}Zr-PRS-110, for comparison purposes in c-Met's specificity *in-vivo*. The anticalin was conjugated with a PEG moiety to extend its half-life. 96 hours post tracer's injection, they observed a tumour accumulation of 5.9 % injected dose per gram (%ID/g) in the high c-Met expresser H441 xenografts using ^{89}Zr-PRS-110. An uptake of 3.9%ID/g by the non-c-Met-binding ^{89}Zr-Tlc-PEG was observed in the same tumour. However, the outcome from this c-Met binding tracer did not look convincing due to similar uptake of the c-Met binding tracer and the control tracer in the lower c-Met expresser U87 MG model (1.2%ID/g vs 1.8%ID/g respectively). This suggests non-specific binding or higher retention of the c-Met binding tracer, ^{89}Zr-PRS-110, in non-targeted tissues, which is a major flaw for its use in clinical imaging.

Other choices such as DN30 and onartuzumab have also been labelled with ^{89}Zr for imaging c-Met expression *in-vivo*, and displayed a good tumour uptake. The radiolabelled monoclonal antibody DN30 (Kd = 2.64 nM)

showed accumulation in tumours that express c-Met [255]. However, as DN30 is a partial agonist and consequently displayed biological effects, onartuzumab was selected for radiolabelling. Onartuzumab, a c-Met-selective humanized 1-armed monoclonal antibody with a molecular weight of 100 kDa, is a pure antagonist with monovalent binding to c-Met [255]. The ^{89}Zr-labelled onartuzumab, named as ^{89}Zr-Df-onartuzumab, displayed a strong signal in the high c-Met expresser MKN-45 tumours, from day 1 onwards after injection. The uptake at the tumour site increased steadily and reached a value of 23%ID/g at day 5 post tracer's injection [255]. This is partly due to the trapping of radioactive metabolites from internalisation [256]. Accumulation in the blood, heart, lung, muscle and gastrointestinal tract decreased slowly overtime. Despite its specificity, the prolonged circulation time and slow clearance can lead to longer timeline prior to imaging and could therefore limit their clinical applicability as diagnostic agents. [215].

The pitfalls of the use of antibodies as PET tracers are their very slow pharmacokinetics, due to their large molecular weight. This consequently results in the exposure of a higher dose of radiation to the patient, along with a delay in the acquisition of a PET scan, making management in clinics not so straightforward.

Kim et al used a c-Met-binding peptide, similar to our study, in a glioma xenografts model [257]. Several linkers were introduced in their tracer forming three versions of the tracer: one that was unchanged (^{125}I-cMBP),

the other had glycine (^{125}I-cMBP-GGG) and another had 8-aminooctanoicacid (^{125}I-cMBP-AOC) introduced in their sequence. Those peptides were then radiolabelled with Iodine-125 and evaluated for tumour uptake using SPECT. Out of the three, the c-Met binding peptide with the insertion of glycine (^{125}I-cMBP-GGG) showed tumour uptake while the other tracers did not. Despite the detection of the tumour by ^{125}I-cMBP-GGG, the uptake at the tumour site was not as clear as the one observed in our study [16]. They speculated that this could be due to their choice of the radioisotope.

^{18}F-FDG was first manufactured in 1978 [229] and has become the most commonly used radiopharmaceutical for PET oncology studies. The use of ^{18}F-FDG was approved by the Food and Drug Administration, in March 2000, to assist in the evaluation of malignancy in patients with known or suspected abnormalities [258]. ^{18}F-FDG is commonly used in the clinic and is used for the diagnosis, staging and restaging in a range of tumours, such as lung, colorectal, head and neck, esophageal cancers, lymphoma and melanoma [258]. ^{18}F-FDG PET has the ability to recognise a fundamental alteration in the cellular metabolism of glucose which is identified in all neoplasms [258]. The rationale behind the use of ^{18}F-FDG PET in various cancers was discussed in a review conducted by Fletcher et al [258]. This review confirms that enough evidence has been provided for the routine use of ^{18}F-FDG PET in the detection of recurrence and metastasis in breast cancer patients, and showed a pooled sensitivity of 90%, while the specificity was 87%. These are very high values and clearly are convincing. However, other studies have

demonstrated ^{18}F-FDG PET's limitations regarding the detection of small (especially <10mm) and microscopic tissue involvement [167, 168, 251]. Additionally, tumours with a low metabolic rate, which could be observed in necrotic tumours, such as the ones observed in our study, would not be detected by ^{18}F-FDG PET [258].

In addition to this, the advantage that a molecular target imaging agent has over ^{18}F-FDG is that it will address key questions related to the expression and inhibition of drug targets and early assessment of the tumour response. Targeting cellular processes are more specific than the readout of glucose metabolism, provided by ^{18}F-FDG. Indeed, imaging a molecular target, such as c-Met, will enable to stratify patients based on the level of c-Met expressed by their tumours, resulting in the administration of suitable therapies, such as specific c-Met inhibitors [230]. Inhibition of the target can be monitored by imaging the blocking of probe uptake by the study drug [259]. Moreover, a molecular imaging agent will provide information on the intrapatient heterogeneity of the expression of target proteins, which would be useful to know, for dosage and drug of choice purposes. Many clinical trials fail to achieve a desired response due to the inadequacy of the dose schedule, which results in the lack of target inhibition, and the drugs given might inhibit the target but not the tumour growth [260]. These issues can only be prevented through the use of specific molecular target imaging agents. Advances in molecular imaging will enable individualised patient management.

One of the few limitations from our study was the lack of a c-Met negative tumour which is a very convincing way to show evidence of the specificity of the tracer for the c-Met positive tumour. In addition to this, it might have been useful to increase the amount of radioactivity injected into the basal-like breast tumour-bearing mice and imaged them at 3 hours post injection of the tracer. We could speculate that there would be a lower retention in the blood pool enabling a considerably higher tumour-to-blood ratio uptake of the tracer. This type of timepoint experiment would only be possible if the biological half-life of the c-Met binding peptide matches with the timepoint for the PET scanning. Additionally, it is possible to re-engineer the c-Met binding peptide for the prolongation of its biological half-life [214].

Future studies include the assessment of the effect of treatment on the locoregional recurrence (c-Met inhibitor), at its early stages after detection with the tracer, on the rate of survival of the tumour bearing mice. This would have provided us and others invaluable insight into the potential clinical effect of early detection and treatment on basal-like breast patients' survival.

Additionally, since ^{18}F-FDG gained clinical acceptance, and has become an important imaging tool in routine clinical oncology, it would have been useful to assess FDG uptake in our basal-like breast cancer model and compare its uptake at the tumour site, especially after surgery, to the uptake observed with [^{18}F]AH113804. This comparison would have potentially led to a concrete conclusion on the use of [^{18}F]AH113804 in the clinic.

On the other hand, GE137, which is the optical, Cy5 labelled version of [^{18}F]AH113804 successfully detected polyps in colorectal patients [213]. In addition to GE137's specificity to human c-Met, it also shows no signs of toxicity in patients. Excluding the potential effect of the radiolabelling which needs to be assessed in patients, the biological c-Met binding peptide appears to be safe for use in patients. In addition to this, c-Met is a particularly useful marker in the locoregional recurrence in BLBC and TNBC as a higher c-Met expression level is detected in recurrent tumours than in primary tumours [261].

Overall, the early detection of loco-regional recurrence in basal-like breast cancer, observed in this study, shows great promise on the use of [^{18}F]AH113804 in the clinic for the assessment of recurrent basal-like breast cancer, and other cancers with c-Met overexpression which include lung, ovary, kidney, colon, thyroid, liver, and gastric carcinomas [3-8, 10-12, 14, 68]. [^{18}F]AH113804 should also be tested to monitor c-Met expression following anti-c-Met therapy *in-vivo* and if successful, [^{18}F]AH113804 could be used as a companion tool in such events. Due to the ability of [^{18}F]AH113804 to detect very small tumour lesions expressing c-Met, which were not visible by CT, [^{18}F]AH113804 could also be assessed for the detection of metastatic lesions, as long as the retention of the tracer in the blood pool does not mask any of the key organs that could be affected by tumour spread.

Chapter 5: The validation and use of a single chain fragment variable antibody, with an engineered Fc domain, against human c-Met in basal like breast cancer

5.1 Introduction and aims:

c-Met has a primordial role in the progression of cancer. There is numerous evidence now validating a correlation between poor prognosis and overexpression of c-Met in many cancers, such lung, breast, ovary, kidney, colon, thyroid, liver, and gastric carcinomas [3-6]. 20-30% of breast cancer displays an upregulation of Met and its ligand HGF [45]. Numerous studies have demonstrated a preferential overexpression of c-Met in the basal-like subgroup [46, 56]. The aggressive nature of basal-like breast cancer combined with a lack of targeted therapy causes a reduced free survival rate in women with BLBC. Due to these reasons, there is a growing interest in the design and production of c-Met inhibitors.

Preclinical and early clinical studies show tumour regression in 64% of the patients with Metastatic Breast Cancer (MBC) when administered with Cabozantinib, which is a multitargeted tyrosine kinase inhibitor (TKI) against c-Met, VEGFR2 and RET [233]. Four phase II clinical trials have recently been completed for the treatment of advanced TN breast cancer, targeting c-

Met. They consist of Tivantinib (also known as ARQ197) [86], cabozantinib (known as XL184) [81], MetMab (onartuzumab) [232] and foretinib (XL880) [80].

In parallel to the development of c-Met targeted drugs, there is an emergent rise in the number of preclinical studies focusing on the development of antibodies, fragment antibodies and non-antibody derivatives against c-Met for diagnostic purposes. Women with BLBC that have had surgery for the removal of the primary tumour tend to display a high rate of locoregional recurrence [31, 36]. The inability to detect locoregional recurrence or metastatic lesions at an early stage leads to progression of the cancer and consequently a reduction in survival rate. Performing a biopsy in women with BLBC at regular intervals after surgery of their primary tumour is not advisable as it is highly invasive and comes with a risk of internal bleeding and other typical surgical risks. Hence, the use of a non-invasive targeted agent is beneficial for the early detection of a recurrent tumour. There is therefore a great need to find molecular imaging agents that have the sensitivity to accurately detect the presence of low numbers of basal-like breast tumour cells in the basal-like subtype of breast cancer.

Both optical and radionuclide imaging are non-invasive methods of investigation for detection and therapeutic purposes. Although their aims are the same, they display a variety of differences which explain the existence of both techniques. The optical imaging method faces a few challenges: light is highly absorbed and experiences great scattering in biological tissues which limits the depth of penetration through the body [169]. However, it is often used in small animals as the required path-length of light is much shorter

making this technique more feasible. It is also a very cost-effective method for assessing *in-vivo* physiologic and biochemical processes. The nuclear imaging method can be challenging due to its high cost, need for a local cyclotron to generate short-lived positron emitting radionuclides and a synthetic unit to produce the biologically useful probes. However, radionuclide technology enables a better depth of penetration and accuracy for detection of the target of interest in a subject.

Regarding the molecular agent, it is crucial to engineer a molecule that will have a high specificity for the target of interest, with the ability to provide high contrast imaging, which can be achieved by high tumour penetrance, high tumour to blood ratio and relatively fast clearance kinetics. A current issue faced by clinics is the long half-life of some molecular imaging agents delaying the acquisition of meaningful images. This also increases the length of exposure to radioactivity for the patient's unaffected organs and the overall cost of the treatment [262]. Hence, in our study, we decided to use a single chain variable fragment Fc protein (scFv-Fc), in the hope of retaining a similar level of specificity to c-Met as one of a full-length antibody, along with a reduction in the blood circulation due to its smaller size. In Chapter 4 of this thesis, we used a ^{18}F radiolabeled c-Met binding peptide to detect BLBC which demonstrated very fast clearance kinetics, potentially reducing tumour uptake, leading us to engineer a scFv-Fc in this current chapter. The scFv-Fc should demonstrate a slower clearance rate than the c-met binding peptide, enabling a higher tumour uptake.

Biological tissues exhibit a high photon absorbance in both the visible wavelength range (350–700 nm) and in the infrared range (> 900 nm). Cy5

has maximum absorbance at 650 nm and maximum emission at 670 nm. It can be detected *in-vivo* at subnanomole quantities and at depths sufficient for experimental or clinical imaging depending on the NIR fluorescence image acquisition techniques. Hence, in our study we initially choose to investigate the targeting ability of a single chain fragment variable fusion protein coupled to Cy5, against human c-Met, in a basal like breast tumour xenograft model. The basal-like breast cancer cell line used, HCC1954, was tagged with luciferase to ensure that the location of the tumour will be identified, via bioluminiscence, prior to the fluorescent imaging.

Following the optical imaging, we decided to conjugate our scFv-Fc to the radionuclide Indium-111 (In-111) for use in SPECT imaging. This radioisotope has a half-life of 2.8 days and is particularly suitable for biodistribution studies. In the case of our scFv-Fc, the use of Indium-111 will allow the tumour-bearing mice that were injected with the radiolabeled scFv-Fc to be imaged at several timepoints up to 24 hours after injection due to its rather long half-life in comparison to other SPECT radioisotopes [263, 264]. In order to conjugate the single chain variable fragment against human c-Met with In-111, it was necessary to use a chelator, and in this case we opted for CHX-A''-DTPA. The reason this chelator was selected was due to its successful binding 111-In described in various studies [265-267]. Previous studies investigated the use of a radiolabelled c-Met-selective humanized 1-armed monoclonal antibody, 89Zr-Df-onartuzumab [255], c-Met binding peptides ^{125}I-cMBP-GGG [257] and ^{18}F-AH113804 [16], the radiolabelled anticalin ^{89}Zr-PRS-110 [214] in cancers which express high level of c-Met. While 18-F and 125-I have shorter half-lives than In-111, 89-Zr displays a

favourable half-life (3.3 days) which is compatible with the time needed to achieve optimal tumour-to-background ratios for intact mAbs (typically a few days) and other large fragment antibodies [268]. However, 89-Zr displays a major disadvantage over 111-In as its high energy gamma emission at 908.97 keV, results in a reduction in the radioactive dose that can be administered into patients.

Following successful radiolabelling and serum stability test, we designed a SPECT imaging experiment in which immunodeficient mice were used to model basal-like breast cancer. In order to effectively compare the uptake of the tracer at the site of the basal-like breast cancer tumour, a c-Met negative tumour was also grown in parallel, through the use of MCF-7 cells. The uptake of the tracer in those tumours was visualised at different timepoints and a quantitative analysis for the amount of radioactivity in the tumours and other organs was performed at the end of the study using a gamma counter.

The aim of this chapter is to demonstrate receptor specificity against human c-Met and tumour accumulation of both the Cy5 labelled scFv-Fc and the radiolabelled ^{111}In-CHX-A''-DTPA- scFv-Fc in human basal-like breast cancer xenografts.

5.2 RESULTS

5.2.1 Selection of a highly specific scFv-Fc against human c- Met from a phage display library

McCafferty et al has kindly provided a phage display library that consists of over 1.1 x 10^{10} human antibodies, which was created by cloning a repertoire of VL regions, followed by VH regions into a pSANG4 vector [269]. This led to the production of plasmid DNA with a scFv format (VH and VL fragments joined by a flexible linker peptide). Antibodies were selected to 404 antigen targets and were subcloned into the expression vector pSNAG14.3F, which fuses the scFv to a tri-FLAG tag sequence along with a dimeric enzyme alkaline phosphatase. This resulted in the primary screening (using ELISA) and sequencing of 94 clones, for each antigen target, and the identification of 22 unique clones per target. Those clones were then assessed for their specificity to target antigen, using a secondary specificity screening and another set of sequencing using 6 primers. In this secondary specificity screening, each antibody clone was tested against the target antigen, the fusion partner used, 8 irrelevant purified proteins and total protein lysates from zebrafish and yeast in order to identify potential cross-reactivity (using ELISA). 64% of antibodies to mammalian-produced antigens were confirmed as antigen-specific and confirmed the results of the initial high throughput screen for the majority of clones. Sensitive detection was displayed in a bead based flow cytometry assay, followed by immunohistochemistry on tissue microarrays, for which 37% of antibodies were found to show positive staining.

Regarding human c-Met, McCafferty et al, used the phage display vector pSANG4 into the mammalian Fc expression vector pBIOCAM5 (Dyson and McCafferty, unpublished) for the subcloning of c-Met scFv. Those individual clones were then auto-induced and their supernatants, that contain the scFv-Fc, were analysed by ELISA .This led to the identification of 222 anti c-Met scFv-Fc fusions.

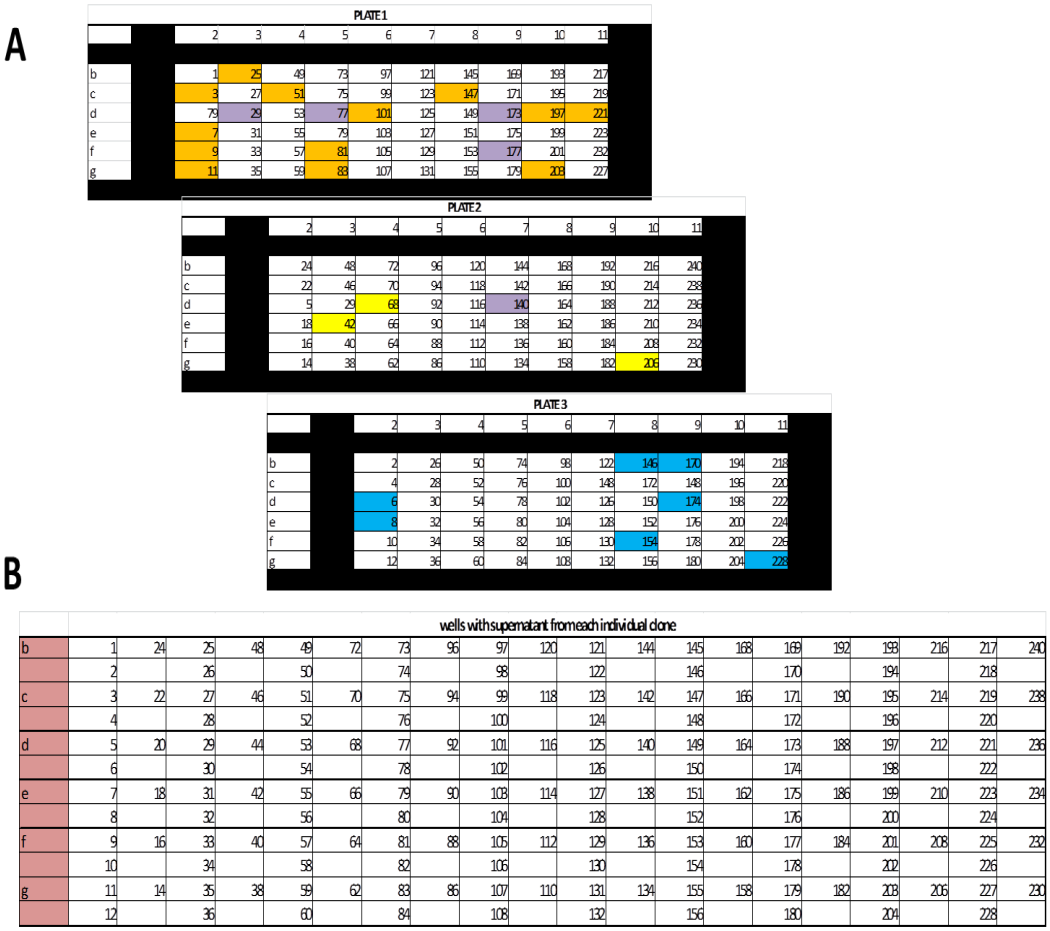

Figure 5-1. Set up for the phage display library assay that contained over 200 scFv-Fc subclones against human c-Met.

A) The phage display library that consists of over 200 scFv-Fc subclones against human c-Met provided by McCafferty et al was used and transfected into HEK293 cells, in three 96 well plate, to produce the respective scFv-Fc of each clone. The supernatant for each clone, which contains the scFv-Fc, was then assessed for c-Met specificity, through the use of MCF-7 cells, that were overexpressed with c-Met,

using Fugene 6 as explained in the Material and Methods, using a 384 well plate**. B)** The supernatant of each clone was collected from the 96 well plates and was to stain the MCF-7 cells, seeded in a 384 well plate. The supernatant was used as a primary antibody for the detection of anti-FLAG. Pipetting and handling of supernatant and transfection reagent was performed using the JANUS Automated Workstation (PerkinElmer) in the 384 well plate.

In order to assess the production of the scFv-Fc of each clone provided by McCafferty's library, each clone was transfected in each of the 96 well plates in which HEK-293 cells were seeded, as demonstrated in Figure 5-1A. A 384 well plate was used to seed MCF-7 cells (Fig 5-1B), whose wells were then transfected with c-Met DNA, to obtain an overexpression of c-Met in those cells, before they could be used to assess the c-Met binding of the various FLAG-tagged scFv-Fc clones. To ensure the consistency and accuracy of the pipetting in the 384 well plate, the JANUS Automated Workstation (PerkinElmer) was used for this assay. Once the wells from the 384 well plates were fixed and stained, it was then visualised using a microscope automated FLIM system with epifluorescence.

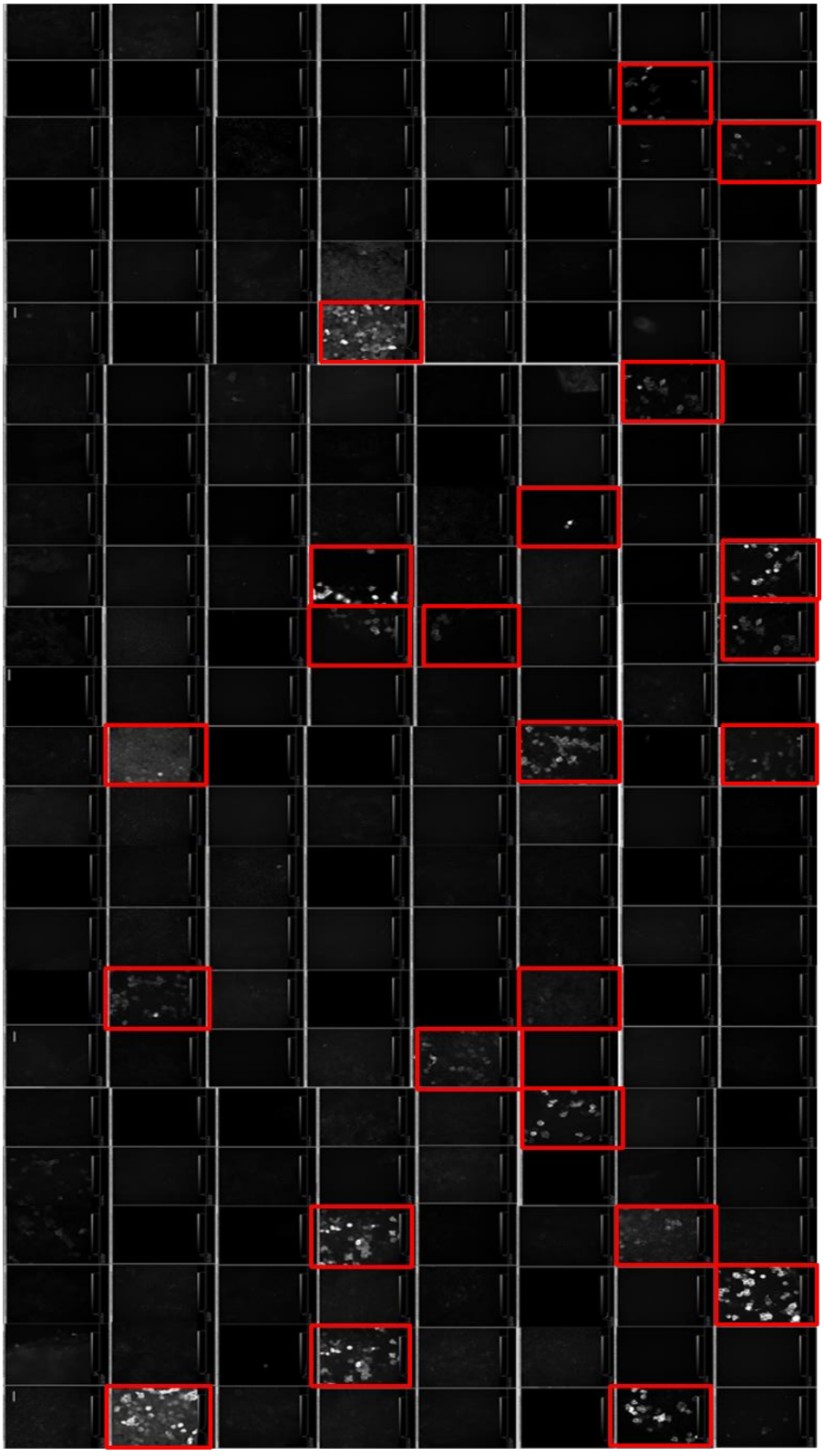

Figure 5-2. Identification of scFv-Fc subclones with high affinity human c-Met using Immunofluorescence.

Detection of scFv-Fc via immunofluorescence. c-Met overexpressed cells were stained with subclones from the display phage library. Anti-FLAG antibody, followed by goat anti-mouse Cy3 was used to visualise the localisation and presence of scFv-Fc. Wells highlighted in red are some of the subclones that display positive staining for the anti-FLAG epitope of the scFv-Fc. Images were captured using an automated epifluorescence microscope. Scalebar: 60µm

Figure 5-2 displays the staining produced using the anti-FLAG antibody that detects the scFv-Fc generated by the supernatant of each subclone. From this screen, we were able to identify 28 clones that show positive staining for anti-FLAG, out of the 240 clones that were transfected to generate a scFv-Fc against human c-Met.

It was then important to quantify the amount of scFv-Fc produced from these 28 clones using SDS-PAGE. The subsequent goal of this assay was to narrow down the number of clones prior to their amplification using the miniprep and maxiprep techniques. The clones with the highest specificity for c-Met were then selected for further characterisation.

A

	wells with supernatant from each individual clone																		
b	1	24	25	48	49	72	73	96	97	120	121	144	145	168	169	192	193	216	217	240
	2		26		50		74		98		122		146		170		194		218	
c	3	22	27	46	51	70	75	94	99	118	123	142	147	166	171	190	195	214	219	238
	4		28		52		76		100		124		148		172		196		220	
d	5	20	29	44	53	68	77	92	101	116	125	140	149	164	173	188	197	212	221	236
	6		30		54		78		102		126		150		174		198		222	
e	7	18	31	42	55	66	79	90	103	114	127	138	151	162	175	186	199	210	223	234
	8		32		56		80		104		128		152		176		200		224	
f	9	16	33	40	57	64	81	88	105	112	129	136	153	160	177	184	201	208	225	232
	10		34		58		82		106		130		154		178		202		226	
g	11	14	35	38	59	62	88	86	107	110	131	134	155	158	179	182	203	206	227	230
	12		36		60		84		108		132		156		180		204		228	

B

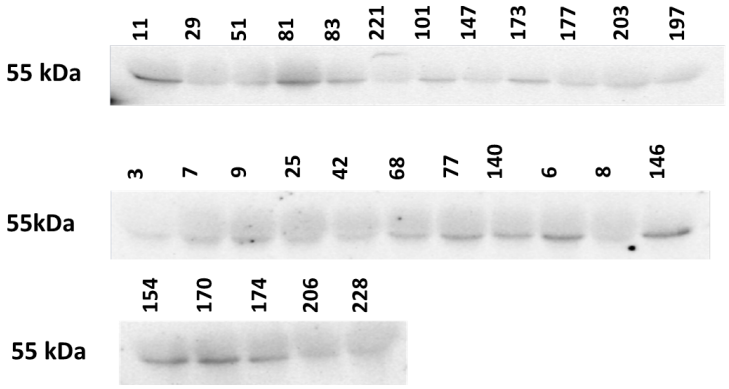

C

clone no	well	plate	average intensity (IF)	band intensity (WB)	intensity/amount of scFv-Fc
3	C2	1	793	4200.12	0.188804
6	D2	3	628	7019.545	0.089464
7	E2	1	1326	6149.741	0.215619
8	E2	3	502	4190	0.119809
9	F2	1	808	7098.93	0.11382
11	G2	1	2188	22460.96	0.097413
25	B3	1	2386	6750.519	0.353454
29	D3	1	842	14172.38	0.059411
42	E3	2	1423	5952.819	0.239046
51	C4	1	709	14521.98	0.048823
68	D4	2	945	6447.61	0.146566
77	D5	1	555	6983.843	0.079469
81	F5	1	1060	23582.64	0.044948
83	G5	1	500	14545.71	0.034374
101	D6	1	208	10653.54	0.019524
140	D7	2	468	6246.977	0.074916
146	B8	3	763	6829.763	0.111717
147	C8	1	1050	9364.761	0.112122
154	F8	3	622	17429.12	0.035687
170	B9	3	2123	20210.6	0.105044
173	D9	1	1012	10552.52	0.095901
174	D9	3	1880	17074.34	0.110107
177	F9	1	562	10350.35	0.054298
197	D10	1	663	10199.56	0.065003
203	G10	1	719	11657.05	0.061679
206	G10	2	1749	14493.14	0.120678
221	D11	1	822	11179.55	0.073527
228	G11	3	500	14738.78	0.033924

Figure 5-3. Identification of 28 clones against human c-Met with detection of scFv-Fc observed via immunofluorescence and SDS-Page.

A) High-content phage display library screen tested on MCF-7 cells that were transfected with c-Met plasmid, to obtain an overexpression of c-Met, in order to validate the presence of scFv-Fc, in those c-Met positive cells, via immunofluorescence. Numbers highlighted in yellow represent the clone number that stained positive for scFv-Fc against human c-Met (anti-FLAG antibody was used). **B)** SDS-PAGE used to validate and quantify amount of scFv-Fc expressed in the clones that tested positive for the FLAG epitope in the immunofluorescence staining. **C)** Quantification of the ratio between the mean immunofluorescence intensity of c-Met staining by the scFv-Fc, from images in **Figure 5-2**; and the protein expression level of the corresponding scFv-Fc observed in the SDS-PAGE (**Figure 5-3 B).** ScFv-Fc clones with the highest ratios were taken forward for further investigations.

Following the identification of 28 clones that showed positivity for the anti-FLAG epitope of the scFv-Fc (Figs 5-2 & 5-3A), the next step was to load an equal amount of those clones in a SDS-PAGE gel and assess the amount of scFv-Fc produced. Figure 5-3B clearly confirmed the identification of the scFv-Fc, via the detection of the anti-FLAG epitope, in each of those 28 clones, albeit to varying degrees. It was then necessary to narrow down the number of clones for further characterisation and this was performed by calculating the ratio of mean intensity for the scFv-Fc, from the immunofluorescence, with the expression level of scFv-Fc observed in the SDS-Page. The 8 clones with the highest ratio were selected for further investigations.

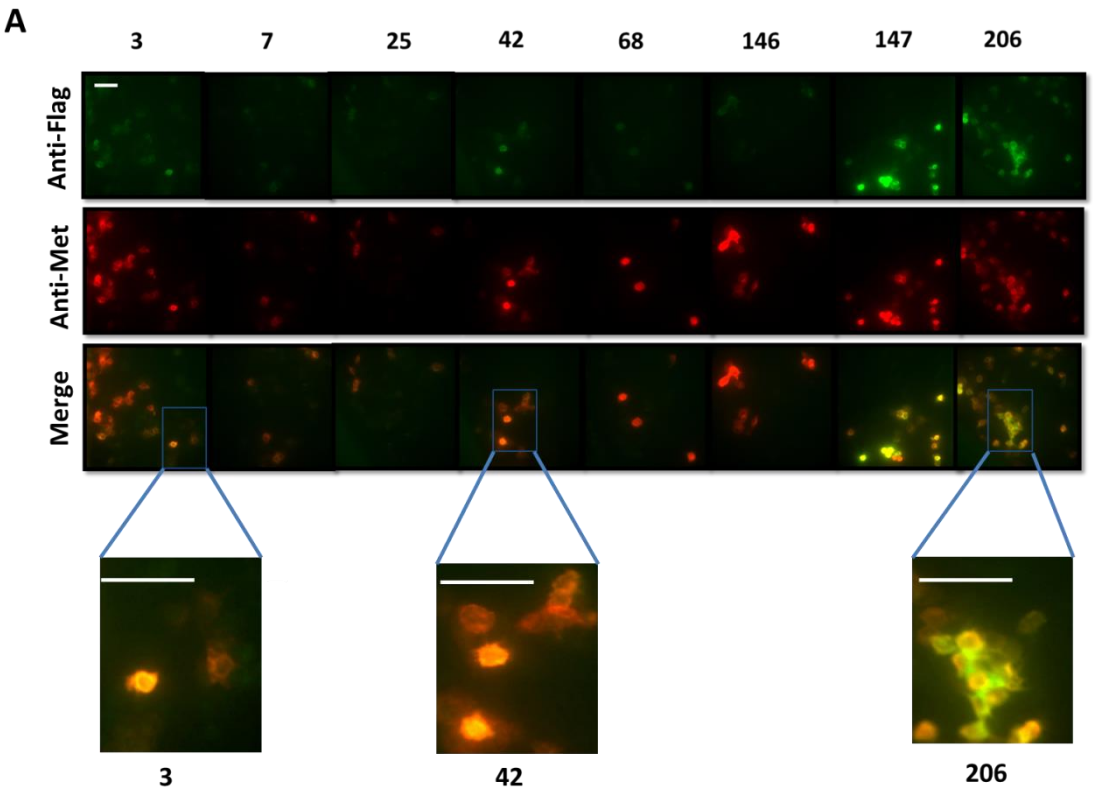

B

clone no	well	plate	average intensity (IF)	band intensity (WB)	intensity/ amount of scFv-Fc	Ratio intensity c-Met/scFv-Fc	Ratio Fluor. Intensity/Densitometry for scFv-Fc
3	C2	1	793	4200.12	0.19	0.26	6.23E-05
7	E2	1	1326	6149.74	0.22	0.39	6.40E-05
25	B3	1	2386	6750.52	0.35	0.45	6.63E-05
42	E3	2	1423	5952.82	0.24	0.27	4.62E-05
68	D4	2	945	6447.61	0.15	0.27	4.21E-05
146	B8	3	763	6829.76	0.11	0.23	3.37E-05
147	C8	1	1050	9364.76	0.11	0.28	2.99E-05
206	G10	2	1749	14493.14	0.12	0.31	2.12E-05

Figure 5-4. Identification of 8 subclones that show highest specificity for c-Met with co-localisation of c-Met and anti-FLAG epitope.

A) Positive staining for anti-FLAGFLAG (top panel) and c-Met (bottom panel) for all 8 scFv-Fc subclones (clones 3, 7, 25, 42, 68, 146, 147 and 206) against human c-Met. Co-localisation observed in all clones, albeit to varying degrees. Higher zoom for clones 3, 42 and 206. Scalebar: 60µm. **B)** Clones selected for further characterisation based on highest ratio between mean intensity staining for scFv-Fc and expression level displayed by the band intensity for anti-FLAG, produced by SDS-Page. Images were acquired by an epifluorescence microscope.

Eight subclones, from McCafferty's phage display library, were selected for further investigation. The supernatants generated from the previous screen were used to stain for anti-FLAG and human c-Met in order to detect potential co-localisation between both epitopes. As observed in Figure 5.4A, all clones showed co-localisation between c-Met and anti-FLAG. Figure 5-4B displays the values for each subclone, taking into account the ratio average intensity for c-Met (using the D1C2 antibody) and anti-FLAG, which was then divided by the amount of scFv-Fc detected by Western blot, highlighted in pink.

We decided to narrow down to 5 subclones for further investigations. The following subclones 7, 25, 42, 146 and 206 were selected based on their production of scFv-Fc and specificity against human c-Met. Clone 3 was not selected due to poorer colocalisation of c-Met stained cells with cells that expressed the anti-FLAG epitope, as observed in the area from the merged image that was magnified (Figure 5-4A). At higher zoom level clones 42 and 206 showed a higher amount of co-localised cells (between c-Met positive and anti-FLAG positive cells).

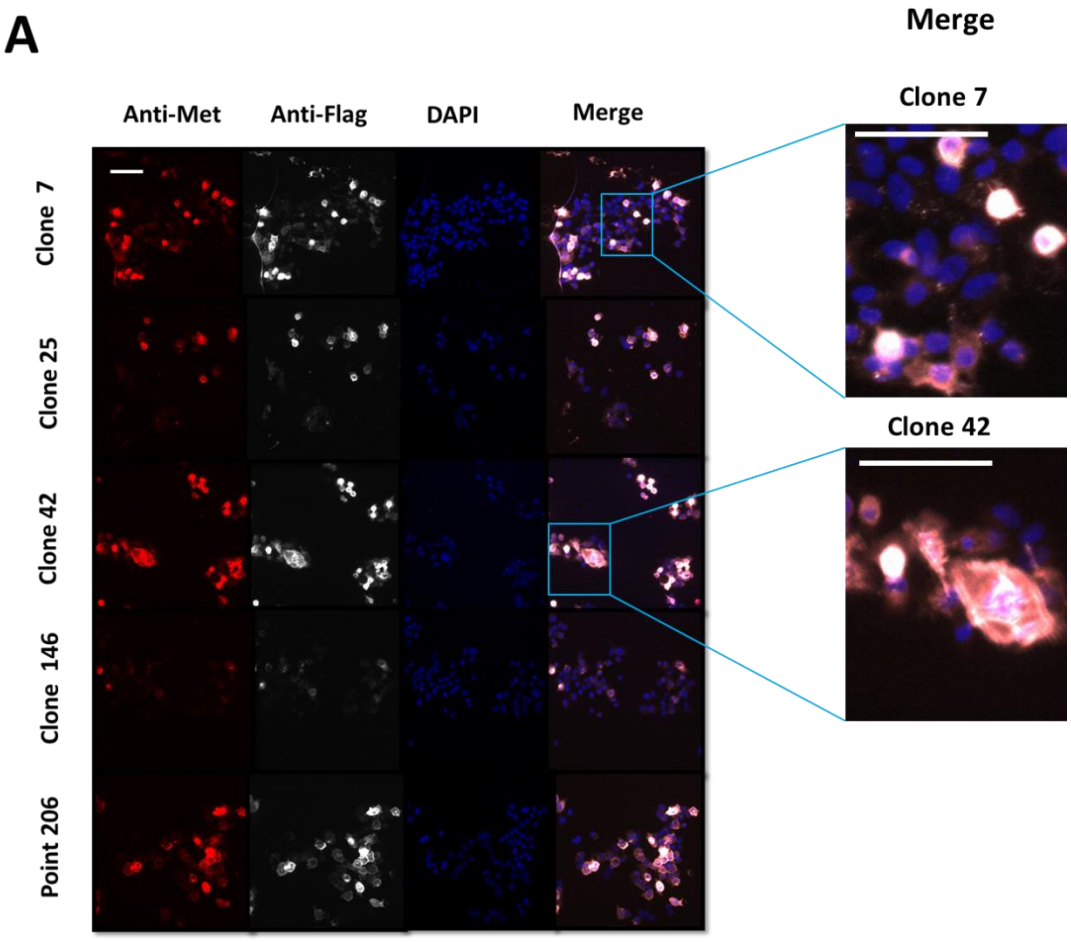

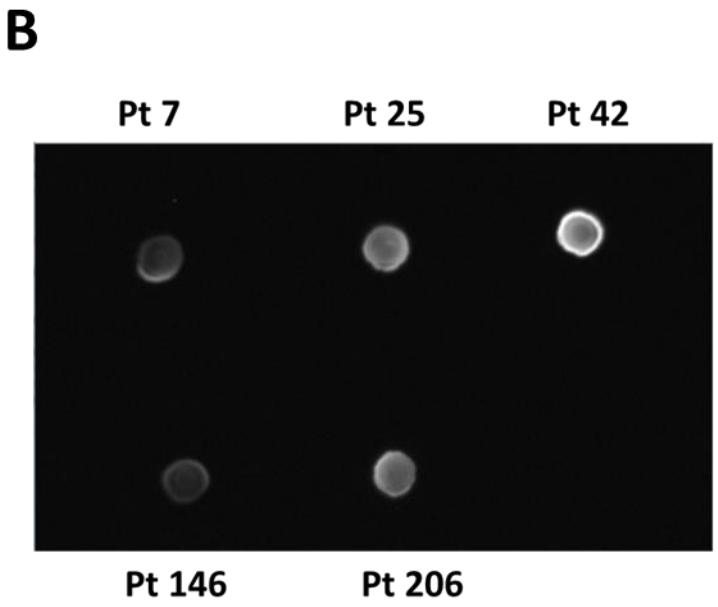

Figure 5-5. Validation of the presence of scFv-Fc and c-Met in the five subclones, amplified using the miniprep technique.

Those clones were previously identified with high c-Met specificity and co-localisation of scFv-Fc and human c-Met. **A)** Positive staining for c-Met and anti-FLAG in the 5 clones. Left panel shows staining for human c-Met, middle panel display staining for scFv-Fc (via anti-FLAG) , right panel shows nuclear staining for each clone and lastly, the far right panel shows the merged images for all the stainings. Higher zoom for clones 7 and 42 on the far right. Scalebar: 60µm**. B)** Dot blot (described in M&M) assessing the presence of scFv-Fc in the five subclones of interest (7, 25, 42,146 and 206) from the supernatant of HEK293 cells that were transfected with the plasmids of interest. Images were acquired by an epifluorescence microscope.

Following our previous experiment and further immunofluorescence staining, we decided to focus on those five subclones (7, 25, 42, 146 and 206) and amplified their DNA plasmid. This was our first step towards the scaling up of our desired clone. Initially, we decided to use the 'Miniprep' technique to validate the immunofluorescence detection of anti-FLAG and human c-Met in those 5 clones and then focus on one or two clones which would then be

amplified using the ‘Maxiprep’ method. The miniprep was performed successfully and did not affect the production of scFv-Fc for those 5 subclones, as shown in Figure 5-5. The specificity of the FLAG epitope is observed clearly as it co-localises with c-Met positive cells. To further validate the production of scFv-Fc from the supernatant collected after transfection of the cells with those DNA plasmids from the minipreps, a dot blot assay was performed in which the anti-FLAG antibody was used for the detection of scFv-Fc (Figure 5-5B). Dot blots are a quick and efficient way to assess the expression level for the scFv-Fc and do not require large amount of samples, hence minimising sample loss. It is clear that all five plasmids successfully generated the scFv-Fc against human c-Met.

Due to previous quantification, as listed in Figure 5-4B and repeats of immunofluorescence staining for those five clones, we were able to identify clones 7 and 42 as suitable for the potential use in the *in-vivo* study. Despite clone 25 showing a high ratio fluorescent staining intensity (c-Met/scFv-Fc) to the expression level of the scFv-Fc, additional immunostaining experiments revealed a poorer co-localisation between c-Met and anti-FLAG positive cells, in comparison to other clones. Clones 7 and 42 showed co-localisation of c-Met and anti-FLAG epitopes as well as a high ratio for average intensity for c-Met/anti-FLAG over level of scFv-fc expression quantified by densitometry. Clones 7 and 42 were therefore selected for further investigations and scaled up using the maxiprep method.

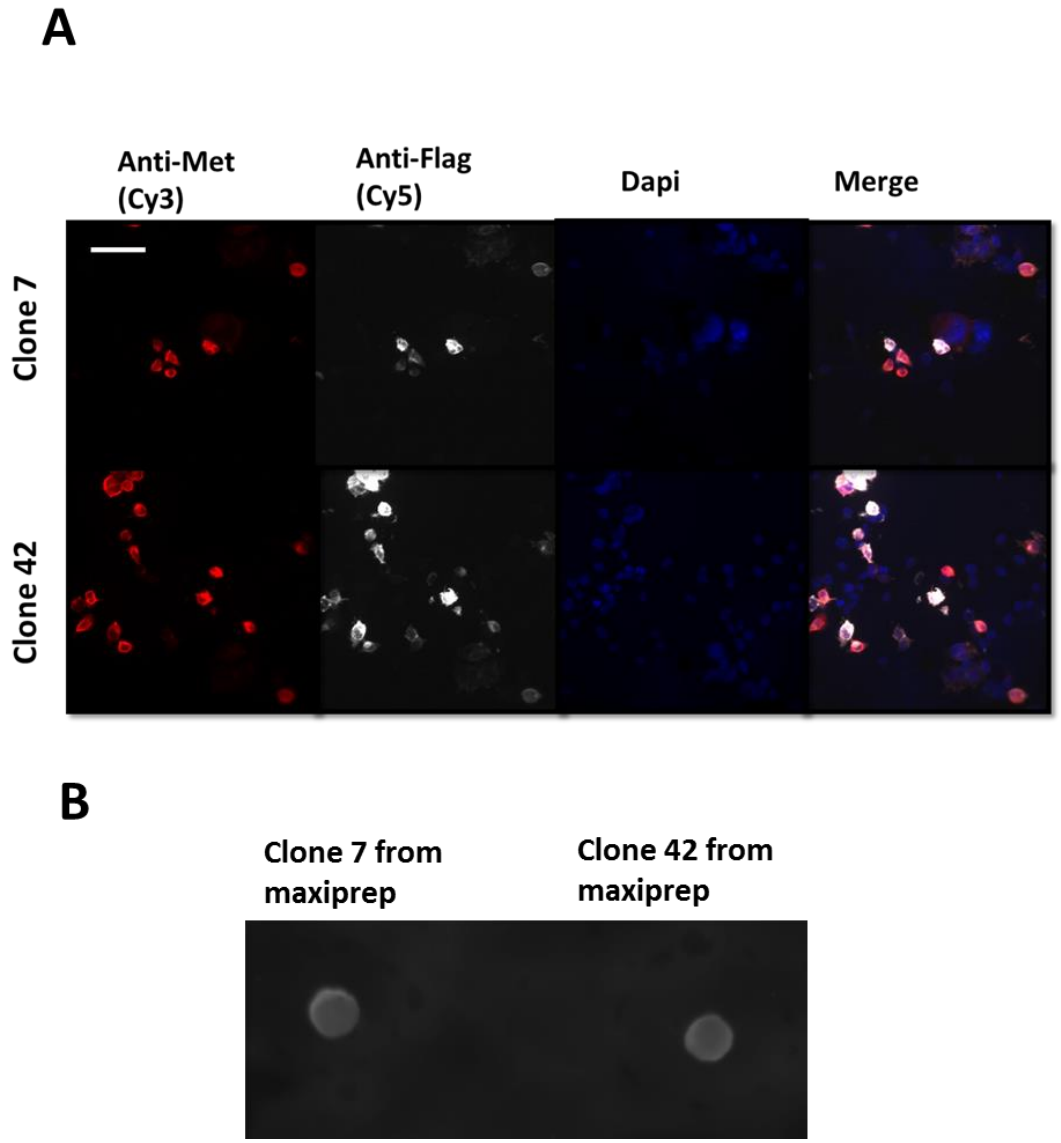

Figure 5-6. Validation of the presence of scFv-Fc and c-Met in two subclones, amplified using the maxiprep technique.

Those clones were previously identified with high c-Met specificity and co-localisation of scFv-Fc and human c-Met. **A)** Positive staining for c-Met and anti-FLAG in the 2 clones. Left panel shows staining for human c-Met, second middle panel display staining for scFv-Fc (via anti-FLAG), middle right panel shows nuclear staining and the far right panel displays the merge for all stainings. Scalebar: 60µm. B) Dot blot assessing the presence of scFv-Fc in the two subclones of interest (7 and 42). Images were acquired by an epifluorescence microscope.

Scaling up the plasmid DNA for clones 7 and 42 using the Maxiprep method was successful, as shown in Figure 5-6. Those images show clear staining of human c-Met and anti-FLAG epitope of the scFv-Fc in both clones. The staining is specific for c-Met as untransfected cells were not positive for the anti-FLAG antibody. Clone 42 shows a higher intensity staining for the anti-FLAG epitope than clone 7 (Fig 5-6A). Figure 5-6B shows evidence of the production of the scFv-Fc in both clones.

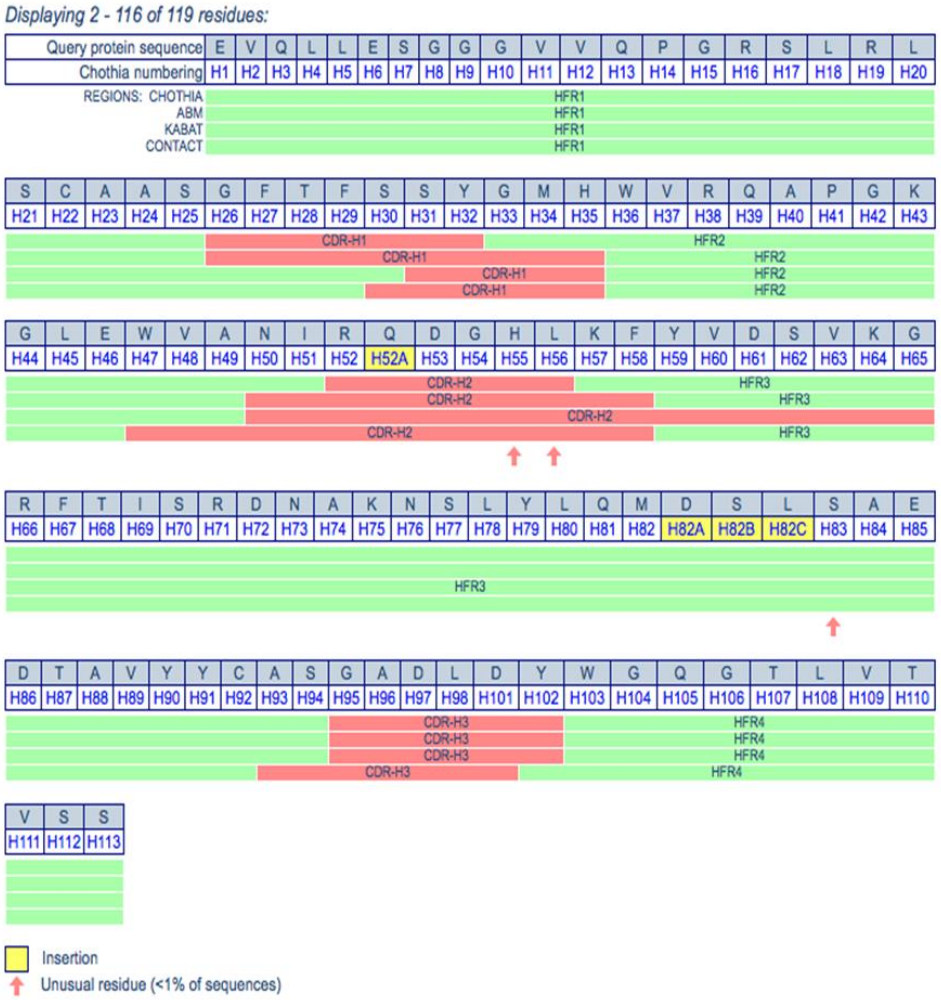

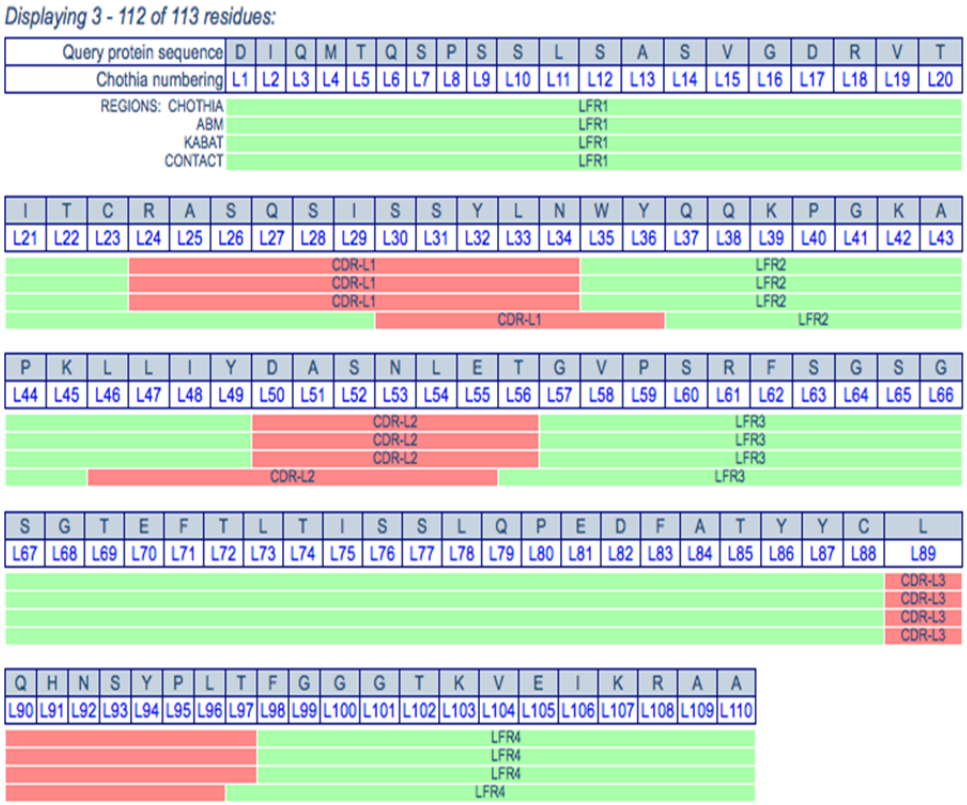

Light chain

Figure 5-7. Protein Sequence for the variable region of the scFv-Fc generated by subclone 42 from the phage display library.

This represents the sequence of the heavy (left panel) and light (right panel) chains of the scFv-Fc of interest. The sequence was analysed by four different methods called chothia, kabat, ABM, and contact, as observed by the four lines beneath the sequence. Those methods use different ways to determine a complementary determining region (CDR), highlighted in red. Inserted amino acids are highlighted in yellow. The sequence of the Fc domain was omitted as it is constant across all subclones generated in the phage display library.

We decided to focus on subclone 42 only for the Cy5 labelling designed to be used in the *in-vivo* imaging of c-Met positive tumour cells. Clone 7 expressed a much lower amount of scFv-Fc in comparison to clone 42, and

was therefore not used in further experiments. Figure 5-7 shows the sequence of the variable domains of the heavy and light chains of the scFv-Fc. A CDR is an immunoglobulin (Ig) hypervariable domain that determine specific antibody (Ab) binding. As observed in this sequence, each chain shows three CDRs (which is expected). Due to the fact that the sequence was analysed by four different methods, we observe a slight variation in the length, start and finish of the CDR. It was important to sequence this scFv-Fc in order to identify the presence of lysine residues that are necessary for Cy5 labelling. The lysine residues or free amino groups would bind to the NHS-ester present in the Cy5 dye. This subclone shows the presence of lysine residues in its heavy and light chains.

5.2.2 Whole body *in-vivo* optical imaging of basal-like breast cancer in mice xenografts model

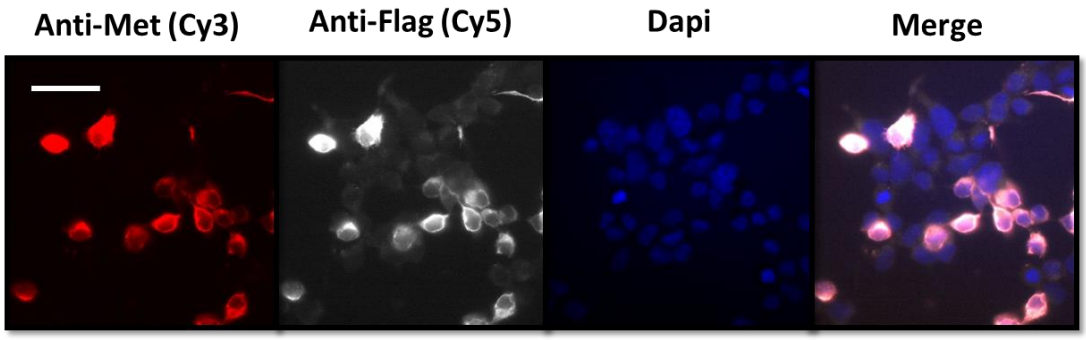

Figure 5-8. Specificity of the Cy5 labelled-scFv-Fc generated by clone 42 against human c-Met.

Subclone 42 generated scFv-Fc against human c-Met that was labelled with Cy5. The tracer shows positive staining for anti-FLAG (middle panel) and co-localises with c-Met positive cells (Left panel and far right panel). Nuclear staining was performed (middle right panel). Scalebar: 60µm. Images were acquired by an epifluorescence microscope.

The initial aim of this study was to identify the ‘best’ clone that would be able to recognise overexpressed c-Met or c-Met positive cells (such as the ones in basal like breast cancer) *in-vitro* in order to use it *in-vivo*. In this experiment, it was possible to fluorescently (Cy5) label the scFv-Fc (described in Material and Methods) produced by the subclone 42 without altering its specificity for human c-Met, as shown in Figure 5-8 (left panel). Figure 5-8 showed the detection and clear co-localisation of the scFv-Fc (anti-FLAG-Cy5) with human c-Met. In addition, a coomassie staining was performed for this Cy5-labelled scFv-Fc to ensure that the scFv-Fc did not aggregate with other molecules, during the Cy5 labelling. The band displayed was strong and slightly higher than the 52kDa expected due to the addition of the Cy5 dye. As those results were convincing, this same batch was used to perform the *in-vivo* experiments, using the IVIS imaging system.

Prior to the *in-vivo* optical imaging, it was needful to identify a cell line that could be used as a negative control for the experiment. A suitable negative control would be a cell line that does not display a high level for c-Met level so that it would be possible to compare the uptake of the tracer in the positive cell line with the negative cell line.

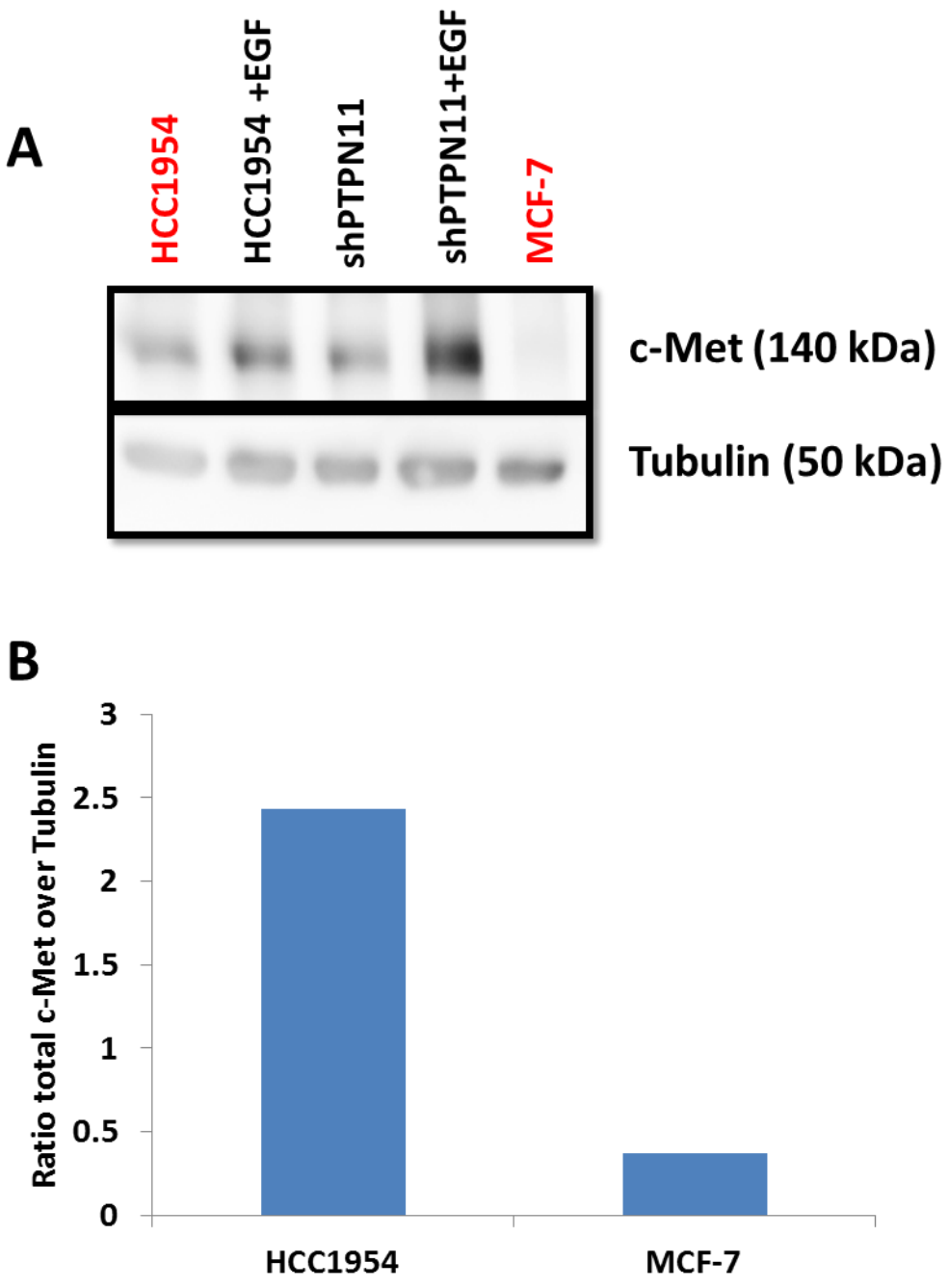

Figure 5-9. Low c-Met expression level in MCF-7 in comparison to HCC1954.

A) Immunoblot displaying the expression level of c-Met in HCC1954 and MCF-7. Cell lines highlighted in red are cell lines that will be used in the *in-vivo* work concerning the labelled scFv-Fc tracer against human c-Met. **B)** Quantification of c-Met expression level in HCC1954 and MCF-7 cell lysate.

The MCF-7 cell line is a type of invasive breast ductal carcinoma. It has been shown in the literature that MCF-7 expresses a low amount of c-Met [270]. Nevertheless, we thought it useful to compare the amount of c-Met protein level in the MCF-7 cells with our cell line of interest, the HCC1954. Fig 5-9A shows a clear difference between the expression level of c-Met in HCC1954, highlighted in red, in comparison to the MCF-7 cell line. With the normalisation of total c-Met against tubulin, Fig 5-9B showed approximately a 5 fold increase in the level of total c-Met in HCC1954 in comparison to MCF-7. This result and the literature gave sufficient confidence in the use of MCF-7 cell line as negative control as a low c-Met expresser.

Following this and the ability of the scFv-Fc to retain its specificity for human c-Met after its Cy5 labelling as shown in Fig 5-9, the same batch of Cy5-labelled scFv-Fc was used to inject intravenously 50µg per tumour-bearing mouse (as 25µg was insufficient as observed in previous experiments).

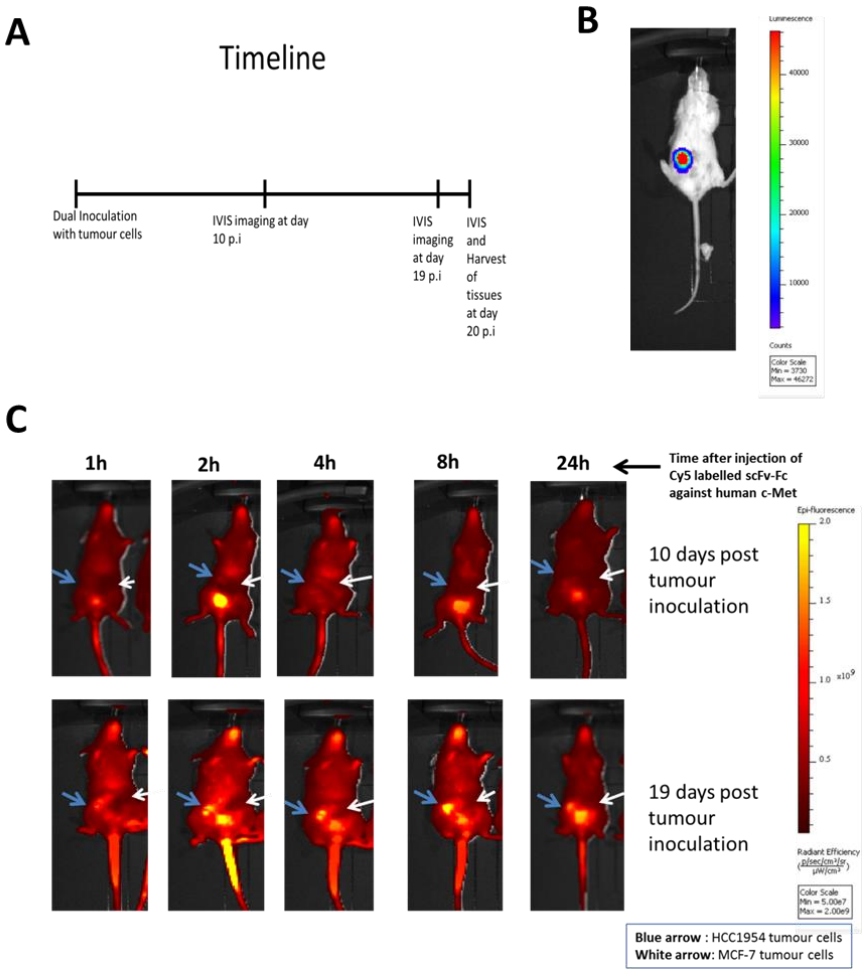
A
Timeline
Dual Inoculation with tumour cells
IVIS imaging at day 10 p.i
IVIS imaging at day 19 p.i
IVIS and Harvest of tissues at day 20 p.i
B
Luminescence
40000
30000
20000
10000
Counts
Color Scale
Min = 3730
Max = 46272
C
1h
2h
4h
8h
24h
Time after injection of Cy5 labelled scFv-Fc against human c-Met
10 days post tumour inoculation
19 days post tumour inoculation
Epi-fluorescence
2.0
1.5
1.0 x10^9
0.5
Radiant Efficiency
Color Scale
Min = 5.00e7
Max = 2.00e9
Blue arrow : HCC1954 tumour cells
White arrow: MCF-7 tumour cells

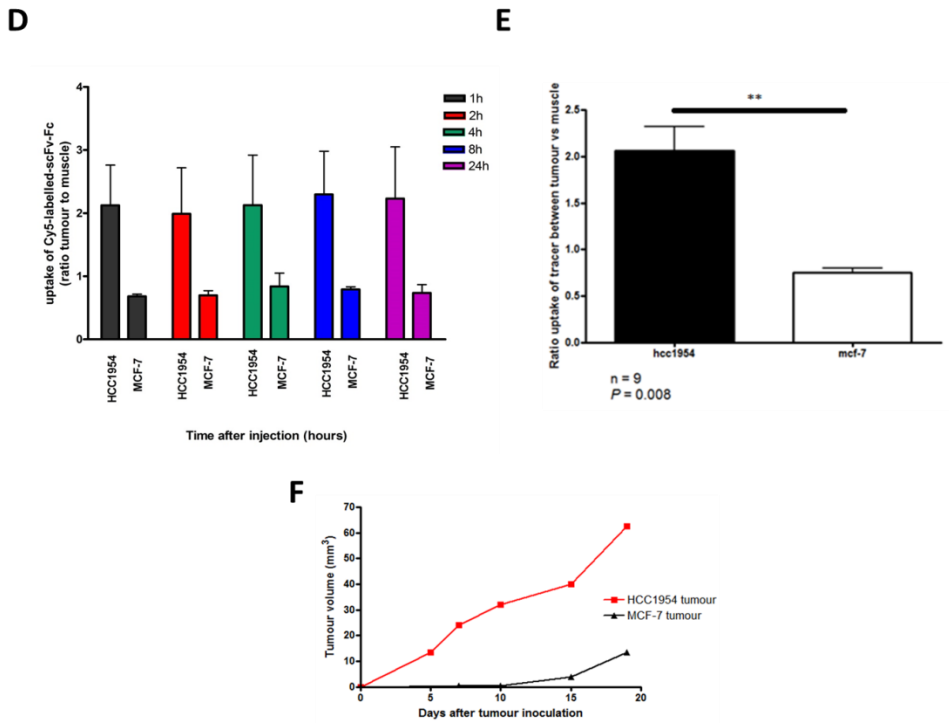

Figure 5-10. Targeting of c-Met positive basal-like breast tumour via the Cy5-labelled-c-Met scFv-Fc.

A) Timeline of the *in-vivo* study to assess the specificity of the Cy5 labelled scFv-Fc to the overexpressed c-Met tumour cells *in-vivo*. Four mice were subcutaneously inoculated at day 0 with 4 million HCC1954 cells on their right hand side, and 4 million MCF-7 cells on their left hand side. 50µg of the Cy5-labelled c-Met scFv-Fc was intravenously injected into each of those tumour bearing mice. IVIS imaging of the mice were performed at day 10 and day 19 post tumour inoculation. Finally, mice were sacrificed at day 20 post tumour inoculation, following the last imaging timepoint, 24h post-injection (p.i.). A biodistribution was performed using the IVIS equipment. **B)** The bioluminescent signal is detected in the HCC1954 tumour at day 19 post tumour inoculation. The bioluminescent signal is represented in a colour scale with red the most intense signal and yellow the weakest signal. **C)** Images of a representative mouse, with a palpable tumour at day 10 (top panel) and at day 19 (bottom panel) after tumour inoculation. There is a detectable fluorescent signal at day 19 post tumour inoculation at all timepoints (exposure: 3 seconds, binning factor: 4 and excitation filter: 640 using Living Image® software). On both days, images were acquired 1h, 2h, 4h, 8h and 24h post tracer's injection. Images were normalised using the same scale. **D)** Ratio of tracer uptake between tumour and muscle in c-Met positive tumour (HCC1954) and c-Met negative tumour (MCF-7),

n=4, cumulative timepoints at 1, 2, 4,8 and 24h and paired t-test $P < 0.05$. **E)** Ratio uptake of tracer between tumour and muscle in c-Met positive tumour (HCC1954) and c-Met negative tumour (MCF-7) at day 10 and day 19 p.i (combined data) across all timepoints (1,2,4,8 and 24h post tracer's injection), n=4 **F)** HCC1954 and MCF-7 tumour growth curve of the representative mouse from day 0 to day 19 post tumour inoculation.

Figure 5-10A outlines the timeline of this study which lasted 20 days. Four mice were inoculated bilaterally and subcutaneously with the HCC1954-luciferase tagged cell line on their right hand side of their 4th set of mammary fat pad, while the MCF-7 cell line was injected, in parallel, on their left hand side. Due to previous work [16], it was possible to estimate the amount of cells to be injected into the mice for the appearance of a visible tumour by day 10 after inoculation, for a first imaging session.

One mouse out of four displayed a palpable tumour, which was detectable using bioluminescence (Fig 5-10B) and fluorescence emitted by the Cy5-labelled-scFv-Fc (Fig 5-10C). Another mouse grew a very small HCC1954 tumour that was not palpable, and was only detectable by bioluminescence once dissected and imaged ex-vivo using the IVIS Illumina machine (Figure 5-11). The signal exhibited by the tracer is specific to the basal-like breast tumour (HCC1954-luciferase at the RHS) as not much signal was recorded from the ER+ve and c-Met low expresser counterpart, MCF-7 (Fig 5-10B). Quantitative analysis revealed a significant difference between the tumour to muscle ratio of the tracer uptake in both the c-Met positive HCC1954 tumour and the c-Met negative MCF-7 tumour (Figure 5-10C, $P < 0.05$). Figure 5-10D shows the ratio uptake in the c-Met positive HCC1954-luciferase tagged tumour and in the c-Met negative MCF-7 tumour, at 1, 2, 4, 8 and 24 hours

after tracer's injection. The tumour to muscle ratio in the basal-like tumour is 3.1 fold greater than the c-Met negative adenocarcinoma tumour at 1 hour post injection. This quantitative difference between both tumours is almost constant across the remaining timepoints (2, 4, 8 and 24h). Despite the increase in the tumour size of MCF-7 at day 19 (palpable then) (Fig 5-10F), the tumour to muscle ratio remains consistent on both day 10 and day 19 post tumour inoculations which explain the presence of a small standard deviation. Figure 5-10E displayed the cumulative mean tumour to muscle ratios, across all timepoints of imaging (Fig 5-10E). It shows a 3 fold greater uptake of the tracer in HCC1954-luciferase tagged tumour in comparison to the MCF-7 tumour (ratio of 2 for HCC1954 while the ratio is 0.75 for MCF-7). Following the imaging session at day 19 post tumour inoculation, it was necessary to assess the amount of fluorescence emitted by individual organs of interest.

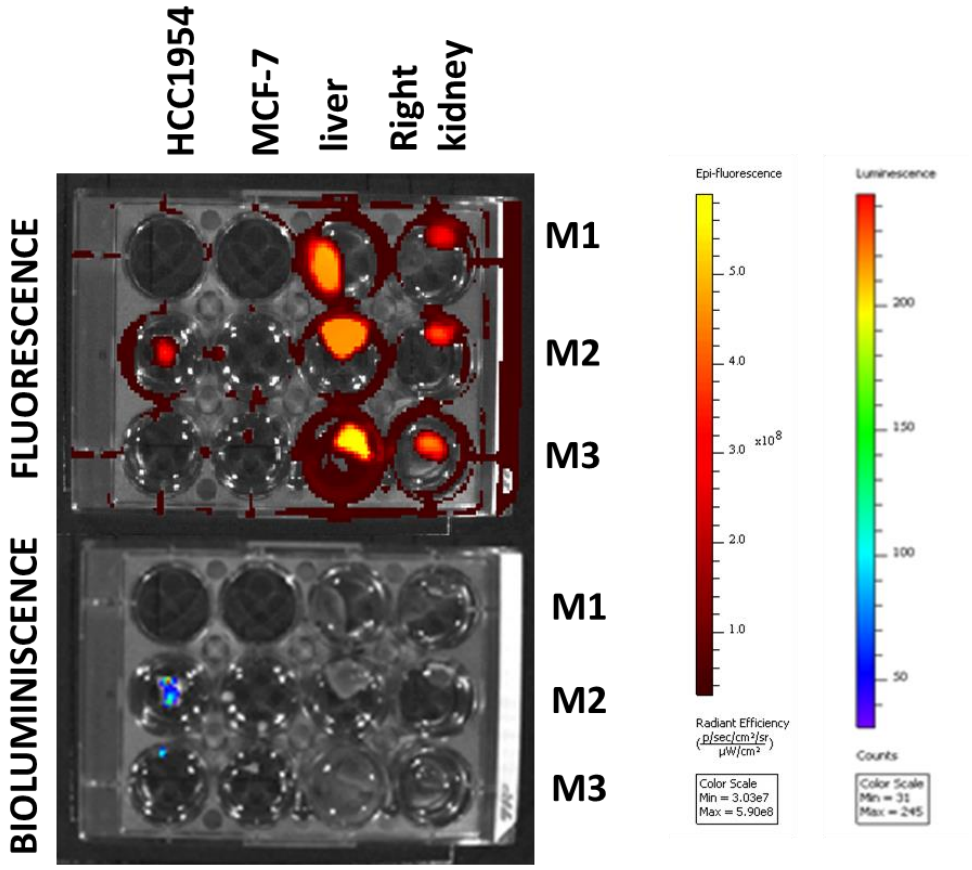

Figure 5-111. Representative images of dissected organs of 3 tumour bearing mouse bearing sacrificed 24 hours after intravenous injection of c-Met-Cy5.

Top plate displays varying level of the fluorescence signal from the c-Met-Cy5 across the c-Met positive basal-like HCC1954 tumour, the c-Met low expresser MCF-7 tumour, the liver and the kidney for mouse 1 (M1), mouse 2 (M2) and mouse 3 (M3). The bottom plate displays the signal from bioluminescence from the same organs as the plate above. However, only the HCC1954 tumours show some signal, as they were tagged with luciferase, and therefore detectable via bioluminescence.

24 hours after Cy5-labelled scFv-Fc injection at day 19 post tumour inoculation, all mice were sacrificed and the organs of interest from 3 tumour-bearing mice were excised and collected. Their tumours, whenever present (both HCC1954 and MCF-7), liver and right kidney were excised and

transferred into a 12 well plate with media, as shown in Figure 5-11. The first tumour bearing mice did not grow any tumours. However, the second and third tumour bearing mice grew both the HCC1954-luciferase tagged tumour and the MCF-7, c-Met low-expresser tumour. Fluorescent and bioluminescent images of those plates were then acquired using the IVIS Illumina machine. The ex vivo evaluation of excised organs showed that the Cy5-labelled tracer was predominantly taken up by the HCC1954 tumour in comparison to a low signal observed for the MCF-7 tumours, and that a high signal is observed in both the liver and the right kidney for all mice. Bioluminescent images confirm the presence of the HCC1954-luciferase tagged cells in 2 tumour bearing mice (M2 and M3).

In order to validate the detection and specificity of the Cy5-labelled-scFv-Fc tracer in overexpressed c-Met tumour cells in basal-like breast cancer, it was then important to stain both the basal-like HCC1954 tumour tissue and the c-Met negative MCF-7 tumour tissues, collected from this imaging experiment, for human c-Met.

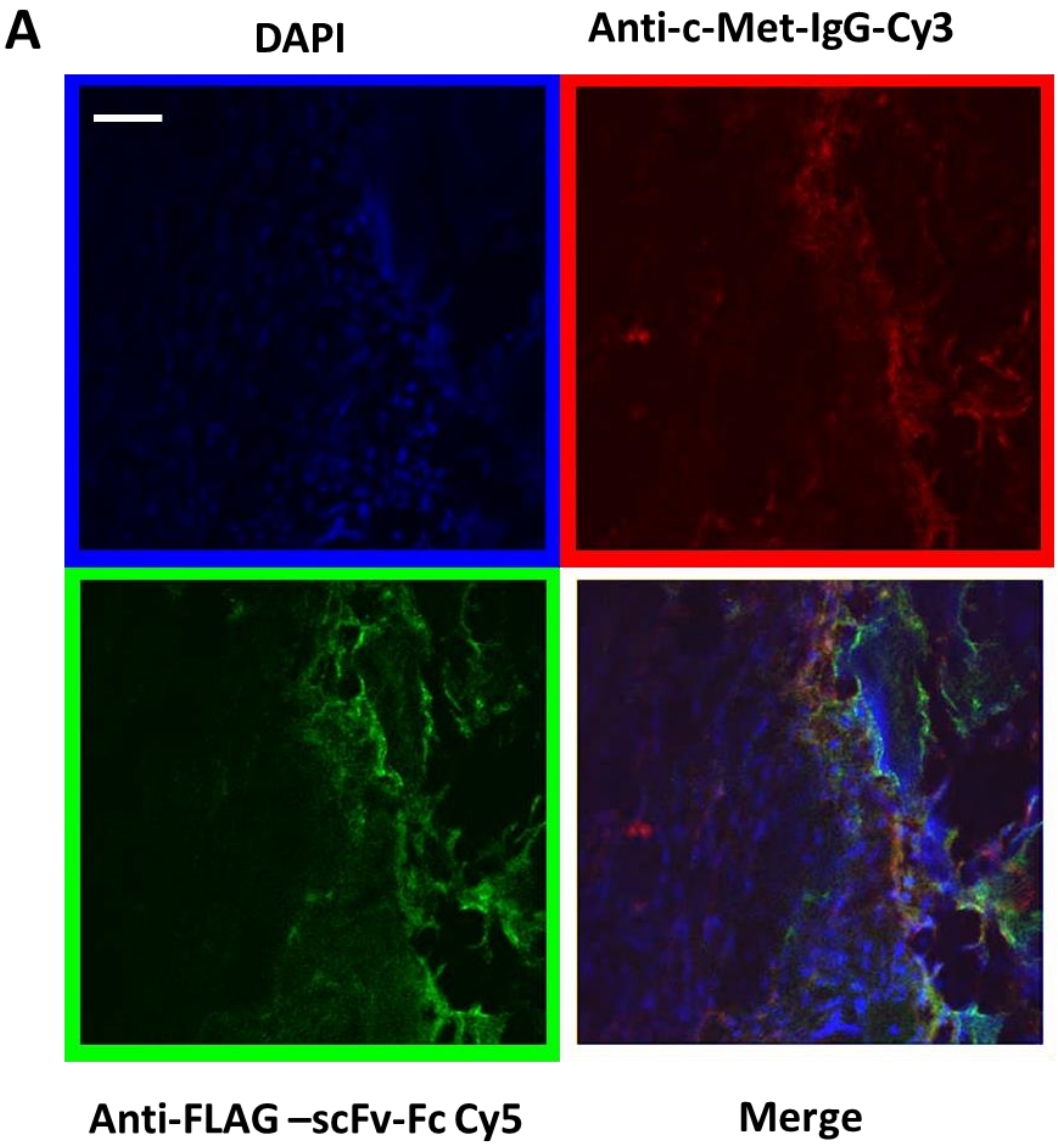
A
DAPI
Anti-c-Met-IgG-Cy3
Anti-FLAG –scFv-Fc Cy5
Merge

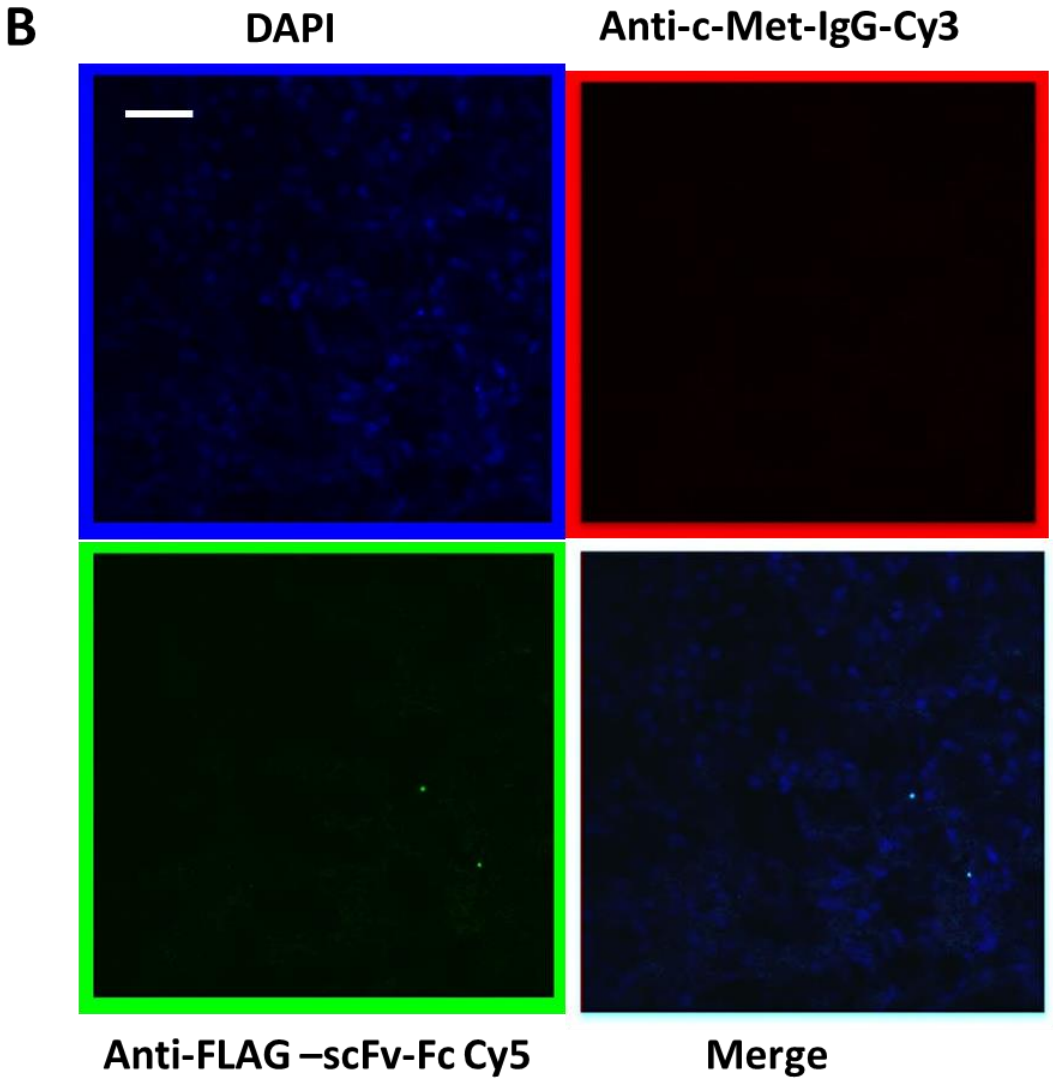

Figure 5-122. Validation of specificity of c-Met-Cy5 for human c-Met in snap-frozen tumour tissue ex-vivo.

A) The images represent staining performed on a snap frozen HCC1954 tumour tissue. Staining (from left to right, clockwise) for nuclear staining (Dapi), c-Met (detected with anti-rabbit Cy3 secondary antibody - red), Merge and anti-FLAG (which shows the presence of the Cy5-labelled scFv-Fc tracer, in green) were performed. The 'Merge' image was also included to identify co-localisation. A clear staining for both c-Met and anti-FLAG is detectable in the basal-like tumour tissue **B)** Staining in the MCF-7 tumour tissue. Those images represent staining performed with the same antibodies as the one used in A) Scalebar for all images: 50µm. All images were acquired using a confocal microscope at 40X magnification.

As depicted in Figure 5-12A & B, there is a clear staining for human c-Met in the HCC1954 tumour tissue, while it was not visible in the MCF-7 tumour xenografts. Additionally, the c-Met staining detected in the basal-like tumour section co-localised with the staining pattern of c-Met-Cy5 (Left panel, Fig 5-12A). As expected, the lack of c-Met staining in the MCF-7 tumour tissue was accompanied by a lack of detection of the ScFv-Fc tracer, as shown in the anti-FLAG-Cy5 channel (Fig 5-12B).

5.2.3 Conjugation and Radiolabelling of the scFv-Fc with In-111

The scFv-Fc was reconstituted in HEPES buffer (0.1 M, pH 8.5) using disposable PD10 size exclusion columns. Details of the procedure are described in Material & Methods, Section 3.10.

The fraction containing the most scFv-Fc (fraction 6, 0.5 mL, 2.7 mg mL-1) was radiolabelled with 111-In. It was found that high radiochemical yields (> 95 %) and maximum specific activity were achieved when the antibody solution was diluted three-fold in ammonium acetate (0.2 M), followed by addition of an equivalent volume of 111-In solution (0.1 M HCl). For example, addition of 10 µL of scFv-Fc (2.7 mg mL-1, 0.2 M ammonium acetate) to 20 µL of ammonium acetate (0.2 M), followed by addition of 111-In (15 MBq, 0.1 M HCl) provided 111-In-CHX-A''DPTA-scFv-Fc in > 95% radiochemical yield, with a specific activity of 555 MBq mg-1. Radiochemical purity was assessed using size exclusion HPLC (SEC-HPLC). In SEC-HPLC, molecules with a higher molecular weight are eluted before molecules of a lower molecular weight.

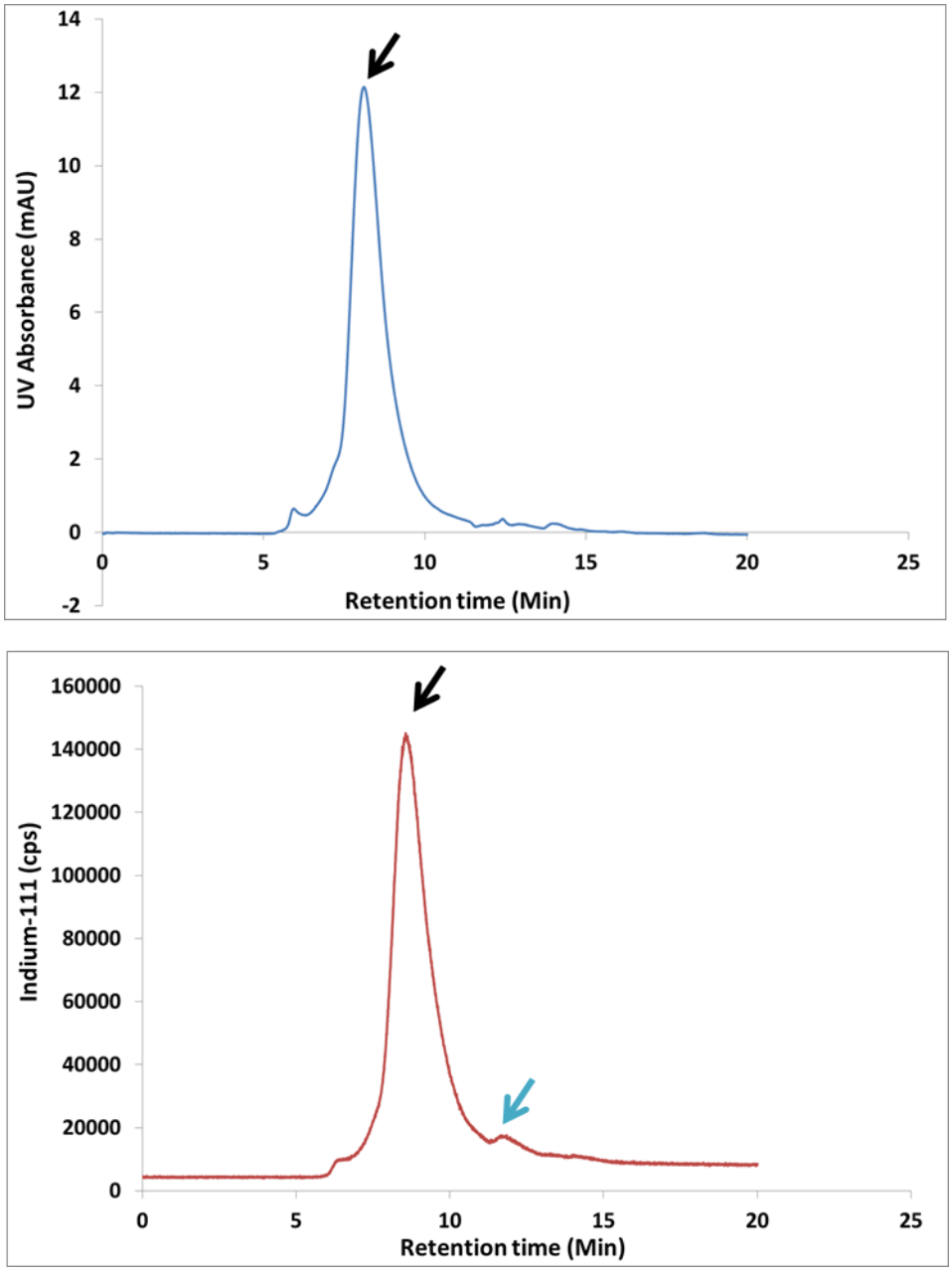

Figure 5-133. Successful SEC-HPLC-chromatogram of 111In-CHX-A''-DTPA-scFv-Fc against human c-Met.

Upper graph shows the UV profile of the compound (blue line) (λ=280 nm). Bottom panel shows the radioactivity signal from the compound. Values are given as counts per second (cps). Retention time for the UV absorbance of ^{111}In-DTPA-c-Met scFv-Fc is 8.5 min (black arrow). Retention for Free Indium-111 is 12.2 min (blue arrow).

Fig 5-134 displays the SEC HPLC chromatograms of In-111-CHX-A''-DPTA-scFv-Fc. The top chromatogram shows the elution profile of CHX-DPTA-

scFv-Fc at 280 nm using a UV-Vis detector. The major species has a retention time of 8.1 mins. The bottom chromatogram displays the radiochromatogram (using a scintillation detector), in which only radiolabelled species are detected. The retention time of the major species (8.5 mins) matches that observed in the UV-Vis chromatogram (allowing for slight differences arising from the configuration of the different detectors in series).

Following the successful radiolabelling of CHX-A''-DPTA-scFv-Fc, an immunostaining was performed to ensure that CHX-A''-DPTA-scFv-Fc retained its affinity for human c-Met.

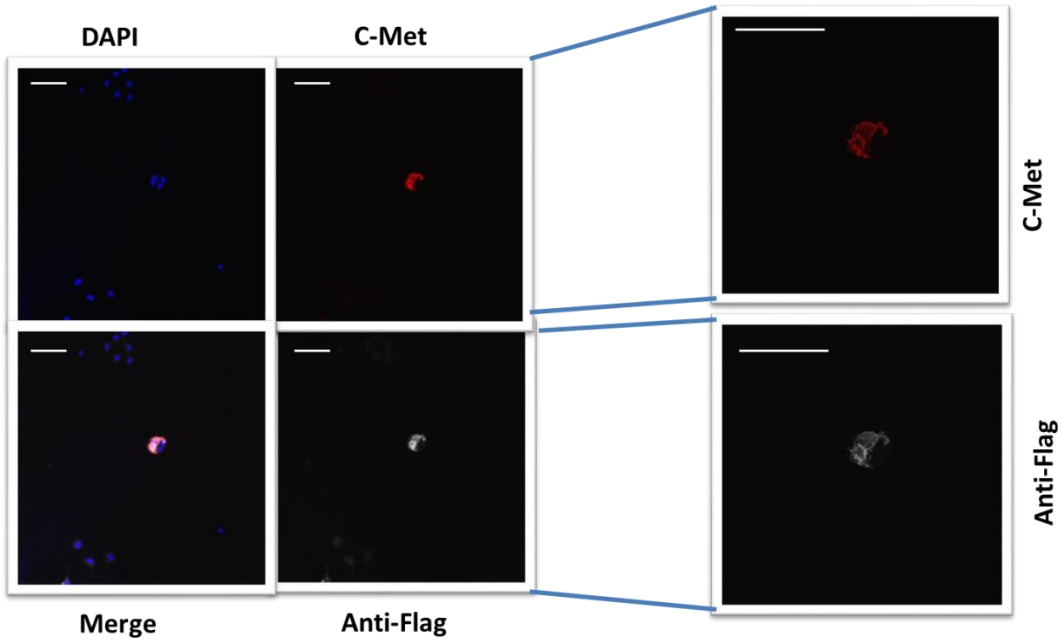

Figure 5-14. Specificity of CHX-A''DTPA-scFv-Fc retained against human c-Met.

Positive staining for c-Met and anti-FLAG in the compound. Clockwise, top left panel shows nuclear staining (DAPI), top right shows staining for human c-Met (Cy3 dye), bottom right shows staining for scFv-Fc (anti-FLAG – Cy5 dye) and bottom left panel shows the merged images from all the stainings. Higher zoom for CHX-A''DTPA-scFv-Fc on the far right. C-Met staining for top far right panel and anti-FLAG staining for bottom far right panel. Scalebar: 100µm

The conjugate CHX-A''-DPTA-scFv-Fc was incubated in MCF-7 cells that were transfected with c-Met (for overexpression of c-Met in MCF-7 cells), and fixed before performing a double immunofluorescence staining in which c-Met was stained, while CHX-A''DPTA-scFv-Fc was detected using the anti-FLAG antibody. As shown in Figure 5-14, the cells that were c-Met positive co-localised with the staining pattern of the anti-FLAG epitope, therefore validating the integrity of the CHX-A''DPTA-scFv-Fc conjugate's specificity for human c-Met.

It was then important to perform a serum stability test in order to validate the integrity of the radiolabelled scFv-Fc for up to 24hours in human serum before performing a SPECT imaging experiment in tumour-bearing mice.

A

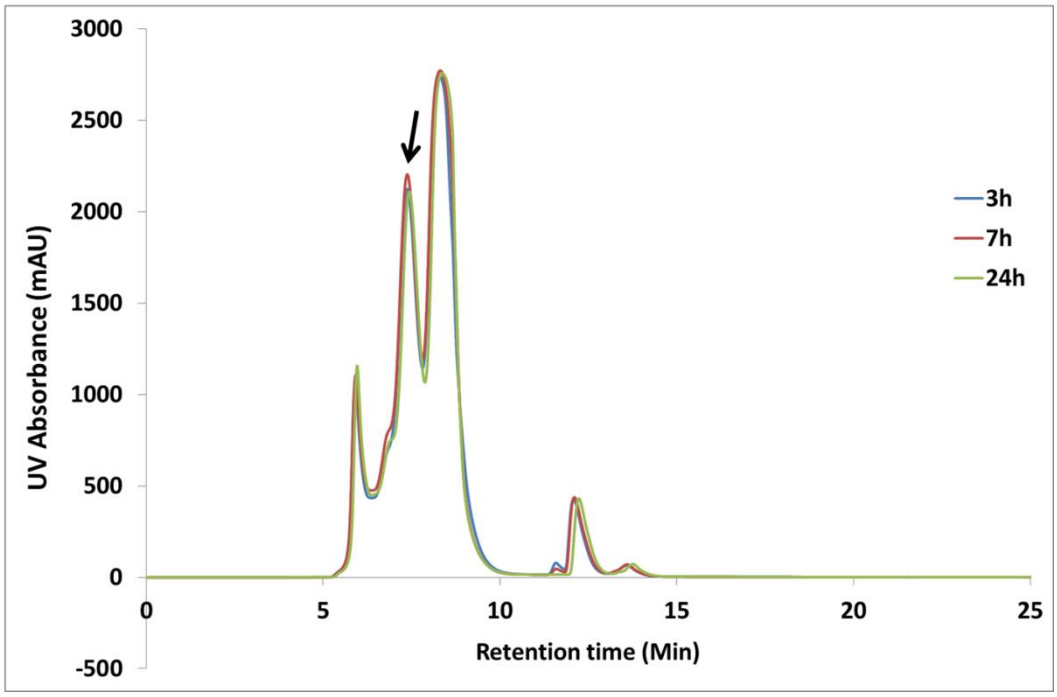

B

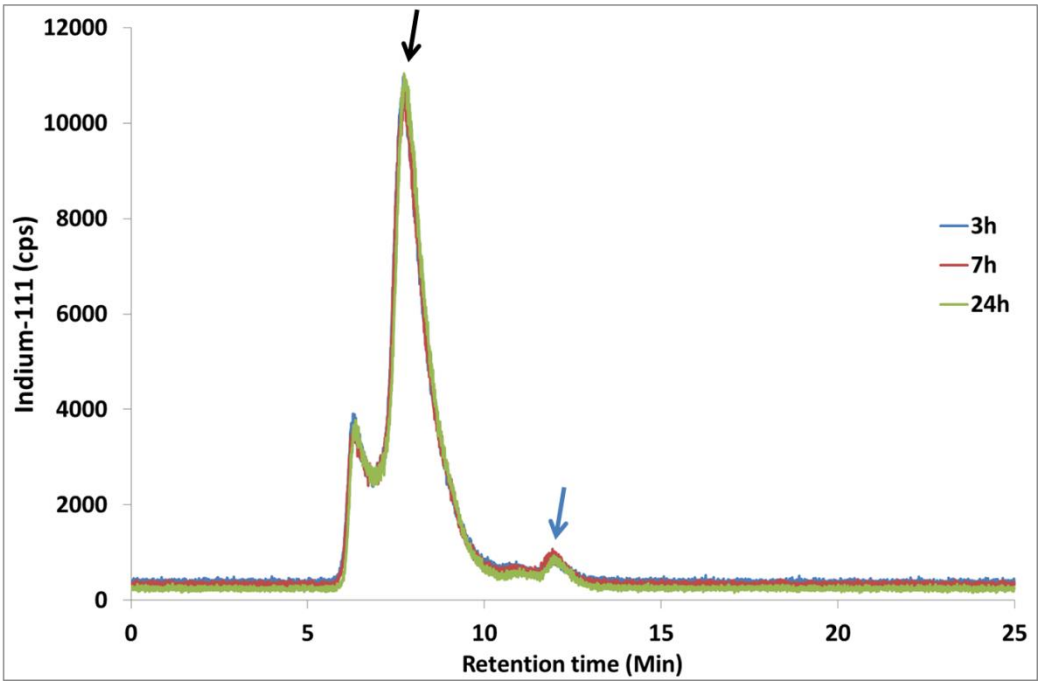

Figure 5-15. Serum stability test for the scFv-Fc against c-Met.

A fraction of the incubated ^{111}In-CHX-A''-DTPA-scFv-Fc was injected at 3h (blue line), 7h (red line) and 24h (green line) after incubation at 37°C in human serum into the SEC-HPLC column **A)** UV absorbance for each fraction at all timepoints mentioned above **B)** Radioactivity signal for each fraction displayed using a scintillation detector, in which only radiolabelled species are detected. The black arrow points towards the peak that corresponds to the ^{111}In-CHX-A''DTPA-scFv-Fc, while the blue arrow points to the free Indium-111 (Indium-111 isotope that did not label the conjugated CHX-A''DTPA-scFv-Fc).

In human serum stored at 37°C, the ^{111}In-CHX-A''-DTPA-scFv-Fc was highly stable at 3h, 7h and 24h after incubation in human serum, as observed in Figure 5-15. HPLC of ^{111}In-CHX-A''DTPA-scFv-Fc used for injection showed a UV absorbance (Fig 5-15A) and radioactivity detector signal at the same elution time (Fig 5-15B).

HPLC of the percentage remaining as intact species was over 96% at each timepoint (see Appendix). The mean retention time for ^{111}In-CHX-A''DPTA-

scFv-Fc that was incubated for 3h, 7h and 24h in human serum was 7’42 minutes with 96% remaining as intact species. Free Indium-111 (that did not react with the conjugated CHX-A’’DTPA-scFv-Fc) was eluted at a mean retention time of 11’54 minutes across all timepoints. Chromatograms that displayed the yield of labelling and retention times of the eluted radiolabelled ^{111}In-CHX-A’’-DPTA-scFv-Fc for each timepoint (3h, 7h and 24h after incubation in human serum) have been inserted in the Appendix (Chapter 9, pages 287, 290 & 292). Controls were performed in order to assess the retention time of free Indium-111 and free indium-111 in human serum (see Appendix, pages 283, 288, 291 & 293).

Due to this successful result, it was then possible to progress onto a SPECT imaging experiment, in which ^{111}In-CHX-A’’-DPTA-scFv-Fc was injected into female NSG mice that were inoculated with both the c-Met positive cell line, HCC1954 (at their right hand side) and the c-Met negative cell line, MCF-7 (at their left hand side).

5.2.4 Whole body SPECT imaging of basal-like breast cancer in mice xenografts model

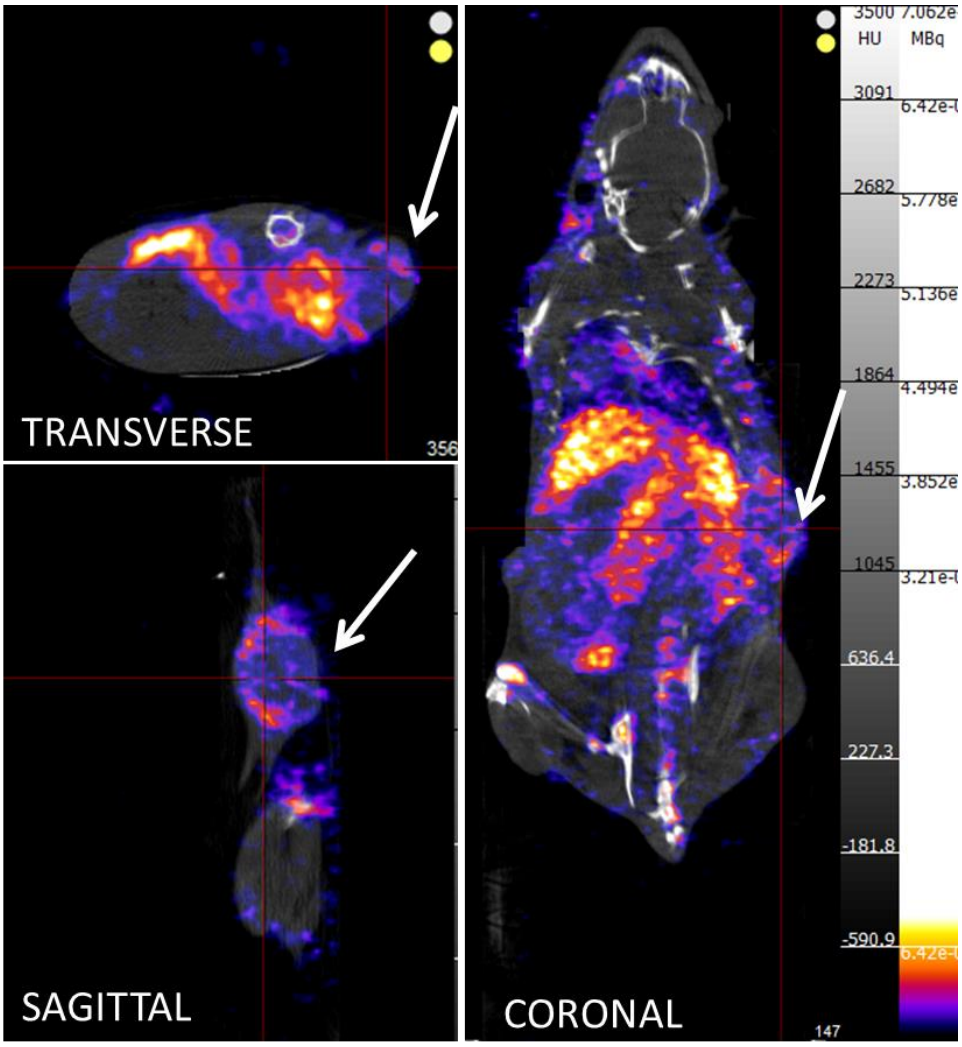

Figure 5-16. c-Met positive tumour uptake observed via SPECT using ^{111}In-CHX-A''DPTA-scFv-Fc in a representative tumour-bearing mouse.

Anticlockwise: transverse, sagittal and coronal sections of a dual tumour bearing mouse, imaged 24h after injection. White arrow points at the basal-like breast tumour. Negative c-Met cell line was not observed in this slice. The SPECT signal is represented in a colour scale with yellow the most intense signal and blue the weakest signal.

The SPECT images acquired from this experiment shows clear uptake at the c-Met positive tumour site, HCC1954. As observed, in Fig 5-16, the white arrow which points towards the basal-like breast tumour site shows clear uptake of the ^{111}In-CHX-A''DPTA-scFv-Fc. The distribution of the uptake looks heterogeneous with the core being devoid of signal. Fig 5-16 also shows high uptake in the liver and some blood pool.

In this experiment, we were interested in assessing the accumulation of the tracer in the basal-like breast tumour overtime, and based on the previous findings from the optical imaging experiment, we decided to image four tumour bearing mice at 3h, 7h and 24h after injection of the tracer.

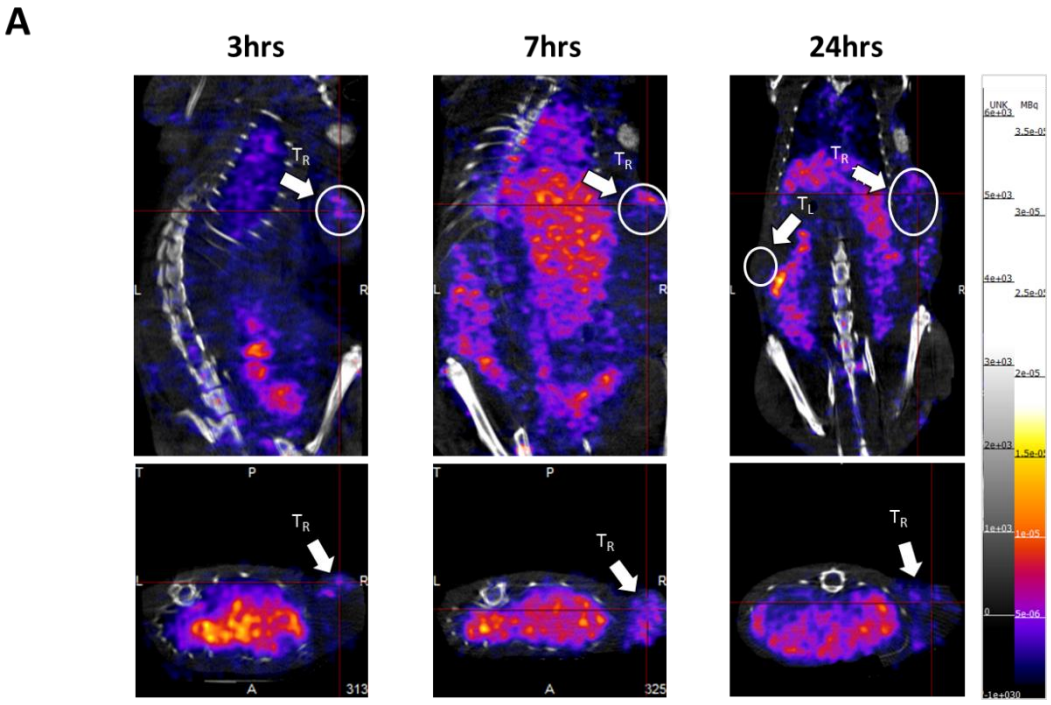

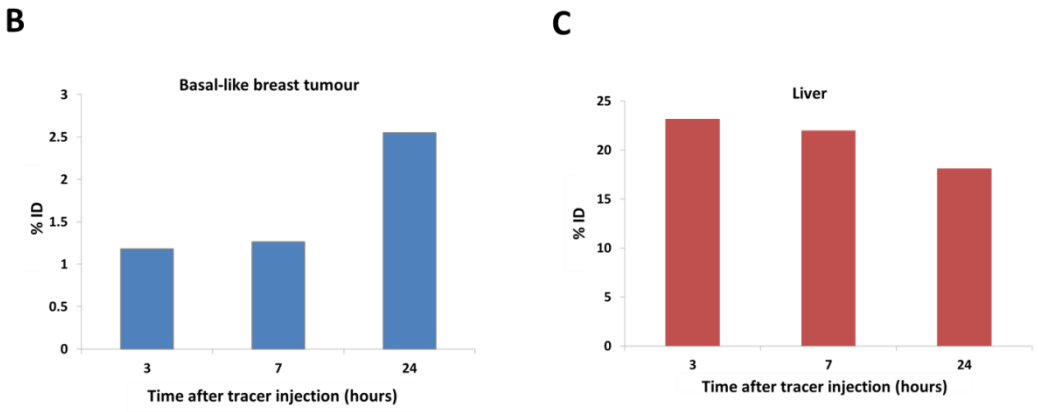

Figure 5-17. Accumulation of tumour uptake and decline in liver uptake in a representative tumour bearing mouse over time after injection of 111In-CHX-A''DPTA-scFv-Fc.

A) The coronal sections were displayed for all. Left panel: SPECT image at 3 hours post injection, middle panel: SPECT image acquired at 7 hours post injection, right panel: SPECT image acquired at 24 hours post injection. T_R represents the c-Met positive HCC1954 tumour while T_L represents the c-Met negative MCF-7 tumour. The SPECT signal is represented in a colour scale with yellow the most intense signal and blue the weakest signal. **B)** Quantification of tumour uptake in the same tumour bearing mouse, using SPECT data, showing accumulation in the tumour uptake over time **C)** Quantification of liver uptake in the same tumour bearing mouse, using SPECT data, showing decline in liver uptake over time.

As displayed in Fig 5-17, there is visible blood pool clearance overtime, with a clear decrease by 24h post injection of the tracer. The uptake at the liver slowly decreases overtime as observed in the bottom panel for each timepoint. There is visible uptake in the colon, as observed at 7h and 24h post injection. The uptake at the c-Met positive tumour is visible up to 24 hours after injection.

It was possible to quantify the uptake of the tracer across all timepoints for one tumour-bearing mouse and we detect a 2 fold increase in tumour uptake

from 7h and 24h post tracer injection (Fig 5-17B). In addition, we also observe a decline in the uptake in the liver, albeit slow. The uptake in the liver decreases by 5% injected dose (ID) between 3 to 24 hours after tracer injection (Fig 5-17C).

All 12 tumour-bearing mice were culled at the end of the imaging session, which was 25h post tracer injection. The organs, listed in table 5-2 were collected for ex-vivo Biodistribution study using the gamma counter. In addition, all the tumours were collected and were either snap-frozen or formalin fixed, and stored appropriately for further investigations.

Table 5-1. Organs collected from the 12 tumour bearing mice after the last imaging session has taken place.

Once the ex-vivo biodistribution had taken place, only the tumours were stored.

Organs collected after last imaging session		
Liver	Heart	Tumours
Spleen	Blood	Lungs
Kidneys	Bone	Stomach
Bladder	Muscle	Lymph nodes
Tail	Carcass	Intestines

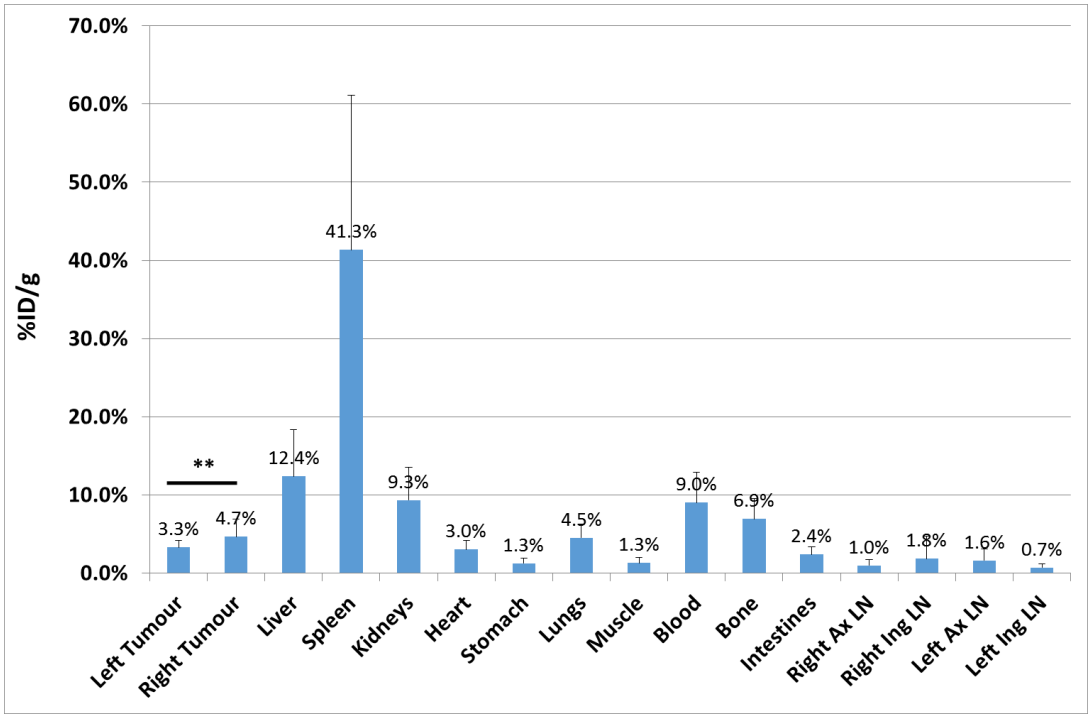

Figure 5-18. ^{111}In-CHX-A''-DPTA-scFv-Fc activity (% ID/g) from ex-vivo assay of dissected organs and tissue samples from HCC1954 tumor bearing mice, following SPECT imaging.

Organs were excised at 25h p.i. of the tracer on Day 32 post tumor inoculation. Gamma activity was quantified using the gamma counter 10 days after tracer's injection. Statistical tests include Student's t-test ($P<0.05$), mean ±SD.

The ex-vivo biodistribution data provide the quantitative information on the uptake of the tracer in different organs (Fig 5-18). We observed a high radioactivity level per gram in the spleen (41.3%ID/g), followed by the liver (12.4%ID/g), the kidneys (9.3%ID/g), the blood (9.0%ID/g) and the bone (6.9%ID/g). This trend was observed in the SPECT images. There was also some moderate uptake in the right c-Met positive tumour (4.7%ID/g), in the lungs (4.5%ID/g). Low uptake was observed in the c-Met negative left tumour (3.3%ID/g) and in the heart (3.0%ID/g). Minimal uptake was observed in the stomach (1.3%ID/g), and muscle (1.3%ID/g). We also observed a 1.4 fold increase in the HCC1954 basal-like tumour uptake in comparison to the

uptake in the c-Met negative MCF-7 tumour, which was statistically significant.

5.3 DISCUSSION:

In this chapter, we identified and validated a novel radiolabelled scFv-Fc that has the ability to bind to human c-Met and therefore detect tumours with high c-Met expression level. By using smaller antibody fragments with shorter serum half-lives, such as a scFv-Fc, PET can be performed at earlier time points with similar or even higher contrast than a full length antibody [254]. This is an important consideration as it is useful to minimise the amount of exposure of radioactivity in healthy tissues. Additionally, scFv-Fc fragment antibodies have the advantage of being compatible with many different immunoassays such as ELISA and immunoblots, unlike smaller fragment antibodies.

In this project, prior to the labelling, the scFv-Fc was selected from a phage display library, kindly donated by Prof McCafferty. Phage-antibody (and antibody-fragments) display libraries are a rich source of antibody diversity, supplying hundreds of unique antibodies per target [269]. The discovery and development of novel antibodies and fragments from a phage display library are faster than generating and screening hybridomas, which also involve the isolation of the antibody gene, their humanisation and the conduction of affinity maturation assays [254]. Our scFv-Fc of interest was expressed in the phage display vector pSANG4 which led to the production of scFv-Fc, as explained previously. This did not lead to the production of many subclones of scFv against human c-Met. To circumvent this issue, McCafferty's team engineered an additional Fc fusion to those clones, by expressing them into the vector pBIOCAM5, and performed another round of

panning in order to produce over 200 clones with specificity against human c-Met. In our study, it was useful to be given a scFv-Fc phage display library, rather than one made of scFvs. ScFv-Fcs offer bivalent binding and a long biological half-life to achieve higher signal-to-noise ratio [271].

Those scFv-Fc clones were transfected into HEK293 cells and their supernatant were collected and stained for the detection of the FLAG epitope displayed by the scFv-Fc using overexpressed c-Met MCF-7 cells. This led to the identification of 28 subclones which were then loaded on an agarose gel electrophoresis. We then identified 8 subclones with the highest ratio between the mean intensity of the scFv-Fc, from immunofluorescence and the expression level of scFv-Fc analysed via SDS-Page. Those subclones co-localised with cells that overexpressed c-Met. Rochefort et al performed SDS-PAGE of the clones that showed binding to the antigen of interest (detected by ELISA) to identify the expression level of their chimeric anti CA19-9 scFv-Fc and thereafter select the clones with the highest amount of scFv-Fc produced [272]. In our study, systematic immunostainings and SDS-PAGE were conducted for the clones that showed binding to human c-Met which were then narrowed down to the clones that showed highest specificity for human c-Met, relative to each other, with a good production level for the scFv-Fc.

Further immunostainings and dot-blot assays were performed for the selection of 1 subclone with high specificity for human c-Met and good level of expression for scFv-Fc. The *in-vitro* assays that were performed for this particular clone after the screen, miniprep and finally maxiprep consistently showed high affinity for human c-Met, with a good expression level for scFv-

Fc which made us confident in assessing its tumour targeting ability *in-vivo* using optical imaging initially.

Sequencing this subclone led to the identification of lysine residues that are necessary for Cy5 labelling. The production of this subclone was amplified and tested for specificity for human c-Met *in-vitro* prior and after Cy5 labelling before injecting it into mice. In this particular study, transient mammalian scFv-Fc expression was used due to the failure of generating producer cell lines. Due to the time scale given, transient mammalian scFv-Fc production seemed to be most suitable for this study and generated up to 0.02mg/mL from transfected HEK293 cells. However, if given the opportunity, the use of non-adherent HEK293-6E cells could have deemed very useful in this study as it has the ability to yield 10 fold more scFv-Fc than HEK293T cells [273]. In addition, the use of cationic polymer polyethyleneimine (PEI) ensured highly efficient plasmid delivery with low cytotoxicity and simple handling [274]. PEI contains a large number of protonable amino groups providing a high pH buffering capacity. This seems to protect the DNA from degradation in endosomal compartments, mediating an early escape of DNA/PEI complexes from lysosomes [275].

The use of a luciferase-tagged basal-like breast cancer cell line in mice enabled the localisation of the c-Met positive tumour via bioluminescence prior to acquiring fluorescent images for the *in-vivo* tumour targeting of the Cy5-labelled scFv-Fc. The signal emitted from the bioluminescence co-localised with the signal from the Cy5 labelled scFv-Fc. Although 2 out of 4 tumour bearing mice grew the HCC1954 tumours, detection with the optical tracer was only possible for the mouse with the biggest basal-like breast

tumour. In this tumour-bearing mouse, the Cy5-labelled scFv-Fc was able to specifically bind to overexpressed c-Met cells *in-vivo*. In addition, the low signal observed in the MCF-7 tumour *in-vivo* provided additional evidence for the optical tracer's specificity for human c-Met. The ex vivo biodistribution of the organs collected from the tumour-bearing animals at the end of the imaging session showed high intensity of fluorescence for liver, moderate intensity for the right kidney and the basal-like breast tumour, while the level of fluorescence intensity was very low for the c-Met negative MCF-7 tumours. Additionally, the ex vivo immunofluorescence staining performed on a frozen section of the HCC1954 and MCF-7 tumour tissues displayed the presence of the Cy5-labelled scFv-Fc and its co-localisation with the c-Met overexpressed cells from the c-Met positive HCC1954 tumour tissue. The MCF-7 tumour tissue did not display any staining with the optical tracer and c-Met was not detected in those sections ex vivo.

The results from the optical imaging experiment in mice demonstrated specificity of the scFv-Fc to human c-Met and additionally showed that our scFv-Fc had the sensitivity to detect endogenous levels of c-Met within our basal-like breast cancer. This is a very exciting finding as optical tracers that bind to human c-Met with high affinity are clinically needed. There has been a study conducted by Kim et al that investigated the use of a Cy5.5 labelled c-Met binding peptide, with the addition of a lipophilic carbon linker, with nanomolar specificity to c-Met in glioma [276]. The latest study on optically labelled c-Met involved the use of c-Met binding peptide conjugated with a fluorescent cyanine dye, GE-137. This fluorescently labelled c-Met binding peptide, GE-137, showed specific targeting of overexpressed c-Met tumour

cells, allowing for the detection of polyps in colorectal cancer patients, that were not visible by light alone [213]. Following this successful study, Purushotham et al are currently conducting a pilot study of intraoperative GE-137 fluorescence imaging with the aim of improving the accuracy of surgical excision of tumours in breast and oral cancer patients [277].

Despite the limited applications of optical imaging in comparison to nuclear medicine, due to tissue scatter, absorption of photons in the visible range and potential autofluorescence [278], optical tracers can be used in endoscopy, laparoscopy, and the intraoperative setting for the detection of superficial lesions. Hence, the identification of an optical tracer against human c-Met with a combination of a high tumour targeting ability, relatively fast clearance kinetics and good safety profile would attract attention for further investigations in the clinic.

Due to the restricted depth of penetration of the optical tracer, we decided to radiolabel the scFv-Fc with Indium-111 (In-111), via conjugation to the chelator CHX-A''-DTPA for use in SPECT imaging. A bifunctional chelator was used as it would form highly stable complexes with the radioisotope In-111 and hence minimise the risk for non-target uptake in the subject [279]. The use of the HPLC system with a SEC column enabled identification of the retention time at which the scFv-Fc would be eluted and assessed its purity after labelling. The retention time for the radiolabelled scFv-Fc, identified by the UV detector, matched with the retention time detected by the gamma detector which implies that the scFv-Fc was successfully radiolabelled. This conjugate (that has the chelator CHX-A''DTPA), was then tested *in-vitro* and was found to retain its specificity for human c-Met in overexpressed c-Met

cells. In addition to this, the serum stability test showed stability and integrity of the scFv-Fc in human serum at body temperature up to 24hours after incubation.

This successful chemical conjugation led to the final imaging experiment using the SPECT imaging modalities. Instead of injecting 50 microgram of the radiolabelled c-Met binding scFv-Fc per mouse (used in the optical imaging experiment), we opted for a lower dose (20 micrograms) due to concerns that the non-radiolabelled 'cold' scFv-Fc would compete with the radiolabelled tracer, potentially reducing the detection of overexpressed c-Met cells. The SPECT imaging of 4 tumour-bearing mice with dual subcutaneous inoculation for the c-Met positive basal like breast tumour and the c-Met negative adenoma carcinoma tumour displayed increased uptake of the radiolabelled scFv-Fc in the basal-like breast tumour. In addition, the quantification of the uptake of the radiolabelled scFv-Fc in the HCC1954 tumour in one of the tumour bearing mice showed a 2-fold increase from 3 to 24 hours after injection of the tracer. In parallel, we observed a decline in the uptake in the liver, suggesting that the uptake in the c-Met positive tumour was specific. The results from the ex-vivo biodistribution assay corresponded with the data acquired from the SPECT images, displaying a high amount of activity in the liver, and suggested hepatobiliary clearance, which is expected in antibody fragments with a molecular weight of 60 kDa or above [279]. We also observed a moderate uptake in the kidneys, which suggests clearance of the tracer. However, at this specific timepoint, there was moderate uptake in the blood and heart which suggests that the tracer had not yet been fully

cleared. It also suggests that the optimal tumour to blood ratio would occur later than 24 hours post injection.

To date, no other radiolabelled scFv-Fc against human c-Met used in SPECT imaging has been designed. Jacoda et al investigated the use of a c-Met binding peptide that has been radiolabelled with Tc-99 and showed good tumour targeting. This tracer showed a tumour uptake (in high c-Met expresser MNK-45 tumours) of 10.13 %ID/g 30 minutes after injection, which decreased considerably (by 46% and 63% respectively) after 2 and 3 hours post injection of the tracer [280]. A very high uptake in the kidneys was observed at all timepoints and suggested clearance of the tracer. The major weakness in this study was the high uptake in the kidneys, masking potential metastatic lesions in these organs and the rather short half-life of the radioisotope, preventing the use of this tracer for the monitoring of therapeutic treatments.

Despite the lower dose of radiolabelled scFv-Fc administered to the mice in comparison to the optical tracer, the tumour targeting ability of the radiolabelled scFv-Fc was not compromised. This might suggest that the higher dose applied in optical imaging was due to Cy5 labelling reaction stopping before complete labelling is achieved. This led to a certain population of scFv-Fc not carrying a Cy5 dye and therefore resulting in the use of a higher dose of optical tracer [281]. Another explanation for a higher dose of the optical tracer could be due to variable tissue attenuation of the fluorescent signal [280].

Surprisingly, despite the administration of oestrogen pellets, the MCF-7 tumours did not grow as quickly as expected, and therefore did not reach the size of the HCC1954 tumours. Although it was clear that the uptake of the radiolabelled scFv-Fc was low in MCF-7, it would have been better to compare the positive and negative tumours of a similar size. Additionally, one can recommend the use of a c-Met knockdown HCC1954 cell line as a c-Met negative tumour in our xenografts. This cell line is currently being developed in our laboratory.

It would have been informative to identify the biological half-life of the scFv-Fc by performing a longer timepoint experiment which would require extra SPECT scans at 48 and 72 hours. It would also be informative to perform an ex-vivo biodistribution study at various timepoints, alongside the timepoints selected for the SPECT imaging.

Additionally, future studies would require the injection of the radiolabelled scFv-Fc into a naïve mouse to assess its pharmacokinetics. It would also be useful to assess the trajectory of free In-111 in a tumour bearing mouse to assess potential non-specific binding sites.

Future studies include the identification of the values for the binding affinity (K_d) for the In-111 labelled scFv-Fc via ELISA for example. Additionally, it would be important to assess any possible off-target effects *in-vitro* and *in-vivo*. Future research also includes the mutation of the Fc constant in order to decrease the half-life of the scFv-Fc in serum. This type of mutation has already been performed before by Kenanova et al, who modulated the half-life of carcinoembryonic antigen (CEA) scFv-Fc by mutating their Fc-FcRn

binding site. Five mutants were engineered and biodistribution studies revealed the half-life in the mutants to range from 83.4 to 7.96 hours, while the wild types displayed a half-life of 12 days. The mutant with the shorter half-life demonstrated a rapid tumour targeting and a better signal:noise ratio, in comparison to the other mutants and wild type [202, 282].

The high uptake of the ^{111}In-CHX-A''DTPA-scFv-Fc in the bone, spleen and liver was also observed in another study, in which the tracer was labelled with indium-111 [265]

These findings derived from the use of ^{111}In-CHX-A''DTPA-scFv-Fc against human c-Met in a basal-like breast cancer model using SPECT imaging are promising. Compared with traditional biopsy and immunohistochemistry, antibody-fragment-based Single Photon Emission Computed Tomography offers a unique opportunity to assess the *in-vivo* expression levels of various biomarkers. Importantly, c-Met molecular imaging in basal-like breast cancer patients will enable a more personalised treatment strategy for each patient. The existence of a highly specific and selective tracer, with a favourable rate of clearance will have a favourable impact on the management of patients through the use of SPECT and PET imaging modalities. These types of imaging agents could be used to monitor a patient's response to neoadjuvant chemotherapy or anti-c-Met therapies in basal-like breast cancer as it provides a direct readout for c-Met expression level *in-vivo*.

Chapter 6: Effect of PTPN11 knockdown in EGFR and c-Met phosphorylations in basal-like breast cancer

6.1 Introductory section:

Over the past decades, much effort was devoted into developing effective and safe tyrosine kinase inhibitors (TKIs). In particular, TKIs against EGFR and c-Met have been designed to target basal like breast cancer [56, 283]. Indeed, cetuximab, an epidermal growth factor receptor (EGFR) inhibitor has been tested in 102 patients with stage IV TNBC. They were given cetuximab and carboplatin on a weekly basis. Despite the combination being well tolerated, it produced a response in fewer than 20% of patients. Biopsies revealed that most TNBcs had EGFR activation after treatment which implies the existence of alternate mechanisms that do not depend on ligand-dependent EGFR-mediated activation [17].

A recent study has shown that Met amplification was responsible for acquired resistance to first-generation EGFR TK inhibitors in up to 20% of EGFR-mutant NSCLCs [284]. Another study also revealed that MET amplification is causative for the acquired resistance to anti-EGFR monoclonal antibodies cetuximab and panitumumab in metastatic colorectal cancers [25]. Lately, a preclinical study was conducted to investigate the

efficacy of targeting c-Met in overcoming resistance to EGFR therapy in TNBC cell lines. They successfully demonstrated the efficacy of a combination of EGFR and c-Met inhibitors in TNBC cell lines that have functionally active ligand-receptor-downstream signaling pathways [285].

De-regulation of EGFR and/or c-Met expression or signaling has been implicated in cancer progression [69, 90]. The dysregulated expression of upstream receptors and kinases can result in the activation of the Ras/Raf/MEK/ERK, Ras/PI3K/PTEN/Akt/mTOR and other signaling pathways. These can contribute to malignant transformation [286]. Approximately 30% of breast cancers over express EGFR and this correlates with poor prognosis [287, 288] and over half of the cases of triple-negative breast cancer (TNBC) overexpress EGFR [289], which is higher than the rates observed in other breast cancer subtypes [31].

The EGFR signalling pathway is mentioned in greater detail in the introduction of this thesis (section 1.3.3). Greater focus will be given on the Tyr 1173 phosphorylation site of EGFR in this chapter, which is a site for EGFR autophosphorylation [290]. Upon EGF stimulation, phospho-Tyr 1173 binds to the cytosolic signalling molecules SHC and Grb2 which leads to ERK activation [291, 292] through the EGFR–SHC–Grb2–SOS–RAS–RAF–MEK–ERK pathway (SOS, son of sevenless) [293]. Phospho-Tyr 1173 also is the main binding site for SHP1, which results in the reduction of EGFR-dependent ERK activation [294]. Hochgrafe et al showed that EGFR Y1173 phosphorylation is significantly higher in the basal-like breast cancer in comparison to other subtypes of breast cancer [69].

c-Met, a receptor that binds to its ligand HGF, also named as scatter factor, is overexpressed and upregulated in the basal like breast cancer cell lines [69-73]. c-Met has the ability to promote breast cancer motility, invasion, metastasis and *in-vivo* tumourigenesis [235]. A strong link between c-Met overexpression and poor survival in BC patients, and more particularly TNBCs exists [75]. c-Met inhibitors are being developed and discussed in more details in section 1.2.2 of this thesis. A recent study conducted by Watermann et al showed the detection of c-Met phosphorylation at Y1234/1235 in 14% of the investigated NSCLC tumour samples [295]. Another study conducted by Hochgräfe et al demonstrated an increased c-Met phosphorylation in the basal-like subtype in comparison with other breast cancer subtypes [69]. The tyrosine residues Y1234 and Y1235 get transphosphorylated, following HGF binding to the extracellular portion of c-Met, which in turn leads to the transphosphorylation of another two tyrosine residues Y1349 and Y1356, located in the C-terminal region. The latter create a multisubstrate docking site which would bind to numerous substrates (e.g. Grb2, Gab1) enabling the activation of a wide range of signalling pathways [296]. These include the MAPK cascade pathway, via Gab1-Shp2-Ras [58, 297], Grb2-SOS-Ras [298] or SHC-Grb2-SOS-Ras [299], the PI3K pathway and the activation of STAT3 [296] which modulate motility, migration, cellular proliferation, invasion and tubulogenesis [56, 60].

EGFR deregulation observed in many cancers, including basal like breast cancer can be a by-effect of other oncogenes. Here, in this chapter, we will be focusing on the phosphatase PTPN11. It has been shown that PTPN11

regulates RTK expression and signalling in BTBC, which suggests its potential involvement for targeted therapy in BTBC [300]. Additionally, recent reports suggest PTPN11 plays a role as an EGFR regulator, by promoting Ras activation through blocking the Ras GTPase-activating protein (RasGAP)-induced downregulation of Ras, via dephosphorylation of the docking site Tyr992 on the EGFR [143]. Additionally, the SH2 domain-containing phosphatases Shp1 (PTPN6) and Shp2 (PTPN11) are recruited to activated EGFR and promote its dephosphorylation in a negative feedback loop [301]. Reports show an upregulation for PTPN11's expression in breast cancer [302] and a positive role in breast cancer cell transformation [140].

In this project, siRNA and shRNA-based inhibition studies will be conducted in order to show the importance of PTPN11 in BLBC and its relation to c-Met and EGFR's phosphorylation status, expression level and cellular proliferation rates.

Lastly, due to the aggressive nature of BLBC, and the ability for EGFR to promote epithelial-mesenchymal transition (EMT) by the activation of ERK and the induction of an EMT transcription factor, ZEB1 [293], the level of expression for the EMT marker e-cadherin [303, 304] will be assessed in the control and PTPN11-silenced cells in this project. EMT is the morphologic switch from a polarised epithelial phenotype to a mesenchymal fibroblastoid phenotype [305]. EMT plays a vital part in tumour progression [306]. E-cadherin, a 120 kDa glycoprotein, is required for the maintenance of stable junctions. Indeed, in epithelial cells, early contacts are mediated by e-cadherin molecules that cluster into small junctional complexes which then

expand to establish stable adherens junctions, forming desmosomes [307]. The loss of e-cadherin increases tumour cell invasion and migration. The expression of e-cadherin is also inversely correlated with tumour grade and stage [308].

6.2 RESULTS:

6.2.1 PTPN11 is an EGFR regulator

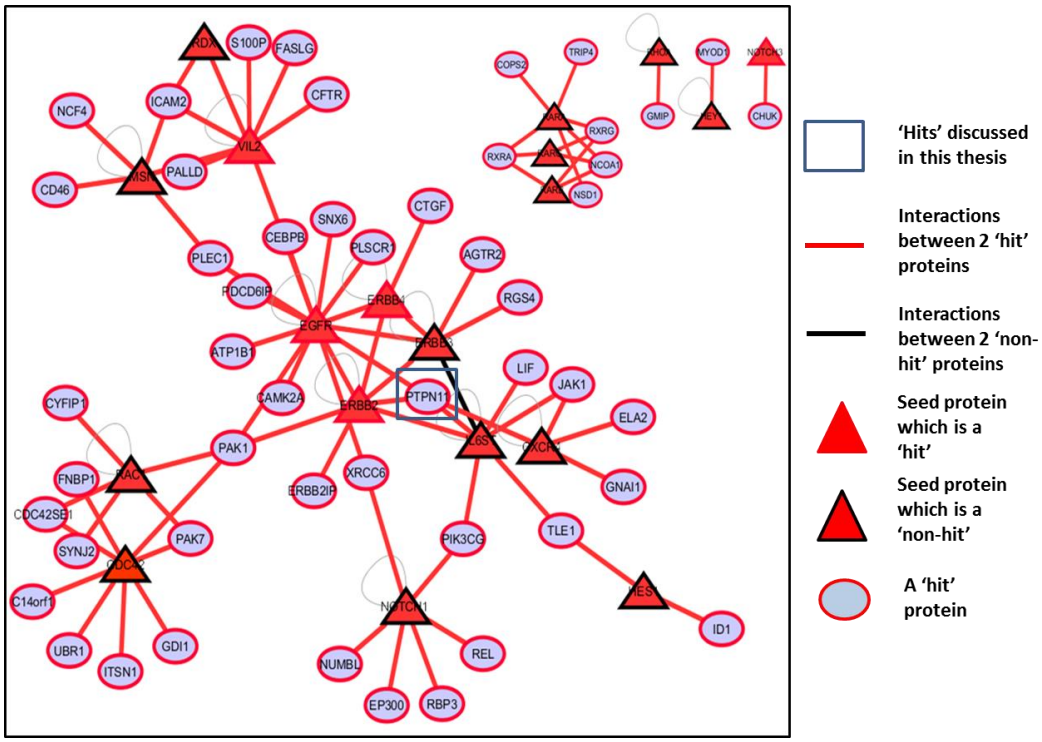

Figure 6-1. Protein Interaction Network Analysis of proteins that interact with EGFR.

The selection of a 533 gene based siRNA screen was taken from the interaction of seed proteins (including EGFR, triangular shaped) to other proteins that were reported as having a binary interaction with the seed proteins up to the second neighbour. The selection of seed proteins was based on their importance in processes related to cancer cell migration, proliferation and stemness. A hit is a protein whose knockdown abolishes EGF-dependent increase in EGFR activity or causes a constitutively activated baseline. Cytoscape was used to visualise those 14 seed proteins (shown as red triangular nodes) that can be 'non-hit' (nodes outlined in black) and connected to 'hit' proteins (nodes outlined in red). Red edges represent protein-protein interaction between a 'hit' protein and another protein (which could either be a 'hit' or a 'non-hit'). Black edges connect two 'non-hits'. HPRD database enabled to identify all the proteins with a binary-binary interaction with the seed proteins, as explained in Section 1.3.5. Please see for a more

detailed description of the bioinformatics basis of this in-house network-based siRNA screen design [116, 117].

A siRNA library that consisted of 533 genes interconnected with EGFR was used to identify proteins affecting the EGFR signalling pathway. In this screen, a sensor was used to conduct this high-content FLIM screen. The screen was performed by Anthony Cheung (a former student of Professor Ng). Briefly, EGFR catalytic activity in cells was measured by using a FRET biosensor known as Picchu (Phosphorylation Indicator of Crk Chimeric Unit) [309]. The Picchu biosensor has been modified in our laboratory to express mRFP1 and eGFP fluorescent proteins to make it suitable for FRET quantification by Fluorescence Lifetime Imaging Microscopy (Picchu-FLIM, similar to our previously published Raichu-FLIM [116, 310, 311]).

Each protein knockdown was compared to the readout provided by its respective control. Using appropriate statistical tests, those proteins were either classified as ‘hits’ (whose knockdown abolish EGF-dependent increase in EGFR activity or constitutively activated baseline) or non-hits. Figure 6-1 displays the interaction found between the ‘hits’ or between protein seeds (regardless of them being a hit) and hits, identified after the screening of 320 proteins. ‘Non-hits’ seed proteins (triangles outlined in black) were also included. The interactions observed between the nodes, via an edge, were established based upon literature search. These interactions can be either direct (observed via a Yeast 2 hybrid for example) or indirect (observed via SILAC) [145].

PTPN11, a phosphatase, was identified as a 'hit' (figure 6-1) from this siRNA screen, implying that PTPN11 has an effect on EGFR signalling. Despite a previous study suggesting PTPN11's potential interaction with EGFR [145], it is the first time that we observe this interaction in the basal-like breast cancer cells, HCC1954.

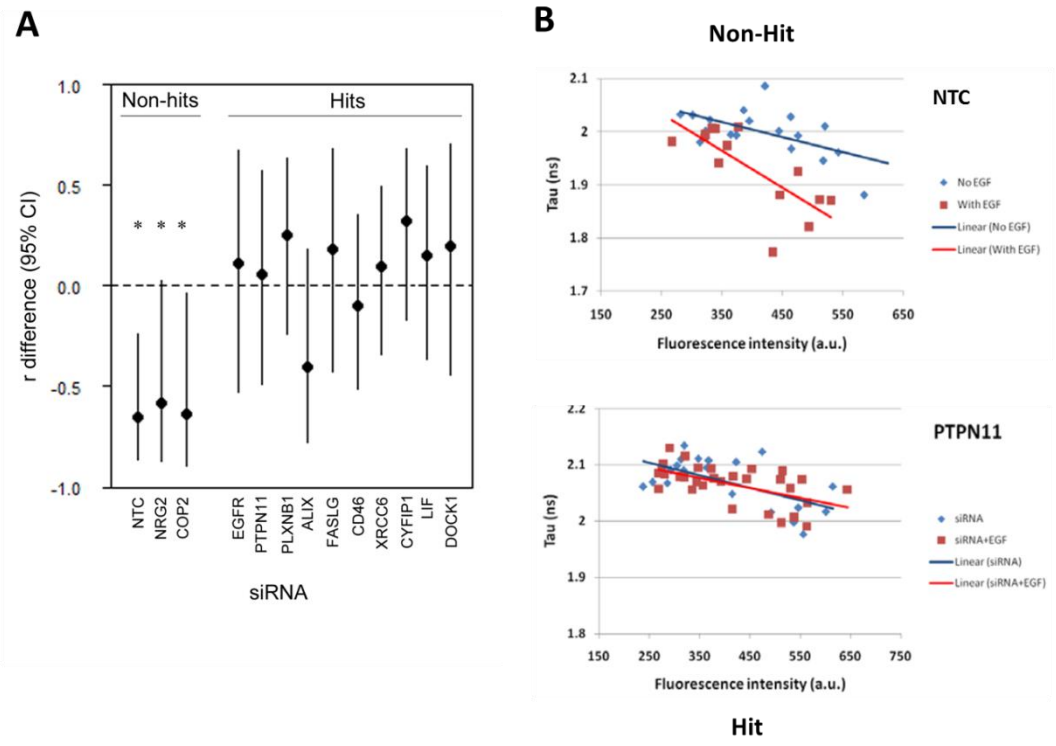

Figure 6-2. (A) Plot summarizing differences in the Pearson correlation coefficients (r) obtained from lifetime–intensity data for EGF-treated and non-treated cells for each of the indicated siRNA experimental groups.

Pearson correlation coefficients and associated confidence intervals were obtained to assess correlation between intensity and tau for each siRNA group both with and without EGF stimulation. To determine the effects of EGF treatment on biosensor activity for a given siRNA experimental group, the difference between r values obtained for tau vs. intensity data in EGF-treated and -untreated subgroups was computed (filled circles). Fisher's r-to-z transformation statistics was used to

estimate confidence intervals (bars) for the differences in r. (B) Fluorescence lifetime–intensity scatter plots and associated regression analysis of four example siRNA experimental groups where cells were treated with or without EGF. Each data point represents a single cell and shows the mean fluorescence lifetime plotted against the mean fluorescence intensity for that cell. Pearson correlation coefficients were obtained to assess the association between lifetime and intensity for the EGF-treated (red) and non-treated (black) subgroups, and the difference in the resultant r values then used to evaluate the effects of target protein knockdown on EGFR activity (as summarized in B).

The Picchu-X sensor was a direct target for EGFR kinase activity and was used to assess the FRET efficiency (explained in more details in Section 1.3.5) changes upon stimulations with EGF. In order to assess whether the knockdown of a protein had an effect on EGFR, FRET-FLIM imaging of Picchu-X sensor in individual basal-like breast cancer cells, transfected with a specific siRNA, was used to study the regulation of EGFR activity on a single cell level. Once the FLIM acquisition was performed, the fluorescence lifetime was calculated and as expected, EGF had a significant effect on tau in cells transfected with non-targeted siRNA (Figure 6-2A). However, Figure 6-2B does not show a change in the FRET efficiency independently of the effect of intensity (which can cause intermolecular quenching; which is different from EGF-dependent fluorescence lifetime quenching of the eGFP donor fluorophore, owing to an intramolecular association between the phosphorylated residue on the Crk-based sensor and the SH2 domain, bringing the eGFP and mRFP1 of the sensor to closer proximity), after EGF stimulation in cells that were transfected with siPTPN11. Therefore the knockdown of PTPN11 abolished the EGF-induced activation of EGFR (Cheung et al, publication under submission).

Prior to investigating the effect of PTPN11 knockdown on the HCC1954 basal-like breast cancer cells, it was necessary to determine the optimal timepoint for the EGF and HGF stimulation in those cells, as those ligands will be used to investigate the EGFR and c-Met signalling pathways in this project.

6.2.2 Optimal timepoint for EGF stimulation in basal-like breast cancer cells

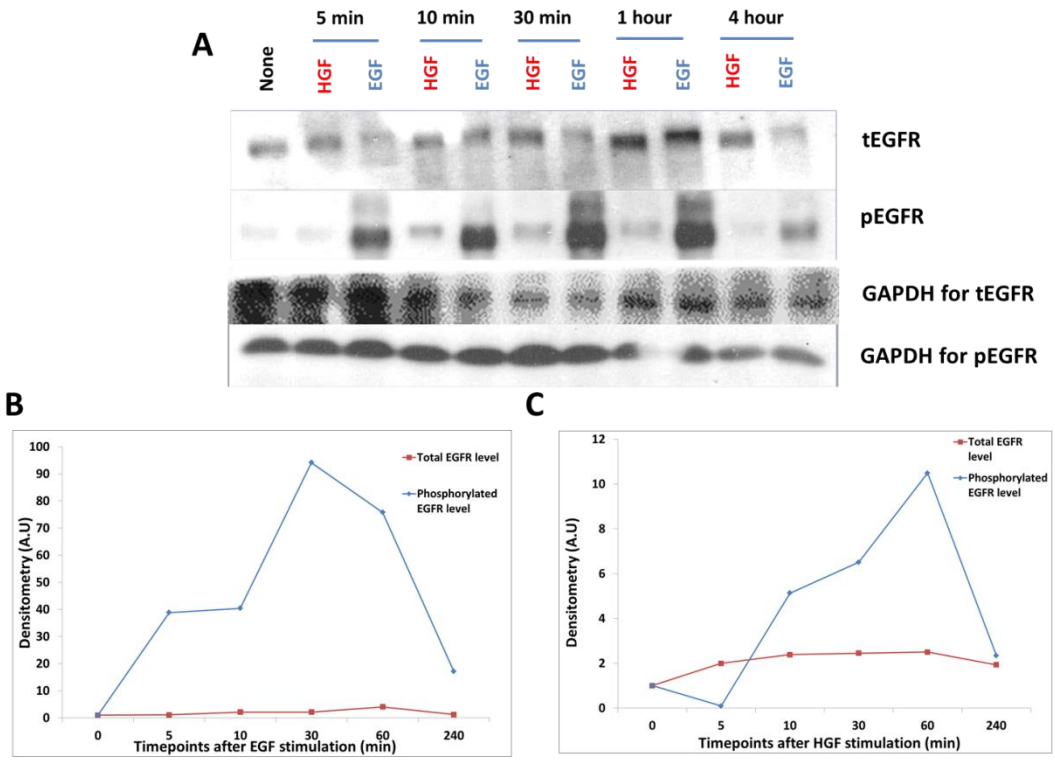

Figure 6-3. Optimisation of EGF and HGF stimulation in HCC1954 cells.

(A) Immunoblot displaying the expression level for total and phosphorylated EGFR at their basal level and after EGF (100ng/ml) or HGF (50ng/ml) stimulation from 0 to 4 hours. **(B)** Analysis of western blot data via densitometry for total and phosphorylated EGFR level after EGF stimulation **(C)** and after HGF stimulation

from 0 to 4 hours. Red line represents the phosphorylated EGFR expression level while the blue line represents the total EGFR expression level.

Figure 6-3 (A&B) shows a sharp increase in phosphorylated EGFR from 0 to 5 minutes after EGF stimulation, with a 38 fold increase in comparison to basal level, followed by a slower increase from 5 to 10 minutes after stimulation and another sharp increase from 10 to 30 minutes, at which point it reached its peak (94 fold increase to basal level). It was then followed by a small decline in the amount of phosphorylated EGFR from 30 to 60 min which was then followed by a sharp decrease up to 4 hours after stimulation. At 4 hours post EGF stimulation, the amount of phosphorylated EGFR was 17 fold higher than the basal level, but dramatically lower than the levels observed at 30 and 60 minutes after EGF stimulation. It was also interesting to observe the slight but noticeable increase (5 fold higher than what was observed at basal level) in phosphorylated EGFR 10 minutes after HGF ligand stimulation in the HCC1954 cells (Figure 6-3 C). This was then followed by a steady decrease in the expression level of phosphorylated EGFR which then reached ‘basal’ level 4 hours after HFG stimulation.

The expression level for total EGFR did not fluctuate as much as the expression level for phosphorylated EGFR after EGF stimulation, which was expected (Fig 6-3B), although some small increase was observed 60 minutes after EGF stimulation. Additionally, the level of expression for total EGFR after HGF stimulation was rather consistent across all timepoints, albeit a very small increase at 5 minutes which remained relatively constant up to 60 minutes after HGF stimulation (Fig 6-3C).

It was possible to identify 30 minutes as the optimal timepoint for EGF stimulation for EGFR phosphorylation. On the other hand, despite the increase in EGFR phosphorylation after HGF stimulation at 60 minutes, the increase was very slight if we were to compare to the expression level observed between 10 to 60 minutes after HGF stimulation. This implied that the optimal timepoint for HGF stimulation to assess EGFR phosphorylation can be between 10 to 60 minutes (Fig 6-3).

Following the identification of the optimal timepoints for EGF ligand, the next step was to investigate the effect of PTPN11 knockdown on EGFR phosphorylation in our cell line of interest.

6.2.3 EGFR hyperphosphorylation in PTPN11-silenced cells

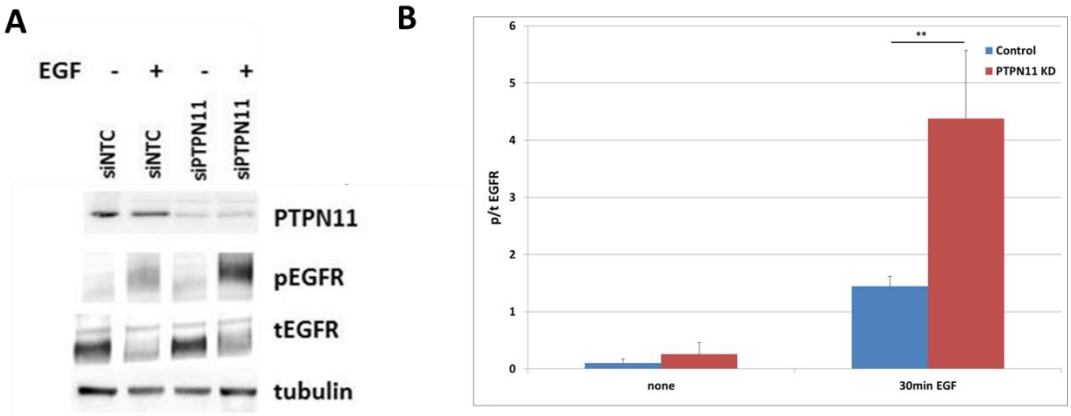

Figure 6-4. EGFR hyperphosphorylation following EGF stimulation in PTPN11-silenced cells as compared to control (NTC: Non-targeted Cells).

(A) Immunoblotting displaying the expression level of total EGFR and phosphorylated EGFR before and after 30 minutes of EGF stimulation in control vs PTPN11-silenced cells. A clear knockdown for PTPN11 is observed in the PTPN11-silenced cells, through a transient transfection using a siRNA smart pool against PTPN11. **(B)** Analysis of western blot data via densitometry for EGFR phosphorylation in both the controls and PTPN11-silenced cells before and after EGF stimulation. Data are the mean values ± S.E.M., over 3 independent experiments; *= $P < 0.05$.

Figure 6-4 shows a clear increase in EGFR phosphorylation in the PTPN11-silenced cells. There is a significant ($P < 0.5$) and a 3 fold increase in the phosphorylation of EGFR in the EGF-stimulated PTPN11-silenced cells in comparison to the EGF-stimulated control cells. There was an obvious difference in EGFR phosphorylation between the unstimulated cells and the EGF-stimulated cells in both the controls and the PTPN11-silenced cells, however, the difference was significant in the PTPN11 knockdown cells. Another observation extracted from this figure was that the basal level of phosphorylated EGFR in both the controls and the PTPN11 knockdown cell line was very similar (Figure 6-4B).

Since we observed a clear hyperphosphorylation of EGFR in the PTPN11 silenced cells 30 minutes after EGF stimulation, we were interested in assessing EGFR phosphorylation for a longer period of time (which was up to 60 minutes after EGF stimulation) and identify any potential changes.

6.2.4 Defect in EGFR dephosphorylation in PTPN11-silenced cells

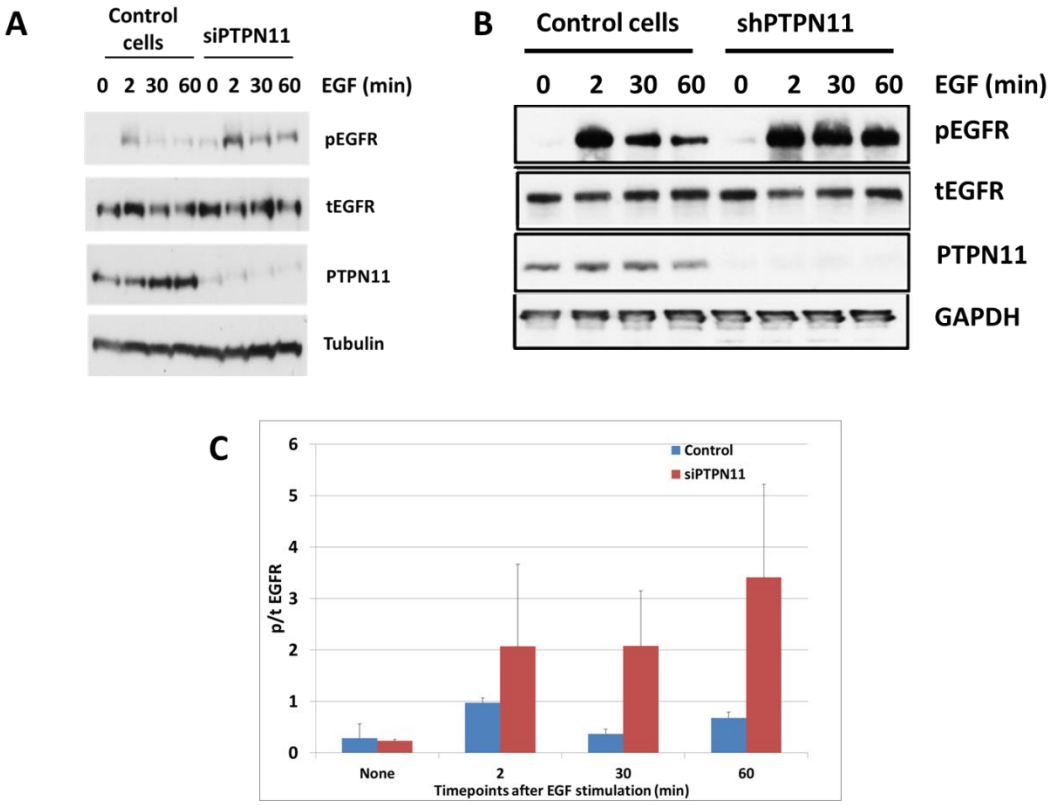

Figure 6-5. Defect in EGFR dephosphorylation in PTPN11-silenced cells in comparison to the control basal-like breast cancer cells.

(A&B) Immunoblot to assess EGFR phosphorylation status in the control cells versus the PTPN11-silenced cells (siRNA for panel A and stable transfection for panel B) over the course of 60 minutes after EGF stimulation. Level of total EGFR and phosphorylated EGFR were probed. PTPN11 was successfully knockdown in the PTPN11-silenced cells. Tubulin shows even loading across the lysates. **(C)** Analysis of western blot data via densitometry for EGFR phosphorylation at 2, 30 and 60 minutes after EGF stimulation in the control and PTPN11-silenced cells. Data are the mean values ± S.E.M., over 2 independent experiments.

In Figure 6-5, we assessed EGFR phosphorylation up to 1 hour after EGF stimulation in both the control and PTPN11 silenced cells. As observed, there was an obvious hyperphosphorylation of EGFR 2 minutes after EGF stimulation in the PTPN11 silenced cells, which was 2 fold higher in comparison to the control cells at the same timepoint. The level of phosphorylated EGFR, in the PTPN11-silenced cells, remained the same 30 minutes after EGF stimulation and showed a 70% increase 60 minutes after EGF stimulation in comparison to the level displayed at 30 minutes in the PTPN11 silenced cells. On the other hand, the control cells showed a peak in EGFR phosphorylation 2 minutes after EGF stimulation, which was then reduced to basal level at 30 minutes post EGF stimulation and a very slight increase at 60 minutes after EGF stimulation.

In comparison to the control cells, the PTPN11 silenced cells displayed an EGFR hyperphosphorylation that was 4 fold higher at 30 minutes and 60 minutes after EGF stimulation in comparison to the control cells at those timepoints (Fig 6-5).

Lastly, this figure suggested a defect in EGFR dephosphorylation, as it took longer for EGFR to be dephosphorylated in the PTPN11 silenced cells in comparison to the control cells.

Since high levels of EGFR had been associated with aggressive biological behaviour and adverse clinical outcome (PMID: 9625170), we found it necessary to assess the expression level of total EGFR in the PTPN11-silenced cells and compare it to the control cells to identify potential changes.

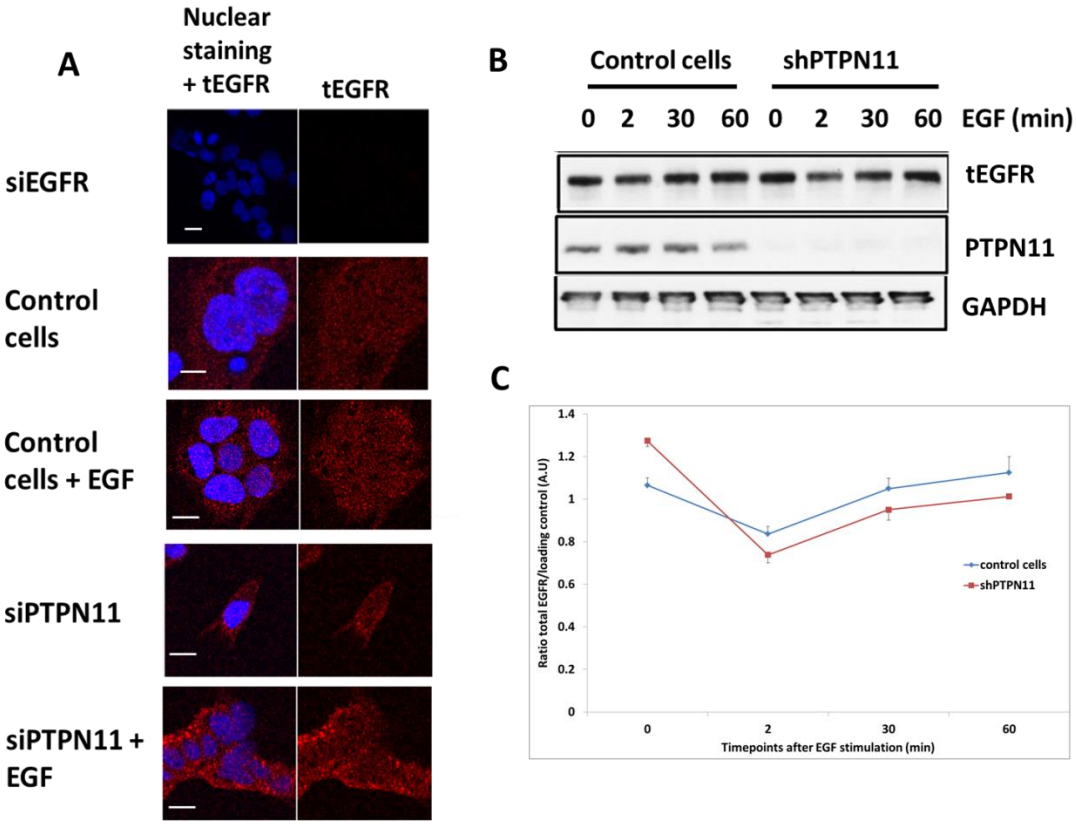

Figure 6-6. Expression level for total EGFR in the controls and PTPN11 silenced cells before and up to 60 minutes after EGF stimulation.

(A) Confocal sections of basal-like breast cancer cells (with transient transfection) stained for total EGFR (red) and DAPI (blue). Cells were starved overnight, stimulated or not with EGF ligand. Scalebar: 20µm **(B)** Immunoblot to assess the expression level for total EGFR in the control cells versus the PTPN11-silenced cells over the course of 60 minutes after EGF stimulation. Tubulin shows even loading across the lysates. **(C)** Analysis of western blot data via densitometry for total EGFR level across after EGF stimulation. Data are the mean values ± S.E.M., over 3 independent experiments.

We used cells that were transiently transfected with siEGFR to confirm the specificity of the staining for total EGFR (Fig 6-6A – top image). As expected, anti-EGFR did not stain cells that were transiently knockdown for EGFR. We

observed a clear cytoplasmic and membranous staining for total EGFR in the control cells, before and after EGF stimulation. We also observed a cytoplasmic and a more distinct membranous staining in the PTPN11-silenced cells (Fig 6-6A). In the control cells, we observed a 21% increase in the level of expression for total EGFR two minutes after EGF stimulation in comparison to its basal level and this is followed by a 19% increase (in comparison to previous timepoint) at 30 minutes after EGF stimulation before another slight increase at 60 minutes after EGF stimulation. On the other hand, a major reduction (42% decrease) in the total EGFR expression level in the PTPN11-silenced cells occurred two minutes after EGF stimulation (in comparison to its basal level) which was then followed by a sharp increase in the total EGFR expression level at 30 minutes (16% increase in comparison to the previous timepoint) after EGF simulation over time and a slight increase at 60 minutes after EGF stimulation (an additional 5% increase in comparison to the total EGFR expression level at 30 min post EGF stimulation). It was also interesting to see a higher basal level for total EGFR in the PTPN11-silenced cells in comparison to control cells.

In addition to assessing the effect of PTPN11 silencing on the EGFR signalling pathway, we also wanted to assess the effect of PTPN11 knockdown on the c-Met/HGF axis due to the potential synergy between both pathways observed in many reports [312]. We were interested to investigate and compare c-Met phosphorylation in the PTPN11-silenced cells in comparison to the control cells.

6.2.5 c-Met hyperphosphorylation in PTPN11-silenced cells

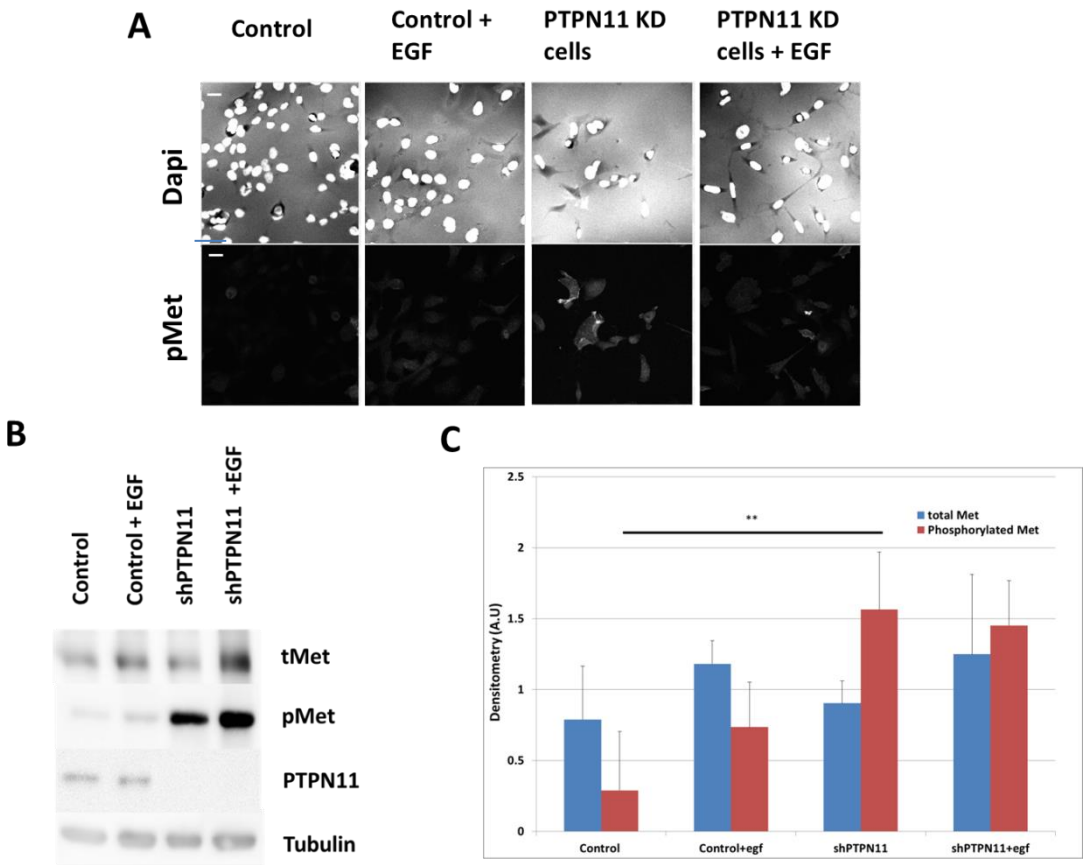

Figure 6-7. c-Met hyperphosphorylation in PTPN11-silenced cells

(A) Fluorescent staining for nucleus (top) and phosphorylated c-Met (bottom) in control cells and PTPN11-silenced cells before and after EGF stimulation. Scalebar: 60µm **(B)** Immunoblot assessing the expression level of phosphorylated c-Met and total c-Met in the control and PTPN11-KD cells. Tubulin was used as a loading control. **(C)** Analysis of western blot data via densitometry for c-Met phosphorylation in both the control and PTPN11-KD cell lines, before and after EGF stimulation. Data are the mean values ± S.E.M., over 3 independent experiments; *= $P < 0.05$.

Figure 6-7A provides evidence for c-Met hyperphosphorylation in the PTPN11-silenced cells. Indeed, the immunofluorescence staining clearly shows a stronger intensity staining for phosphorylated c-Met in the PTPN11-

silenced cells in comparison to the control cells with and without EGF stimulation. This is also observed by Western Blot in Figure 6-7B, where there is a clear increase in c-Met phosphorylation in the PTPN11 silenced cells. Quantifying the bands from the western blot showed a 8 fold increase in phosphorylated c-Met in the unstimulated PTPN11 knockdown cells in comparison to the unstimulated control cells. This difference was significant ($P < 0.05$). We observed an increase in the expression level for phosphorylated c-Met in the EGF-stimulated control cells in comparison to the unstimulated control cells, although statistically non-significant. We also observed a greater increase in c-Met phosphorylation in the EGF-stimulated PTPN11 knockdown cells in comparison to the EGF-stimulated control cells, which was not statistically significant. Finally, we observed a rather similar expression level for phosphorylated EGFR in the EGF-stimulated and unstimulated PTPN11-silenced cells.

Similarly to the way total EGFR expression level was assessed in the control and PTPN11-silenced cells (with and without EGF stimulation), we thought it useful to assess the level of total c-Met in those sets of cell lines as the overexpression of c-MET was shown to contribute to the development of an invasive phenotype in the progression of breast cancer [313].

6.2.6 Total c-Met level increased in PTPN11 knockdown cells

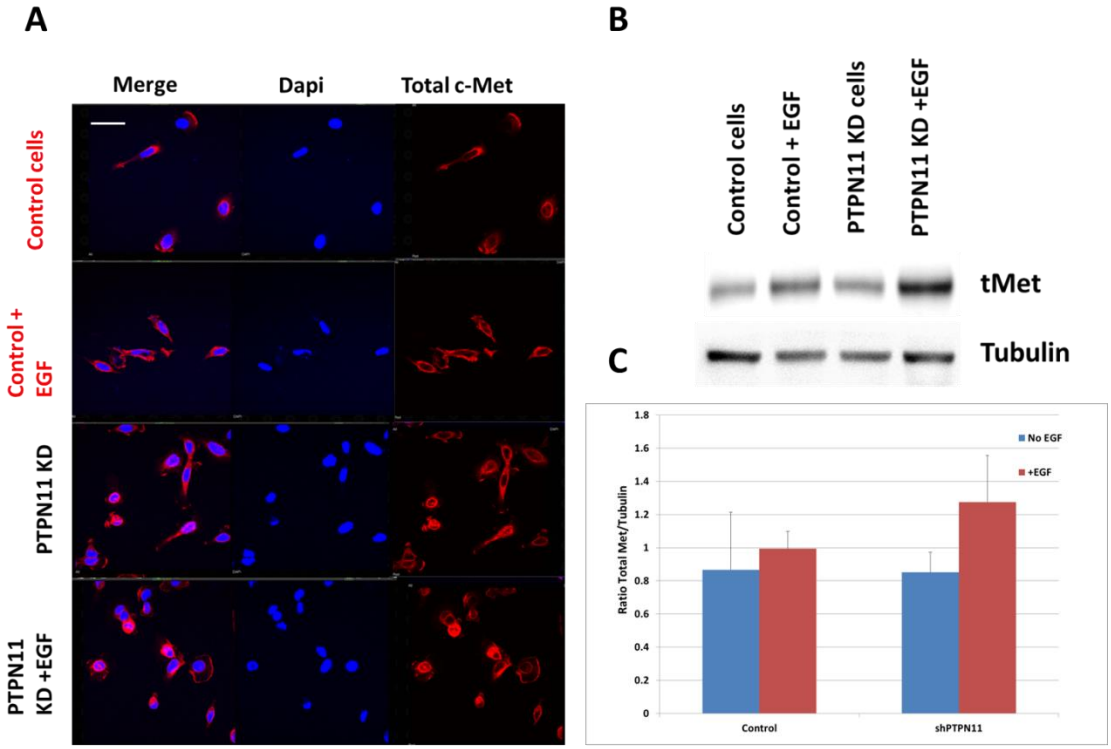

19

Figure 6-8. Increase in total c-Met in PTPN11-silenced cells after EGF stimulation.

(A) Confocal section of control and PTPN11KD basal-like breast cancer cells stained for total c-Met (red) and nucleus (blue) before and after EGF stimulation (30 minutes). A clear increase in the amount of total c-Met in the PTPN11 knockdown cells following EGF stimulation. **(B**) Immunoblot to assess level of expression of total c-Met in the control and knockdown cells before and after EGF stimulation. Scalebar: 50µm **(C)** Analysis of western blot data via densitometry which were normalized to Tubulin, used as a loading control for the level of total c-Met. Data are the mean values ± S.E.M, over 3 independent experiments.

Figure 6-8A shows an increase in the total c-Met expression level in the EGF-stimulated PTPN11 silenced cells in comparison to the stimulated and unstimulated controls cells and the unstimulated PTPN11 silenced cells. The images also display a clear membranous staining for total c-Met in all cells. An increase in cytoplasmic staining for total c-Met is demonstrated in the EGF-stimulated PTPN11-silenced cells. Figure 6-8B displays bands for the expression level of total c-Met in the control and PTPN11 knockdown cells before and after EGF stimulation. It is clear that the level of total c-Met is upregulated in the EGF-stimulated PTPN11 knockdown cells, and displays a 1.5 fold increase in comparison to the non-stimulated PTPN11 cells, however this was not significant statistically (P = 0.06). Figure 6-8C displays a small increase in the total c-Met expression level in the EGF-stimulated control cells in comparison to the unstimulated control cells. However, there is a more obvious increase in the EGF-stimulated PTPN11 silenced cells in comparison to the unstimulated ones.

Previous reports have shown that the increased expression of EGFRs and c-Met are key to enhancing both tumour cell replication and metastasis [90]. In order to assess whether the increase in EGFR and c-Met phosphorylation observed in the PTPN11-silenced cells is accompanied with a change in the rate of tumour growth, cell proliferation assays were carried out.

6.2.7 Decrease in growth rate of PTPN11-silenced cells in comparison to control cells, when both were treated with the c-Met inhibitor, SGX-523

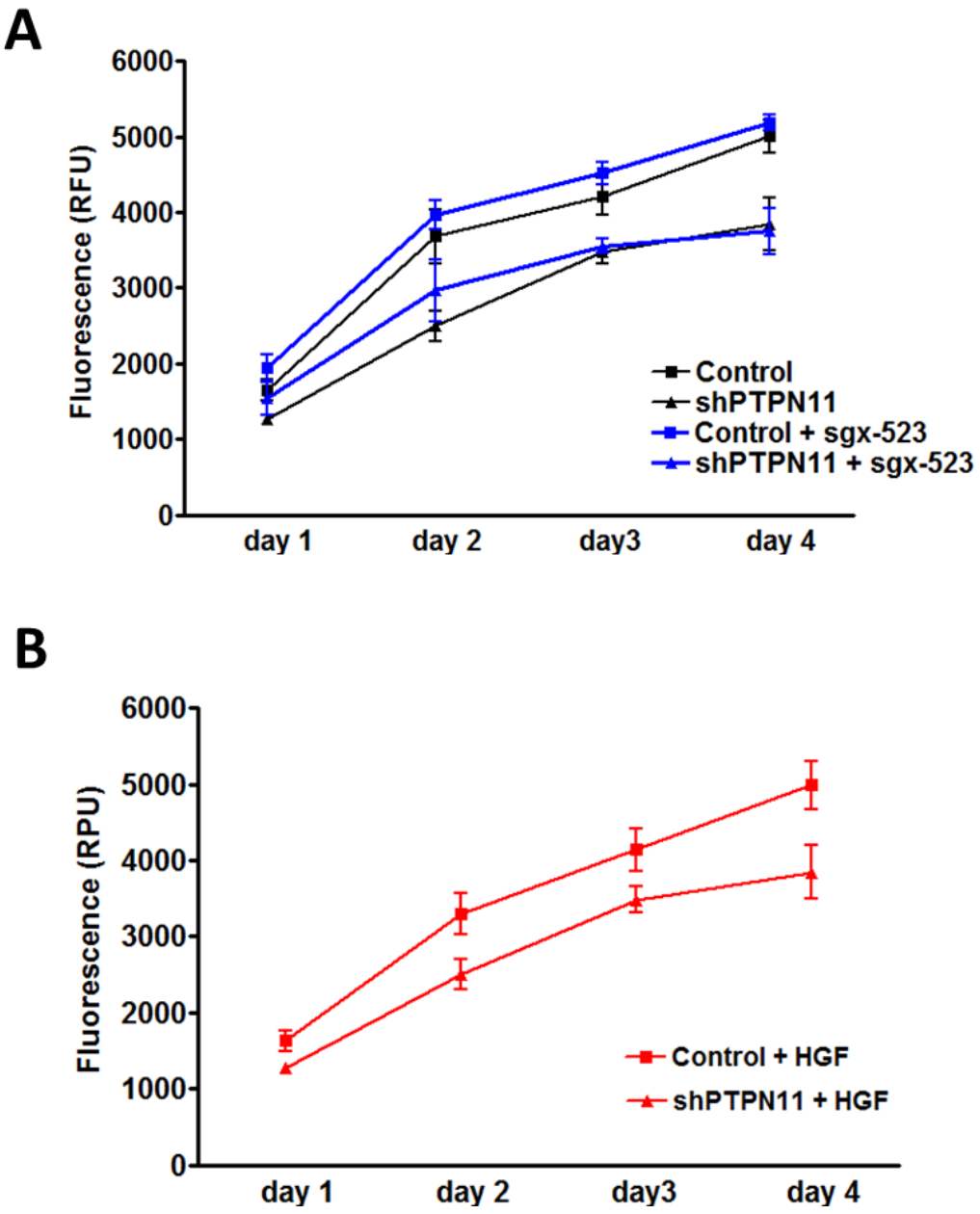

C

Stimulation	None	+ HGF	+ SGX-523
Control cells	0.37	0.37	0.33
shPTPN11 cells	0.37	0.37	0.30

Figure 6-9. Cell growth rate for control and PTPN11-silenced basal like breast cancer cell lines.

Cells were grown over 4 days, after which they were incubated in Alarmar Blue solution for four hours prior to measurement. The fluorescence was measured using a plate reader and normalised relative to the fluorescence emitted from the RPMI media incubated with the Alarmar Blue solution, as described in Material & Methods. **(A)** Cell proliferation for control and PTPN11-silenced cells, with and without SGX-523 treatment (c-Met inhibitor) **(B)** Cell proliferation in both sets of cell lines stimulated with HGF ligand. **(C)** *k* values calculated to determine growth rates. Data are mean values ± S.E.M., over 4 independent experiments.

Three sets of cell lines were seeded at the same time and stimulated with HGF (at a concentration of 50ng/ml) or treated with SGX-523 (a c-Met inhibitor at 5µM) in both the control and PTPN11-silenced cells to assess potential differences in their growth rates. Figure 6-9A displays the amount of fluorescence emitted from day 1 to day 4 after seeding of the control cells, control cells with the addition of SGX-523, PTPN11-silenced cells, and finally PTPN11-silenced cells with the addition of SGX-523. The growth curves for both the untreated and treated control cells look very similar. Additionally, we

do not observe any major difference between the growth curves of the untreated PTPN11-silenced cells and the treated cells. However, the growth curves for the untreated control cells seem to be higher than the PTPN11-silenced cells. We observe a similar shift when both cell lines are treated with SGX-523. Figure 6-9B also displays a similar shift in the growth curves of the control and PTPN11 silenced cells when stimulated with HGF. Due to the observed shifts, the *K* values for those growth curves were calculated to assess potential difference in the growth rate between cell lines (Fig 6-9C). Despite the visible difference in the growth curves in those sets of cell lines, the calculated *K* values show that the growth rates for the non-stimulated control and PTPN11 silenced cell lines are the same, as well as when they were both stimulated with the HGF ligand. However, there is a decrease in the growth rate for both the control and PTPN11 knockdown cell lines when treated with SGX-523, in comparison to the HGF-stimulated and non-stimulated cell lines. This decrease is not statistically significant. Additionally, we also observe a decrease, which is not statistically significant, in the growth rate of the PTPN11 knockdown cells treated with the c-Met inhibitor in comparison to the control cells that also were treated with the c-Met inhibitor.

As downregulation of E-cadherin is a hallmark of EMT, we next assess the cellular localization and expression levels of E-cadherin in control and PTPN11-silenced cells.

6.2.8 Increase in e-cadherin level in PTPN11-silenced cells

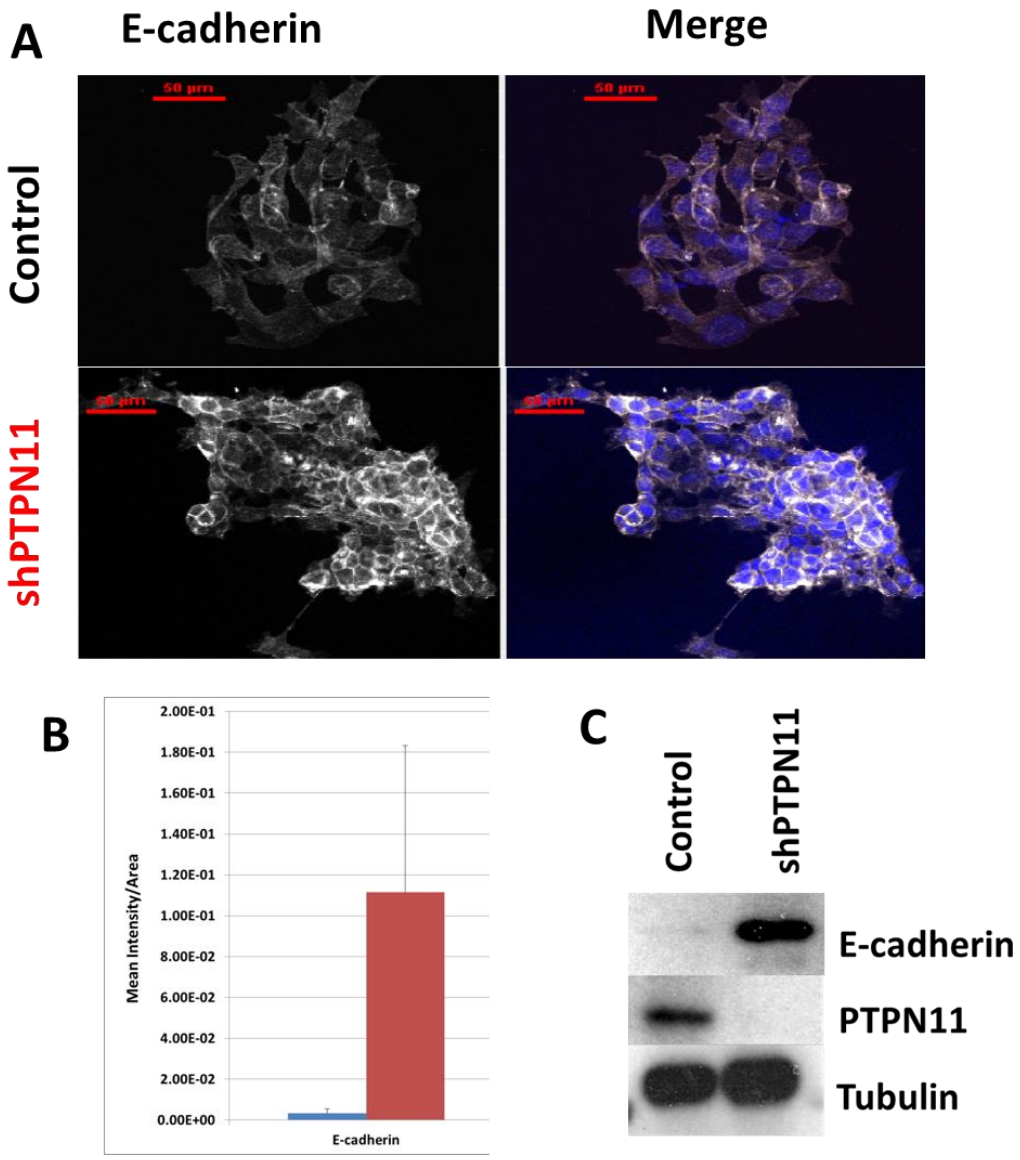

Figure 6-10. Increase in e-cadherin in PTPN11-silenced cells in comparison to control.

(A) Confocal sections of PTPN11-KD and control cells stained for e-cadherin (grey) and DAPI (blue) **(B)** Analysis of fluorescent staining for e-cadherin via mean intensity per area, using 'NIS Element' software in both sets of cell lines **(C)** Immunoblotting for the protein expression level of e-cadherin in both control and

PTPN11-KD cells. **(A-C)** Data are mean values ± S.E.M., over 3 independent experiments. Scalebar: 50µm

To confirm a change in the e-cadherin expression level in the control and PTPN11-silenced cells, both confocal sections were stained with e-cadherin and a western blot were conducted. As shown in Fig 6-10, there is a clear increase in the intensity of the staining for e-cadherin in the PTPN11 knockdown cells (Fig 6-10A&B). As expected, the staining for e-cadherin is localised at the membranes and at the cell junctions. Figure 6-10C demonstrates the increase in the expression level of e-cadherin in the PTPN11 knockdown cells in comparison to the control cells, which display a very faint band.

6.3 DISCUSSION

This chapter investigated the effect of PTPN11 silencing on c-Met's and EGFR's phosphorylation status, expression level, proliferation rates and metastatic property, in basal-like breast cancer cells.

PTPN11, a phosphatase, was identified as a 'hit' from the high content siRNA screen, which consisted of 533 genes interconnected with EGFR. The knockdown of PTPN11 abolished the EGF-induced activation of EGFR, suggesting that PTPN11 had a potential effect on EGFR signalling. Despite the fact that PTPN11 was previously reported as an EGFR regulator [300], it is the first time that this interaction has been observed in the basal-like breast cancer cells, HCC1954.

It was important to identify the optimal timepoint for EGF stimulation to compare the EGFR phosphorylation in the PTPN11-deficient cells and in the control cells. The optimal timepoint was identified as 30 minutes after EGF stimulation.

One of the main findings of this study was the significant increase in the phosphorylation of EGFR at Tyrosine 1173 in the EGF-stimulated PTPN11-silenced cells in comparison to the EGF-stimulated control cells. Studies have demonstrated the ability of PTPN11 to mediate the dephosphorylation of EGFR in COS-1 and NIH3T3 cells and have suggested this role to be translated in breast cancer cells [143]. However, many recent reports also revealed the major pro-oncogenic role that PTPN11 has in human

malignancies, including in breast cancer [314]. PTPN11 translates growth and survival signals from multiple RTK to mediate Erk1/Erk2 and the Akt pathway [314]. Additionally, previous reports gave phospho-Tyr 1173 two conflicting roles in EGFR signalling and specified that Tyr 1173 phosphorylation may cooperate with phospho-Tyr 992, Tyr 1068, Tyr 1086 and Tyr 1148 to promote ERK signalling through recruitment of SHC and Grb2, or may work alone to diminish ERK activation through SHP1 binding [290]. In agreement with the literature, it is possible that the hyperphosphorylation of EGFR in the PTPN11-silenced cells, detected in our study, might lead onto the attenuation of ERK activation, to satisfy the oncogenic role that PTPN11 have displayed in previous reports.

This EGFR hyperphosphorylation was further investigated by conducting a timecourse EGF stimulation experiment which resulted in the identification of a possible defect in EGFR dephosphorylation in the PTPN11-silenced cells. The EGFR phosphorylation was constantly higher in the PTPN11-silenced cells than in the control cells which lasted up to 60 minutes after EGF stimulation. Although recent studies reported that dephosphorylation precedes degradation under normal conditions [315], it is unclear as to whether this order needs to be maintained. Speculations could be that the EGFR may be targeted for degradation even if the receptor remains phosphorylated for an abnormally long time after EGF stimulation in PTPN11−/− cells. This could be made possible if other phosphatases substitute for this role of PTPN11 [316]. In addition to this, we must bear in

mind that other RTK-inactivating mechanism could help compensate for the absence of PTPN11 [317].

It was also interesting to see, within this same timecourse for EGF stimulation, a major reduction in the expression level for total EGFR in the PTPN11-silenced cells in comparison to the control cells 2 minutes after EGF stimulation. We also observed a slightly lower expression level for total EGFR at 30min and 60min post EGF stimulation in the PTPN11-silenced cells in comparison to the control cells. This might suggest that there is a higher turnover and/or recycling rate for EGFR in the control cells than in the PTPN11-deficient cells or could also suggest a higher degradation rate for EGFR in the PTPN11-deficient cells, as suggested previously [300].

Due to the effect observed in the EGFR phosphorylation in the PTPN11-silenced cells, we hypothesized that PTPN11 deficiency in basal-like breast cancer cells might have an effect in c-Met phosphorylation due to EGFR and c-Met well documented cross-talk [90]. This project identified a significant increase in c-Met phosphorylation in the PTPN11-silenced cells in comparison to the control cells. Previous findings have demonstrated the increased levels of c-Met phosphorylation in PTP1B-null mice that were injected with 15 nm HGF via the hepatic portal vein [318]. However, in our study, this hyperphosphorylation was ligand-independent. It is possible that c-Met in those PTPN11-silenced cells, was transactivated with other receptors (e.g members of the family of semaphorin receptors), to bypass the need for a ligand-dependent activation [319].To confirm such statement, the identification of such receptors would be necessary in an

immunoprecipitation experiment. Besides, c-Met hyperphosphorylation was also observed in melanocytes whose tumour suppressor gene, Plexin 1B, was knockdown. It also displayed lower levels for PTPN11 accompanied by a decrease in cell proliferation and an abrogation for c-Met dependent activation of Erk1/Erk2 and Akt in melanocytes [320].

Additionally, in this study, we detected a potential increase in total c-Met expression level in the EGF-stimulated PTPN11-silenced cells. EGFR might be causative for this increase as it was not observed in the unstimulated cells. This is consistent with the finding from Xu et al, in which they showed that activated EGFR enhanced c-Met levels [321]. Besides, the higher expression level for total c-Met might suggest a defect in the removal of c-Met from the cell surface and subsequent degradation through endocytosis which could lead to sustained oncogenic signalling [90].

To further elucidate the role of PTPN11 knockdown, we wanted to investigate its effect on cell proliferation. We identified a slight decrease in the growth rate of the PTPN11 knockdown cell lines when treated with the c-Met inhibitor, in comparison to the controls that were also treated with the c-Met inhibitor. This difference was not statistically significant but this might be due to the low sample size. If this decrease is real, this suggests that c-Met inhibitors might be more efficient in reducing proliferation in basal like breast cancer cells that are depleted of PTPN11. Previous studies have reported a major reduction in cell proliferation (3-4 fold) in the PTPN11-silenced basal-like breast cancer cells in comparison to the EGFR-silenced cells (1.5 fold). In addition, they assessed the formation of colonies in the PTPN11 and

EGFR-silenced cells and discovered that the PTPN11-silenced cells formed fewer and smaller colonies than the EGFR-silenced cells, suggesting that the inhibition of PTPN11 had a greater impact on supressing cell transformation than EGFR inhibition [300].

Finally, it was interesting to see an increase in the intensity of the staining and expression level for e-cadherin in the PTPN11 knockdown cells. This is in line with a study performed by Zhao et al, which demonstrated the restoration of epithelial morphology in PTPN11-silenced MDA-MB231 cells, which are basal-like, while the control and parental cell line exhibited a spindle shaped mesenchymal morphology [322]. This reinforced the idea of PTPN11's migratory role in BTBC cells [322].

It is surprising to identify a high phosphorylated c-Met along with an increase in e-cadherin expression in the PTPN11-silenced cells. Both phenotypes contradict each other. It is well documented that c-Met is involved in the cell proliferative and motility in cancer cells [323] and should therefore be accompanied with a reduced e-cadherin expression [323]. If time permitted, it would have been useful to investigate further the migratory properties of PTPN11-silenced cells by performing a wound-healing assay. It would have also been informative to modulate c-Met phosphorylation, by using the c-Met inhibitor sgx-523 in the PTPN11-silenced cells and perform a scratch assay on those cells and compare it with the ones whose c-Met remains activated. We could speculate that c-Met phosphorylation in those PTPN11-silenced cells does not have an effect on the downstream signalling pathways that regulates cell proliferation due to a defect in the activation of those pathways.

This is in line with the study conducted by Soong et al, et in which they show that PTPN11 is necessary for full activation of Erk1/Erk2 and Akt in melanocytes in response to HGF [320].

Based on the results obtained in this chapter, it can be concluded that there is a defect in EGFR phosphorylation in cells depleted of PTPN11 that suggests PTPN11's involvement in the maintenance of EGFR regulation in basal-like breast cancer. In addition, the c-Met hyperphosphorylation in conjunction with a lack of effect on cell proliferation in cells depleted with PTPN11, which mimic the findings from the study conducted by Soong et al [320] suggests that more work, focusing on the mechanistic regulation of PTPN11, needs to be done in order to understand those phenotypes. The link between the increase in e-cadherin expression and c-Met hyperphosphorylation in the PTPN11-silenced cells in basal-like breast cancer needs further elucidation. E-cadherin downregulation is known to be related to ubiquitin ligases Hakai, or MDM2 (reviewed in [324]). The interaction of Numb with e-cadherin or the Par protein complex which is dynamically regulated by HGF/c-Met activation may modulate e-cadherin stability via the same interaction motif (NVYY) that Hakai binds to target e-cadherin [324, 325]. The biochemical interplay between PTPN11, c-Met and E-cadherin is likely to be complex and remains to be elucidated.

Chapter 7: Conclusion and Future Work

7.1 Conclusion

In this thesis, we initially report:

1. The novel finding of the use of [^{18}F]AH113804, a c-Met binding peptide tracer with high affinity to human c-Met (Kd = 2nM) in the detection of locoregional recurrence of basal-like breast cancer at an early stage [16].

2. A novel c-Met scFv-Fc binding tracer which successfully detects c-Met positive cells in basal-like breast cancer *in-vivo*.

In greater details, [^{18}F]AH113804 was able to detect the recurrent HCC1954 tumour lesion 6 days after removal of the primary tumour, while this is not detectable by eye nor by CT. We also observed a statistically significant difference in the uptake of the tracer at the tumour site in comparison to the control site, at all timepoints excluding 50 days after removal of the primary tumour. The reason given for the lack of statistically significant difference at this latter timepoint is the lower, inhomogenous distribution of radioactivity in the tumors, indicative of the presence of necrosis in the c-Met positive tumours, HCC1954.

Additionally, the non-specific blood pool distribution of [^{18}F]AH113804 decreased over time, after injection of the tracer, while we observed an increasing signal within the site of the basal-like breast cancer tumours.

c-Met expression level, quantified from the ex vivo histology performed on the resected recurrent tumours and primary tumours, correlated with the uptake of the tracer in those tumours *in-vivo* ($P = 0.005$, $r = 0.83$). These results combined gave us confidence in the reliability of this tracer for the detection of c-Met positive cells and show potential utility for the detection of loco-regional recurrence, in basal like breast cancer, from an early stage. Further preclinical work is necessary to determine whether [^{18}F]AH113804 uptake in the regrowth provides a useful predictive tool for anti-c-Met therapeutic intervention [16].

Following this, we focused on the design of an optically and radiolabelled scFv-Fc with specificity to human c-Met for the detection of basal-like breast cancer *in-vivo*. The choice of a scFv-Fc is based on its high targeting ability for the detection of c-Met positive tumour lesions, and a longer biological half-life (than a c-Met binding peptide for example) enabling the potential monitoring of anti-c-Met therapies. The two versions of the tracer, which consists of an optical Cy5-labelled scFv-Fc and the radiolabelled 111-In-CHX-A''-DTPA-scFv-Fc show a higher uptake in the c-Met positive HCC1954 tumours, in comparison to the c-Met negative MCF-7 tumours, which is statistically significant.

The scFv-Fc was selected from a phage display library, which led to the production of plasmid DNA with a scFv format, via the use of the vector pSANG4, and then subcloned into pBIOCAM5 for the production of c-Met scFv-Fc. This led to the identification of 222 anti c-Met scFv-Fc fusions, as described in chapter 5. The selection of our FLAG epitope-tagged scFv-Fc was based on displaying one of the highest ratio average intensity for c-Met (using the D1C2 antibody) and anti-FLAG, relative to the scFv-Fc expression level, detected by western blot, and the presence of good co-localisation between c-Met positive cells and cells that expressed the anti-FLAG epitope. This subclone was amplified and optically labelled with the Cy5 fluorochrome.

After injection of the optical tracer Cy5-scFv-Fc, we observed an uptake in the c-Met positive basal like breast cancer HCC1954-luciferase expressing tumour while no uptake was seen in the c-Met negative MCF-7 tumour in the tumour bearing mice. The difference in the uptake of the optical tracer in both tumours was statistically significant. The fluorescent signal emitted at the site of the c-Met positive tumour was identified at the same location as the bioluminescent signal from the HCC1954 tumour. The ex vivo biodistribution, performed at 24 hours after injection, confirmed a high uptake in the HCC1954 tumour, as well as the liver and moderate uptake in the kidneys. The ex vivo staining performed on the frozen HCC1954-luciferase tagged tumour sections, collected from the tumour bearing mice, showed c-Met overexpression which co-localised with the staining for the Cy5-labelled scFv-Fc. We did not observe c-Met staining in the MCF-7 frozen tumour section which validated the specificity of Cy5-scFv-Fc to human c-Met.

Following the successful conjugation (with the chelator CHX-A''-DTPA) and radiolabelling (111-In) of the scFv-Fc, we observed specific tumour targeting of the radiolabelled tracer in the c-Met positive HCC1954 tumours in the tumour bearing mice while a very low uptake was observed in the c-Met negative MCF-7 tumours, at 3h, 7h and 24h after tracer's injection. The serum stability test confirmed the stability of 111-In-CHX-A''-DTPA-scFv-Fc in human serum at 37°C up to 24 hours, which was the latest timepoint determined by the length of the experiment. Quantification of the tracer's uptake revealed an increase at the tumour site over time while in parallel, the uptake in the liver decreased. The ex-vivo biodistribution data revealed a statistically significant difference between the uptake of the tracer in the c-Met positive HCC1954 tumours and the uptake in the c-Met negative MCF-7 tumours.

The novel use of the c-Met binding peptide tracer [^{18}F]AH113804 in the detection of locoregional recurrence of basal-like breast cancer at an early stage and the design of a novel c-Met specific scFv-Fc binding tracer, 111-In-CHX-A''-DTPA-scFv-Fc, for the detection of c-Met positive tumour cells are of significant values.

Indeed, the ubiquity of c-Met dysregulation in numerous cancers and its known influence in tumour progression makes it an attractive target for diagnostic and therapeutic intervention. Decades have been spent on the elucidation of c-Met signalling in normal and in tumour cells [49, 56, 60, 326, 327]. c-Met overexpression, amplification and dysregulation in many cancers resulted in the development of c-Met binding tracers in the aim to assess, non-invasively, c-Met expression level and localisation *in-vivo* [16, 212, 214,

254, 328]. Recent literature shows the use of c-Met specific radiolabelled tracers such as anticalin [214], 89-Zr Onartuzumab [214, 255], cMBP-GGG [257] in the detection of tumour lesions that overexpress c-Met but sadly, those tracers presented flaws that prevent them from being assessed in patients as described in more details in Section 4.3 of this thesis.

Despite the use of ^{18}F-FDG in breast cancer staging and recurrence, it is not currently used for the screening of primary breast cancer [258]. In addition to this, despite the sensitivity and specificity of FDG in the detection of tumour cells, it lacks the ability to detect lesions that are smaller than 1cm [167, 168, 251], and is not a direct readout for the expression level of a target protein, hence making its use rather inadequate for the monitoring of, for example, c-Met inhibition *in-vivo*. 18-FDG cannot be used for the *in-vivo* quantification of a protein expression level. A molecular targeted agent would enable the assessment of an appropriate dose schedule in a patient, as the tracer would provide quantifiable values of the protein expression level that is targeted by the drug at a specific dose.

Additionally, prognostic biomarkers for patient stratification are a necessity in clinical trials, in order to eliminate non-responder phenotypes before the assessment of specific molecular-targeted therapies. This is particularly useful in assessing the efficacy of inhibitors whose target is overexpressed in the tumour. Hence, c-Met stratification in patients would enable an increase in the efficiency of anti-c-Met therapies and possibly anti-EGFR therapies in patients. Indeed, reports show that some patients develop resistance to EGFR inhibitors and in some of those cases, the resistance is assigned to c-Met over-activation or amplification, bypassing the need for the activation of

EGFR as c-Met promotes cell proliferation and other tumour driven pathways [329]. Hence, such molecular targeted imaging agents could also be used in image guided therapy, allowing the discontinuation of ineffective treatments early on in the course of treatment. Additionally, molecular targeted imaging agents would also offer an early indication of potential normal organ toxicities (in case of the equivalent radioimmunotherapies, by estimating the dose delivered to for instance bone marrow), hence preventing the subject to go through fatal illnesses owed to toxicity level [330]. Lastly, the use of a c-Met targeted tracer would circumvent the need for a biopsy, which is invasive and not necessarily achievable, especially if the tumour lesions are not visible by eye nor by CT.

Lately, numerous clinical studies have been focusing on antibody engineering for the optimisation of molecular targeted imaging agents. Indeed, it is necessary for the imaging agent to display a high tumour targeting, fast clearance kinetics, a high tumour to blood ratio in order to acquire high quality images. Although c-Met binding peptide tracers show fast clearance kinetics and therefore allow the use of a short half-life radioisotope for the acquisition of a PET scan within minutes to hours after tracer's injection, they do not display a very high tumour targeting ability, unlike intact monoclonal antibodies (mAbs) and cannot be used to monitor long-term therapies due to their short biological half-life. The major challenge faced by mAbs is their persistent circulation time in the serum, despite their high affinity for the target. Fragment antibodies provide a solution to those issues [279]. It is possible to maintain the targeting ability of a mAb, by engineering it into a scFv-Fc fusion antibody for example, as observed in this

study. Additionally, faster clearance and good image contrast can be achieved by blocking the FcRn salvage receptor with Fc-engineered antibodies [331, 332], or by removing it altogether, like in the case of a minibody or diabody and other smaller fragment antibodies, as described in Section 1.11 in this thesis.

Lastly, in this thesis, we report:

3. The potential oncogenic role of PTPN11 in basal-like breast cancer

Briefly, chapter 6 in this thesis (Section 6.2) described the novelty of PTPN11 being an EGFR regulator in BLBC. It also described the increase in EGFR phosphorylation following EGF stimulation in PTPN11-silenced cells, and the fact that this hyperphosphorylation was maintained for longer in comparison to control cells. This hyperphosphorylation might be a direct effect of PTPN11 knockdown as a study has shown the ability of PTPN11 to regulate the amount of phosphorylated EGFR [315]. Speculations are that PTPN11 would diffuse on the surface of endosomes, dephosphorylating phosphorylated EGFR molecules before being itself inactivated in the absence of further interaction with phosphorylated EGFR [315].

Additionally, reports had shown that EGFR phosphorylation might lead to the attenuation of Erk activation [290]. Despite the increase in EGFR phosphorylation, it is still possible that EGFR may be targeted for

degradation as other phosphatases could substitute for this role of PTPN11 [316].

We also observed c-Met hyperphosphorylation in PTPN11-silenced BLBC cells. This mimicked previous findings, although ligand-independent in our study, in which increased levels of c-Met phosphorylation was observed in PTP1B-null mice that were injected with 15 nm HGF via the hepatic portal vein [318]. The hyperphosphorylation observed in our study could be due to transactivation of c-Met with other receptors [319].

It was also interesting to observe an increase in e-cadherin expression level and mean fluorescent intensity in PTPN11-silenced BLBC cells. This suggests the migratory role of PTPN11 in BLBC cells and is in agreement with other studies in which they demonstrate the restoration of epithelial morphology PTPN11-silenced basal like breast cancer MDA-MB231 cells [322]. More mechanistic studies are however needed to elucidate the biochemical interplay between PTPN11, c-Met and E-cadherin before being able to consider therapeutic strategies using PTPN11 as a target.

Due to drug resistance observed in patients who are given TKIs, it is crucial to identify biochemical interplays and proteins that prevent the efficiency of TKIs, such as cetuximab (an anti-EGFR TKI) and cabozantinib (an anti-c-

Met, VEGFR2 and Ret TKI) in cancer patients, especially in BLBC patients. PTPN11 is an interesting target as it modulates both c-Met and EGFR activation, as observed in our study. A study conducted by Furcht et al revealed that PTPN11 knockdown leads to the decrease in ERK phosphorylation in NSCLC cells expressing wild-type EGFR , basally

accompanied by an increased in cellular sensitivity to gefitinib [333]. Interestingly, PTPN11 was also required for sustained activation of ERK and epithelial morphogenesis downstream from the c-Met receptor tyrosine kinase [334]. It has been shown that C-Met is highly dependent on Gab1 for signalling [335] as Gab1 becomes phosphorylated upon c-Met binding providing binding sites for multiple signalling proteins such as PTPN11 [336]. A specific study has shown the importance of the association of Gab1 with PTPN11 and PI3K for cell cycle progression and the inability of Gab1 mutant, which cannot bind to PTPN11 to activate MAPK downstream of c-Met [336]. These suggest the involvement of PTPN11 in tumour progression and the potential role of PTPN11 inhibitors as therapeutic targets [337, 338].

7.2 Future work

Based on the findings in this thesis, [^{18}F]AH113804 has the ability to detect locoregional recurrence in BLBC as early as 6 days following primary tumour removal. It would be informative to assess the survival rate in those tumour bearing mice following the early administration of therapeutic treatment, due to early detection of LRR. This would have provided us and others invaluable insight into the direct effect of early detection and treatment on basal-like breast patients' survival.

Since 18F-FDG gained clinical acceptance, and has become an important imaging tool in routine clinical oncology, it would have been useful to assess FDG uptake in our basal-like breast cancer model and compare its uptake at

the tumour site, especially after surgery, to the uptake observed with [^{18}F]AH113804. Additionally, it would also be very useful to monitor anti-c-Met therapies *in-vivo* in BLBC using both tracers and delineate the exact use of [^{18}F]AH113804 in the clinic.

Before ^{111}In-CHX-A''DTPA-scFv-Fc against human c-Met could be assessed in man, it would be useful to reduce its biological half-life and liver uptake via directed mutagenesis of the Fc fragment, as described in Section 5.3 [202, 282] and assess any potential off-target effects *in-vitro*.

Although SPECT is more cost-effective than PET, the latter displays a better spatial and contrast resolution enabling the acquisition of higher quality images [339]. Hence, it might be useful to radiolabel our scFv-Fc with a PET radioisotope and compare the images acquired with the images from the SPECT to assess the best modality for the optimal use of the scFv-Fc in cancer imaging.

Lastly, for a better understanding of the mechanisms behind c-Met hyperactivation in PTPN11-silenced cells, it would be useful to identify potential transactivation of c-Met with other receptors via immunoprecipitation. It would also be useful to identify downstream signalling pathways that are being upregulated following c-Met activation.

Additionally, to better understand the functional phenotype of PTPN11-silenced cells, it would be needful to perform migratory assays in our model,

both *in-vitro* and *in-vivo*. Previous studies have revealed the role of PTPN11 in cell motility *in-vivo*, as well as cell migration and invasion *in-vitro*, through the activation of several SRC-family kinases and downstream targets [340].

It would also be informative to gain a better understanding of the interplay between c-Met, PTPN11 and e-cadherin by performing immunoprecipitation assays and identify the proteins involved in the maintenance of e-cadherin, as observed in this *study*, in the PTPN11-silenced cells as compared to the control cells.

Chapter 8: References

1. Shastry, M. and D.A. Yardley, *Updates in the treatment of basal/triple-negative breast cancer.* Curr Opin Obstet Gynecol, 2013. **25**(1): p. 40-8.
2. Rakha, E.A., J.S. Reis-Filho, and I.O. Ellis, *Basal-like breast cancer: a critical review.* J Clin Oncol, 2008. **26**(15): p. 2568-81.
3. Knowles, L.M., et al., *HGF and c-Met participate in paracrine tumorigenic pathways in head and neck squamous cell cancer.* Clin Cancer Res, 2009. **15**(11): p. 3740-50.
4. Lengyel, E., et al., *C-Met overexpression in node-positive breast cancer identifies patients with poor clinical outcome independent of Her2/neu.* Int J Cancer, 2005. **113**(4): p. 678-82.
5. Tokunou, M., et al., *c-MET expression in myofibroblasts: role in autocrine activation and prognostic significance in lung adenocarcinoma.* Am J Pathol, 2001. **158**(4): p. 1451-63.
6. Ramirez, R., et al., *Over-expression of hepatocyte growth factor/scatter factor (HGF/SF) and the HGF/SF receptor (cMET) are associated with a high risk of metastasis and recurrence for children and young adults with papillary thyroid carcinoma.* Clin Endocrinol (Oxf), 2000. **53**(5): p. 635-44.
7. Tsao, M.S., et al., *Differential expression of Met/hepatocyte growth factor receptor in subtypes of non-small cell lung cancers.* Lung Cancer, 1998. **20**(1): p. 1-16.
8. Koochekpour, S., et al., *Met and hepatocyte growth factor/scatter factor expression in human gliomas.* Cancer Res, 1997. **57**(23): p. 5391-8.
9. Olivero, M., et al., *Overexpression and activation of hepatocyte growth factor/scatter factor in human non-small-cell lung carcinomas.* Br J Cancer, 1996. **74**(12): p. 1862-8.
10. Tuck, A.B., et al., *Coexpression of hepatocyte growth factor and receptor (Met) in human breast carcinoma.* Am J Pathol, 1996. **148**(1): p. 225-32.
11. Di Renzo, M.F., et al., *Expression of the Met/hepatocyte growth factor receptor in human pancreatic cancer.* Cancer Res, 1995. **55**(5): p. 1129-38.
12. Furukawa, T., et al., *Hepatocyte growth factor and Met receptor expression in human pancreatic carcinogenesis.* Am J Pathol, 1995. **147**(4): p. 889-95.
13. Liu, C., M. Park, and M.S. Tsao, *Overexpression of c-met proto-oncogene but not epidermal growth factor receptor or c-erbB-2 in primary human colorectal carcinomas.* Oncogene, 1992. **7**(1): p. 181-5.
14. Houldsworth, J., et al., *Gene amplification in gastric and esophageal adenocarcinomas.* Cancer Res, 1990. **50**(19): p. 6417-22.
15. Gastaldi, S., P.M. Comoglio, and L. Trusolino, *The Met oncogene and basal-like breast cancer: another culprit to watch out for?* Breast Cancer Res, 2010. **12**(4): p. 208.

16. Arulappu, A., et al., *c-Met PET Imaging Detects Early Stage Loco-Regional Recurrence of Basal-Like Breast Cancer.* J Nucl Med, 2015.
17. Carey, L.A., et al., *TBCRC 001: randomized phase II study of cetuximab in combination with carboplatin in stage IV triple-negative breast cancer.* J Clin Oncol, 2012. **30**(21): p. 2615-23.
18. Baselga, J., et al., *Randomized phase II study of the anti-epidermal growth factor receptor monoclonal antibody cetuximab with cisplatin versus cisplatin alone in patients with metastatic triple-negative breast cancer.* J Clin Oncol, 2013. **31**(20): p. 2586-92.
19. Hudis, C.A. and L. Gianni, *Triple-negative breast cancer: an unmet medical need.* Oncologist, 2011. **16 Suppl 1**: p. 1-11.
20. Braunstein, L.Z. and A.G. Taghian, *Molecular Phenotype, Multigene Assays, and the Locoregional Management of Breast Cancer.* Semin Radiat Oncol, 2016. **26**(1): p. 9-16.
21. Colditz, G.A. and K. Bohlke, *Priorities for the primary prevention of breast cancer.* CA Cancer J Clin, 2014. **64**(3): p. 186-94.
22. McCready, T., D. Littlewood, and J. Jenkinson, *Breast self-examination and breast awareness: a literature review.* J Clin Nurs, 2005. **14**(5): p. 570-8.
23. Badve, S., et al., *Basal-like and triple-negative breast cancers: a critical review with an emphasis on the implications for pathologists and oncologists.* Mod Pathol, 2011. **24**(2): p. 157-67.
24. Blows, F.M., et al., *Subtyping of breast cancer by immunohistochemistry to investigate a relationship between subtype and short and long term survival: a collaborative analysis of data for 10,159 cases from 12 studies.* PLoS Med, 2010. **7**(5): p. e1000279.
25. Minuti, G. and L. Landi, *MET deregulation in breast cancer.* Ann Transl Med, 2015. **3**(13): p. 181.
26. Zanardi, E., et al., *Better Together: Targeted Combination Therapies in Breast Cancer.* Semin Oncol, 2015. **42**(6): p. 887-95.
27. Nielsen, T.O., et al., *Immunohistochemical and clinical characterization of the basal-like subtype of invasive breast carcinoma.* Clin Cancer Res, 2004. **10**(16): p. 5367-74.
28. Cheang, M.C., et al., *Basal-like breast cancer defined by five biomarkers has superior prognostic value than triple-negative phenotype.* Clin Cancer Res, 2008. **14**(5): p. 1368-76.
29. Gluz, O., et al., *Triple-negative breast cancer--current status and future directions.* Ann Oncol, 2009. **20**(12): p. 1913-27.
30. Fadoukhair, Z., et al., *Evaluation of targeted therapies in advanced breast cancer: the need for large-scale molecular screening and transformative clinical trial designs.* Oncogene, 2015.
31. Dent, R., et al., *Triple-negative breast cancer: clinical features and patterns of recurrence.* Clin Cancer Res, 2007. **13**(15 Pt 1): p. 4429-34.
32. Haffty, B.G., et al., *Ipsilateral breast tumor recurrence as a predictor of distant disease: implications for systemic therapy at the time of local relapse.* J Clin Oncol, 1996. **14**(1): p. 52-7.
33. Veronesi, U., et al., *Twenty-year follow-up of a randomized study comparing breast-conserving surgery with radical mastectomy for early breast cancer.* N Engl J Med, 2002. **347**(16): p. 1227-32.

34. Panoff, J.E., et al., *Risk of locoregional recurrence by receptor status in breast cancer patients receiving modern systemic therapy and post-mastectomy radiation.* Breast Cancer Res Treat, 2011. **128**(3): p. 899-906.
35. Nguyen, P.L., et al., *Breast cancer subtype approximated by estrogen receptor, progesterone receptor, and HER-2 is associated with local and distant recurrence after breast-conserving therapy.* J Clin Oncol, 2008. **26**(14): p. 2373-8.
36. Lee, J.H., et al., *Independent Prognostic Factors for Overall Survival after Salvage Operation for Ipsilateral Breast Tumor Recurrence Following Breast-Conserving Surgery.* J Breast Cancer, 2015. **18**(4): p. 386-93.
37. Anders, C. and L. Carey. *Epidemiology, risk factors and the clinical approach to ER/PR negative, HER2-negative (Triple-negative) breast cancer*. 2015; Available from: http://www.uptodate.com/contents/epidemiology-risk-factors-and-the-clinical-approach-to-er-pr-negative-her2-negative-triple-negative-breast-cancer?source=search_result&search=basal+like+breast+cancer&selectedTitle=1~22.
38. Rouzier, R., et al., *Breast cancer molecular subtypes respond differently to preoperative chemotherapy.* Clin Cancer Res, 2005. **11**(16): p. 5678-85.
39. Tian, M., et al., *Platinum-based therapy for triple-negative breast cancer treatment: A meta-analysis.* Mol Clin Oncol, 2015. **3**(3): p. 720-724.
40. Gelmon, K., et al., *Targeting triple-negative breast cancer: optimising therapeutic outcomes.* Ann Oncol, 2012. **23**(9): p. 2223-34.
41. De Vos, M., V. Schreiber, and F. Dantzer, *The diverse roles and clinical relevance of PARPs in DNA damage repair: current state of the art.* Biochem Pharmacol, 2012. **84**(2): p. 137-46.
42. De Summa, S., et al., *BRCAness: a deeper insight into basal-like breast tumors.* Ann Oncol, 2013. **24 Suppl 8**: p. viii13-viii21.
43. Gelmon, K.A., et al., *Olaparib in patients with recurrent high-grade serous or poorly differentiated ovarian carcinoma or triple-negative breast cancer: a phase 2, multicentre, open-label, non-randomised study.* Lancet Oncol, 2011. **12**(9): p. 852-61.
44. Brufsky, A., et al., *Second-line bevacizumab-containing therapy in patients with triple-negative breast cancer: subgroup analysis of the RIBBON-2 trial.* Breast Cancer Res Treat, 2012. **133**(3): p. 1067-75.
45. Edakuni, G., et al., *Expression of the hepatocyte growth factor/c-Met pathway is increased at the cancer front in breast carcinoma.* Pathol Int, 2001. **51**(3): p. 172-8.
46. Ho-Yen, C.M., et al., *C-Met in invasive breast cancer: is there a relationship with the basal-like subtype?* Cancer, 2014. **120**(2): p. 163-71.
47. Dieras, V., et al., *Randomized, phase II, placebo-controlled trial of onartuzumab and/or bevacizumab in combination with weekly paclitaxel in patients with metastatic triple-negative breast cancer.* Ann Oncol, 2015. **26**(9): p. 1904-10.

48. Yap, T.A., et al., *Phase I trial of a selective c-MET inhibitor ARQ 197 incorporating proof of mechanism pharmacodynamic studies.* J Clin Oncol, 2011. **29**(10): p. 1271-9.
49. Trusolino, L., A. Bertotti, and P.M. Comoglio, *MET signalling: principles and functions in development, organ regeneration and cancer.* Nat Rev Mol Cell Biol, 2010. **11**(12): p. 834-48.
50. Zhang, L., et al., *Molecular imaging of c-Met tyrosine kinase activity.* Anal Biochem, 2011. **412**(1): p. 1-8.
51. Organ, S.L. and M.S. Tsao, *An overview of the c-MET signaling pathway.* Ther Adv Med Oncol, 2011. **3**(1 Suppl): p. S7-s19.
52. Ma, P.C., et al., *c-Met: structure, functions and potential for therapeutic inhibition.* Cancer Metastasis Rev, 2003. **22**(4): p. 309-25.
53. Comoglio, P.M., *Structure, biosynthesis and biochemical properties of the HGF receptor in normal and malignant cells.* Exs, 1993. **65**: p. 131-65.
54. Comoglio, P.M., S. Giordano, and L. Trusolino, *Drug development of MET inhibitors: targeting oncogene addiction and expedience.* Nat Rev Drug Discov, 2008. **7**(6): p. 504-16.
55. Bottaro, D.P., et al., *Identification of the hepatocyte growth factor receptor as the c-met proto-oncogene product.* Science, 1991. **251**(4995): p. 802-4.
56. Ho-Yen, C.M., J.L. Jones, and S. Kermorgant, *The clinical and functional significance of c-Met in breast cancer: a review.* Breast Cancer Res, 2015. **17**: p. 52.
57. Merchant, M., et al., *Monovalent antibody design and mechanism of action of onartuzumab, a MET antagonist with anti-tumor activity as a therapeutic agent.* Proc Natl Acad Sci U S A, 2013. **110**(32): p. E2987-96.
58. Maroun, C.R. and T. Rowlands, *The Met receptor tyrosine kinase: a key player in oncogenesis and drug resistance.* Pharmacol Ther, 2014. **142**(3): p. 316-38.
59. Furge, K.A., Y.W. Zhang, and G.F. Vande Woude, *Met receptor tyrosine kinase: enhanced signaling through adapter proteins.* Oncogene, 2000. **19**(49): p. 5582-9.
60. Gherardi, E., et al., *Targeting MET in cancer: rationale and progress.* Nat Rev Cancer, 2012. **12**(2): p. 89-103.
61. Graziani, A., et al., *Hepatocyte growth factor/scatter factor stimulates the Ras-guanine nucleotide exchanger.* J Biol Chem, 1993. **268**(13): p. 9165-8.
62. Xiao, G.H., et al., *Anti-apoptotic signaling by hepatocyte growth factor/Met via the phosphatidylinositol 3-kinase/Akt and mitogen-activated protein kinase pathways.* Proc Natl Acad Sci U S A, 2001. **98**(1): p. 247-52.
63. Liu, Y., *Hepatocyte growth factor in kidney fibrosis: therapeutic potential and mechanisms of action.* Am J Physiol Renal Physiol, 2004. **287**(1): p. F7-16.
64. Syed, Z.A., et al., *HGF/c-met/Stat3 signaling during skin tumor cell invasion: indications for a positive feedback loop.* BMC Cancer, 2011. **11**: p. 180.

65. Hui, A.Y., et al., *Src and FAK mediate cell-matrix adhesion-dependent activation of Met during transformation of breast epithelial cells.* J Cell Biochem, 2009. **107**(6): p. 1168-81.
66. Maulik, G., et al., *Modulation of the c-Met/hepatocyte growth factor pathway in small cell lung cancer.* Clin Cancer Res, 2002. **8**(2): p. 620-7.
67. Muller, M., A. Morotti, and C. Ponzetto, *Activation of NF-kappaB is essential for hepatocyte growth factor-mediated proliferation and tubulogenesis.* Mol Cell Biol, 2002. **22**(4): p. 1060-72.
68. Soman, N.R., et al., *The TPR-MET oncogenic rearrangement is present and expressed in human gastric carcinoma and precursor lesions.* Proc Natl Acad Sci U S A, 1991. **88**(11): p. 4892-6.
69. Hochgrafe, F., et al., *Tyrosine phosphorylation profiling reveals the signaling network characteristics of Basal breast cancer cells.* Cancer Res, 2010. **70**(22): p. 9391-401.
70. Charafe-Jauffret, E., et al., *Gene expression profiling of breast cell lines identifies potential new basal markers.* Oncogene, 2006. **25**(15): p. 2273-84.
71. Goncalves, A., et al., *Protein profiling of human breast tumor cells identifies novel biomarkers associated with molecular subtypes.* Mol Cell Proteomics, 2008. **7**(8): p. 1420-33.
72. Ponzo, M.G. and M. Park, *The Met receptor tyrosine kinase and basal breast cancer.* Cell Cycle, 2010. **9**(6): p. 1043-50.
73. Graveel, C.R., et al., *Met induces diverse mammary carcinomas in mice and is associated with human basal breast cancer.* Proc Natl Acad Sci U S A, 2009. **106**(31): p. 12909-14.
74. Garcia, S., et al., *Poor prognosis in breast carcinomas correlates with increased expression of targetable CD146 and c-Met and with proteomic basal-like phenotype.* Hum Pathol, 2007. **38**(6): p. 830-41.
75. Yan, S., et al., *Prognostic significance of c-Met in breast cancer: a meta-analysis of 6010 cases.* Diagn Pathol, 2015. **10**: p. 62.
76. Mueller, K.L., et al., *EGFR/Met association regulates EGFR TKI resistance in breast cancer.* J Mol Signal, 2010. **5**: p. 8.
77. Landi, L., et al., *Targeting c-MET in the battle against advanced nonsmall-cell lung cancer.* Curr Opin Oncol, 2013. **25**(2): p. 130-6.
78. Scagliotti, G.V., S. Novello, and J. von Pawel, *The emerging role of MET/HGF inhibitors in oncology.* Cancer Treat Rev, 2013. **39**(7): p. 793-801.
79. https://clinicaltrials.gov/ct2/show/NCT01186991, *Study Evaluating the Safety and Efficacy of Onartuzumab (Metmab) And/Or Bevacizumab in Combination With Paclitaxel in Patients With Metastatic, Triple Negative Breast Cancer.* Aug 2010.
80. https://clinicaltrials.gov/ct2/show/NCT01147484, *A Study of Foretinib in Patients With Recurrent/Metastatic Breast Cancer (IND197)*

May 2010.
81. https://clinicaltrials.gov/show/NCT01738438, *Cabozantinib for Metastatic Triple Negative BrCa. Institute D-FC.* Nov 2012
82. *Tivantinib in Treating Patients With Recurrent or Metastatic Breast Cancer*. 2012; Available from: https://clinicaltrials.gov/ct2/show/NCT01575522.

83. Schettino, C., et al., *Erlotinib: an EGF receptor tyrosine kinase inhibitor in non-small-cell lung cancer treatment.* Expert Rev Respir Med, 2008. **2**(2): p. 167-78.
84. *A Safety and Efficacy Study of INC280 and Gefitinib in Patients With EGFR Mutated, c-MET-amplified NSCLC Who Have Progressed After EGFRi Treatment*. 2012; Available from: https://clinicaltrials.gov/ct2/show/NCT01610336?term=c-Met+inhibition+and+lung+cancer&rank=1.
85. *Study Efficacy and Safety of INC280 in Patients With Advanced Hepatocellular Carcinoma*. 2012; Available from: https://clinicaltrials.gov/ct2/show/NCT01737827?term=%28INC280%29+in+advanced+hepatocellular+carcinoma+%28HCC%29.&rank=2.
86. *Phase I/II Trial of Tivantinib With FOLFOX for the Treatment of Advanced Solid Tumors and Previously Untreated Metastatic Adenocarcinoma of the Distal Esophagus, Gastroesophageal Junction or Stomach* 2012; Available from: https://clinicaltrials.gov/ct2/show/NCT01611857?term=gastroesophageal+cancer+and+c-met+inhibitors&rank=1.
87. Yu, H.A., et al., *Analysis of tumor specimens at the time of acquired resistance to EGFR-TKI therapy in 155 patients with EGFR-mutant lung cancers.* Clin Cancer Res, 2013. **19**(8): p. 2240-7.
88. Xu, M., et al., *The latest therapeutic strategies after resistance to first generation epidermal growth factor receptor tyrosine kinase inhibitors (EGFR TKIs) in patients with non-small cell lung cancer (NSCLC).* Ann Transl Med, 2015. **3**(7): p. 96.
89. Zhang, Y.W., et al., *MET kinase inhibitor SGX523 synergizes with epidermal growth factor receptor inhibitor erlotinib in a hepatocyte growth factor-dependent fashion to suppress carcinoma growth.* Cancer Res, 2010. **70**(17): p. 6880-90.
90. Lai, A.Z., J.V. Abella, and M. Park, *Crosstalk in Met receptor oncogenesis.* Trends Cell Biol, 2009. **19**(10): p. 542-51.
91. Witton, C.J., et al., *Expression of the HER1-4 family of receptor tyrosine kinases in breast cancer.* J Pathol, 2003. **200**(3): p. 290-7.
92. Tovey, S.M., et al., *Outcome and human epidermal growth factor receptor (HER) 1-4 status in invasive breast carcinomas with proliferation indices evaluated by bromodeoxyuridine labelling.* Breast Cancer Res, 2004. **6**(3): p. R246-51.
93. Generali, D., et al., *EGFR mutations in exons 18-21 in sporadic breast cancer*, in *Ann Oncol*. 2007: England. p. 203-5.
94. Bhargava, R., et al., *EGFR gene amplification in breast cancer: correlation with epidermal growth factor receptor mRNA and protein expression and HER-2 status and absence of EGFR-activating mutations.* Mod Pathol, 2005. **18**(8): p. 1027-33.
95. Nieto, Y., et al., *Prognostic significance of overexpression and phosphorylation of epidermal growth factor receptor (EGFR) and the presence of truncated EGFRvIII in locoregionally advanced breast cancer.* J Clin Oncol, 2007. **25**(28): p. 4405-13.
96. Herbst, R.S., M. Fukuoka, and J. Baselga, *Gefitinib--a novel targeted approach to treating cancer.* Nat Rev Cancer, 2004. **4**(12): p. 956-65.
97. Herbst, R.S. and D.M. Shin, *Monoclonal antibodies to target epidermal growth factor receptor-positive tumors: a new paradigm for cancer therapy.* Cancer, 2002. **94**(5): p. 1593-611.

98. Xu, B., et al., *MiR-146a suppresses tumor growth and progression by targeting EGFR pathway and in a p-ERK-dependent manner in castration-resistant prostate cancer.* Prostate, 2012. **72**(11): p. 1171-8.
99. Purvis, J., V. Ilango, and R. Radhakrishnan, *Role of network branching in eliciting differential short-term signaling responses in the hypersensitive epidermal growth factor receptor mutants implicated in lung cancer.* Biotechnol Prog, 2008. **24**(3): p. 540-53.
100. Hynes, N.E. and H.A. Lane, *ERBB receptors and cancer: the complexity of targeted inhibitors.* Nat Rev Cancer, 2005. **5**(5): p. 341-54.
101. Monteleone, G., et al., *Silencing of SH-PTP2 defines a crucial role in the inactivation of epidermal growth factor receptor by 5-aminosalicylic acid in colon cancer cells.* Cell Death Differ, 2006. **13**(2): p. 202-11.
102. Sorkin, A. and L.K. Goh, *Endocytosis and intracellular trafficking of ErbBs.* Exp Cell Res, 2008. **314**(17): p. 3093-106.
103. Mosesson, Y., G.B. Mills, and Y. Yarden, *Derailed endocytosis: an emerging feature of cancer.* Nat Rev Cancer, 2008. **8**(11): p. 835-50.
104. Tomas, A., C.E. Futter, and E.R. Eden, *EGF receptor trafficking: consequences for signaling and cancer.* Trends Cell Biol, 2014. **24**(1): p. 26-34.
105. Bauerfeind, R., T. Galli, and P. De Camilli, *Molecular mechanisms in synaptic vesicle recycling.* J Neurocytol, 1996. **25**(12): p. 701-15.
106. Marmor, M.D. and Y. Yarden, *Role of protein ubiquitylation in regulating endocytosis of receptor tyrosine kinases.* Oncogene, 2004. **23**(11): p. 2057-70.
107. Chang, C.P., et al., *Ligand-induced internalization and increased cell calcium are mediated via distinct structural elements in the carboxyl terminus of the epidermal growth factor receptor.* J Biol Chem, 1991. **266**(34): p. 23467-70.
108. Hershko, A. and A. Ciechanover, *The ubiquitin system.* Annu Rev Biochem, 1998. **67**: p. 425-79.
109. Levkowitz, G., et al., *Ubiquitin ligase activity and tyrosine phosphorylation underlie suppression of growth factor signaling by c-Cbl/Sli-1.* Mol Cell, 1999. **4**(6): p. 1029-40.
110. Waterman, H., et al., *A mutant EGF-receptor defective in ubiquitylation and endocytosis unveils a role for Grb2 in negative signaling.* Embo j, 2002. **21**(3): p. 303-13.
111. Woodman, P., *ESCRT proteins, endosome organization and mitogenic receptor down-regulation.* Biochem Soc Trans, 2009. **37**(Pt 1): p. 146-50.
112. Petrelli, A., et al., *The endophilin-CIN85-Cbl complex mediates ligand-dependent downregulation of c-Met.* Nature, 2002. **416**(6877): p. 187-90.
113. Wong, C.I., et al., *Lack of somatic ErbB2 tyrosine kinase domain mutations in hepatocellular carcinoma.* Hepatol Res, 2008. **38**(8): p. 838-41.
114. Felder, S., et al., *Kinase activity controls the sorting of the epidermal growth factor receptor within the multivesicular body.* Cell, 1990. **61**(4): p. 623-34.

115. French, A.R., et al., *Postendocytic trafficking of epidermal growth factor-receptor complexes is mediated through saturable and specific endosomal interactions.* J Biol Chem, 1994. **269**(22): p. 15749-55.
116. Carlin, L.M., et al., *Visualisation of signalling in immune cells.* Methods Mol Biol, 2010. **616**: p. 97-113.
117. Fruhwirth, G.O., et al., *How Forster resonance energy transfer imaging improves the understanding of protein interaction networks in cancer biology.* Chemphyschem, 2011. **12**(3): p. 442-61.
118. Patel, G.S., et al., *The challenges of integrating molecular imaging into the optimization of cancer therapy.* Integr Biol (Camb), 2011. **3**(6): p. 603-31.
119. Kelleher, M.T., et al., *The potential of optical proteomic technologies to individualize prognosis and guide rational treatment for cancer patients.* Target Oncol, 2009. **4**(3): p. 235-52.
120. Peter, M. and S.M. Ameer-Beg, *Imaging molecular interactions by multiphoton FLIM.* Biol Cell, 2004. **96**(3): p. 231-6.
121. Sun, T., et al., *Activation of multiple proto-oncogenic tyrosine kinases in breast cancer via loss of the PTPN12 phosphatase.* Cell, 2011. **144**(5): p. 703-18.
122. Spring, K., et al., *The protein tyrosine phosphatase DEP-1/PTPRJ promotes breast cancer cell invasion and metastasis.* Oncogene, 2015. **34**(44): p. 5536-47.
123. Andersen, J.N., et al., *A genomic perspective on protein tyrosine phosphatases: gene structure, pseudogenes, and genetic disease linkage.* Faseb j, 2004. **18**(1): p. 8-30.
124. Raugei, G., G. Ramponi, and P. Chiarugi, *Low molecular weight protein tyrosine phosphatases: small, but smart.* Cell Mol Life Sci, 2002. **59**(6): p. 941-9.
125. Boutros, R., V. Lobjois, and B. Ducommun, *CDC25 phosphatases in cancer cells: key players? Good targets?* Nat Rev Cancer, 2007. **7**(7): p. 495-507.
126. Tonks, N.K., *Protein tyrosine phosphatases--from housekeeping enzymes to master regulators of signal transduction.* Febs j, 2013. **280**(2): p. 346-78.
127. Lilien, J. and J. Balsamo, *The regulation of cadherin-mediated adhesion by tyrosine phosphorylation/dephosphorylation of beta-catenin.* Curr Opin Cell Biol, 2005. **17**(5): p. 459-65.
128. Ostman, A., C. Hellberg, and F.D. Bohmer, *Protein-tyrosine phosphatases and cancer.* Nat Rev Cancer, 2006. **6**(4): p. 307-20.
129. Xunyi, Y., et al., *Clinicopathological significance of PTPN12 expression in human breast cancer.* Braz J Med Biol Res, 2012. **45**(12): p. 1334-40.
130. Kontaridis, M.I., et al., *Deletion of Ptpn11 (Shp2) in cardiomyocytes causes dilated cardiomyopathy via effects on the extracellular signal-regulated kinase/mitogen-activated protein kinase and RhoA signaling pathways.* Circulation, 2008. **117**(11): p. 1423-35.
131. Zhou, X., et al., *SHP2 is up-regulated in breast cancer cells and in infiltrating ductal carcinoma of the breast, implying its involvement in breast oncogenesis.* Histopathology, 2008. **53**(4): p. 389-402.

132. Qu, C.K., *Role of the SHP-2 tyrosine phosphatase in cytokine-induced signaling and cellular response.* Biochim Biophys Acta, 2002. **1592**(3): p. 297-301.
133. Mohi, M.G. and B.G. Neel, *The role of Shp2 (PTPN11) in cancer.* Curr Opin Genet Dev, 2007. **17**(1): p. 23-30.
134. Loh, M.L., et al., *Mutations in PTPN11 implicate the SHP-2 phosphatase in leukemogenesis.* Blood, 2004. **103**(6): p. 2325-31.
135. Hess, J.L., et al., *Juvenile chronic myelogenous leukemia.* Am J Clin Pathol, 1996. **105**(2): p. 238-48.
136. Mohi, M.G., et al., *Prognostic, therapeutic, and mechanistic implications of a mouse model of leukemia evoked by Shp2 (PTPN11) mutations.* Cancer Cell, 2005. **7**(2): p. 179-91.
137. Brummer, T., et al., *Increased proliferation and altered growth factor dependence of human mammary epithelial cells overexpressing the Gab2 docking protein.* J Biol Chem, 2006. **281**(1): p. 626-37.
138. Bentires-Alj, M., et al., *A role for the scaffolding adapter GAB2 in breast cancer.* Nat Med, 2006. **12**(1): p. 114-21.
139. Dong, S., et al., *Expression and clinical significance of SHP2 in gastric cancer.* J Int Med Res, 2012. **40**(6): p. 2083-9.
140. Aceto, N., et al., *Tyrosine phosphatase SHP2 promotes breast cancer progression and maintains tumor-initiating cells via activation of key transcription factors and a positive feedback signaling loop.* Nat Med, 2012. **18**(4): p. 529-37.
141. Feng, Y., et al., *EGF signalling pathway regulates colon cancer stem cell proliferation and apoptosis.* Cell Prolif, 2012. **45**(5): p. 413-9.
142. Bard-Chapeau, E.A., et al., *Ptpn11/Shp2 acts as a tumor suppressor in hepatocellular carcinogenesis.* Cancer Cell, 2011. **19**(5): p. 629-39.
143. Agazie, Y.M. and M.J. Hayman, *Molecular mechanism for a role of SHP2 in epidermal growth factor receptor signaling.* Mol Cell Biol, 2003. **23**(21): p. 7875-86.
144. Kamer, A.R., S.A. Hoghooghi, and C. Liebow, *Epidermal growth factor downregulates the expression of SH-PTP2.* Int J Mol Med, 1998. **1**(4): p. 735-9.
145. Blagoev, B., et al., *A proteomics strategy to elucidate functional protein-protein interactions applied to EGF signaling.* Nat Biotechnol, 2003. **21**(3): p. 315-8.
146. J, B. *THE ADDITION OF CETUXIMAB TO CISPLATIN INCREASES*

OVERALL RESPONSE RATE (ORR) AND PROGRESSIONFREE

SURVIVAL (PFS) IN METASTATIC TRIPLE-NEGATIVE

BREAST CANCER (TNBC): RESULTS OF A RANDOMIZED

PHASE II STUDY (BALI-1). 2010; Available from: http://annonc.oxfordjournals.org/content/21/suppl_8/viii96.
147. Spigel, D.R., et al., *Treatment Rationale Study Design for the MetLung Trial: A Randomized, Double-Blind Phase III Study of Onartuzumab (MetMAb) in Combination With Erlotinib Versus Erlotinib Alone in Patients Who Have Received Standard Chemotherapy for*

Stage IIIB or IV Met-Positive Non-Small-Cell Lung Cancer. Clin Lung Cancer, 2012. **13**(6): p. 500-4.
148. Soultati, A., D.H. Josephs, and J.F. Spicer, *Effect of onartuzumab added to erlotinib on metastasis in patients with lung cancer*, in *J Clin Oncol*. 2014: United States. p. 3781.
149. EMMA, S. *On the Failure of Lung Cancer Drug Onartuzumab in a Phase III Clinical Trial*. 2014; Available from: https://www.cancercommons.org/2014/03/17/on-the-failure-of-lung-cancer-drug-onartuzumab-in-a-phase-iii-clinical-trial/.
150. Alan, R., L. Simon, and L. Alice *Imaging techniques in breast cancer*. 2016. **34**, 8-18.
151. Nakashima, K., et al., *Comparison of visibility of circumscribed masses on Digital Breast Tomosynthesis (DBT) and 2D mammography: are circumscribed masses better visualized and assured of being benign on DBT?* Eur Radiol, 2016.
152. Bednarski, P., et al., *Breast ultrasound scans - surgeons' expectations.* J Ultrason, 2015. **15**(61): p. 164-71.
153. Berg, W.A., et al., *Combined screening with ultrasound and mammography vs mammography alone in women at elevated risk of breast cancer.* Jama, 2008. **299**(18): p. 2151-63.
154. Benndorf, M., et al., *Breast MRI as an adjunct to mammography: Does it really suffer from low specificity? A retrospective analysis stratified by mammographic BI-RADS classes.* Acta Radiol, 2010. **51**(7): p. 715-21.
155. Berg, W.A., *Nuclear Breast Imaging: Clinical Results and Future Directions.* J Nucl Med, 2016. **57 Suppl 1**: p. 46s-52s.
156. Gaeta, C.M., et al., *Recurrent and metastatic breast cancer PET, PET/CT, PET/MRI: FDG and new biomarkers.* Q J Nucl Med Mol Imaging, 2013. **57**(4): p. 352-66.
157. Pengel, K.E., et al., *The impact of preoperative MRI on breast-conserving surgery of invasive cancer: a comparative cohort study.* Breast Cancer Res Treat, 2009. **116**(1): p. 161-9.
158. Gallamini, A., C. Zwarthoed, and A. Borra, *Positron Emission Tomography (PET) in Oncology.* Cancers (Basel), 2014. **6**(4): p. 1821-89.
159. Paul, S. and T. David, *Clinical PET-CT in Radiology: Integrated Imaging in Oncology*. 2011: Springer.
160. Massoud, T.F. and S.S. Gambhir, *Molecular imaging in living subjects: seeing fundamental biological processes in a new light.* Genes Dev, 2003. **17**(5): p. 545-80.
161. Saleem, A., N. Charnley, and P. Price, *Clinical molecular imaging with positron emission tomography.* Eur J Cancer, 2006. **42**(12): p. 1720-7.
162. Vercher-Conejero, J.L., et al., *Positron Emission Tomography in Breast Cancer.* Diagnostics (Basel), 2015. **5**(1): p. 61-83.
163. Eubank, W.B., et al., *Impact of FDG PET on defining the extent of disease and on the treatment of patients with recurrent or metastatic breast cancer.* AJR Am J Roentgenol, 2004. **183**(2): p. 479-86.
164. van Es, S.C., et al., *Translation of New Molecular Imaging Approaches to the Clinical Setting: Bridging the Gap to Implementation.* J Nucl Med, 2016. **57 Suppl 1**: p. 96s-104s.

165. *Special report: screening asymptomatic women with dense breasts and normal mammograms for breast cancer.* Technol Eval Cent Assess Program Exec Summ, 2014. **28**(15): p. 1-2.
166. Adejolu, M., et al., *False-positive lesions mimicking breast cancer on FDG PET and PET/CT.* AJR Am J Roentgenol, 2012. **198**(3): p. W304-14.
167. Schneble, E.J., et al., *Future directions for the early detection of recurrent breast cancer.* J Cancer, 2014. **5**(4): p. 291-300.
168. Kumar, R., et al., *Clinicopathologic factors associated with false negative FDG-PET in primary breast cancer.* Breast Cancer Res Treat, 2006. **98**(3): p. 267-74.
169. Olafsen, T. and A.M. Wu, *Antibody vectors for imaging.* Semin Nucl Med, 2010. **40**(3): p. 167-81.
170. Soloviev, D., et al., *[(18)F]FLT: an imaging biomarker of tumour proliferation for assessment of tumour response to treatment.* Eur J Cancer, 2012. **48**(4): p. 416-24.
171. Deng, S.M., et al., *Assessment of tumor response to chemotherapy in patients with breast cancer using (18)F-FLT: a meta-analysis.* Chin J Cancer Res, 2014. **26**(5): p. 517-24.
172. Lim, H.S., et al., *FDG PET/CT for the detection and evaluation of breast diseases: usefulness and limitations.* Radiographics, 2007. **27 Suppl 1**: p. S197-213.
173. Yang, S.K., N. Cho, and W.K. Moon, *The role of PET/CT for evaluating breast cancer.* Korean J Radiol, 2007. **8**(5): p. 429-37.
174. Pooley, R.A., *AAPM/RSNA physics tutorial for residents: fundamental physics of MR imaging.* Radiographics, 2005. **25**(4): p. 1087-99.
175. Kang, J.H. and J.K. Chung, *Molecular-genetic imaging based on reporter gene expression.* J Nucl Med, 2008. **49 Suppl 2**: p. 164s-79s.
176. Contag, P.R., et al., *Bioluminescent indicators in living mammals.* Nat Med, 1998. **4**(2): p. 245-7.
177. Chi, C., et al., *Intraoperative imaging-guided cancer surgery: from current fluorescence molecular imaging methods to future multi-modality imaging technology.* Theranostics, 2014. **4**(11): p. 1072-84.
178. de Boer, E., et al., *Optical innovations in surgery.* Br J Surg, 2015. **102**(2): p. e56-72.
179. Hirche, C., et al., *An experimental study to evaluate the Fluobeam 800 imaging system for fluorescence-guided lymphatic imaging and sentinel node biopsy.* Surg Innov, 2013. **20**(5): p. 516-23.
180. Mieog, J.S., et al., *Image-guided tumor resection using real-time near-infrared fluorescence in a syngeneic rat model of primary breast cancer.* Breast Cancer Res Treat, 2011. **128**(3): p. 679-89.
181. Korb, M.L., et al., *Use of monoclonal antibody-IRDye800CW bioconjugates in the resection of breast cancer.* J Surg Res, 2014. **188**(1): p. 119-28.
182. Menke, J., *Photoacoustic breast tomography prototypes with reported human applications.* Eur Radiol, 2015. **25**(8): p. 2205-13.
183. Manohar, S., et al., *Initial results of in vivo non-invasive cancer imaging in the human breast using near-infrared photoacoustics.* Opt Express, 2007. **15**(19): p. 12277-85.

184. Agdeppa, E.D. and M.E. Spilker, *A review of imaging agent development.* Aaps j, 2009. **11**(2): p. 286-99.
185. Pantel, A.R. and D.A. Mankoff, *Molecular imaging to guide systemic cancer therapy: Illustrative examples of PET imaging cancer biomarkers.* Cancer Lett, 2016.
186. Chen, K. and X. Chen, *Positron emission tomography imaging of cancer biology: current status and future prospects.* Semin Oncol, 2011. **38**(1): p. 70-86.
187. Wu, A.M. and P.J. Yazaki, *Designer genes: recombinant antibody fragments for biological imaging.* Q J Nucl Med, 2000. **44**(3): p. 268-83.
188. Capala, J. and K. Bouchelouche, *Molecular imaging of HER2-positive breast cancer: a step toward an individualized 'image and treat' strategy.* Curr Opin Oncol, 2010. **22**(6): p. 559-66.
189. Holliger, P. and P.J. Hudson, *Engineered antibody fragments and the rise of single domains.* Nat Biotechnol, 2005. **23**(9): p. 1126-36.
190. Ward, E.S., et al., *From sorting endosomes to exocytosis: association of Rab4 and Rab11 GTPases with the Fc receptor, FcRn, during recycling.* Mol Biol Cell, 2005. **16**(4): p. 2028-38.
191. Rosebrough, S.F., et al., *Thrombus imaging with indium-111 and iodine-131-labeled fibrin-specific monoclonal antibody and its F(ab')2 and Fab fragments.* J Nucl Med, 1988. **29**(7): p. 1212-22.
192. Hu, S., et al., *Minibody: A novel engineered anti-carcinoembryonic antigen antibody fragment (single-chain Fv-CH3) which exhibits rapid, high-level targeting of xenografts.* Cancer Res, 1996. **56**(13): p. 3055-61.
193. Kim, Y.J., et al., *Improving the productivity of single-chain Fv antibody against c-Met by rearranging the order of its variable domains.* J Microbiol Biotechnol, 2008. **18**(6): p. 1186-90.
194. P, M.P., V.R. J, and T.N. G *In Vivo Applications of Single Chain Fv (Variable Domain) (scFv) Fragments*. Antibodies, 2013. **2**, 193-208.
195. Hudson, P.J., *Recombinant antibody fragments.* Curr Opin Biotechnol, 1998. **9**(4): p. 395-402.
196. Holliger, P., T. Prospero, and G. Winter, *"Diabodies": small bivalent and bispecific antibody fragments.* Proc Natl Acad Sci U S A, 1993. **90**(14): p. 6444-8.
197. Olafsen, T., et al., *ImmunoPET using engineered antibody fragments: fluorine-18 labeled diabodies for same-day imaging.* Tumour Biol, 2012. **33**(3): p. 669-77.
198. Kampmeier, F., et al., *Design and preclinical evaluation of a 99mTc-labelled diabody of mAb J591 for SPECT imaging of prostate-specific membrane antigen (PSMA).* EJNMMI Res, 2014. **4**(1): p. 13.
199. Fung, E.K., et al., *Targeting of radiolabeled J591 antibody to PSMA-expressing tumors: optimization of imaging and therapy based on non-linear compartmental modeling.* EJNMMI Res, 2016. **6**(1): p. 7.
200. Olafsen, T., et al., *Covalent disulfide-linked anti-CEA diabody allows site-specific conjugation and radiolabeling for tumor targeting applications.* Protein Eng Des Sel, 2004. **17**(1): p. 21-7.

201. Olafsen, T., et al., *Characterization of engineered anti-p185HER-2 (scFv-CH3)2 antibody fragments (minibodies) for tumor targeting.* Protein Eng Des Sel, 2004. **17**(4): p. 315-23.
202. Kenanova, V., et al., *Tailoring the pharmacokinetics and positron emission tomography imaging properties of anti-carcinoembryonic antigen single-chain Fv-Fc antibody fragments.* Cancer Res, 2005. **65**(2): p. 622-31.
203. Israel, E.J., et al., *Increased clearance of IgG in mice that lack beta 2-microglobulin: possible protective role of FcRn.* Immunology, 1996. **89**(4): p. 573-8.
204. Stern, L.A., B.A. Case, and B.J. Hackel, *Alternative Non-Antibody Protein Scaffolds for Molecular Imaging of Cancer.* Curr Opin Chem Eng, 2013. **2**(4).
205. Feldwisch, J. and V. Tolmachev, *Engineering of affibody molecules for therapy and diagnostics.* Methods Mol Biol, 2012. **899**: p. 103-26.
206. Lofblom, J., et al., *Affibody molecules: engineered proteins for therapeutic, diagnostic and biotechnological applications.* FEBS Lett, 2010. **584**(12): p. 2670-80.
207. Sorensen, J., et al., *Measuring HER2-Receptor Expression In Metastatic Breast Cancer Using [(68)Ga]ABY-025 Affibody PET/CT.* Theranostics, 2016. **6**(2): p. 262-71.
208. Dijkers, E.C., et al., *Development and characterization of clinical-grade 89Zr-trastuzumab for HER2/neu immunoPET imaging.* J Nucl Med, 2009. **50**(6): p. 974-81.
209. Smith-Jones, P.M., et al., *Imaging the pharmacodynamics of HER2 degradation in response to Hsp90 inhibitors.* Nat Biotechnol, 2004. **22**(6): p. 701-6.
210. Reddy, S., et al., *Evaluation of the anti-HER2 C6.5 diabody as a PET radiotracer to monitor HER2 status and predict response to trastuzumab treatment.* Clin Cancer Res, 2011. **17**(6): p. 1509-20.
211. Goldstein, R., et al., *Development of the designed ankyrin repeat protein (DARPin) G3 for HER2 molecular imaging.* Eur J Nucl Med Mol Imaging, 2015. **42**(2): p. 288-301.
212. Liu, S., et al., *Toward operative in vivo fluorescence imaging of the c-Met proto-oncogene for personalization of therapy in ovarian cancer.* Cancer, 2015. **121**(2): p. 202-13.
213. Burggraaf, J., et al., *Detection of colorectal polyps in humans using an intravenously administered fluorescent peptide targeted against c-Met.* Nat Med, 2015. **21**(8): p. 955-61.
214. Terwisscha van Scheltinga, A.G., et al., *In vivo visualization of MET tumor expression and anticalin biodistribution with the MET-specific anticalin 89Zr-PRS-110 PET tracer.* J Nucl Med, 2014. **55**(4): p. 665-71.
215. Luo, H., et al., *PET of c-Met in Cancer with (6)(4)Cu-Labeled Hepatocyte Growth Factor.* J Nucl Med, 2015. **56**(5): p. 758-63.
216. Almuhaideb, A., N. Papathanasiou, and J. Bomanji, *18F-FDG PET/CT imaging in oncology.* Ann Saudi Med, 2011. **31**(1): p. 3-13.
217. Leidy, J., A. Khan, and D. Kandil, *Basal-like breast cancer: update on clinicopathologic, immunohistochemical, and molecular features.* Arch Pathol Lab Med, 2014. **138**(1): p. 37-43.

218. Yehiely, F., et al., *Deconstructing the molecular portrait of basal-like breast cancer.* Trends Mol Med, 2006. **12**(11): p. 537-44.
219. Kim, Y.J., et al., *MET is a potential target for use in combination therapy with EGFR inhibition in triple-negative/basal-like breast cancer.* Int J Cancer, 2014. **134**(10): p. 2424-36.
220. Lowery, A.J., et al., *Locoregional recurrence after breast cancer surgery: a systematic review by receptor phenotype.* Breast Cancer Res Treat, 2012. **133**(3): p. 831-41.
221. Pogoda, K., et al., *Analysis of pattern, time and risk factors influencing recurrence in triple-negative breast cancer patients.* Med Oncol, 2013. **30**(1): p. 388-95.
222. Giuliano, A.E., et al., *Locoregional recurrence after sentinel lymph node dissection with or without axillary dissection in patients with sentinel lymph node metastases: the American College of Surgeons Oncology Group Z0011 randomized trial.* Ann Surg, 2010. **252**(3): p. 426-32; discussion 432-3.
223. Oakman, C., G. Viale, and A. Di Leo, *Management of triple negative breast cancer.* Breast, 2010. **19**(5): p. 312-21.
224. Overgaard, M., et al., *Postoperative radiotherapy in high-risk postmenopausal breast-cancer patients given adjuvant tamoxifen: Danish Breast Cancer Cooperative Group DBCG 82c randomised trial.* Lancet, 1999. **353**(9165): p. 1641-8.
225. Schneble, E.J., et al., *Current approaches and challenges in early detection of breast cancer recurrence.* J Cancer, 2014. **5**(4): p. 281-90.
226. Clarke, M., et al., *Effects of radiotherapy and of differences in the extent of surgery for early breast cancer on local recurrence and 15-year survival: an overview of the randomised trials.* Lancet, 2005. **366**(9503): p. 2087-106.
227. Coenen, H.H., et al., *Fluorine-18 radiopharmaceuticals beyond [18F]FDG for use in oncology and neurosciences.* Nucl Med Biol, 2010. **37**(7): p. 727-40.
228. Jacobson, O., D.O. Kiesewetter, and X. Chen, *Fluorine-18 radiochemistry, labeling strategies and synthetic routes.* Bioconjug Chem, 2015. **26**(1): p. 1-18.
229. Kanazawa, Y., et al., *2-Deoxy-2-fluoro-D-glucose as a functional probe for NMR: the unique metabolism beyond its 6-phosphate.* J Neurochem, 1996. **66**(5): p. 2113-20.
230. Quon, A. and S.S. Gambhir, *FDG-PET and beyond: molecular breast cancer imaging.* J Clin Oncol, 2005. **23**(8): p. 1664-73.
231. Sharma, N. and A.A. Adjei, *In the clinic: ongoing clinical trials evaluating c-MET-inhibiting drugs.* Ther Adv Med Oncol, 2011. **3**(1 Suppl): p. S37-50.
232. *Study Evaluating the Safety and Efficacy of Onartuzumab (Metmab) And/Or Bevacizumab in Combination With Paclitaxel in Patients With Metastatic, Triple Negative Breast Cancer*. 2010; Available from: https://clinicaltrials.gov/ct2/show/NCT01186991.
233. Eric, W. *Activity of cabozantinib (XL184) in metastatic breast cancer (MBC): Results from a phase II randomized discontinuation trial (RDT).* . 2012; Available from: http://meetinglibrary.asco.org/content/95393-114.

234. Garajova, I., et al., *c-Met as a Target for Personalized Therapy.* Transl Oncogenomics, 2015. **7**(Suppl 1): p. 13-31.
235. Birchmeier, C., et al., *Met, metastasis, motility and more.* Nat Rev Mol Cell Biol, 2003. **4**(12): p. 915-25.
236. Bean, J., et al., *MET amplification occurs with or without T790M mutations in EGFR mutant lung tumors with acquired resistance to gefitinib or erlotinib.* Proc Natl Acad Sci U S A, 2007. **104**(52): p. 20932-7.
237. Rong, S., et al., *Invasiveness and metastasis of NIH 3T3 cells induced by Met-hepatocyte growth factor/scatter factor autocrine stimulation.* Proc Natl Acad Sci U S A, 1994. **91**(11): p. 4731-5.
238. Bandla, S., et al., *Comparative genomics of esophageal adenocarcinoma and squamous cell carcinoma.* Ann Thorac Surg, 2012. **93**(4): p. 1101-6.
239. Gastaldi, S., P.M. Comoglio, and L. Trusolino, *The Met oncogene and basal-like breast cancer: another culprit to watch out for?* Breast Cancer Res, 2010. **12**(4): p. 208-17.
240. Eiermann, W. and K.A. Vallis, *Locoregional treatments for triple-negative breast cancer.* Ann Oncol, 2012. **23**: p. (Suppl 6):vi30-4.
241. Wapnir, I.L., et al., *Prognosis after ipsilateral breast tumor recurrence and locoregional recurrences in five National Surgical Adjuvant Breast and Bowel Project node-positive adjuvant breast cancer trials.* J Clin Oncol, 2006. **24**(13): p. 2028-37.
242. Voogd, A.C., et al., *Long-term prognosis of patients with local recurrence after conservative surgery and radiotherapy for early breast cancer.* Eur J Cancer, 2005. **41**(17): p. 2637-44.
243. Montgomery, D.A., K. Krupa, and T.G. Cooke, *Alternative methods of follow up in breast cancer: a systematic review of the literature.* Br J Cancer, 2007. **96**(11): p. 1625-32.
244. Burggraaf, J., et al., *Detection of colorectal polyps in humans using an intravenously administered fluorescent peptide targeted against c-Met.* Nat Med, 2015.
245. Ng, T., et al., *PKCalpha regulates beta1 integrin-dependent cell motility through association and control of integrin traffic.* EMBO J, 1999. **18**(14): p. 3909-23.
246. Battle, M.R., et al., *Monitoring tumor response to antiangiogenic sunitinib therapy with 18F-fluciclatide, an 18F-labeled alphaVbeta3-integrin and alphaV beta5-integrin imaging agent.* J Nucl Med, 2011. **52**(3): p. 424-30.
247. Meyers, M.O., et al., *Impact of breast cancer molecular subtypes on locoregional recurrence in patients treated with neoadjuvant chemotherapy for locally advanced breast cancer.* Ann Surg Oncol, 2011. **18**(10): p. 2851-7.
248. Sohn, Y.J., et al., *Early detection of recurrence after endoscopic treatment for early gastric cancer.* Scand J Gastroenterol, 2009. **44**(9): p. 1109-14.
249. Evans P, B.M., Getvoldsen G, McRobbie G, Bjerke R, Morrison M, Johannesen E, Dalsgaard GT, *Nonclinical tumor efficacy studies of [18F]AH113804, a novel PET imaging agent with high affinity for the*

human c-Met receptor [Abstract]. . Proceedings of the AACR 103rd Annual Meeting 2012. 31 Mar – 4 Apr 2012, Chicago, IL., 2012.
250. Vallabhajosula, S., *(18)F-labeled positron emission tomographic radiopharmaceuticals in oncology: an overview of radiochemistry and mechanisms of tumor localization.* Semin Nucl Med, 2007. **37**(6): p. 400-19.
251. Cullinane, C., et al., *Differential (18)F-FDG and 3'-deoxy-3'-(18)F-fluorothymidine PET responses to pharmacologic inhibition of the c-MET receptor in preclinical tumor models.* J Nucl Med, 2011. **52**(8): p. 1261-7.
252. McKinley, E.T., et al., *Limits of [18F]-FLT PET as a biomarker of proliferation in oncology.* PLoS One, 2013. **8**(3): p. e58938.
253. Jagoda, E.M., et al., *Immuno-PET of the hepatocyte growth factor receptor Met using the 1-armed antibody onartuzumab.* J Nucl Med, 2012. **53**(10): p. 1592-600.
254. Li, K., et al., *Anti-MET immunoPET for non-small cell lung cancer using novel fully human antibody fragments.* Mol Cancer Ther, 2014. **13**(11): p. 2607-17.
255. Leung, K., *89Zr-Desferrioxamine p-isothiocyanatobenzyl-anti-hepatocyte growth factor receptor 1-armed antibody onartuzumab*, in *Molecular Imaging and Contrast Agent Database (MICAD)*. 2004, National Center for Biotechnology Information (US): Bethesda (MD).
256. Wu, A.M. and T. Olafsen, *Antibodies for molecular imaging of cancer.* Cancer J, 2008. **14**(3): p. 191-7.
257. Kim, E.M., et al., *Characterization, biodistribution and small-animal SPECT of I-125-labeled c-Met binding peptide in mice bearing c-Met receptor tyrosine kinase-positive tumor xenografts.* Nucl Med Biol, 2009. **36**(4): p. 371-8.
258. Fletcher, J.W., et al., *Recommendations on the use of 18F-FDG PET in oncology.* J Nucl Med, 2008. **49**(3): p. 480-508.
259. Dehdashti, F., et al., *Positron emission tomographic assessment of "metabolic flare" to predict response of metastatic breast cancer to antiestrogen therapy.* Eur J Nucl Med, 1999. **26**(1): p. 51-6.
260. Weber, W.A., et al., *Technology Insight: novel imaging of molecular targets is an emerging area crucial to the development of targeted drugs.* Nat Clin Pract Oncol, 2008. **5**(1): p. 44-54.
261. Pool, M., G.M. van Dam, and E.G. de Vries, *Emerging Opportunities for c-MET Visualization in the Clinic.* J Nucl Med, 2016. **57**(5): p. 663-4.
262. Kraeber-Bodere, F., et al., *Tumor immunotargeting using innovative radionuclides.* Int J Mol Sci, 2015. **16**(2): p. 3932-54.
263. Yadav, N., et al., *Synthesis, Characterization, and Preclinical Evaluation of (99m) Tc-Labeled Macrobicyclic and Tricyclic Chelators as Single Photon Emission Computed Tomography Tracer.* Chem Biol Drug Des, 2016. **87**(5): p. 730-6.
264. van Wieringen, J.P., et al., *Ex Vivo Characterization of a Novel Iodine-123-Labelled Aminomethylchroman as a Potential Agonist Ligand for SPECT Imaging of Dopamine D2/3 Receptors.* Int J Mol Imaging, 2014. **2014**: p. 507012.

265. Malmberg, J., et al., *Comparative biodistribution of imaging agents for in vivo molecular profiling of disseminated prostate cancer in mice bearing prostate cancer xenografts: focus on 111In- and 125I-labeled anti-HER2 humanized monoclonal trastuzumab and ABY-025 affibody.* Nucl Med Biol, 2011. **38**(8): p. 1093-102.
266. Parry, R., et al., *Identification of a novel prostate tumor target, mindin/RG-1, for antibody-based radiotherapy of prostate cancer.* Cancer Res, 2005. **65**(18): p. 8397-405.
267. Tolmachev, V., et al., *The influence of Bz-DOTA and CHX-A''-DTPA on the biodistribution of ABD-fused anti-HER2 Affibody molecules: implications for (114m)In-mediated targeting therapy.* Eur J Nucl Med Mol Imaging, 2009. **36**(9): p. 1460-8.
268. Zhang, Y., H. Hong, and W. Cai, *PET tracers based on Zirconium-89.* Curr Radiopharm, 2011. **4**(2): p. 131-9.
269. Schofield, D.J., et al., *Application of phage display to high throughput antibody generation and characterization.* Genome Biol, 2007. **8**(11): p. R254.
270. Parr, C. and W.G. Jiang, *Expression of hepatocyte growth factor/scatter factor, its activator, inhibitors and the c-Met receptor in human cancer cells.* Int J Oncol, 2001. **19**(4): p. 857-63.
271. Bujak, E., et al., *Reformatting of scFv antibodies into the scFv-Fc format and their downstream purification.* Methods Mol Biol, 2014. **1131**: p. 315-34.
272. Rochefort, M.M., et al., *A mutated anti-CA19-9 scFv-Fc for positron emission tomography of human pancreatic cancer xenografts.* Mol Imaging Biol, 2014. **16**(5): p. 721-9.
273. Jager, V., et al., *High level transient production of recombinant antibodies and antibody fusion proteins in HEK293 cells.* BMC Biotechnol, 2013. **13**: p. 52.
274. Thomas, M. and A.M. Klibanov, *Enhancing polyethylenimine's delivery of plasmid DNA into mammalian cells.* Proc Natl Acad Sci U S A, 2002. **99**(23): p. 14640-5.
275. Godbey, W.T., K.K. Wu, and A.G. Mikos, *Tracking the intracellular path of poly(ethylenimine)/DNA complexes for gene delivery.* Proc Natl Acad Sci U S A, 1999. **96**(9): p. 5177-81.
276. Kim, E.M., et al., *In vivo imaging of mesenchymal-epithelial transition factor (c-Met) expression using an optical imaging system.* Bioconjug Chem, 2009. **20**(7): p. 1299-306.
277. Anand, P. *Intraoperative GE-137 fluorescence imaging in breast and oral cancer - See more at: http://www.hra.nhs.uk/news/research-summaries/intraoperative-ge-137-fluorescence-imaging-in-breast-and-oral-cancer/#sthash.8W7tB1rW.dpuf*. 2015; Available from: http://www.hra.nhs.uk/news/research-summaries/intraoperative-ge-137-fluorescence-imaging-in-breast-and-oral-cancer/.
278. Suemizu, H., et al., *A versatile technique for the in vivo imaging of human tumor xenografts using near-infrared fluorochrome-conjugated macromolecule probes.* PLoS One, 2013. **8**(12): p. e82708.
279. Kameswaran, M., et al., *Preparation & in vitro evaluation of (90) Y-DOTA-rituximab.* Indian J Med Res, 2016. **143**(1): p. 57-65.

280. Jagoda, E.M., et al., *Imaging the Met Receptor Tyrosine Kinase (Met) and Assessing Tumor Responses to a Met Tyrosine Kinase Inhibitor in Human Xenograft Mouse Models with a [99mTc] (AH-113018) or Cy 5** (AH-112543) Labeled Peptide.* Mol Imaging, 2015. **14**: p. 499-515.
281. Panke, C., et al., *Quantification of cell surface proteins with bispecific antibodies.* Protein Eng Des Sel, 2013. **26**(10): p. 645-54.
282. Olafsen, T., V.E. Kenanova, and A.M. Wu, *Tunable pharmacokinetics: modifying the in vivo half-life of antibodies by directed mutagenesis of the Fc fragment.* Nat Protoc, 2006. **1**(4): p. 2048-60.
283. Crown, J., J. O'Shaughnessy, and G. Gullo, *Emerging targeted therapies in triple-negative breast cancer.* Ann Oncol, 2012. **23 Suppl 6**: p. vi56-65.
284. Kobayashi, S., et al., *EGFR mutation and resistance of non-small-cell lung cancer to gefitinib.* N Engl J Med, 2005. **352**(8): p. 786-92.
285. Sohn, J., et al., *cMET Activation and EGFR-Directed Therapy Resistance in Triple-Negative Breast Cancer.* J Cancer, 2014. **5**(9): p. 745-53.
286. Davis, N.M., et al., *Deregulation of the EGFR/PI3K/PTEN/Akt/mTORC1 pathway in breast cancer: possibilities for therapeutic intervention.* Oncotarget, 2014. **5**(13): p. 4603-50.
287. Nicholson, R.I., J.M. Gee, and M.E. Harper, *EGFR and cancer prognosis.* Eur J Cancer, 2001. **37 Suppl 4**: p. S9-15.
288. Tsutsui, S., et al., *Prognostic value of epidermal growth factor receptor (EGFR) and its relationship to the estrogen receptor status in 1029 patients with breast cancer.* Breast Cancer Res Treat, 2002. **71**(1): p. 67-75.
289. Masuda, H., et al., *Role of Epidermal Growth Factor Receptor in Breast Cancer.* Breast Cancer Res Treat, 2012. **136**(2).
290. Hsu, J.M., et al., *Crosstalk between Arg 1175 methylation and Tyr 1173 phosphorylation negatively modulates EGFR-mediated ERK activation.* Nat Cell Biol, 2011. **13**(2): p. 174-81.
291. Okutani, T., et al., *Grb2/Ash binds directly to tyrosines 1068 and 1086 and indirectly to tyrosine 1148 of activated human epidermal growth factor receptors in intact cells.* J Biol Chem, 1994. **269**(49): p. 31310-4.
292. Ward, A.C., et al., *Direct binding of Shc, Grb2, SHP-2 and p40 to the murine granulocyte colony-stimulating factor receptor.* Biochim Biophys Acta, 1998. **1448**(1): p. 70-6.
293. Fukuda, S., et al., *Reversible interconversion and maintenance of mammary epithelial cell characteristics by the ligand-regulated EGFR system.* Sci Rep, 2016. **6**: p. 20209.
294. Keilhack, H., et al., *Phosphotyrosine 1173 mediates binding of the protein-tyrosine phosphatase SHP-1 to the epidermal growth factor receptor and attenuation of receptor signaling.* J Biol Chem, 1998. **273**(38): p. 24839-46.
295. Watermann, I., et al., *Improved diagnostics targeting c-MET in non-small cell lung cancer: expression, amplification and activation?* Diagn Pathol, 2015. **10**: p. 130.

296. Barrow-McGee, R. and S. Kermorgant, *Met endosomal signalling: in the right place, at the right time.* Int J Biochem Cell Biol, 2014. **49**: p. 69-74.
297. Montagner, A., et al., *A novel role for Gab1 and SHP2 in epidermal growth factor-induced Ras activation.* J Biol Chem, 2005. **280**(7): p. 5350-60.
298. Ponzetto, C., et al., *A multifunctional docking site mediates signaling and transformation by the hepatocyte growth factor/scatter factor receptor family.* Cell, 1994. **77**(2): p. 261-71.
299. Pelicci, G., et al., *Constitutive phosphorylation of Shc proteins in human tumors.* Oncogene, 1995. **11**(5): p. 899-907.
300. Matalkah, F., et al., *SHP2 acts both upstream and downstream of multiple receptor tyrosine kinases to promote basal-like and triple-negative breast cancer.* Breast Cancer Res, 2016. **18**.
301. Lemmon, M.A. and J. Schlessinger, *Cell signaling by receptor tyrosine kinases.* Cell, 2010. **141**(7): p. 1117-34.
302. Muenst, S., et al., *Src homology phosphotyrosyl phosphatase-2 expression is an independent negative prognostic factor in human breast cancer.* Histopathology, 2013. **63**(1): p. 74-82.
303. Roxanis, I., *Occurrence and significance of epithelial-mesenchymal transition in breast cancer.* J Clin Pathol, 2013. **66**(6): p. 517-21.
304. Kang, Y. and J. Massague, *Epithelial-mesenchymal transitions: twist in development and metastasis.* Cell, 2004. **118**(3): p. 277-9.
305. Radisky, D.C., *Epithelial-mesenchymal transition.* J Cell Sci, 2005. **118**(Pt 19): p. 4325-6.
306. Thiery, J.P., *Epithelial-mesenchymal transitions in tumour progression.* Nat Rev Cancer, 2002. **2**(6): p. 442-54.
307. Kowalczyk, A.P., et al., *Desmosomes: intercellular adhesive junctions specialized for attachment of intermediate filaments.* Int Rev Cytol, 1999. **185**: p. 237-302.
308. Singhai, R., et al., *E-Cadherin as a diagnostic biomarker in breast cancer.* N Am J Med Sci, 2011. **3**(5): p. 227-33.
309. Kurokawa, K., et al., *A pair of fluorescent resonance energy transfer-based probes for tyrosine phosphorylation of the CrkII adaptor protein in vivo.* J Biol Chem, 2001. **276**(33): p. 31305-10.
310. Makrogianneli, K., et al., *Integrating receptor signal inputs that influence small Rho GTPase activation dynamics at the immunological synapse.* Mol Cell Biol, 2009.
311. Vega, F.M., et al., *RhoA and RhoC have distinct roles in migration and invasion by acting through different targets.* J Cell Biol, 2011. **193**(4): p. 655-65.
312. Breindel, J.L., et al., *EGF receptor activates MET through MAPK to enhance non-small cell lung carcinoma invasion and brain metastasis.* Cancer Res, 2013. **73**(16): p. 5053-65.
313. Beviglia, L., et al., *Expression of the c-Met/HGF receptor in human breast carcinoma: correlation with tumor progression.* Int J Cancer, 1997. **74**(3): p. 301-9.
314. Hu, Z., et al., *A tyrosine phosphatase SHP2 gain-of-function mutation enhances malignancy of breast carcinoma.* Oncotarget, 2016. **7**(5): p. 5664-76.

315. Villasenor, R., et al., *Regulation of EGFR signal transduction by analogue-to-digital conversion in endosomes.* Elife, 2015. **4**.
316. Haj, F.G., et al., *Regulation of receptor tyrosine kinase signaling by protein tyrosine phosphatase-1B.* J Biol Chem, 2003. **278**(2): p. 739-44.
317. Prahallad, A., et al., *PTPN11 Is a Central Node in Intrinsic and Acquired Resistance to Targeted Cancer Drugs.* Cell Rep, 2015. **12**(12): p. 1978-85.
318. Sangwan, V., et al., *Regulation of the Met receptor-tyrosine kinase by the protein-tyrosine phosphatase 1B and T-cell phosphatase.* J Biol Chem, 2008. **283**(49): p. 34374-83.
319. Sierra, J.R., et al., *Tumor angiogenesis and progression are enhanced by Sema4D produced by tumor-associated macrophages.* J Exp Med, 2008. **205**(7): p. 1673-85.
320. Soong, J. and G. Scott, *Plexin B1 inhibits MET through direct association and regulates Shp2 expression in melanocytes.* J Cell Sci, 2013. **126**(Pt 2): p. 688-95.
321. Xu, L., et al., *Epidermal growth factor receptor regulates MET levels and invasiveness through hypoxia-inducible factor-1alpha in non-small cell lung cancer cells.* Oncogene, 2010. **29**(18): p. 2616-27.
322. Zhao, H. and Y.M. Agazie, *Inhibition of SHP2 in basal-like and triple-negative breast cells induces basal-to-luminal transition, hormone dependency, and sensitivity to anti-hormone treatment.* BMC Cancer, 2015. **15**: p. 109.
323. Yonemura, Y., et al., *E-cadherin and c-met expression as a prognostic factor in gastric cancer.* Oncol Rep, 1997. **4**(4): p. 743-8.
324. Le Bras, G.F., K.J. Taubenslag, and C.D. Andl, *The regulation of cell-cell adhesion during epithelial-mesenchymal transition, motility and tumor progression.* Cell Adh Migr, 2012. **6**(4): p. 365-73.
325. Wang, Z. and S.S. Li, *Numb: A new player in EMT.* Cell Adh Migr, 2010. **4**(2): p. 176-9.
326. Gholamin, S., et al., *Targeting c-MET/HGF signaling pathway in upper gastrointestinal cancers: rationale and progress.* Curr Drug Targets, 2014. **15**(14): p. 1302-11.
327. Hammond, D.E., S. Carter, and M.J. Clague, *Met receptor dynamics and signalling.* Curr Top Microbiol Immunol, 2004. **286**: p. 21-44.
328. Perk, L.R., et al., *Quantitative PET imaging of Met-expressing human cancer xenografts with 89Zr-labelled monoclonal antibody DN30.* Eur J Nucl Med Mol Imaging, 2008. **35**(10): p. 1857-67.
329. Nguyen, K.S., S. Kobayashi, and D.B. Costa, *Acquired resistance to epidermal growth factor receptor tyrosine kinase inhibitors in non-small-cell lung cancers dependent on the epidermal growth factor receptor pathway.* Clin Lung Cancer, 2009. **10**(4): p. 281-9.
330. Freise, A.C. and A.M. Wu, *In vivo imaging with antibodies and engineered fragments.* Mol Immunol, 2015. **67**(2 Pt A): p. 142-52.
331. Swiercz, R., et al., *Use of Fc-Engineered Antibodies as Clearing Agents to Increase Contrast During PET.* J Nucl Med, 2014. **55**(7): p. 1204-7.

332. Ward, E.S., S.C. Devanaboyina, and R.J. Ober, *Targeting FcRn for the modulation of antibody dynamics.* Mol Immunol, 2015. **67**(2 Pt A): p. 131-41.
333. Furcht, C.M., et al., *Diminished functional role and altered localization of SHP2 in non-small cell lung cancer cells with EGFR-activating mutations.* Oncogene, 2013. **32**(18): p. 2346-55, 2355.e1-10.
334. Miura, K., et al., *Involvement of EphA2-mediated tyrosine phosphorylation of Shp2 in Shp2-regulated activation of extracellular signal-regulated kinase.* Oncogene, 2013. **32**(45): p. 5292-301.
335. Leung, K.K., et al., *Enhanced prediction of Src homology 2 (SH2) domain binding potentials using a fluorescence polarization-derived c-Met, c-Kit, ErbB, and androgen receptor interactome.* Mol Cell Proteomics, 2014. **13**(7): p. 1705-23.
336. Mood, K., et al., *Gab1 is required for cell cycle transition, cell proliferation, and transformation induced by an oncogenic met receptor.* Mol Biol Cell, 2006. **17**(9): p. 3717-28.
337. Grosskopf, S., et al., *Selective inhibitors of the protein tyrosine phosphatase SHP2 block cellular motility and growth of cancer cells in vitro and in vivo.* ChemMedChem, 2015. **10**(5): p. 815-26.
338. Zhen, X.L., et al., *Synthesis and biological evaluation of open-chain analogs of cyclic peptides as inhibitors of cellular Shp2 activity.* Bioorg Med Chem, 2015. **23**(10): p. 2562-7.
339. Ayush, G. *SPECT VS PET*. Available from: http://radiopaedia.org/articles/spect-vs-pet.
340. Sausgruber, N., et al., *Tyrosine phosphatase SHP2 increases cell motility in triple-negative breast cancer through the activation of SRC-family kinases.* Oncogene, 2015. **34**(17): p. 2272-8.

Chapter 9: Appendix

9.1 Chromatograms from the serum stability assay

Integration c:\GINA_NT\MICHELLE SEC2000\160512_IN111_FREE, 160512_In111_free Start: 12/05/2016 11:28

Indium-free: Labelling control

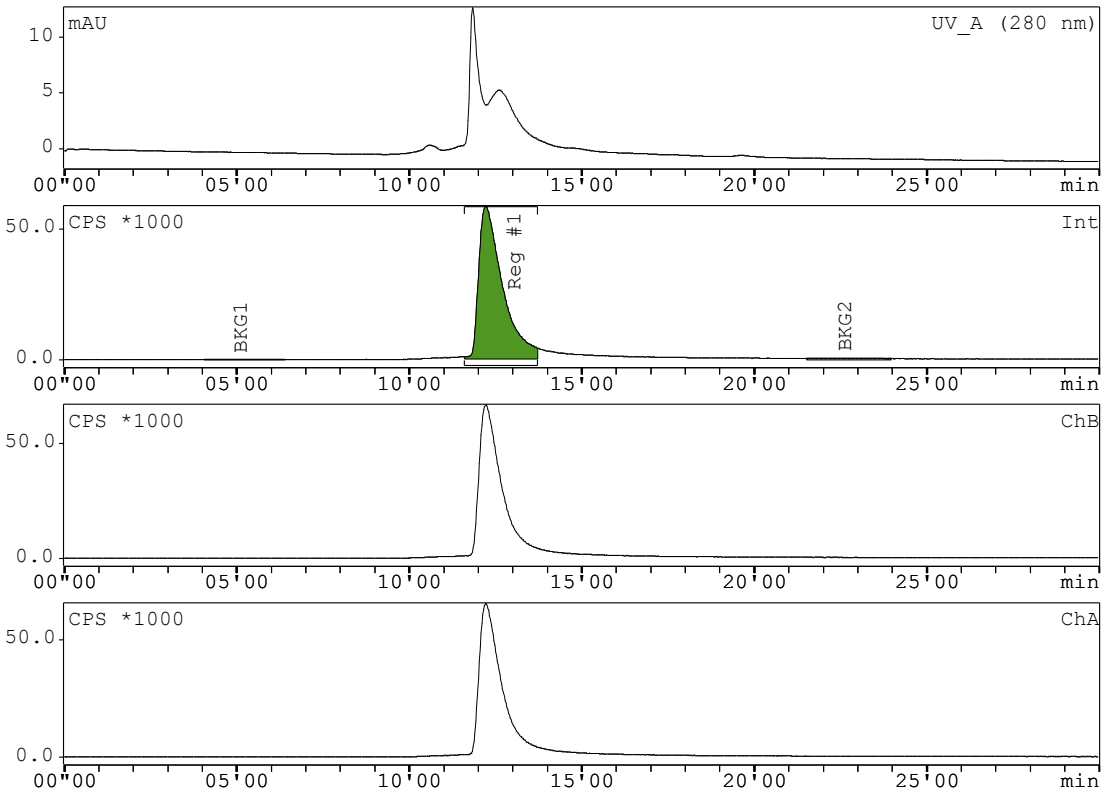

Sample description

Measurement: 160512_In111_free, injection : 12/05/2016 11:28

Method: MICHELLE SEC2000 from: 03/03/2016 12:02

Dead time of column: 01'00 s

Radio detector: raytest Gabi Star Serial Nr.: #30484 raytest GINA star 20.04.09 Firmware V4.8

Integration Int

Substance	R/T	Type	Area	%Area	Conc

	s		Counts	%	
Reg #1	12'12	DD(M)	2803397	100.00	No comp.

Integration c:\GINA_NT\MICHELLE SEC2000\160512_APPI_IN11_EXTRA, 160512_appi_In11_extra Start: 12/05/2016 12:03

QC reaction of ^{111}In-CHX-A''DTPA-scFv-Fc

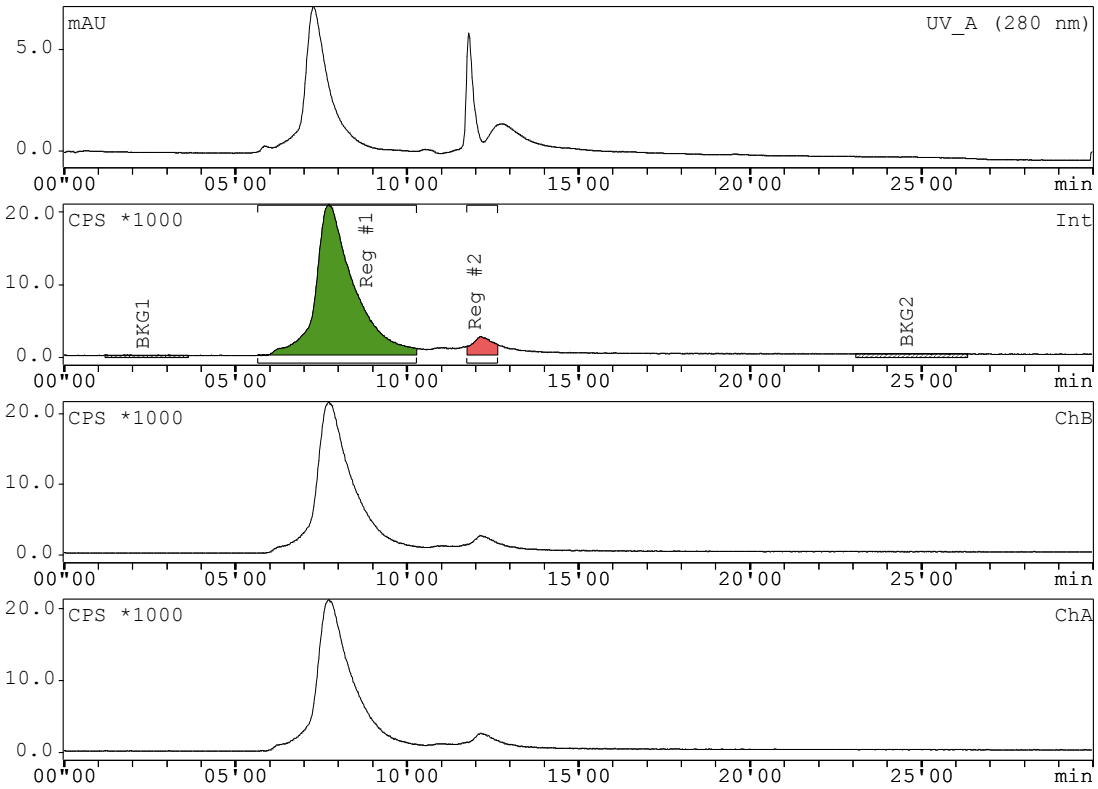

Sample description

Measurement: 160512_appi_In11_extra, injection : 12/05/2016 12:03

Method: MICHELLE SEC2000 from: 03/03/2016 12:02

Dead time of column: 01'00 s

Radio detector: raytest Gabi Star Serial Nr.: #30484 raytest GINA star 20.04.09 Firmware V4.8

Integration Int

Substance	R/T	Type	Area	%Area	Conc
	s		Counts	%	

Reg #1	07'43	DD(M)	1597145	94.07	No comp.
Reg #2	12'08	DD(M)	100722	5.93	No comp.

Integration c:\GINA_NT\MICHELLE SEC2000\160512_S1, 160512_s1 Start: 12/05/2016 13:12

^{111}In-CHX-A''DTPA-scFv-Fc in human serum for 1h

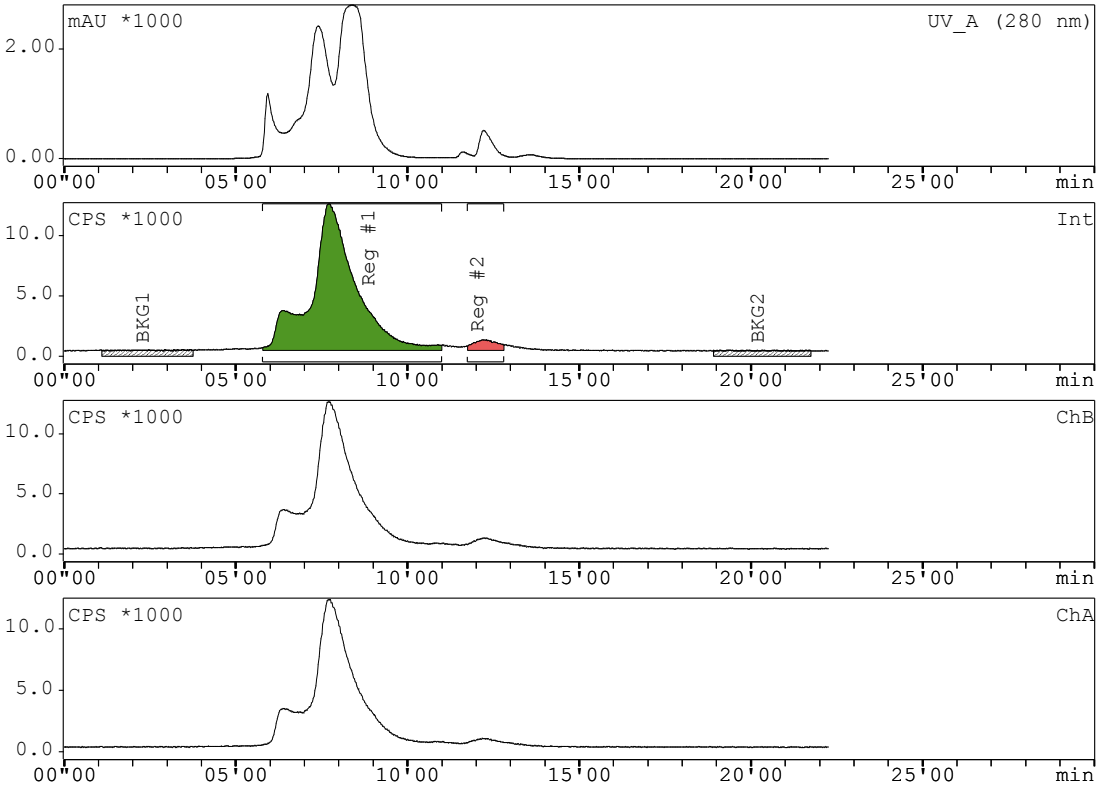

Sample description

Measurement: 160512_s1, injection : 12/05/2016 13:12

Method: MICHELLE SEC2000 from: 03/03/2016 12:02

Dead time of column: 01'00 s

Radio detector: raytest Gabi Star Serial Nr.: #30484 raytest GINA star 20.04.09 Firmware V4.8

Integration Int

Substance	R/T	Type	Area	%Area	Conc
	s		Counts	%	

Reg #1	07'42	DD(M)	1101729	96.23	No comp.
Reg #2	12'10	DD(M)	43147	3.77	No comp.

Integration c:\GINA_NT\MICHELLE SEC2000\160512_IN111_S11, 160512_In111_s11 Start: 12/05/2016 14:16

Indium-111 in human serum for 1h

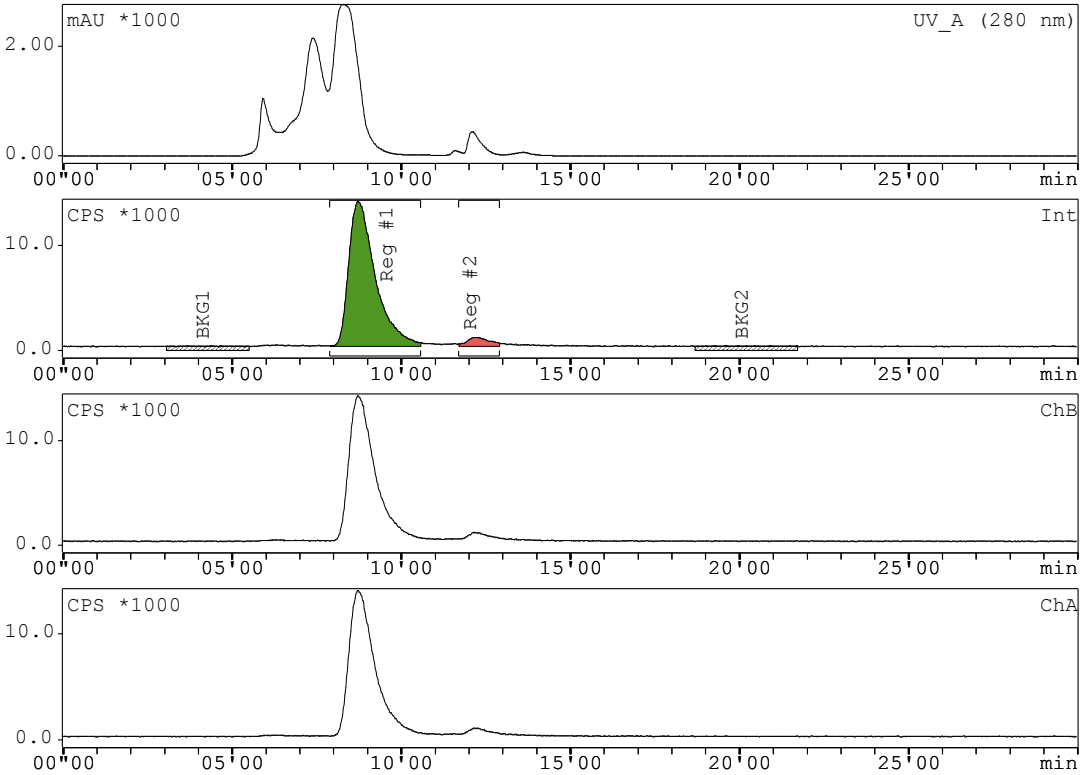

Sample description

Measurement: 160512_In111_s11, injection : 12/05/2016 14:16

Method: MICHELLE SEC2000 from: 03/03/2016 12:02

Dead time of column: 01'00 s

Radio detector: raytest Gabi Star Serial Nr.: #30484 raytest GINA star 20.04.09 Firmware V4.8

Integration Int

Substance	R/T	Type	Area	%Area	Conc
	s		Counts	%	

Reg #1	08'43	DD(M)	753021.6	95.08	No comp.
Reg #2	12'10	DD(M)	38927.2	4.92	No comp.

Integration c:\GINA_NT\MICHELLE SEC2000\160512_IN111_S7, 160512_In111_s7 Start: 12/05/2016 15:39

^{111}In-CHX-A''DTPA-scFv-Fc in human serum for 3h

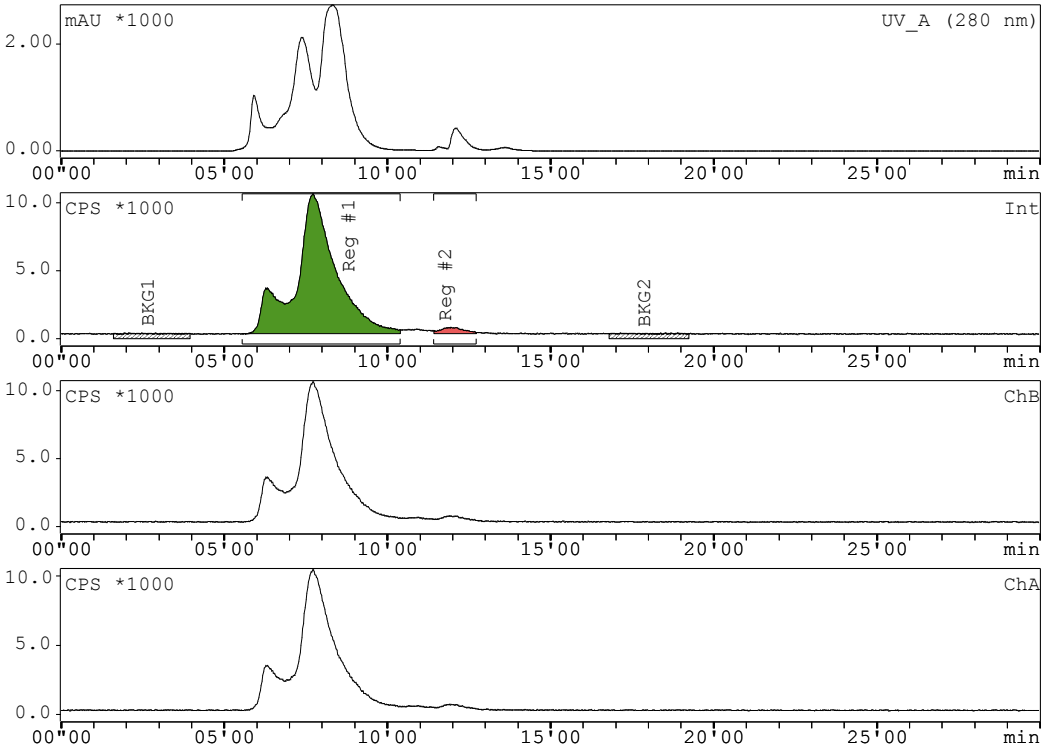

Sample description

Measurement: 160512_In111_s7, injection : 12/05/2016 15:39

Method: MICHELLE SEC2000 from: 03/03/2016 12:02

Dead time of column: 01'00 s

Radio detector: raytest Gabi Star Serial Nr.: #30484 raytest GINA star 20.04.09 Firmware V4.8

Integration Int

Substance	R/T	Type	Area	%Area	Conc
	s		Counts	%	
Reg #1	07'42	DD(M)	893670.9	97.49	No comp.
Reg #2	11'54	DD(M)	22976.2	2.51	No comp.

Integration c:\GINA_NT\MICHELLE SEC2000\160512_IN111_S12, 160512_In111_s12 Start: 12/05/2016 16:12

Indium-111 in human serum for 3h

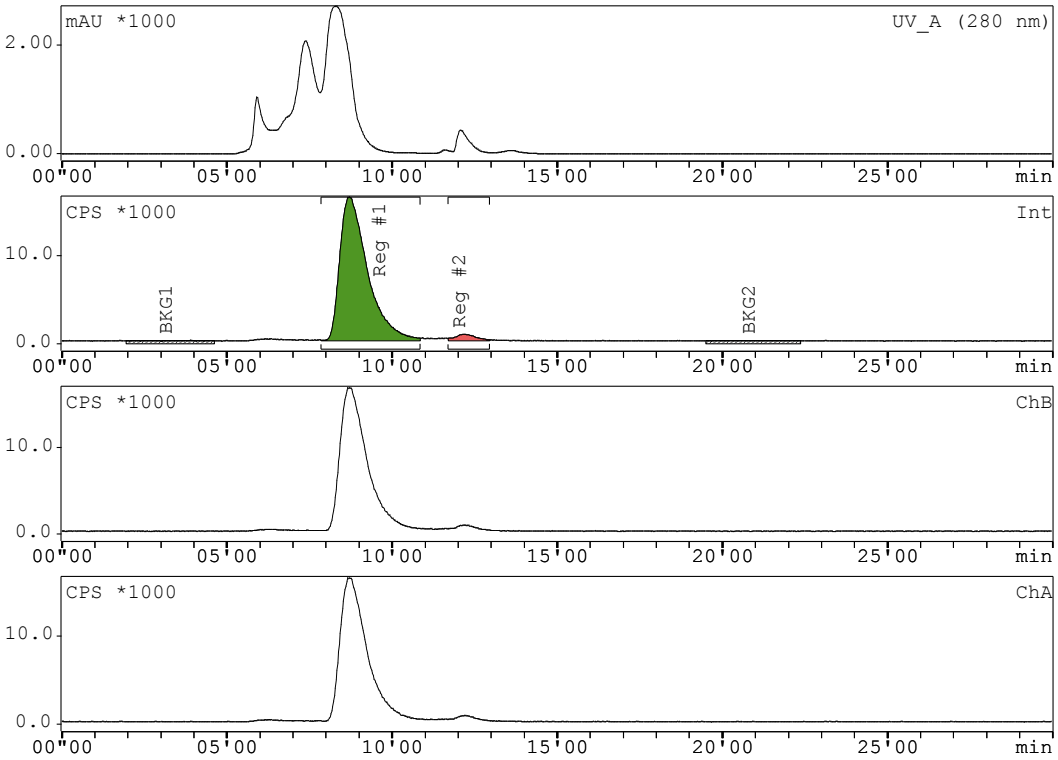

Sample description

Measurement: 160512_In111_s12, injection : 12/05/2016 16:12

Method: MICHELLE SEC2000 from: 03/03/2016 12:02

Dead time of column: 01'00 s

Radio detector: raytest Gabi Star Serial Nr.: #30484 raytest GINA star 20.04.09 Firmware V4.8

Integration Int

Substance	R/T	Type	Area	%Area	Conc
	s		Counts	%	
Reg #1	08'43	DD(M)	954432.0	96.66	No comp.
Reg #2	12'10	DD(M)	32948.8	3.34	No comp.

Integration c:\GINA_NT\MICHELLE SEC2000\160512_IN111_EXTRA_QC2, 160512_In111_extra_QC2 Start: 12/05/2016 17:24

QC of ^{111}In-CHX-A''DTPA-scFv-Fc (no human serum)

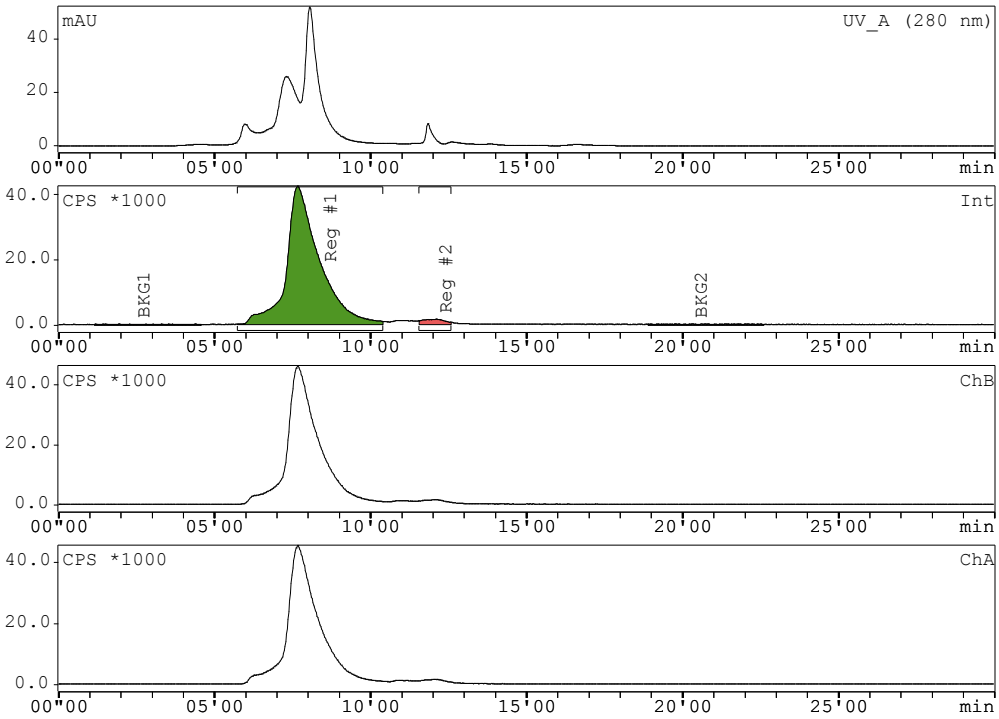

Sample description

Measurement: 160512_In111_extra_QC2, injection : 12/05/2016 17:24

Method: MICHELLE SEC2000 from: 03/03/2016 12:02

Dead time of column: 01'00 s

Radio detector: raytest Gabi Star Serial Nr.: #30484 raytest GINA star 20.04.09 Firmware V4.8

Integration Int

Substance	R/T	Type	Area	%Area	Conc
	s		Counts	%	
Reg #1	07'39	DD(M)	3099254	97.60	No comp.
Reg #2	12'32	DD(M)	76355	2.40	No comp.

Integration c:\GINA_NT\MICHELLE SEC2000\160512_IN111_S8, 160512_In111_S8 Start: 12/05/2016 19:48

^{111}In-CHX-A''DTPA-scFv-Fc in human serum for 7h

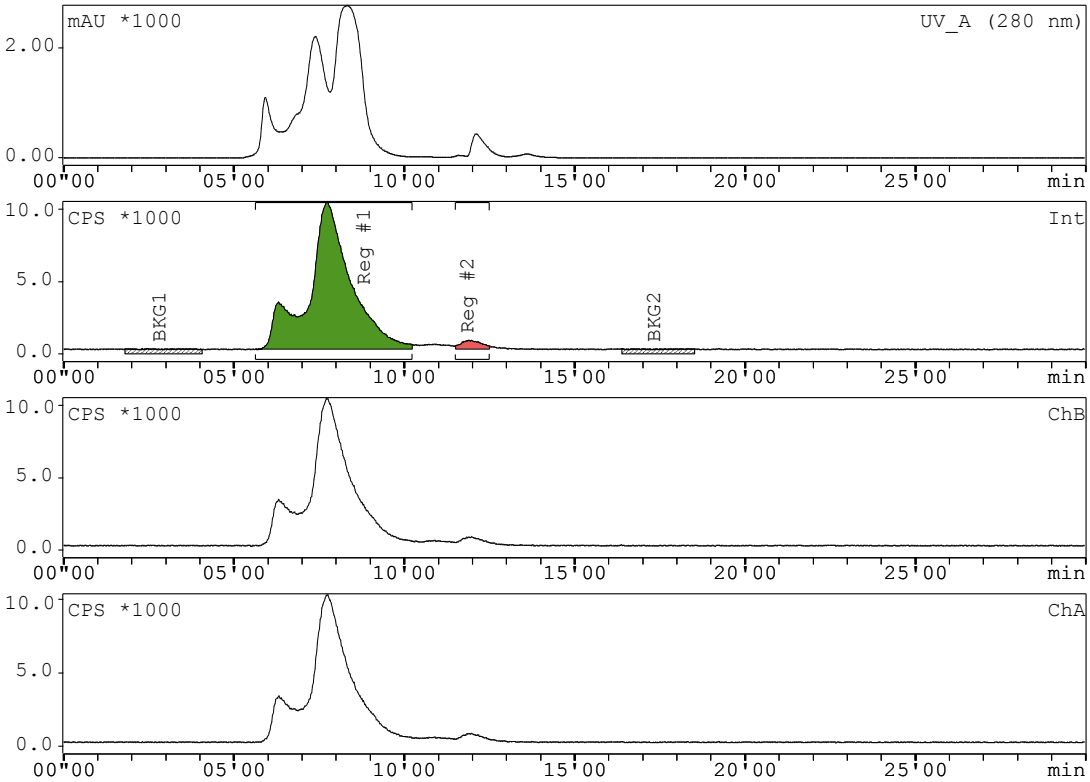

Sample description

Measurement: 160512_In111_S8, injection : 12/05/2016 19:48

Method: MICHELLE SEC2000 from: 03/03/2016 12:02

Dead time of column: 01'00 s

Radio detector: raytest Gabi Star Serial Nr.: #30484 raytest GINA star 20.04.09 Firmware V4.8

Integration Int

Substance	R/T	Type	Area	%Area	Conc
	s		Counts	%	
Reg #1	07'44	DD(M)	889189.8	97.16	No comp.
Reg #2	11'59	DD(M)	26004.3	2.84	No comp.

Integration c:\GINA_NT\MICHELLE SEC2000\160512_IN111_S13, 160512_In111_S13 Start: 12/05/2016 20:25

Indium-111 in human serum for 7h

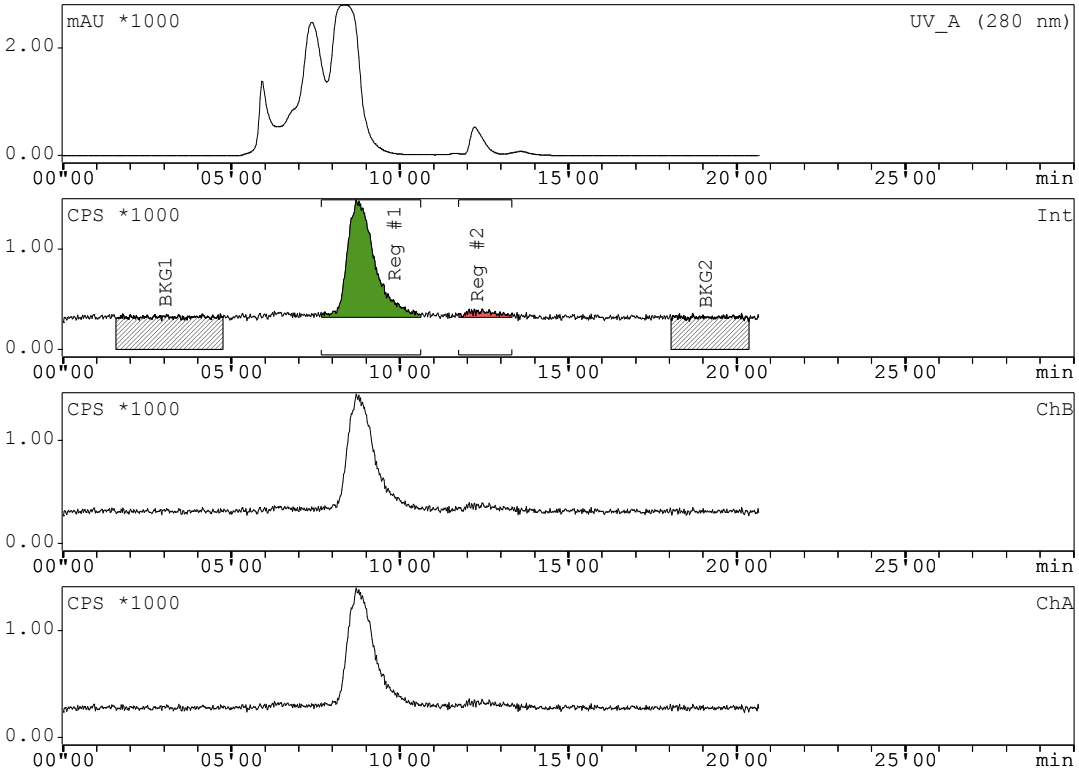

Sample description

Measurement: 160512_In111_S13, injection : 12/05/2016 20:25

Method: MICHELLE SEC2000 from: 03/03/2016 12:02

Dead time of column: 01'00 s

Radio detector: raytest Gabi Star Serial Nr.: #30484 raytest GINA star 20.04.09 Firmware V4.8

Integration Int

Substance	R/T	Type	Area	%Area	Conc
	s		Counts	%	
Reg #1	08'41	DD(M)	65788.49	94.59	No comp.
Reg #2	12'26	DD(M)	3762.15	5.41	No comp.

Integration c:\GINA_NT\MICHELLE SEC2000\160513_IN111_S9, 160513_In111_s9 Start: 13/05/2016 13:04

^{111}In-CHX-A''DTPA-scFv-Fc in human serum for 24h

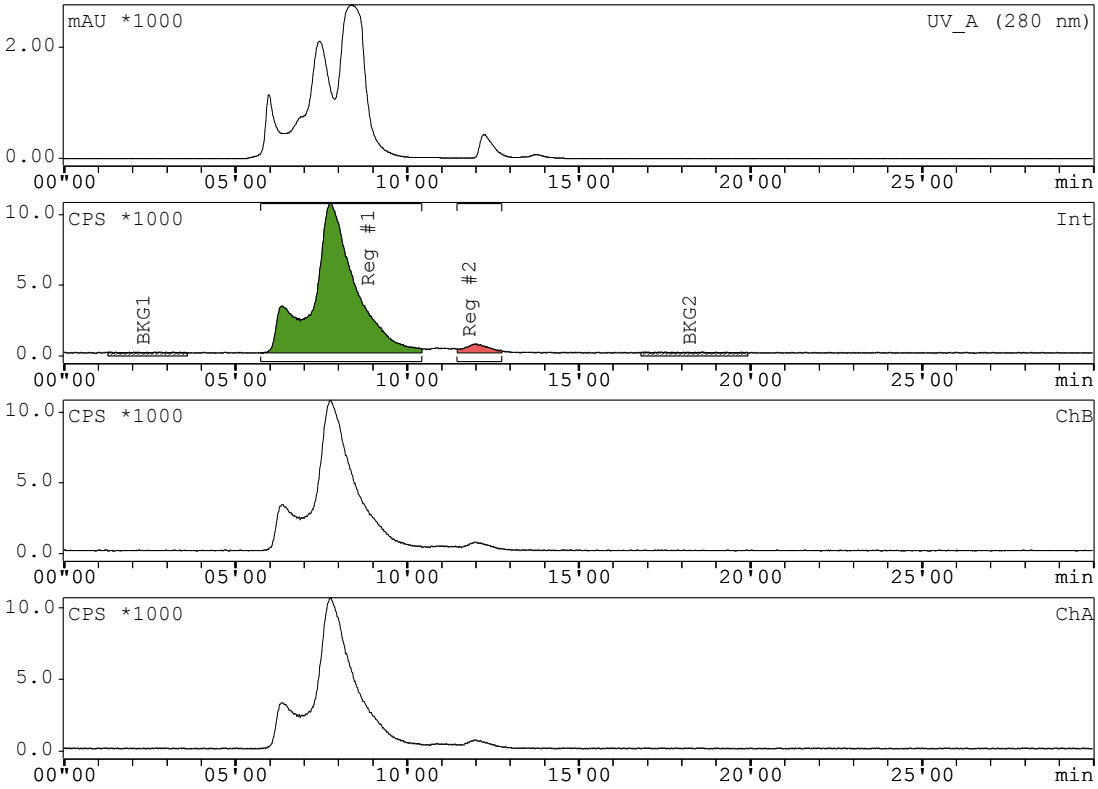

Sample description

Measurement: 160513_In111_s9, injection : 13/05/2016 13:04

Method: MICHELLE SEC2000 from: 03/03/2016 12:02

Dead time of column: 01'00 s

Radio detector: raytest Gabi Star Serial Nr.: #30484 raytest GINA star 20.04.09 Firmware V4.8

Integration Int

Substance	R/T	Type	Area	%Area	Conc
	s		Counts	%	
Reg #1	07'44	DD(M)	915397.3	96.96	No comp.
Reg #2	11'56	DD(M)	28744.8	3.04	No comp.

Integration c:\GINA_NT\MICHELLE SEC2000\160513_IN111_S14, 160513_In111_s14 Start: 13/05/2016 13:38

Indium-111 in human serum for 24h

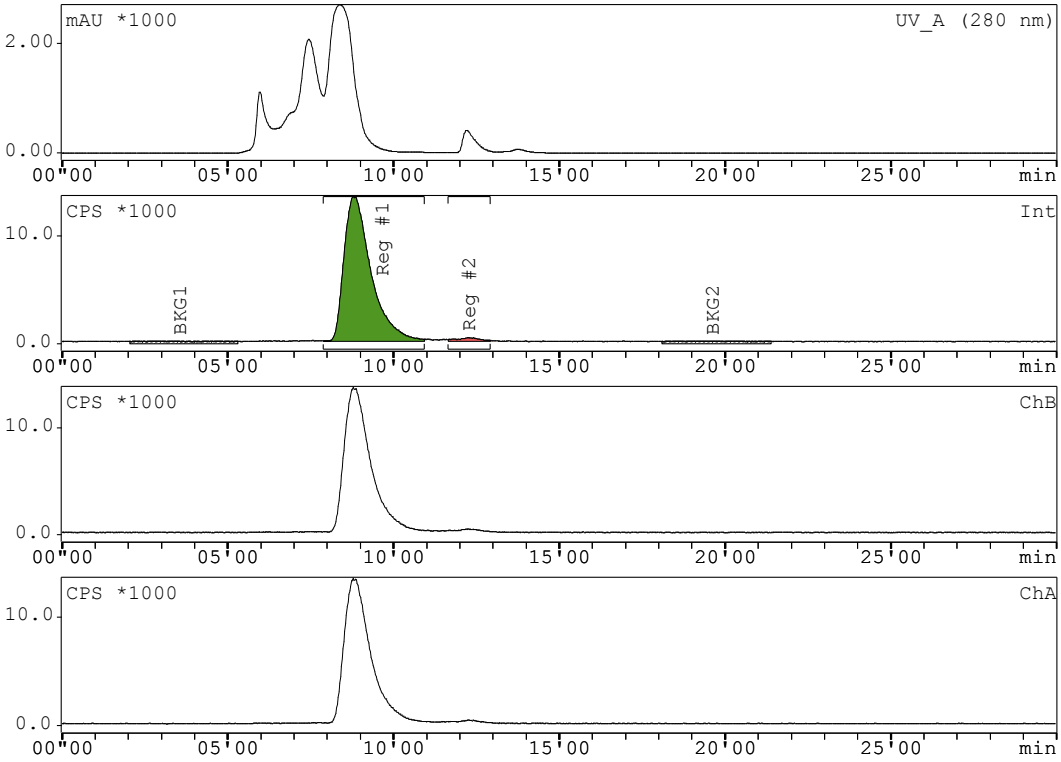

Sample description

Measurement: 160513_In111_s14, injection : 13/05/2016 13:38

Method: MICHELLE SEC2000 from: 03/03/2016 12:02

Dead time of column: 01'00 s

Radio detector: raytest Gabi Star Serial Nr.: #30484 raytest GINA star 20.04.09 Firmware V4.8

Integration Int

Substance	R/T	Type	Area	%Area	Conc
	s		Counts	%	
Reg #1	08'46	DD(M)	762102.4	97.91	No comp.
Reg #2	12'25	DD(M)	16231.2	2.09	No comp.

9.2 Other Publications

PLoS One. 2015 May 7;10(5):e0125994. doi: 10.1371/journal.pone.0125994. eCollection 2015.

The Breast Cancer-Associated Glycoforms of MUC1, MUC1-Tn and sialyl-Tn, Are Expressed in COSMC Wild-Type Cells and Bind the C-Type Lectin MGL.

Beatson R1, Maurstad G2, Picco G1, Arulappu A1, Coleman J1, Wandell HH3, Clausen H3, Mandel U3, Taylor-Papadimitriou J1, Sletmoen M2, Burchell JM1.

http://journals.plos.org/plosone/article?id=10.1371/journal.pone.0125994